WINDBACK SEAL DESIGN FOR GAS COMPRESSORS:

A NUMERICAL AND EXPERIMENTAL STUDY

A Dissertation

by

ADNAN MAHMOUD AL-GHASEM

Submitted to the Office of Graduate Studies of
Texas A&M University
in partial fulfillment of the requirements for the degree of

DOCTOR OF PHILOSOPHY

May 2007

Major Subject: Mechanical Engineering

WINDBACK SEAL DESIGN FOR GAS COMPRESSORS:

A NUMERICAL AND EXPERIMENTAL STUDY

A Dissertation

by

ADNAN MAHMOUD AL-GHASEM

Submitted to the Office of Graduate Studies of
Texas A&M University
in partial fulfillment of the requirements for the degree of

DOCTOR OF PHILOSOPHY

Approved by:

Chair of Committee,	Gerald L. Morrison
Committee Members,	Dara W. Childs
	John Vance
	Kenneth R. Hall
Head of Department,	Dennis L. O'Neal

May 2007

Major Subject: Mechanical Engineering

ABSTRACT

Windback Seal Design for Gas Compressors: A Numerical and Experimental Study.

(May 2007)

Adnan Mahmoud Al-Ghasem, B.Sc.; M.Sc., Jordan University of Science and Technology;

M.S., Texas A&M University

Chair of Advisory Committee: Dr. Gerald L. Morrison

Seals are considered one of the important flow elements of a turbomachinery device. Traditional labyrinth seals have proven their performance functionality by reducing leakage rates. Significant improvements on labyrinth seal functionality were obtained through altering the design geometry of labyrinth seals to prevent contamination across a seal and maintaining small leakage flowrates. This results in a windback seal that has only one tooth which continuously winds around the shaft like a screw thread. These seals are used in gas compressors to isolate the gas face seal from bearing oil. A purge gas is passed through the seal into the bearing housing. The helical design allows the seal to clear itself of any oil contamination. Windback seal performance is controlled through changing the seal geometry. A 2D graphical design tool for calculating the total and cavity leakage flowrates for windback seals is introduced.

The effectiveness of the Fluent CFD (Computational Fluid Dynamics) commercial code to accurately predict the leakage rate for windback seals was evaluated. The objective is to determine if CFD simulations can be used along with a few experimental tests to study windback seals of this design with air as the working fluid. Comparison of measurement and predictions for a windback seal using the κ-ε turbulence model with enhanced wall treatment functions show predictions and measurements comparing very well with a maximum difference of 5% for leakage rate. Similarly, the leakage rate of the tested smooth seal compares favorably with two dimensional CFD predictions, with a difference of 2%-11% and 8%-15% using laminar and κ-ε turbulent flow models, respectively. The variation of leakage with shaft speed and pressure ratio across the seals is accurately predicted by the CFD simulations. Increasing the rotor speed to 15000 rpm increases the measured leakage flowrate for the windback seal by 2% at high differential pressure and 4.5% at low differential pressure, and decreases it by 10 % for the smooth seal.

The effects of seal clearance, tooth pitch, cavity depth and the tooth number of starts on leakage flowrate, velocity and pressure distributions were studied numerically for three differential pressures and four rotor speeds.

DEDICATION

To my family:

Parents, ***brothers*** and ***sisters***

To my sons *Mahmoud* and *Mohammad*

To my daughter *Salma*

To *Samya* my wife

ACKNOWLEDGMENTS

"*Thanks to Allah for guidance and success*"

I would like to express my deepest thanks and appreciation to Dr. Gerald L. Morrison for his supervision, direction and continuous support through my graduate research and studies. My sincere thanks go also to Dr. Dara W. Childs, for his support, and encouragement, and for serving on my committee, as well as for allowing me to use his test rig facility to conduct my experiments. I would like also to thank Dr. John Vance and Dr. Kenneth R. Hall for their help in serving as committee members. Special thanks to John P. Platt of BP Company, for their support and for funding this project.

I also thank my coworkers and friends at the Turbomachinery Laboratory for their support and understanding.

Finally, I am indebted to the Jordan University of Science and Technology for everything, starting with my B.Sc. degree and ending with supporting my graduate studies at Texas A&M University.

TABLE OF CONTENTS

Page

LIST OF FIGURES

FIGURE Page

FIGURE Page

FIGURE Page

FIGURE Page

FIGURE Page

FIGURE Page

LIST OF TABLES

NOMENCLATURE

A	Leakage area of the seal πDc [m^2]
c	Radial seal clearance [m]
c^*	Normalized radial clearance
C_d	Discharge coefficient
D	Shaft diameter [m]
e	Eccentricity ratio
EV	Velocity magnitude maximum error indicator
EP	Static pressure maximum error indicator
DP	differential pressure across the seal [kPa]
h	Cavity depth [m]
h^*	Normalized cavity depth
i, j	index notation (1,2,3 representing x , y and z directions)
k	Specific heat ratios
L	Seal length [m]
$\dot{m}$	Leakage mass flowrate [kg/s]
n	Equivalent number of teeth L/s
P	Static pressure [Pa]
P^*	Non-dimensional pressure ratio $(P-P_e)/(P_i-P_e)$
$\dot{Q}$	Air volumetric flowrate [m^3/s]
R	Air constant [$J/(kg.K)$]
Re_{axial}	Axial Reynolds number $\dot{m}/\pi D\mu_{avg}$
Re_{cir}	Circumferential Reynolds number $\rho\Omega Dc/(2\mu_{avg})$
s	Tooth pitch [m]
s^*	Normalized tooth pitch
t	Tooth thickness [m]
T	Temperature [K^o]
Ta	Taylor number $\mathrm{Re}_{cir}^2(2c/D)$
V_2	Circumferential velocity in the windback seal second cavity
V_6	Circumferential velocity in the windback seal sixth cavity

x, y, z	Rectangular coordinate direction
r,θ,x	Cylindrical coordinate direction

Greek symbols

ρ	density [kg/m^3]
μ	Dynamic viscosity [$Pa.s$]
Ω	Rotor speed [rpm]
κ	Turbulence kinetic energy [m^2/s^2]
α	Flow coefficient
γ	Kinetic energy carry over coefficient
ψ	Expansion coefficient or Pressure function
ν	Specific Volume [m^3/kg]
ε	Turbulent dissipation rate [m^2/s^3]
φ	Helix angle [$degree$]
β	Stream spread angle [$degree$]
χ	Kinetic energy ration within the seal cavity $V_{\min}^2 / V_{\max}^2$
τ	Wall shear stress [Pa]

Subscripts

i	Inlet condition
e	Exit condition
h	Hydraulic
$circ.$	Circumferential direction
min	Minimum
max	Maximum
avg	Average
mag	Magnitude

Abbreviations

CFD	Computational fluid dynamics
DE	Drive end
NDE	Non-drive end

EXP	Experiment
TH	Theory (Numerical simulation)
TOS	Tooth on Stator
TOR	Tooth on Rotor
rpm	Revolution per minute
LP	Low pressure difference (34.5 kPa)
MP	Medium pressure difference (68.9 kPa)
HP	High pressure difference (103.4 kPa)

INTRODUCTION

Introduction

Seals are considered one of the important flow elements of a turbomachinery device. A seal is defined as an element which keeps the integrity of a particular substance intact by either preventing the escape of a fluid or controlling leakage to prevent a contamination. The most common seal types that affect the operation and performance of a turbomachinery device such as gas turbines, compressors, or steam turbines are labyrinth seals. Geometrical parameters of a labyrinth seal are shown in Fig. 1. Fig. 2 shows the basic design of three types of labyrinth seals which are: (a) straight-through, (b) stepped and (c) staggered seals. The tooth can be either on the rotor (TOR) or on the stator (TOS) which produce different flow characteristics, except for staggered type because of symmetry. The labyrinth seals have proven their performance functionality by reducing leakage rates as seen from the wide literature studies for various seal geometric designs. Its principle of operation is to change the available static pressure head into kinetic energy across a constriction which is dissipated by viscous effects in the downstream chambers. If all the energy is dissipated it is called the ideal labyrinth seal. The flow's kinetic energy in the next cavity in a real seal will be (1) dissipated by turbulence viscosity interaction into heat (2) recovered as a static pressure and (3) carried over to the next cavity. This will continue until the flow exits the last tooth. The second and third effects reduce the effectiveness of the seal.

A windback seal design can produce a significant improvement in preventing contamination across a seal. In this seal, the groove ring creates a wind or small counter pressure when rotating which reduces oil leakage flowrate according to Dresser-Rand [1]. Fig. 3 shows a windback seal which is defined as a helically grooved liner, installed either on a stationary member or on a rotating shaft, or on both and operating with a clearance between the shaft and the stator. It has similar geometrical parameters to labyrinth seals with the addition of a helix angle, φ, which is defined such that, a helix with zero degree represents a circumferential groove seal (labyrinth seal) and a helix with 90° represents an axial groove seal. It works as a labyrinth seal except that it can have lower leakage flowrates resulting from a pumping action through transferring the momentum to the fluid in a direction opposite to the main flow direction.

This dissertation follows the style of Journal of Tribology.

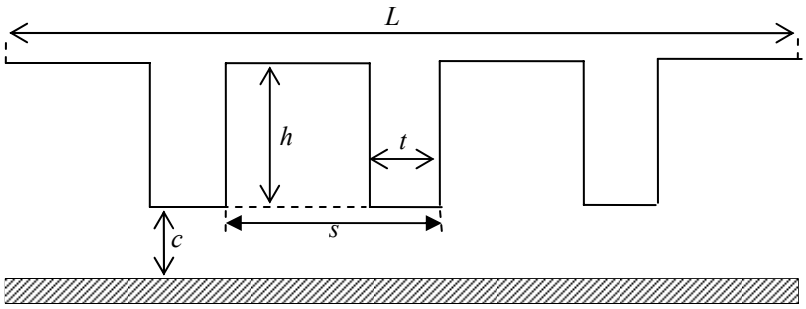

Fig. 1 Labyrinth seal geometrical parameters.

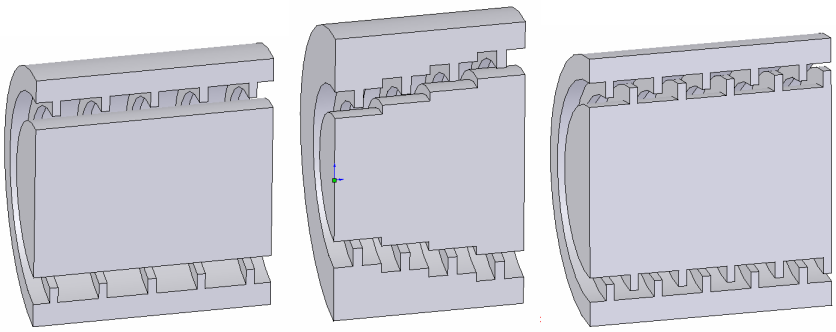

(a) (b) (c)

Fig. 2 Type of labyrinth seals (TOS): (a) straight-through, (b) stepped and (c) staggered.

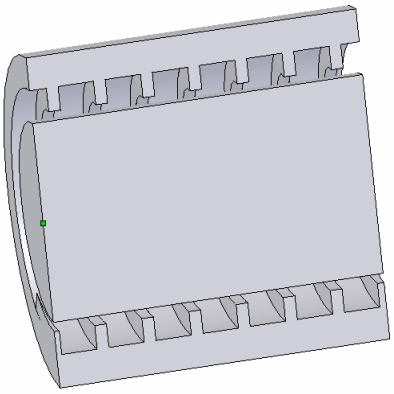

Fig. 3 Windback seal (TOS).

The direction of a helix in a windback seal plays a major role in determination of its work performance such that:

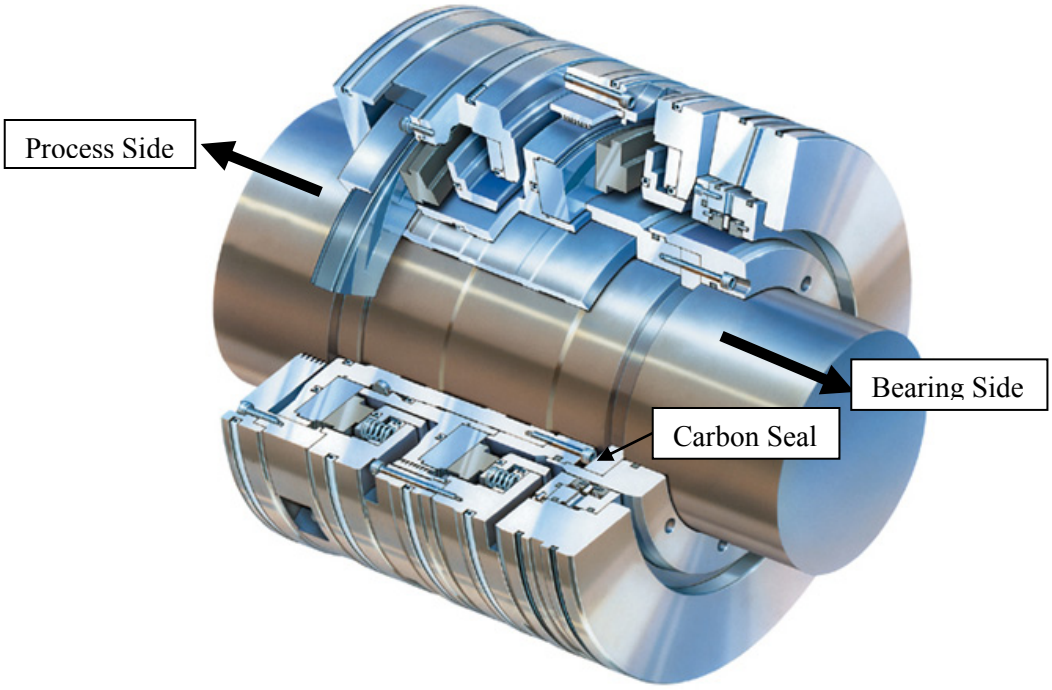

Fig. 4 Gas seal after John-crane [2].

(1) Helix in the direction of shaft rotation will increase the leakage flowrate for both air and oil seals compared to labyrinth seals. This flushing action has this major advantage of keeping contamination out.

(2) Helix in the opposite direction of shaft rotation will reduce the leakage flowrate for oil seals by 1400% [1] compared to other seals having the same size. For gases it will leak the same as labyrinth seal or higher by a small percent. This configuration is used for sealing purposes.

One of the most popular applications for a windback seal is in centrifugal gas compressors, where the gas face seal will fail if exposed to lubricating oil. Therefore the windback seal is placed between the low pressure sides of the gas face seal and the hydrodynamic bearings used to support the rotor to prevent this contamination from occurring. Fig. 4 shows a high pressure gas lubricated, non-contacting gas seal type 28EXP for turbo-compressors, John-crane [2]. The carbon seal, which runs in the shaft groove, is designed to protect the gas seal from oil contamination coming from the bearing side. The windback seal device described in this study will replace both the fragile carbon ring and the shaft groove in gas seals, similar to the one shown in Fig. 4. The windback seal in this location with this

configuration serves the following purposes: (1) If at start up or some other time the seal has oil inside, the thread will act as a screw pump helping move the oil back to the bearing housing (acts as a seal for the bearing). (2) The gas purge will pass not only under the seal tooth (like labyrinth seal) but also through the thread cavity which acts as a flow conduit of gas purging the oil back into the bearing housing (acts to keep oil away from the gas face seal). The purged gas through the windback seal is normally Nitrogen. The exhaust mixture of Nitrogen and oil mist vapor are cleaned from oil mist, and then ventilated.

The main objective of development and performance evaluation of windback seals for gas compressors is to protect the face gas seal from oil contamination, while assuring the seal operates efficiently and is effective in terms of operational cost and reliability. Therefore the operation of the windback seal must be understood from the perspective of the flow field (pressure distribution, air velocities and leakages).

Literature Review

The main objective of designing any seal is to reduce the leakage of the desired liquid used in a process. Therefore it is important to understand how the seal works in order to predict its leakage rate and to optimize the leakage considering different geometrical parameters for its crucial role in operating turbomachinery devices in an efficient and economic way.

The type of seal under study is a windback seal with helix angles less than 1^0. The author did not find much data in the open literature relating the leakage rate and the design parameters for such a seal. Bootsma [3] discussed the operational principle of oil-lubricated spiral-groove bearings and their advantages in terms of self sealing, load capacity and stability in comparison with plain bearings. The self sealing effect was experimentally tested for spiral-groove bearings (herringbone type) for different geometrical configuration with TOS and TOR cases and for different oil types and rotor surface speeds. The rectangular groove shape was chosen because of its high pumping pressure compared to other cavity shapes. The herringbone bearings were tested for different shaft diameters (10 to 20 mm), *h/c* ratios from (1 to 9), groove width to depth ratio from (3.7 to 41.7) and for different groove angles (from 3.7^0 to 16.2^0). The leakage rates of these self sealing bearings were due to either plain face leakage or groove leakage and are in consequence of break down of the air to liquid interface at certain rotor running speed. He found that the speed of rotation at which leakage started was particularly independent of whether the TOR or the TOS design was used. In addition, the surface speed at which the leakage rate starts

via the plain bearing face was found to depend mainly on surface tension, on the other hand a strong dependence on surface tension, viscosity and groove width for leakages via the groove.

Gansle and Childs [4] compared the measured leakage rate for four different gas seals; two grooved with helix angles of 15^0 and 30^0 against rotation, and one smooth and one honeycomb seals. Their test includes rotational effects up to 16000 rpm and different seal pressure ratios. They found that increasing the helix angle will increase the leakage rate, and that the 15^0 and 30^0 helix angle, and the smooth seals leaked approximately 1.66, 2.2, and 2.3 times more than the honeycomb seal, respectively.

The windback seal is similar in many design aspects to the labyrinth seals in terms of tooth thickness, cavity depth and width, number of equivalent tooth and operating clearances. For that reason and because of the large number of publications for both theoretical design and experimental results of labyrinth seals, a short summary of what have been done will be presented.

Two summaries of the important published papers pertaining to labyrinth seals were found. Sneck [5] in 1974 published a literature survey of the labyrinth seal theory and design, from the thermodynamic and fluid mechanics perspective. The labyrinth seal was introduced by C. A. Parsons accompanied by his development of the steam turbine to "interpose a tortuous flow path between high and low pressure regions by means of a series of non contacting restrictors and separating chambers" and published in 1938 [6]. Parson's original design geometry was then modified, and the staggered and step labyrinth seals were introduced. Cogan [7] in 1982 summarized most of the work that had been done in the open literature for labyrinth seal design up to 1981 in terms of empirical code.

The earliest fundamental analytical method for predicting the labyrinth seal leakage was introduced by Martin [8] in 1908 for a series of orifices. He derived a leakage equation for staggered and radial labyrinth seals for compressible gas with no shaft rotation using the ideal gas law with the assumption of isothermal flow process neglecting the kinetic energy carry – over from one throttling to the next. Stodola [9] did a similar analysis to Martin's, but he compared his leakage predictions to the available experimental data, a 14% leakage difference was found. Dollin and Brown [10] developed a more general analytical leakage flow equation using the ideal gas law with a $Pv^k = const.$ thermodynamic process where k =1, 1.3, ∞ which represents isothermal, steam isentropic process and incompressible flows, respectively. The flow

was assumed to pass through a series of constant area orifices with no shaft rotation and neglected the carry-over effects.

An empirical and analytical modification of labyrinth seal leakage analysis was performed by Egli [11] which is still the most popular and widely used. He developed an approximate leakage equation for both straight-through and staggered type labyrinth seals. In his equation he includes experimentally determined coefficients to account for the kinetic energy carry-over (γ =1 for a well-staggered labyrinth) and a flow coefficient to compensate for the effects of the flow friction through the seal throttling as a function of number of throttles, clearance to pitch ratio, tooth thickness and pressure ratio. His leakage equation is given by

$$\dot{m} = A\alpha\psi\gamma\sqrt{P_i/v_i} \tag{1}$$

Where, γ is the carry-over coefficient and ψ is the expansion coefficients and is given as a function of the total pressure ratio and the number of throttles by

$$\psi = \sqrt{\left(1-(P_e/P_i)^2\right)/\left(n-\ln(P_e/P_i)\right)} \tag{2}$$

Egli [11] conducted static tests on various types of labyrinth seals and established $\alpha\psi$ curves as a function of pressure ratio, number of throttles and clearance to tooth thickness ratio (*c/t*). Then he calculated the flow coefficient α and found that it is constant for *c/t* greater than 3.5. He summarized his conclusion in a practical design table for different labyrinth seals with the same leakage rate, for different total lengths, clearances, number of throttles, pitch and seal types. Hodkinson [12] proposed a formula for calculating the carry-over coefficient given by,

$$\gamma = \sqrt{1\Big/\left(1-\frac{n-1}{n}.\frac{c/s}{c/s+0.02}\right)} \tag{3}$$

Many researchers have evaluated techniques to optimize the leakage of labyrinth seals by varying geometrical design parameters using either experimental or numerical means. Zabriskie and Sternlicht [13] present a simplified theoretical method for calculating the leakage rates for different labyrinth seal geometries (tooth width and angle, cavity size and clearance) in terms of a non-dimensional weight factor. Their analysis is based on charts; friction factor as a function of Reynolds number and flow coefficient as a function of pressure ratio for different friction factors. Their predictions were within 20% of published experimental studies. Leakage rate can be minimized by optimizing the tooth depth to pitch ratio, tooth width to clearance ratio and forward angle of the teeth with respect to the flow direction. A value of one for the tooth

depth to pitch ratio and a 40° tooth angle will minimize the leakage rate. In addition, decreasing the tooth width to clearance ratio will decrease the flow coefficient.

Heffner [14] introduced a method for correlating test data in order to calculate the leakage rate of labyrinth seals from the same family using two tests which neglected the rotation effects. In his experiments, a straight-through labyrinth seal was used. The coefficient of contraction was determined through experimental tests, and is a function of seal geometry and pressure ratio. He measures the coefficient of contraction for one blade as a function of Reynolds number. Then, he measures the specific leakage rate for a whole seal with a minimum number of blades and for different spacing and clearances as a function of the expansion coefficient defined by Egli [11]. The accuracy of his method for predicting the leakage rate is on the order of 3% which is mainly the average deviation of his measurements from the mean with the assumption that the calibrated orifice meter has no error. Prasad et al. [15] tested a static straight- through labyrinth seal for different pressure ratios and radial clearances. They compared their tests to a computer simulation based using the κ-ε turbulence model in the CFD program Fluent. The maximum variation between the experiments and simulations was 8.6%. The velocities, kinetic energy, static pressure and Mach number were presented in contour plots, to have a better understanding of the maximum kinetic energy and how it affected the flow resistance and hence the leakage rate. In addition, they summarize the available literature for labyrinth seal design based on the seal geometries and how it affects the flow parameters.

Rhode and Hibbs [16] developed a finite difference computer program code based on solving the Reynolds Averaged Navier-Stokes equations using a κ-ε turbulence model to predict leakage rates. A variety of quantity distributions (turbulence energy, axial velocity, swirl velocity, pressure and temperature) were presented for both annular and straight-through labyrinth seals with different clearances. The up and down stream reservoir pressures were used as the boundary conditions for the simulated flow. Their prediction agreed well with the measurements taken from the open literature to within 8%. They compared smooth and labyrinth seals numerically for different clearances and showed that the smooth seal leaks more than the labyrinth by 20% for a wide range of clearances. In addition, larger pressure drops across the exit of the annular seal was seen.

Yucel and Kazakia [17] presented a new approach for calculating the leakage rate of labyrinth seals in a simple analytical and explicit method by incorporating a constant and a pressure dependent flow coefficient to extend the analysis for higher pressure differences across

the seal. Their predictions compared favorably with the previous numerical analysis and experimental tests. Isothermal flow with constant pressure at each cavity and an ideal gas were assumed. Willenbarg et al. [18] studied the effect of axial Reynolds number and pressure ratio on leakage rate of a stepped labyrinth seal for different seal clearance and tip geometry. They found that pressure ratio, Re_{axial}, tip geometry, and seal clearance, affected the sealing performance. Increasing seal clearance and/or pressure ratios increases the flow coefficient. In addition, the critical axial Reynolds number for which the flow coefficient is constant was found to be in the 30000 to 40000 range, compared to Egli [11] value of 1000 for a sharp edged orifice. Furthermore, they found that increasing the fin tip radius increases the flow coefficient.

In addition to varying geometric seal parameters, other researchers have studied the effects of changing operating conditions, such as rotation speed on seal leakage rate. Komotori and Miyake [19] developed a theoretical method for calculating the leakage rate of straight-through labyrinth seals (tooth on rotor) based on the fundamental assumptions of flow pattern in the labyrinth passages such as a constant diverging angle of the flow (6°) , pressure and temperature are constant in a single cavity, etc. Different seal geometries were studied namely seal clearance (0.2-0.36 mm), tooth number (1-12), tooth thicknesses (1-6 mm), and pitch and depth of the groove (0-2.5 mm). In addition to different pressure ratios and rotor surface speeds up to 250 *m/s*. Good agreement between predictions and measurements performed by the authors was found. Their predictions were under-estimated from the measurements of the labyrinth coefficient by a maximum of 20%. Rotation effects on leakage rate were studied experimentally and found to reduce leakage rate considerably, especially at small clearances and shallow grooves. Increasing peripheral surface velocity up to 250 *m/s* reduces the leakage rate between 8% and a maximum of 21% for simple annular passage. It is interesting to notice that the leakage characteristics with rotation for tooth on stator case differ from the case when the tooth on rotor. It was found that the rotation has a minimal effect on leakage rates with tooth on stator, with a 4% or less reduction in leakage rate at 80 *m/s*.

Stocker [20] tested a new design of staggered labyrinth seals with different geometries (clearance, tooth pitch, and number of teeth) in order to minimize the leakage through increasing the internal turbulence inside the seal cavity. His experiments consisted of three stages (1) water test rig to visualize and improve the turbulence in the cavities, (2) the improved design was then tested in an air static test rig, and (3) a dynamic air test rig was used to determine the influence of rotation speed on leakage. He presented his data as a non-dimensional flow coefficient

$\alpha = \dot{m}\sqrt{T}/(PA)$ versus pressure ratio with maximum inlet pressure of 2.5 *atm* and maximum rotor surface speed of 240 *m/s*. His improved design reduced the leakage by 10-25%. The rotational speeds had minimal effect varying from 0 to 3% reduction in leakage. These values were within the accuracy of the measurements.

Waschka et al. [21] studied the effect of rotational speed (up to 10000 rpm) on the leakage rate for different clearances and pressure ratios for a straight-through labyrinth seal (TOR). They presented the results in terms of a discharge coefficient ($C_d = \dot{m}_{meas}/\dot{m}_{ideal}$) and found that the discharge coefficient decreased with increasing rotational speed beyond $Ta/\mathrm{Re} \rangle 0.2$, the Taylor and Reynolds numbers were calculated based on the hydraulic diameter $D_h = 2c$. A good agreement between their measurements and predictions based on a 2-D model at 0 rpm was found. Their predictions under-estimated the measured discharge coefficient by a maximum of 12%.

Zimmermann and Wolff's [22] work was based upon unpublished test results and a survey from literature. They presented a correlation mostly in the form of figures for straight through and stepped labyrinth seals to predict the leakage rate for different seal geometries (*n*, *c/t*, *s/c, h/s*, pressure ratios) in terms of a discharge coefficient defined by $\dot{m} = \gamma\, C_d \dot{m}_{ideal}$ as a function of axial Reynolds number $\mathrm{Re} = UD_h/\nu$. They found that the effect of rotation was negligible for $\mathrm{Re} \rangle 10{,}000$ but the effect is high for laminar flow especially at low *Re*.

Labyrinth seals are used in gas compressors to reduce leakage flowrates. Additionally, they are used to protect the process gas and to prevent oil contamination from the bearing side. Boyman and Suter [23] identified the oil contamination transport mechanisms in a buffered straight-through labyrinth seal (TOR). They describe two mechanisms of oil transport: (i) diffusion of the oil-vapor due to the difference in concentration between the oil-vapor and the buffering –fluid (ii) transport of small oil droplets in the opposite direction of the buffering flow due to the complex flow created in the labyrinth seal. They conducted two tests: a diffusion test using propane gas as the back–flow fluid with air as the buffering fluid, and a large-scale flow visualizing test using water as the buffering fluid with the injection of a colored dyes to determine the flow direction within the seal cavity and clearance, varying the shaft speed and the axial flow velocity. They found that transport with diffusion occurs when the buffering axial flow velocity is low, as well as for a low number of teeth. In addition, the oil droplets transport occurs due to the fluctuation in the axial velocity (measured using a Laser-Doppler-Velocimeter)

and especially under the teeth. Increasing rotor speed has no clear effect on transport with diffusion. Also, they found from the visualizing tests that there are two similar overlapping helices generated within the seal cavities due to rotor speed only, and when introducing a buffering fluid the two helices are distorted.

Park and Rhode [24] studied the effect of injection pressure in a buffer labyrinth seal on preventing oil vapor contamination from reaching the process gas side of the seal. They found through numerical investigation that the oil vapor leakage can be completely prevented if the buffer-gas injection is higher by at least 6% from the bearing gas pressure. The effect of changing the clearance from 0.25 mm to 0.36 mm increases the injection gas flowrate but did not change the critical pressure ratio. Park and Rhode [25] numerically investigated the geometry effects on oil vapor flow through buffer gas straight through labyrinth seals. They found that the vapor mass transfer from the flooded, non-mist regime labyrinth seal decreases by increasing the pitch and decreasing the cavity depth. In addition, the vapor mass flowrate increases by increasing the seal radial clearance and by increasing the oil film surface area.

Objectives

The primary objective of this study is to compare the CFD (Fluent simulation software package) simulations to measurements in order to evaluate a prediction tool. The resulting procedure will be used to perform simulations to: (i) develop a better understanding of the flow physics of the windback seal, and (ii) to develop a design methodology for the windback seal. Two seals had been simulated and tested experimentally. The CFD code was validated by comparing the measured and predicted leakage rates of these two seals.

Minimizing the leakage flowrate of a windback seal, and maximizing the axial and circumferential velocities within the seal clearance and cavity, respectively, constitutes a well designed seal. This can be achieved through proper selection of the seal geometrical parameters. Although the axial and circumferential velocities are used as an indication tool of how the seal will perform in preventing oil contamination by diffusion as described by Boyman and Suter [23] for labyrinth seals, the diffusion process of oil vapor was not addressed in the numerical simulations of this study, due to its complexity in three dimensional simulations. The wall shear stresses are also used as an indication tool of how the seal will perform in displacing an oil film from the seal cavities. Therefore the wall shear stresses in the seal cavity were calculated to give an idea about their magnitude. The magnitude of the wall shear stresses required to displace an

oil film from seal cavities were not addresses in this study. Including: (i) the oil vapor diffusion and (ii) displacing oil films through high wall shear stresses in windback seals in numerical simulations are highly recommended in future studies.

The effects of multiple-tooth start geometries for variable clearances, tooth pitches, cavity depths and helix angle (given in Table 1) on the performance of the windback seal have been evaluated using CFD simulations. In addition, the effects of different operation conditions (namely differential pressures and rotation speed) on leakage flowrate were studied for each case given in Table 1. Double tooth starts is two-intertwined grooves, where the two tooth starts are separated by a 180° with twice the pitch of single start geometry.

Table 1 Simulation matrix.

No. of start	*c* (*mm*)	*s* (mm)	*h(mm)*	φ (deg)
Single	0.05	3.56	2.94	0.56
	0.10	3.12	2.94	0.49
		3.56	0	0.56
			1.47	
			2.94	
		4.14	2.94	0.65
	0.15	3.56	2.94	0.56
Double	0.10	7.11	2.94	1.11

EXPERIMENTAL AND NUMERICAL SETUP

Test Rig Description

Main Test Rig

The test rig described by Kaul [26] for oil seals static and dynamic testing was used with some modification. Fig. 5 shows a photograph of the test rig that will be used to study the flow characteristics of the windback and smooth seals with air as the working fluid.

The test rig consists of the following two major components: (1) the base which is fabricated from welded mild steel plates to support the main test section and the air drive turbine, (2) two pedestals spaced approximately 381 mm (15 *in*) apart to support the test rotor. An air turbine delivers approximately 65 *kW* is used to drive the rotor up to a maximum speed of 17,000

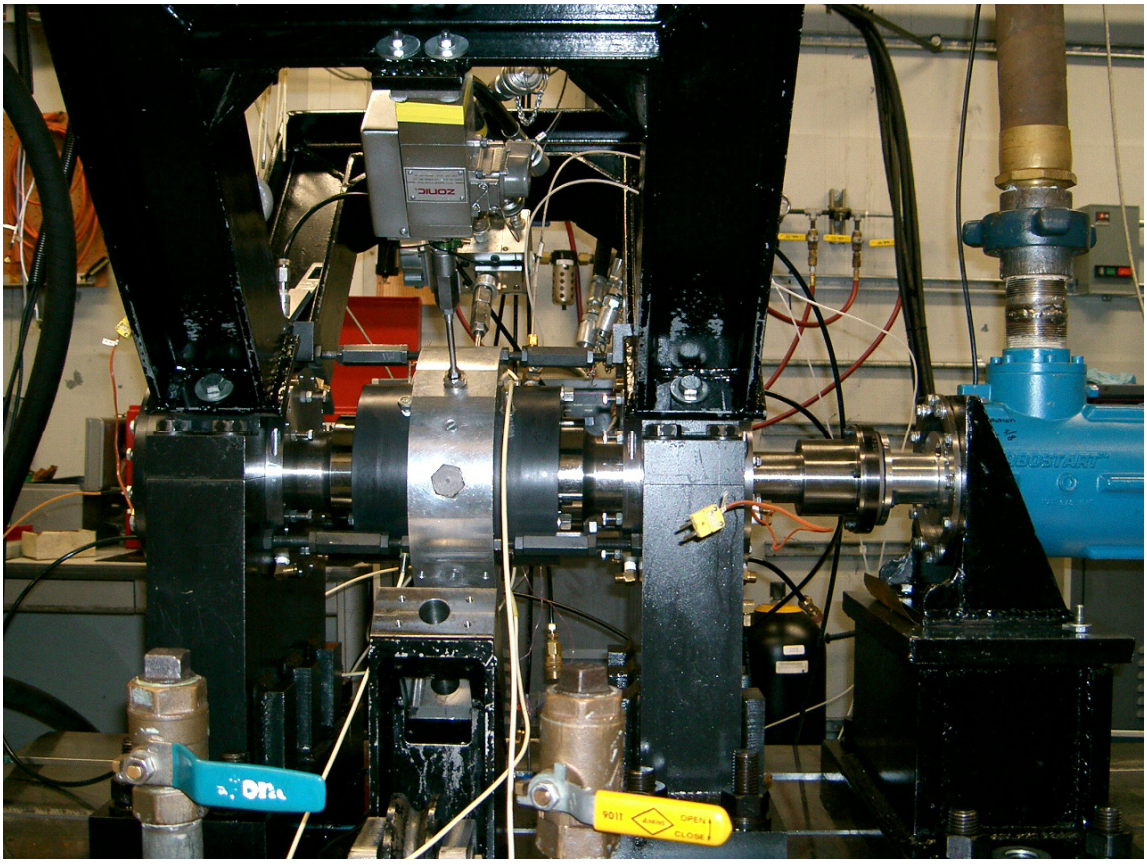

Fig. 5 Test rig description photo.

rpm through a high-speed flexible-disc coupling. The test rotor has a diameter of 0.1168 *m* (4.599 *in*). The rotor is supported on two ball bearings. They are lubricated through an oil-mist system.

A stator is used to hold the seal under test and all the associated instrumentation which mainly consist of: thermocouples, pressure taps and Pitot probes. Two hydraulic shakers are used to move the stator statically. Six pitch stabilizers are used to hold the stator axially. These pitch stabilizers are also used to angularly align the shaft with the rotor.

Shaker System

Two orthogonally mounted hydraulic shaker heads are attached to the stator middle section via elastic stingers. The stator-shaker-stinger arrangement is shown in Fig. 6. The *x*-direction shaker can displace the stator with static loads up to 4.45 *kN* (1000 *lbf*) in tension and compression, while the *y*-direction shaker can displace the stator with static loads up to 4.45 *kN* (1000 *lbf*) in tension and 11.1 *kN* (2500 *lbf*) in compression.

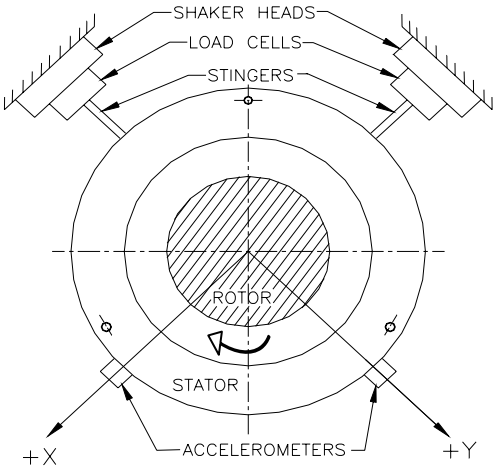

Fig. 6 Shaker-stinger configuration (NDE side).

Air Supply System

Fig. 7 shows the supply air monitoring/control system. A 17.24 *bar* (250 *psi*) air supply line supplies the air to the test facility room, which passes through an 8.62 *bar* (125 *psi*)

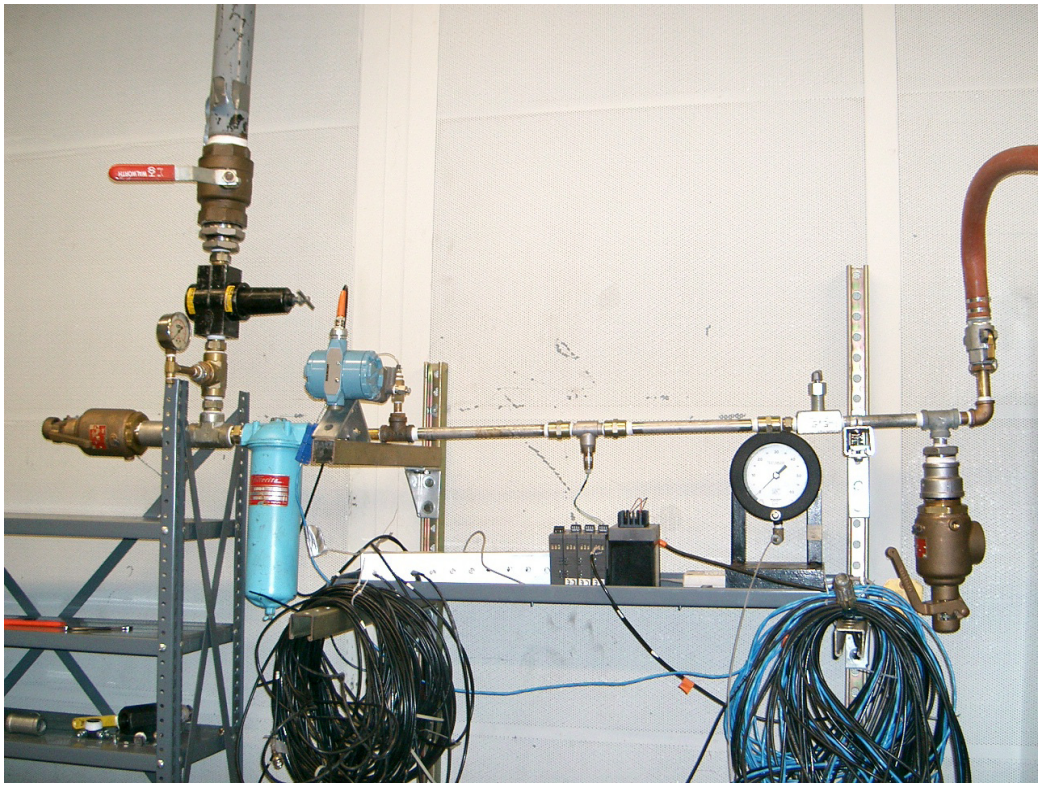

Fig. 7 Air supply system.

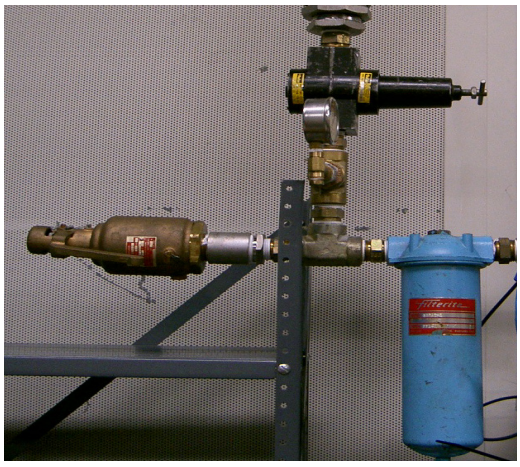

Fig. 8 Regulator and HP safety valves and air filter.

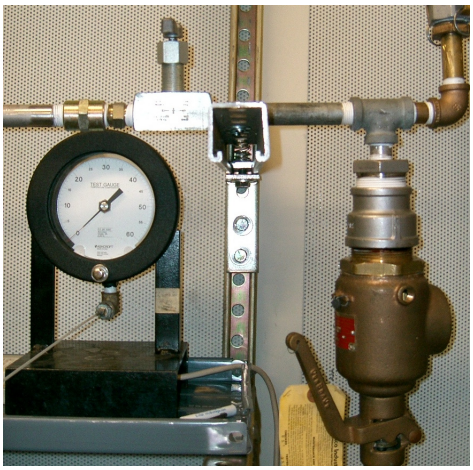

Fig. 9 Air flowrate control valve and the seal inlet pressure gage and safety release valve.

maximum pressure regulator valve to the test rig for the seal operation. The pressure regulator, shown in Fig. 8, is used to decrease the air supply pressure to less than 6.9 *bar* (100 *psi*). A safety relief high pressure valve 10.34 *bar* (150 *psi*) and air filter (10 μm) are installed downstream of the pressure regulator.

Fig. 9 shows the air flowrate control valve, the seal inlet pressure gage, and a low pressure 2.07 *bar* (30 *psi*) safety relief valve. The air flowrate is controlled through a fine needle valve and pressure is monitored by a high accuracy pressure gage. Air is supplied to the test seal through a 0.0254 *m* (1 *in)* hose. Because the seals are made from Peek which has high temperature sensitivity, an electric air heater equipped with a temperature PID controller shown in Fig. 10 is used to control the temperature of the air flowing through the test seal.

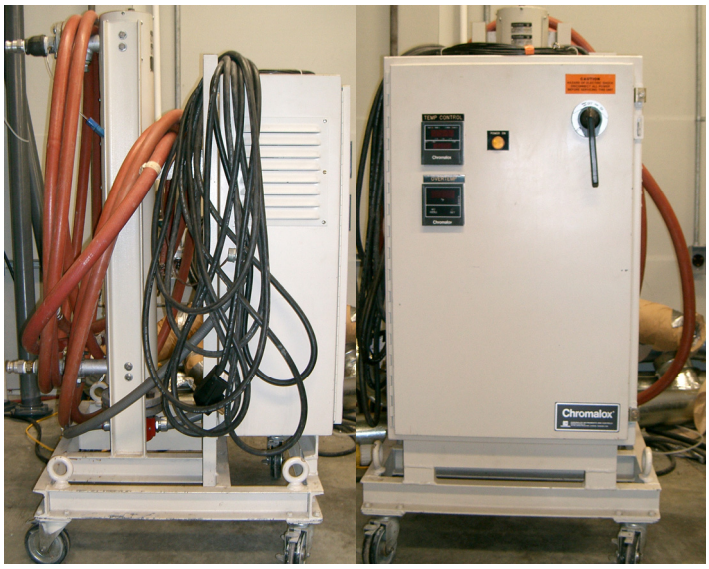

Fig. 10 Electric air heater.

Test Seal Material and Geometries

Seal Material

The smooth and windback seals were made from X-455 PEEK material with coefficient of thermal expansion (CTE) equal to 1.39×10^{-5} *m/ (m. °C)*. After manufacturing the seals, they

were measured along with their temperature. Their radial clearance is determined based on these measurements according to the following equations,

$$D_{seal} = D_{base}(1 + \beta(T_{seal} - T_{base})) \tag{4}$$

$$c = \left(D_{seal} - D_{rotor}\right)/2 \tag{5}$$

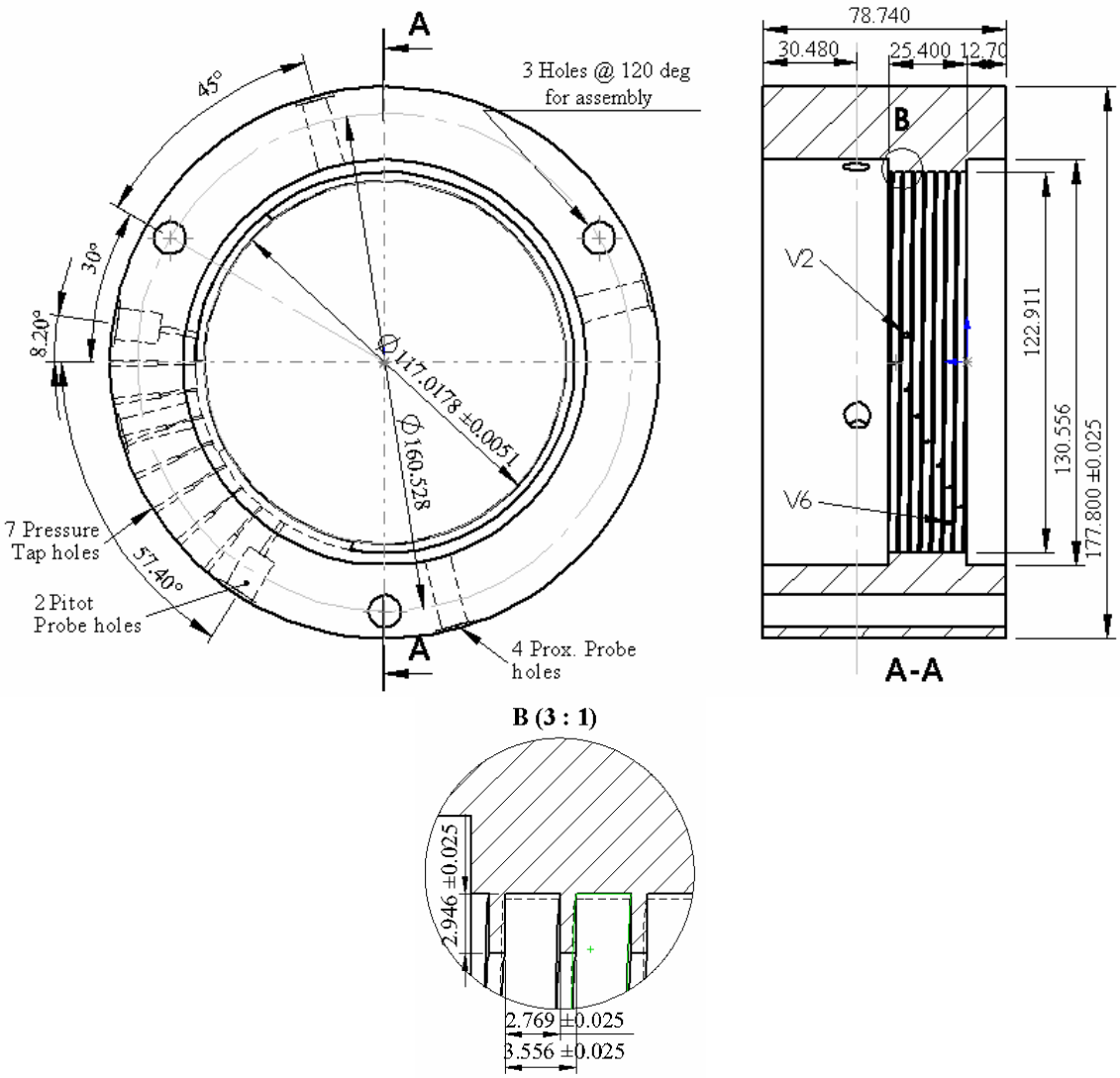

Fig. 11 Schematic drawing for the windback seal.

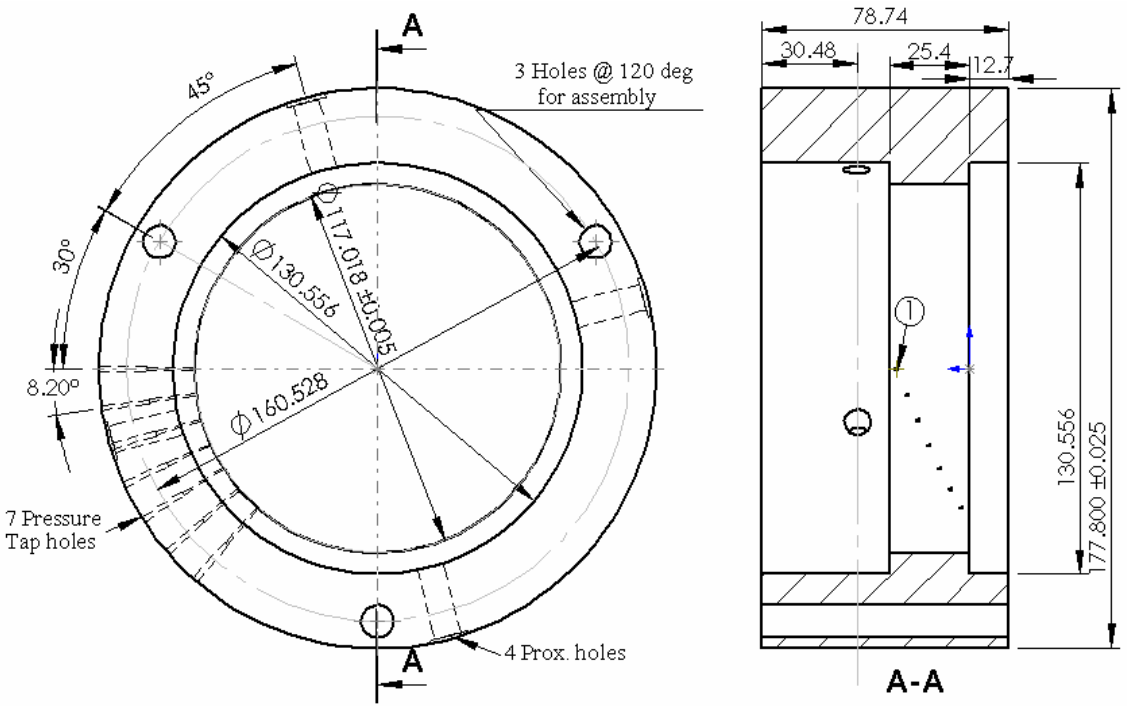

Fig. 12 Schematic drawing for the smooth seal.

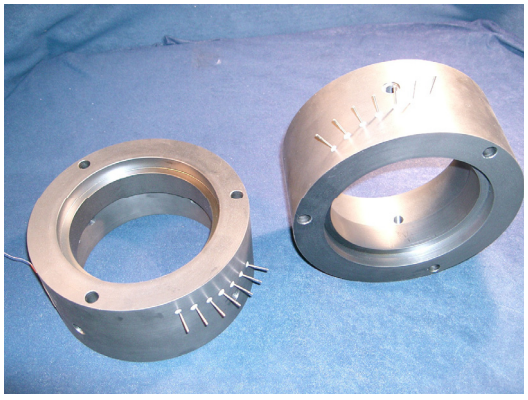

Fig. 13 Smooth seal.

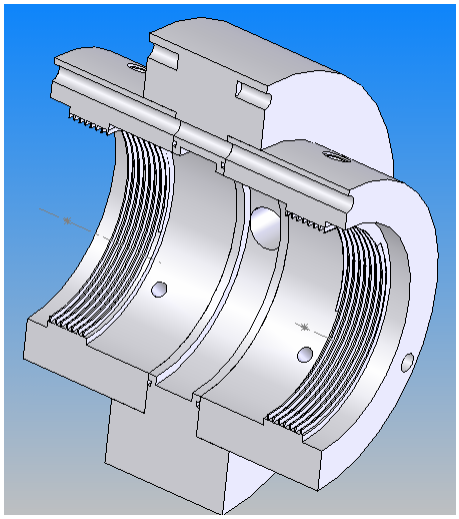

Fig. 14 Section of windback seal assembly.

Test Seal Geometries

Two seals were tested during this study

(1) Windback seal with 101.6 *μm* (4 *mils*) radial clearance at Peek temperature of 31.7 °C (89 F), 3.556 mm pitch (0.14 *in*), 0.7874 mm (31 *mils*) tooth thickness, 2.9464 mm (0.116 *in*) tooth height and 25.4 mm (1 *in*) length is shown in Fig. 11.

(2) Smooth seal with 101.6 *μm* (4 *mils*) radial clearance at Peek temperature of 30.6 °C (87 F), and 25.4 mm (1 *in*) length as shown in Figs. 12 and 13.

Instrumentation

Six high-sensitivity proximity probes, located on the stator exit sides, record the relative position of the stator with respect to the rotor in the *x* and *y* directions. Two radial proximity probes are installed in the non-drive end (NDE) seal side. In addition, four probes are installed in the drive end (DE) seal side to measure the pitch and yaw of the stator. Two of the probes installed in the end cap at the DE side are used to provide a feedback to the shakers' control system.

Two test seal are used in assembling the stator with 0.0762 mm shim (Fig. 14), in order to perform leakage tests with shaft rotation. One of these two seals is instrumented for measurements purposes namely the DE seal. The stator assembly was configured such that the effect of shaft rotation will pump the air in both seal cavities toward the exit of each seal, and since the turbine drives the shaft in the CCW direction from the DE side. The DE seal was right-hand threaded, while the NDE seal was left-hand threaded.

Two boundary layer Pitot probes with sensing head diameter of 0.635 mm and tip height of 2.54 mm are used to measure the air circumferential velocity at the center of the second and

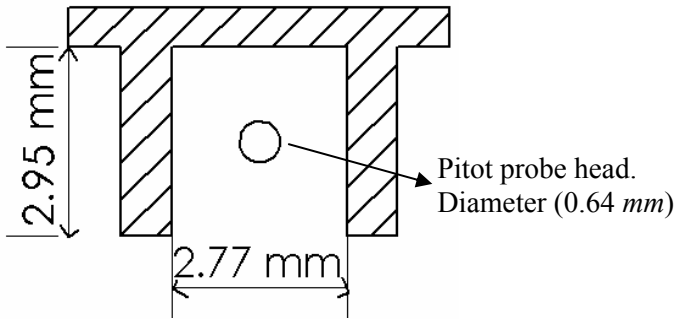

Fig. 15 Relative size of Pitot probe head diameter to cavity dimensions.

sixth cavities of the windback seal. Fig. 15 shows the relative size of the Pitot probe head to cavity dimensions. For each Pitot probe, a differential Rosemount pressure transducer with a range from 0 to 62.3 *kPa* (0 to 250 *in* H_2O) shown in Fig. 16, is used to measure the difference between the Pitot pressure and the static wall pressure at the installation location of the probe. The velocity is calculated based on Bernoulli equation as,

$$V_{cavity} = \sqrt{2(P_{stagnation} - P_{static})/\rho_{cavity}} \quad (6)$$

Fig. 17 shows the turbine flowmeter used to measure the volumetric air flowrate which has a range from 0.028 to 0.283 m^3/min (1 to 10 *ACFM)*. A frequency to DC voltage converter is used to acquire the signal of the turbine flowmeter. To calculate the mass flowrate of the air through the seals, the absolute pressure and static temperature upstream of the turbine flowmeter is measured using an absolute pressure Rosemount transducer which has a range from 0 to 10.2 *atm* (0-150 psia) and T-type thermocouple, respectively. In order to operate in the mid range of the turbine flowmeter for different inlet pressure conditions, the pressure regulator is set between 241.4 to 344.8 *kPa* (35 to 50 *psig*) to increase the volumetric flowrate and hence increasing the accuracy of the turbine meter.

Fig. 16 Rosemount DP transducer.

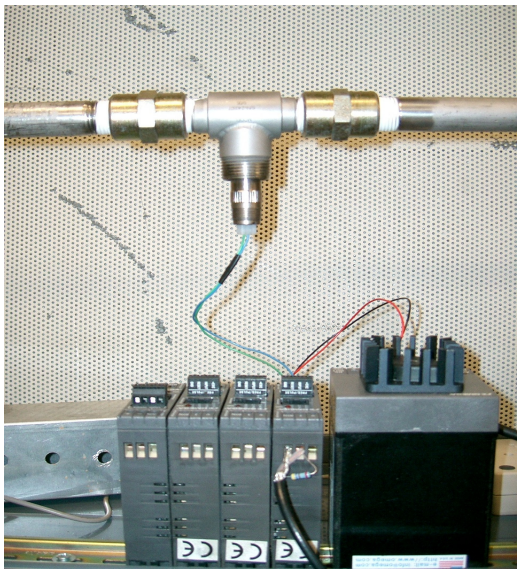

Fig. 17 Air turbine flowmeter with frequency to DC voltage converter.

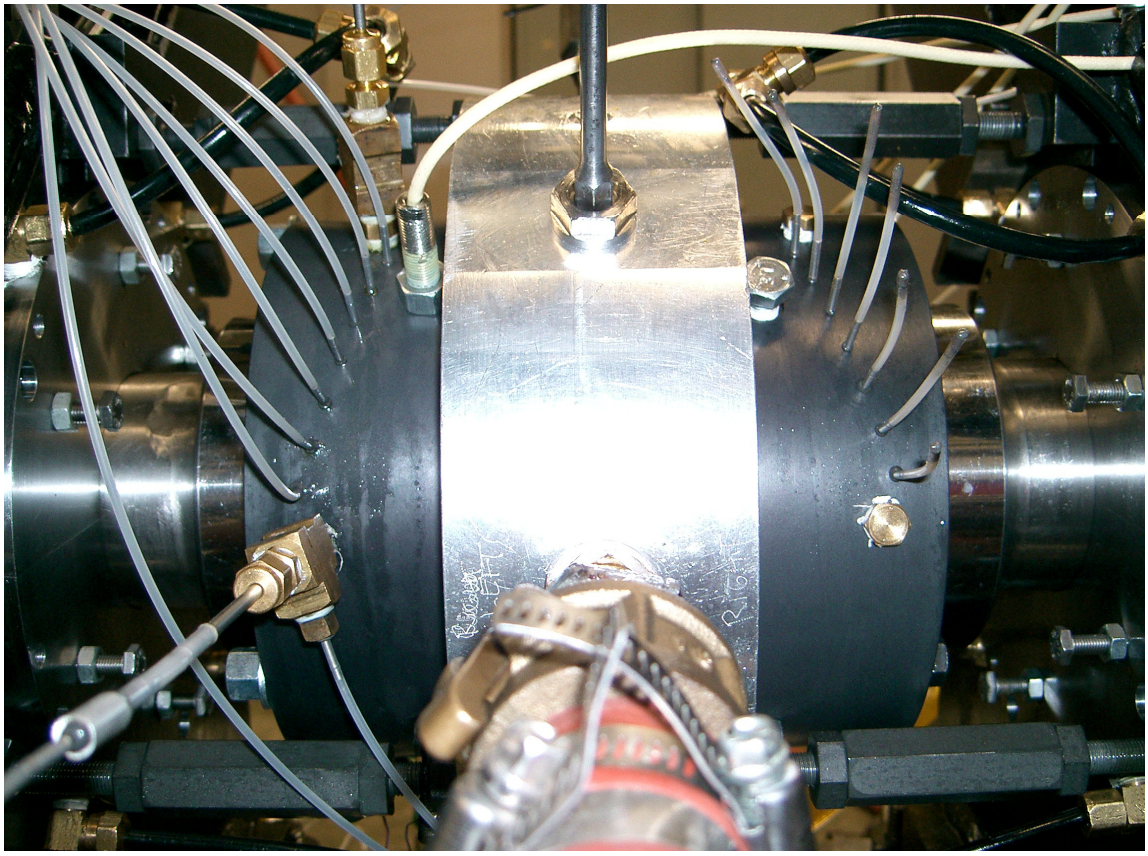

Fig. 18 Instrumented stator.

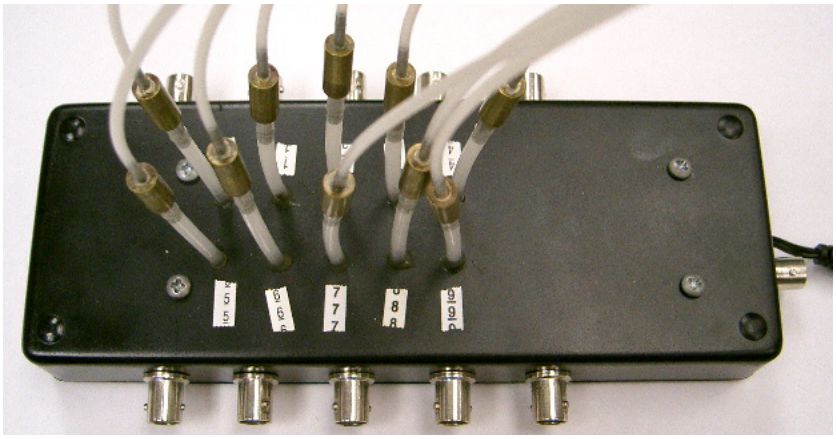

Fig. 19 Pressure transducers.

Ten pressure transducers with a linear range from 0 to 206.9 *kPa* (0 to 30 *psig*) are used to measure the pressure distribution along the length for the smooth seal and inside each cavity for the wind back seal. One of these ten transducers is used to measure the inlet pressure to the seal. Fig. 18 shows the location of the pressure taps. 1.5875 mm (1/16 *in*) plastic hoses are used to connect the pressure taps to the pressure transducers shown in Fig.19. Three T-type thermocouples are used to measure the air inlet temperature, the seal surface temperature and the inside seal temperature to insure that the seal are near thermal equilibrium in terms of constant temperature distribution.

Data Acquisition System

Three data acquisition boards of Measurement Advantage™ brand were used

USB-TC

Fig. 20 shows a USB based 8 differential channel thermocouple input module with 24 bit resolution, 2 *S/s* sampling rate and eight different sensor types from which to choose. The T-type was used in this experiment with maximum board measuring error of $\pm 0.629\ C^o$ and a temperature range of -200 to $1372\ C^o$. Four channels were acquired by this board namely: air supply temperature, air inlet temperature, and surface and inside seal temperatures.

USB-1616FS

Fig. 20 shows a USB based 16 single ended analog input and digital I/O channels with a resolution of 16 bit, 50 *kS/s* maximum sampling rate and four selectable voltage input ranges. A $\pm 10V$ voltage range is selected for this experiment with maximum board measuring error of $\pm 5.66mV$. The board is set at 15500 Samples at a rate of 10 kS/s for this experiment. Five channels are acquired using this board namely; two Rosemount DP signals, absolute Rosemount supply pressure signal, turbine flowmeter signal and the supply voltage of the 10 pressure transducers.

PC-CARD-DAS16/16-AO

Fig. 21 shows a PCMCIA type-2 slot based card with either 16 single ended or 8 differential input channels with a resolution of 16 bit, 200 kS/s maximum sampling rate and four

selectable voltage input range. A $\pm 1.25V$ voltage range was selected for this experiment with maximum board measuring error of $\pm 0.19\ mV$. The board is set at 15500 samples at a rate of 10 *kS/s* for this experiment. Eight differential pressure transducer channels are acquired using this board namely; 7 pressure measurement along seal axis and inlet seal pressure.

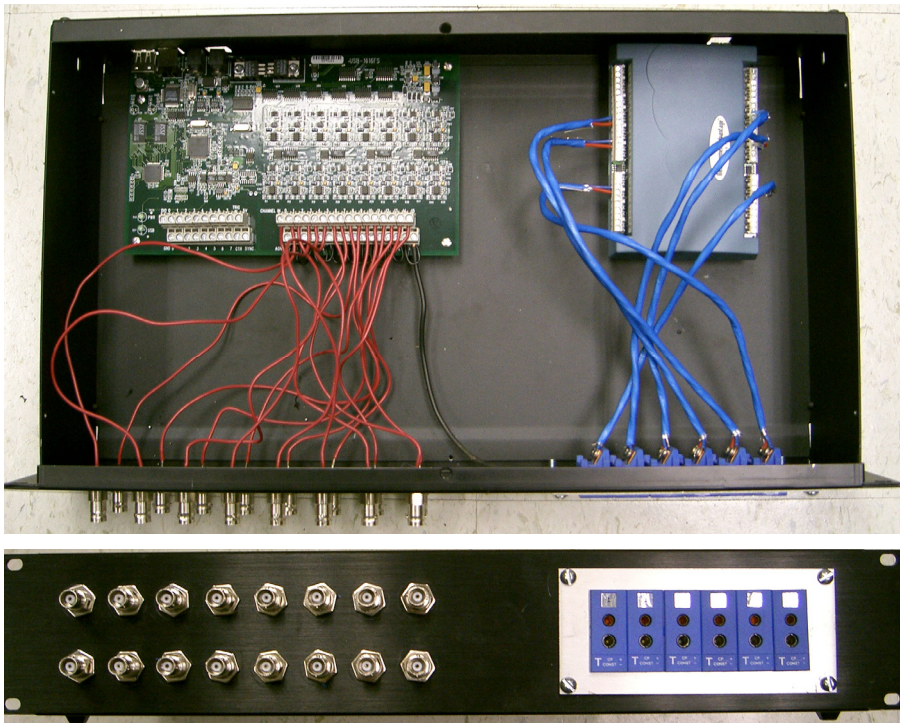

Fig. 20 USB-TC and USB-1616FS boards.

Fig. 21 PCMCIA type-2 card.

The three boards are connected to a 1.2 GHz AMD Athlon^{TM} processor Laptop computer running Microsoft Windows XP professional service pack 2 with 512 *MB* of RAM through out the experiments. The data were acquired using Labview software Version 7.1. Figs. 22 and 23 show the front panel and block diagram, respectively, of Labview used in acquiring the experimental data. The rotor speed was measured using another system, therefore it was recorded separately. The rotor speed was controlled through a dial switch and within ± 75 *rpm* from the targeted speed.

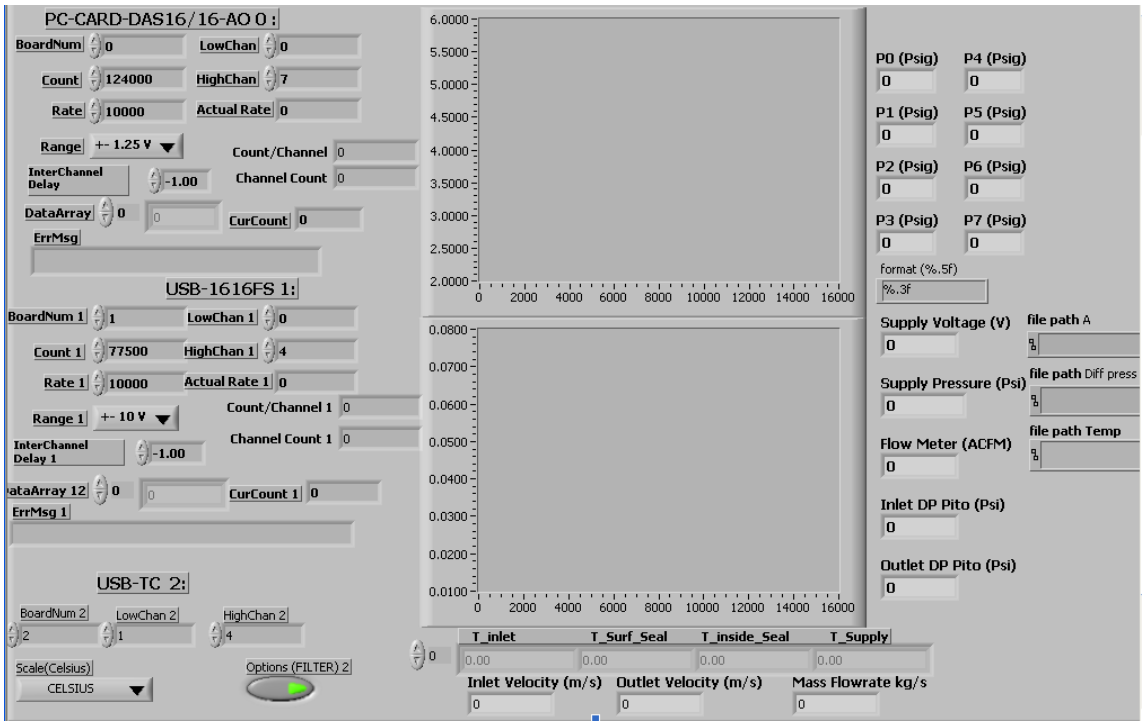

Fig. 22 Labview software front panel for the three board used in acquiring experimental data.

Uncertainty Analysis

The uncertainty analysis in calculating the mass flowrate and the average velocity in the cavities were based on Kline and McClintock [27]. The density is calculated using the ideal gas law,

$$\rho = P / RT \tag{7}$$

where the uncertainty in air density was calculated using

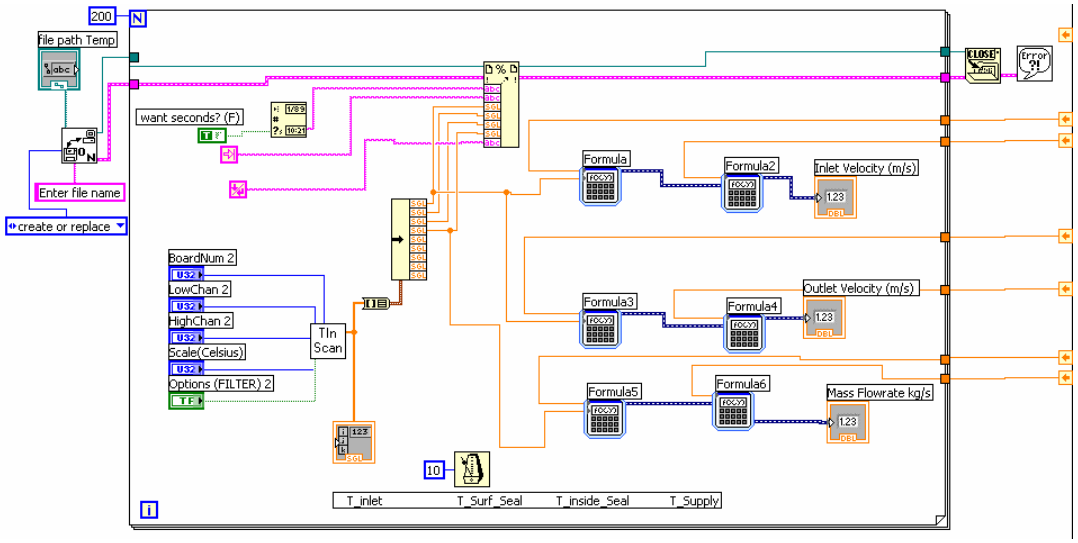

(a) Labview block diagram for USB-TC

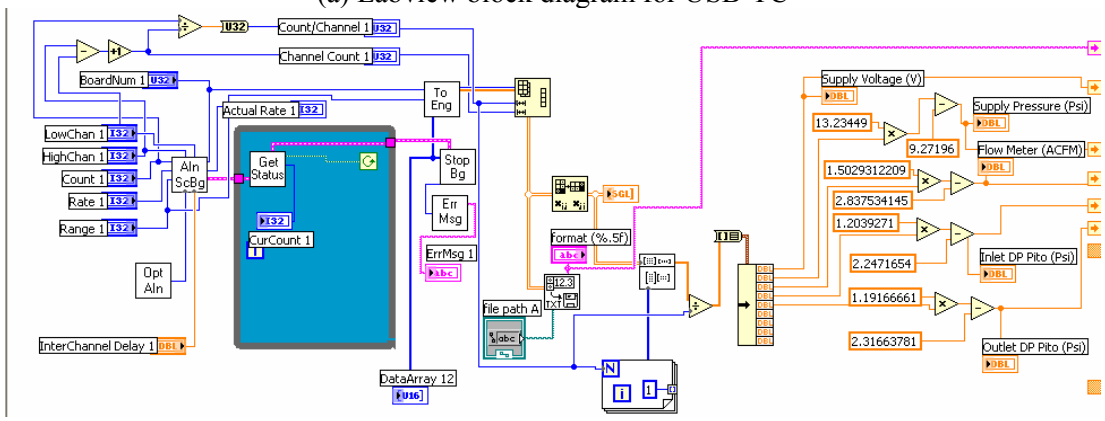

(b) Labview block diagram for USB-1616FS

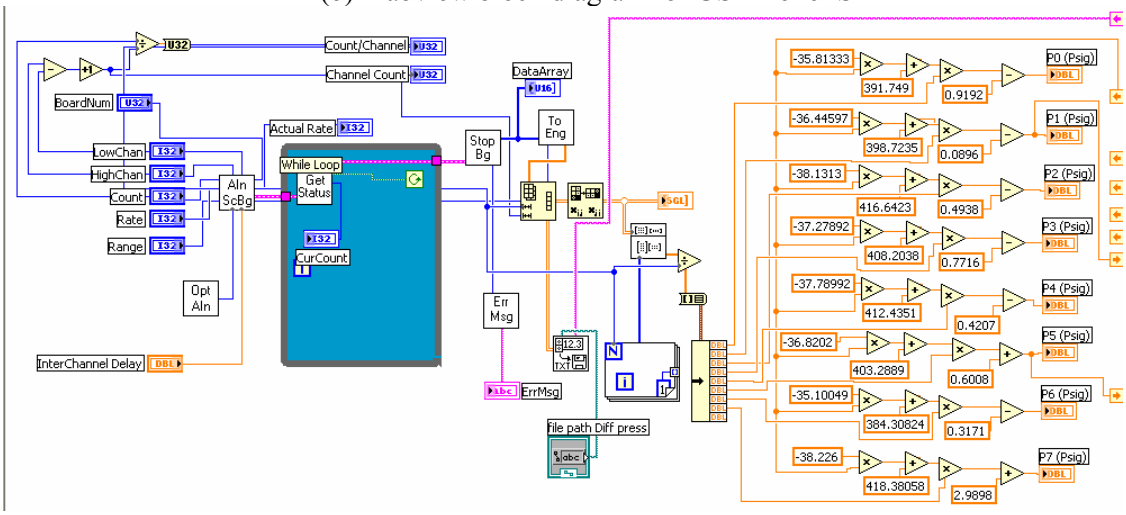

(c) Labview block diagram for PC-CARD-DAS16/16-AO

Fig. 23 Labview software block diagram for the three boards used in acquiring experimental data.

$$\delta\rho = \sqrt{(\frac{\partial\rho}{\partial P}\delta P)^2 + (\frac{\partial\rho}{\partial R}\delta R)^2 + (\frac{\partial\rho}{\partial T}\delta T)^2} \quad (8)$$

Ignoring the uncertainty in *R* (Universal gas constant), Eq.(8) simplifies to

$$\frac{\delta\rho}{\rho} = \sqrt{(\frac{\delta P}{P})^2 + (\frac{\delta T}{T})^2} \quad (9)$$

The mass flowrate was calculated using

$$\dot{m} = \rho Q \quad (10)$$

where the uncertainty in the mass flowrate was calculated using

$$\frac{\delta\dot{m}}{\dot{m}} = \sqrt{(\frac{\delta\rho}{\rho})^2 + (\frac{\delta Q}{Q})^2} \quad (11)$$

The mean average circumferential velocity in the middle of the seal cavities was calculated using the Bernoulli's equation Eq.(12). The compressibility effect in Bernoulli's equation was ignored, since the maximum calculated Mach number was less than 0.25.

$$\Delta p = \frac{1}{2}\rho V^2 \quad (12)$$

hence,

$$V = \sqrt{\frac{2\Delta p}{\rho}} \quad (13)$$

The uncertainty in the average circumferential velocity is calculated using

$$\delta V = \sqrt{(\frac{\partial V}{\partial(\Delta p)}\delta(\Delta p))^2 + (\frac{\partial V}{\partial\rho}\delta\rho)^2} \quad (14)$$

And simplify to

$$\frac{\delta V}{V} = \frac{1}{2}\sqrt{(\frac{\delta(\Delta p)}{\Delta p})^2 + (\frac{\delta\rho}{\rho})^2} \quad (15)$$

There are two sources of errors in this experiment. One is from the variability of the measurement readings and represented by the standard deviation and these are the random errors. The other is from the specified instrument inaccuracies and these are the systematic errors. The systematic errors of the measuring instruments shown in Table 2 are used in calculating the total uncertainty error of the leakage flowrate, inlet and outlet velocities according to Eq.(11) and Eq.(15), respectively. Table 3 shows a summary of the uncertainty calculation at 0 rpm for

density, leakage flowrate, and inlet and outlet velocities for the windback seal, and density and leakage flowrate for the smooth seal.

Table 2 Instruments uncertainty.

Instrument	*Range*	*Uncertainty*
Rosemount pressure transducer	0-10.2 *atm* (0-150 *psia*)	0.075% span (776 Pa)
Rosemount differential pressure transducer	0-62.3 *kPa* (0-250 *in/H2O*)	0.075% span (47 Pa)
Turbine flow meter	0.028 to 0.283 m^3/min (1-10 *ACFM*)	0.11% measurement
Piezoresistive pressure sensor	0 to 206.9 *kPag* (0-30 *psig*)	0.3% span (621 Pa)
T-type thermocouples	-250-350 ^oC	Greater of $1.0\,^oC$ or 0.75%

Table 3 Summary of uncertainty calculations for the windback and the smooth seals.

Windback					**Smooth**	
P_{in} (kPa)	$\delta\rho$ (kg/m^3)	$\delta\dot{m}$ *(kg/s)*	δV_{in} *(m/s)*	δV_{out} *(m/s)*	$\delta\rho$ *(kg/m^3)*	$\delta\dot{m}$ *(kg/s)*
34.5	0.022	0.000023	1.53	0.88	0.022	0.000020
68.9	0.021	0.000038	1.18	0.56	0.021	0.000039
103.4	0.020	0.000052	1.01	0.45	0.021	0.000056

Numerical Simulation Setup

The objective of using numerical simulations is, in general, to evaluate the performance of the element under study to develop an optimum design before manufacturing and employment in a real machine, which in turn will insure the reliability of that product with minimal development cost. Nevertheless, the numerical simulation must be verified first through experimental tests.

The computational fluid dynamic (CFD) simulations for this study were performed using the Fluent software package version 6.1.22. This software can solve both structured and unstructured grid domains with the capability of adaptively varying the grid using different flow and/or geometrical parameters such as (pressure gradient, volume, boundary layer, etc.). Fluent solves the averaged conservation of mass and Navier-Stokes equations, and are given by

$$\frac{\partial \rho}{\partial t} + \frac{\partial}{\partial x_i}(\rho u_i) = 0 \tag{16}$$

$$\frac{\partial}{\partial t}(\rho u_i) + \frac{\partial}{\partial x_j}(\rho u_i u_j) = -\frac{\partial p}{\partial x_i} + \frac{\partial}{\partial x_j}\left[\mu(\frac{\partial u_i}{\partial x_j} + \frac{\partial u_j}{\partial x_i} - \frac{2}{3}\delta_{ij}\frac{\partial u_i}{\partial x_i})\right] + \frac{\partial}{\partial x_j}(-\rho\overline{u_i' u_j'}) \tag{17}$$

Where, $\rho\overline{u_i' u_j'}$ are the Reynolds stresses and given by

$$\rho\overline{u_i' u_j'} = \mu_t\left(\frac{\partial u_i}{\partial x_j} + \frac{\partial u_j}{\partial x_i}\right) - \frac{2}{3}\left(\rho\kappa + \mu_t\frac{\partial u_i}{\partial x_i}\right)\delta_{ij} \tag{18}$$

Different turbulence models are available to solve for the Reynolds stresses given in Eq.(18) . The standard $\kappa - \varepsilon$ model was used in this simulation with the enhanced wall treatment function.

Simulation Matrix

Table 4 shows the simulation matrix that was considered using the Fluent numerical analysis package. For each seal condition in Table 4, numerical simulations* were carried out for three differential pressures DP = 34.5, 68.9, and 103.4 *kPa* (5, 10 and 15 *psi*) and 4 rotational rotor speeds (Ω = 0, 5000, 10000 and 15000 rpm) including the no-rotation condition.

Table 4 Simulation and experimental case studies.

No. of start	*c* (*mm*)	*s* (mm)	*h(mm)*	φ (deg)
Single	0.05	3.56	2.94	0.56
	0.10	3.12	2.94	0.49
		3.56	0*	0.56
			1.47	
			2.94*	
		4.14	2.94	0.65
	0.15	3.56	2.94	0.56
Double	0.10	7.11	2.94	1.11

Seal Mesh

Gambit software version 2.1.6 is used for griding the seal cavity domains. The number of elements used in griding the seal in the circumferential direction is 44 elements. The seal is meshed generally with Hexagonal elements. Wedge shape elements are used at the cut off sharp

* These conditions have been tested experimentally.

edge corners of the seal. The initial number of elements used is approximately 370,000 for this case and increases accordingly by grid adaptation based on static pressure and velocity magnitude gradients, in such a way to meet predetermined values. Pressure and velocity gradient of 0.2 and 0.005 are used, respectively. The maximum number of elements is around 900,000 for the highest differential pressure and rotation speed. A sample cross sectional view of a windback seal grid is shown in Figs. 24, 25 and 26. Note the compression of the grid spacing near the seal walls, the adaptive girding, and the very tight spacing next to the shaft. Upstream and downstream of the seal, the shaft was extended 5.08 mm and the seal face was extended radially 5.08 mm. Rectangular plenums were then constructed where the remaining two faces were pressure boundary conditions. In this gas seal, the velocity gradient is largest in the radial direction followed by the axial then circumferential directions. The result is the grid being comprised of hexagonal elements with large aspect ratios, especially in the clearance regions. This grid design is based upon the same concept as used in solving a boundary layer where the stream wise grid spacing is much larger than the grid spacing normal to the wall. The grid spacing is based upon the magnitude of the spatial gradient in a given direction. These large aspect ratio elements are one of the main reasons for performing the experimental verification of the computational results.

Boundary Conditions

For a single case numerical simulation run, the seal inlet and exit plenums boundaries were set to be at a constant pressure and temperature (300° *K*) except for the cases, that were compared with the experimental results, where the seals measured inlet temperatures were used. The shaft was extended to cover the inlet and exit plenums. The seal walls were set to stationary with no heat flux (adiabatic walls) through the seal walls. The rotor wall was set to be a moving surface with no heat flux and with no slip conditions. The rotor surface rotates a bout the positive *x*-direction.

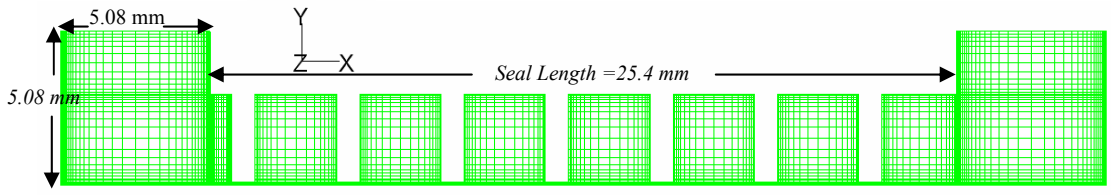

Fig. 24 Cross sectional view of a windback seal mesh.

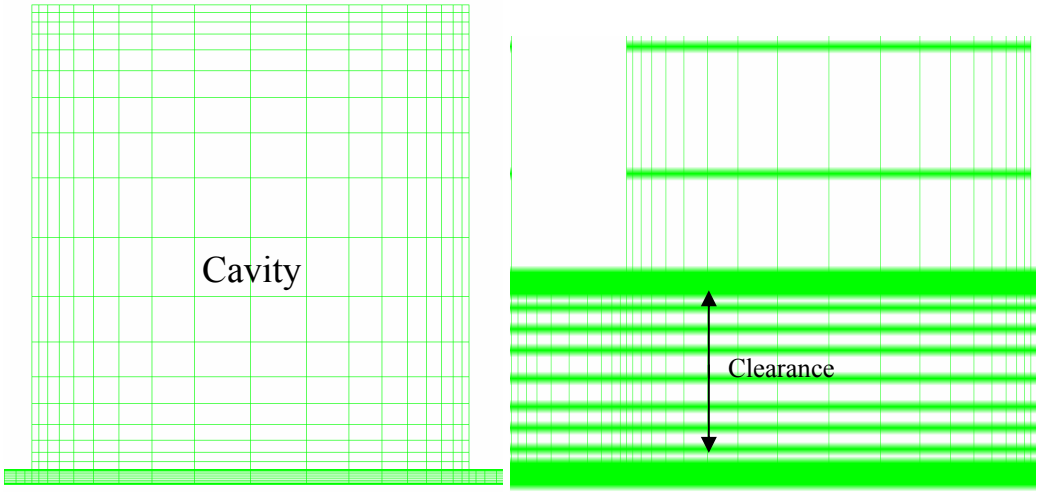

Fig. 25 Zoomed view, showing seal cavity and clearance mesh.

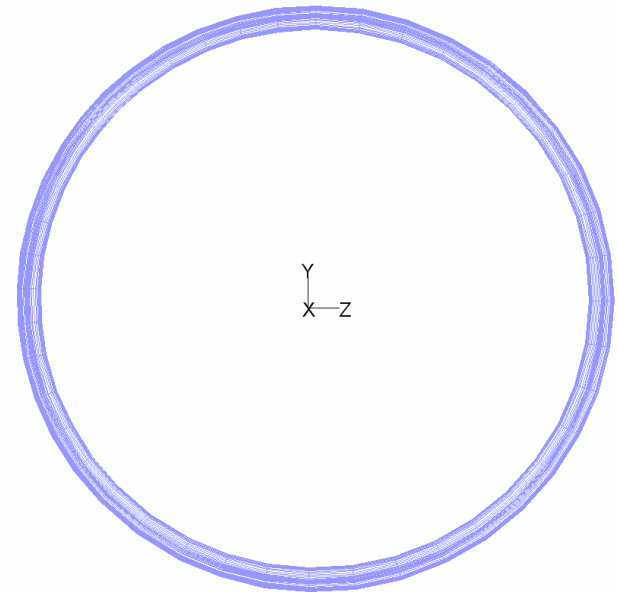

Fig. 26 Seal grid in the circumferential direction.

Adaptive Grid Refinement

To show that the CFD numerical solutions are grid independent, and to reduce the numerical solution errors with minimal number of cells used in girding the geometry of the flow field under consideration a solution-adaptive gird refinement function in Fluent package

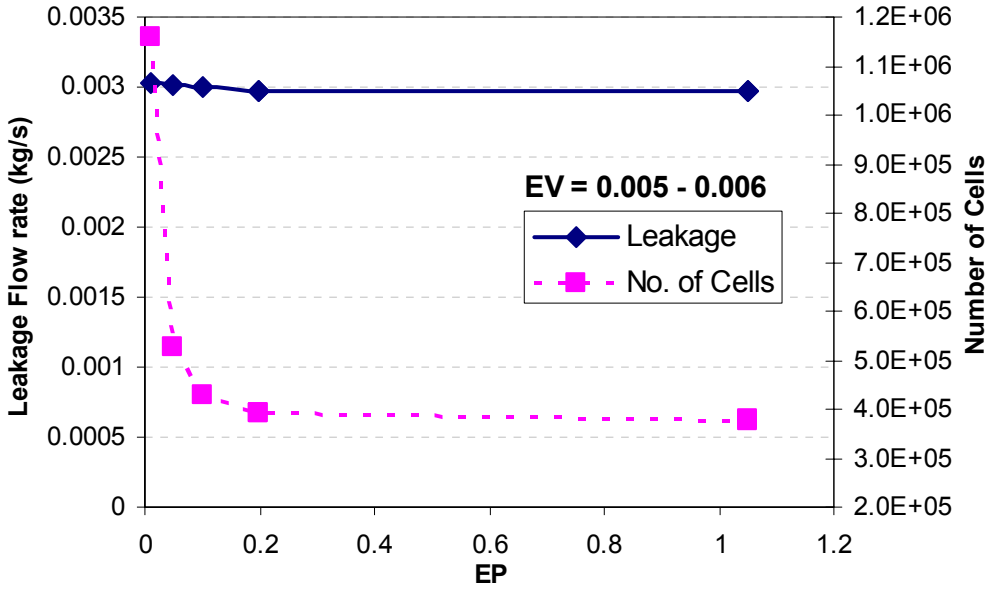

Fig. 27 Leakage flow rate and number of cells versus static pressure maximum error indicator.

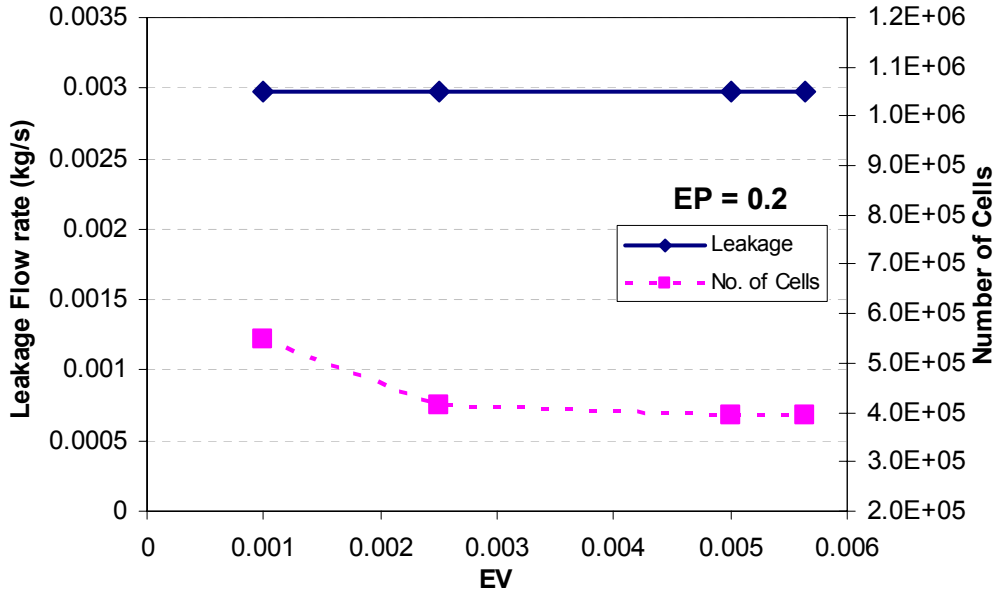

Fig. 28 Leakage flow rate and number of cells versus velocity magnitude maximum error indicator.

software was used. The cells are marked and adapted based on the curvature of selected flow field variables such as the static pressure and/or the velocity magnitude. The error indicator in

this case is a function of the cell area, gradient volume weight, and undivided Laplacian of the desired flow field variable.

Grid independent case study for windback seal with c=0.1 mm, h= 2.94 mm, s= 3.56 mm, DP=34.5 kPa and no shaft rotation were carried out and the results are presented in Figs. 27 and 28. Fig. 27 shows the leakage flow rate and the number of cells versus the maximum pressure error indicator at a maximum velocity error indicator of 0.005. When reducing the pressure error indicator from 1.05 (0.38 million cell) to 0.01 (1.16 million cell), the leakage flowrate increased less than 2%. Fig. 28 shows that reducing the maximum velocity error indicator from 0.005 (0.39×10^6 cell) to 0.001(0.55×10^6 cell) at a constant maximum pressure error indicator of 0.2 does not affect the leakage flowrate. Therefore the static pressure and velocity magnitude variables were adapted for all cases under study with a maximum of 0.2 and 0.005 error indicators, respectively.

Seal Coordinate System Transformation

The seal geometries were created and numerically solved in right handed rectangular coordinate system (x, y, and z).Where the x-direction represents the axial direction of the seal. The flow velocity components were transformed to a cylindrical coordinate system (r, θ, and x), where $r = \sqrt{y^2 + z^2}$, $\theta = \tan^{-1}(z / y)$, and x=x. Therefore, the velocity components in the cylindrical system were calculated using the following equations.

$$V_r = V_z \sin\theta + V_y \cos\theta \tag{19}$$

$$V_\theta = V_z \cos\theta - V_y \sin\theta \tag{20}$$

$$V_x = V_x \tag{21}$$

THEORY VERSUS EXPERIMENT

The primary objective of this chapter is to evaluate the effectiveness of the CFD (Fluent simulation software package) as a design tool for windback seals. Two seals, a windback and a smooth, with geometrical parameters given in Table 5, are simulated and tested experimentally. The effectiveness of the CFD is determined by comparing the measured and predicted leakage rates of these two seals.

Table 5 Tested seals geometrical parameters.

Seal Type	*c(mm)*	*s(mm)*	*h(mm)*	*t(mm)*	*L(mm)*	*R(mm)*
Windback	0.1	3.556	2.9464	0.7874	25.4	58.42
Smooth	0.1	0	0	25.4	25.4	58.42

Windback Seal

The comparison between the experimentally tested and the numerically simulated windback seals mainly includes the leakage mass flowrate, flow coefficient, pressure distribution and inlet and exit velocities for different rotor speeds, from 0 to 15000 rpm and for different differential pressures (*DP*), from 34.5 to 103.4 *kPa*.

Leakage Mass Flowrate

Fig. 29 presents both the experimentally measured and the numerically simulated values of the leakage mass flowrate as a function of rotor speed for different differential pressures across the seal. The exit pressure for all cases is atmospheric pressure (101.325 *kPa*). The experimental results do not include the 15000 rpm points because of safety and stability issues of the test rig for that particular test. The measured and predicted leakage flowrate show an excellent agreement with a maximum difference of 5% at the lowest *DP*. Both measured and predicted leakages flowrate show the same trend of a slight increase in leakage flowrate with increasing shaft speed from 0 to 15000 rpm. The increase in leakage flowrate with shaft speed ranges from 2% at the highest *DP* to 4.5% at the lowest *DP*. At these low differences in leakage flowrate, the CFD predictions under-predict and over-predict the leakage flowrates, at low and high *DP*, respectively. Increasing rotor speed increases the leakage flowrate, through increasing

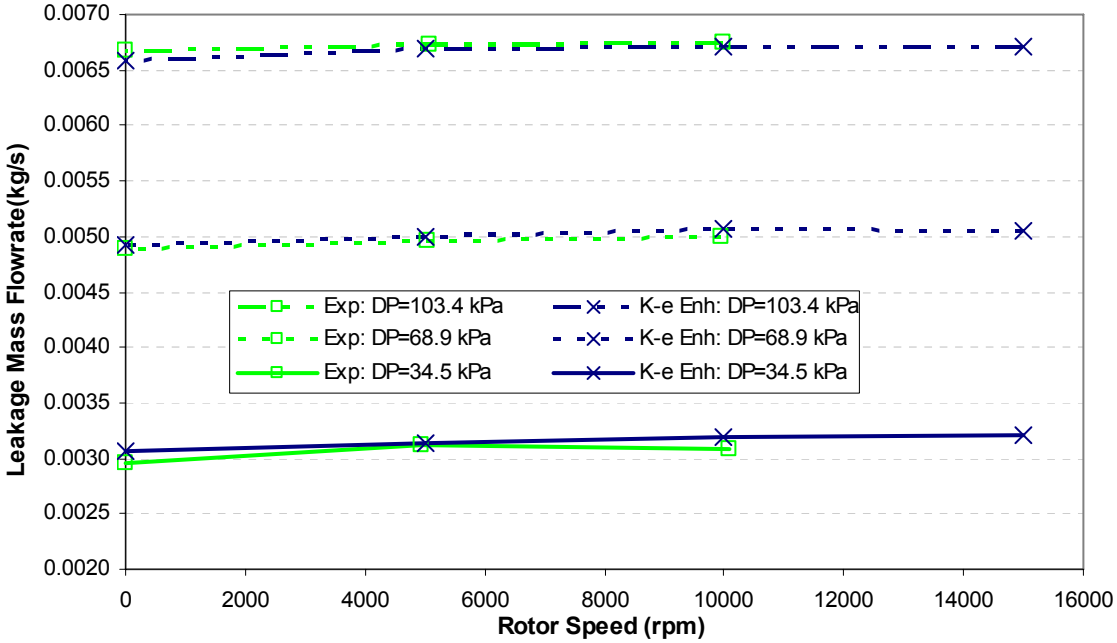

Fig. 29 Windback leakage mass flowrate versus rotor speed for different DP.

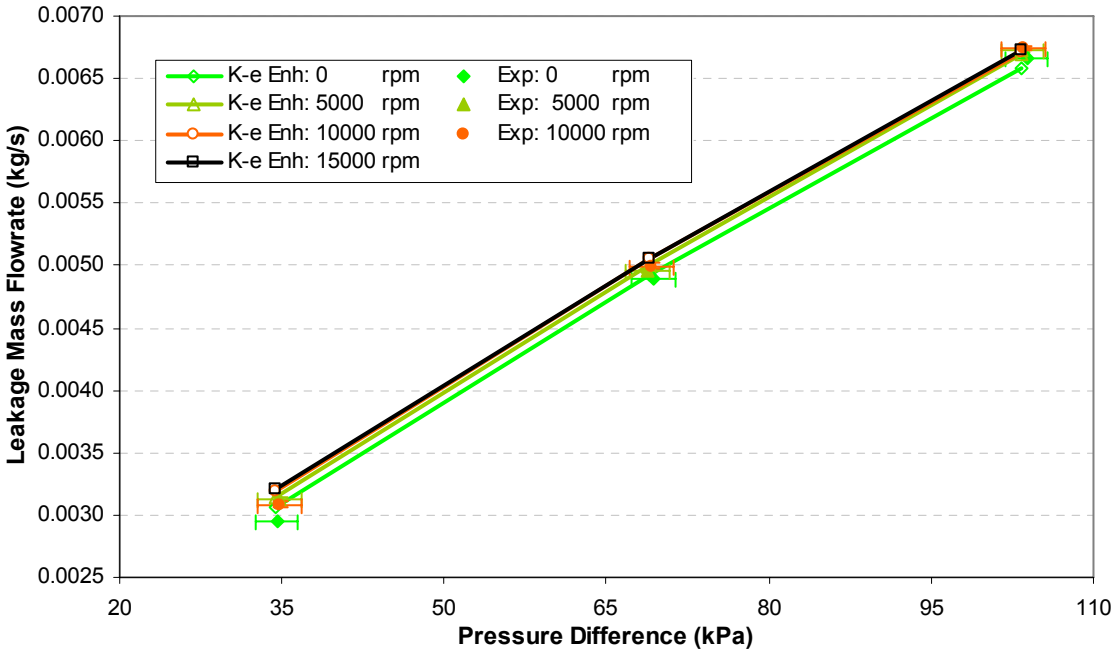

Fig. 30 Windback leakage mass flowrate versus DP for different rotor speed.

the flow velocity magnitude in general and in particular the circumferential velocity throughout the seal cavity and clearance. This increase in the leakage flowrate is due to increasing rotor speed and is limited because of the low viscosity of the air. Fig.30 shows that the leakage flowrate increases almost linearly with increasing *DP*. In addition, Fig.30 shows clearly the ability of the CFD simulation to predict the shaft rotation effect on leakage flowrates. This can be used to justify performing static experimental programs and compensating for shaft speed effects using CFD. These data show that the CFD simulation can predict the leakage flowrates and its variations with *DP*'s and shaft speeds to an excellent degree. This indicates that CFD simulations can be used for leakage prediction upon varying the operating conditions.

Flow Coefficients

The leakage rate can be presented in a non-dimensional form as a flow coefficient using Egli's [11] equation for labyrinth seals and utilizing the carry over coefficient proposed by Hodkinson [12] given in Eqs.(1 to 3). To represents the data in a useful and practical way, the flow coefficient was plotted versus the following non-dimensional numbers.

(1) Pressure ratio: The absolute pressure ratio P_e/P_i , where P_e is the absolute exit pressure and P_i is the absolute inlet pressure.

(2) Axial Reynolds number: The axial Reynolds number, $\mathrm{Re}_{axial} = \dot{m}/\pi D\mu_{avg}$, where $\dot{m}$ is the leakage rate in *kg/s*, *D* is the shaft diameter, and μ_{avg} is the dynamic viscosity of air calculated at the average of the inlet and exit air temperatures of 302° *K* and equal to $1.88\text{x}10^{-5}$ *Pa.s*.

(3) Circumferential Reynolds number: The circumferential Reynolds number, $\mathrm{Re}_{cir} = \rho\Omega Dc/(2\mu_{avg})$, where ρ is the air density in kg/m^3, calculated using the ideal gas law, Ω is the rotor speed in *rad/s*, *D* is the shaft diameter in *m*, and *c* is the radial seal clearance in *m*. For calculating the maximum $Re_{cir,}$ ρ was calculated at the inlet pressure and temperature, while for the minimum Re_{cir}, ρ was calculated at the exit pressure (1 *atm*) and temperature (300° *K*).

(4) Taylor number: $Ta = \mathrm{Re}_{cir}^2\,(2c/D)$

Figs. 31 to 37 represent the same data shown in Figs. 29 and 30 but in a non-dimensional form. Fig. 31 shows the flow coefficient versus the pressure ratio. Increasing the pressure ratio (reducing inlet seal pressure) reduces the flow coefficient in a linear relationship. The excellent

agreement between the experimental measurements and the predictions is shown again, especially at lower pressure ratios (higher *DP*). At higher pressure ratios, the difference is seen clearly because of the expanded axis range but is still less than 5%. The axial Reynolds number for this study is mainly a function of the leakage rate. Therefore, for constant shaft speed and for constant pressure ratio, increasing Re_{axial} will increase the flow coefficient as seen in Fig. 32 and Fig. 33, respectively. In addition, the limited effect of increasing rotor speed on α is clearly seen in these figures. Increasing rotor speed will increase the circumferential velocity in both the seal cavity and clearance. Keeping in mind that the seal cavity depth is 29 times larger than the clearance, with the low viscosity of air, rotor speed effects depends largely on the *DP*, in which higher *DP* means higher leakage flowrate, higher Re_{axial} and axial velocity component. If the axial velocity V_x is larger than the surface speed of the rotor, 91.7 *m/s* at 15000 rpm, the direction of air flow will be toward the axial direction of the seal. Therefore, the rpm effect on the circumferential velocity in the seal cavity will be limited at high *DP*, and that has been confirmed by both experimental tests and CFD simulations. In addition, the residence time of air in both the seal clearance and cavity is higher for low *DP* than higher *DP* cases. Therefore, more viscous drag effect due to increasing rotor speeds and hence, higher leakage drives the channel flow.

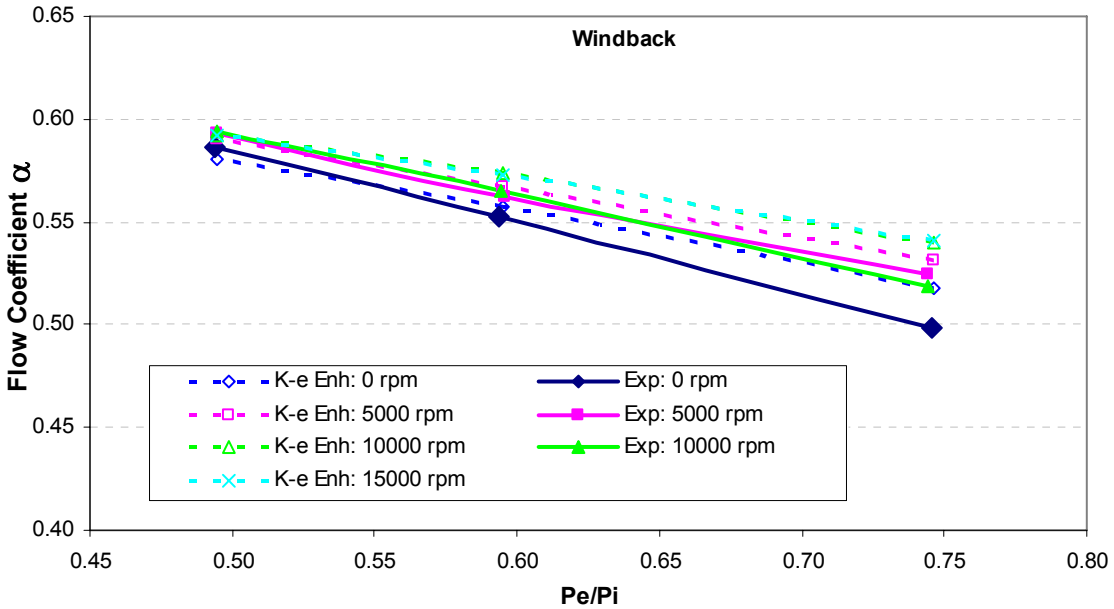

Fig. 31 Windback flow coefficient versus pressure ratio for different rotor speed.

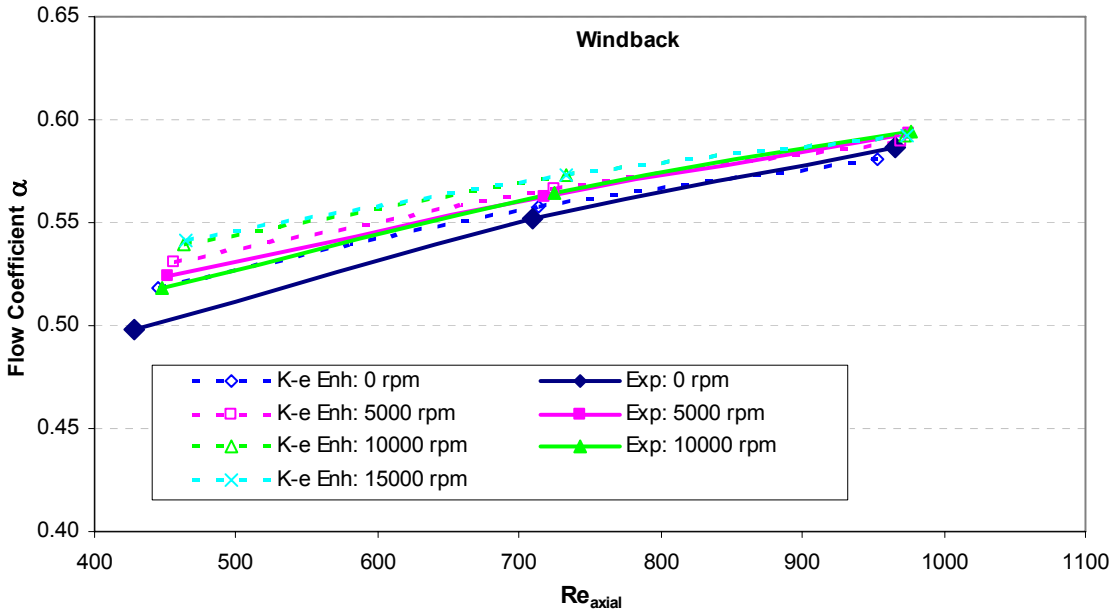

Fig. 32 Windback flow coefficient versus axial Reynolds number for different rotor speed.

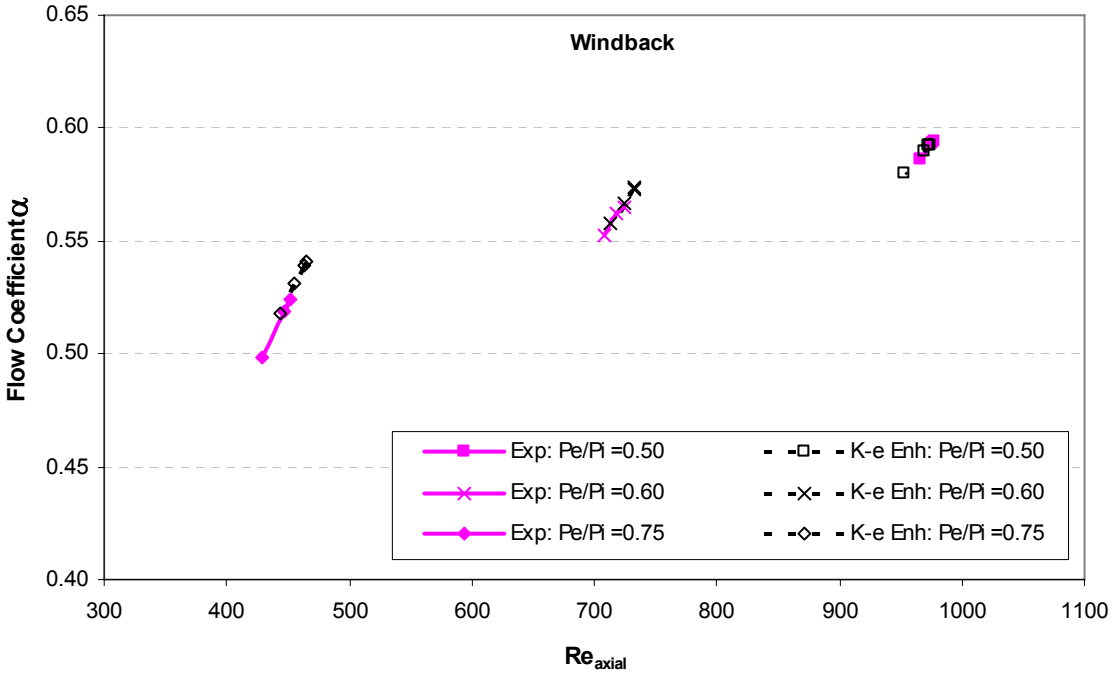

Fig. 33 Windback flow coefficient versus axial Reynolds number for different pressure ratios.

Fig. 33 shows that the ratio between the flow coefficient and the axial Reynolds number is a function of seal geometry, air viscosity, temperature and pressure and can be described utilizing Eqs.(1 to 3) and $\mathrm{Re}_{axial} = \dot{m}/\pi D\mu_{avg}$ into,

$$\frac{\alpha}{\mathrm{Re}_{axial}} = \frac{\mu}{c} f(T_i, P_i, P_e, \gamma) \tag{22}$$

Therefore, for constant seal geometry and operating conditions $\alpha/\mathrm{Re}_{axial}$ ratio is constant. The theory and the experimental results are lined up in Fig.33, as a result of the similarity of the non-dimensional analysis used in calculating both experimental and theoretical flow coefficients.

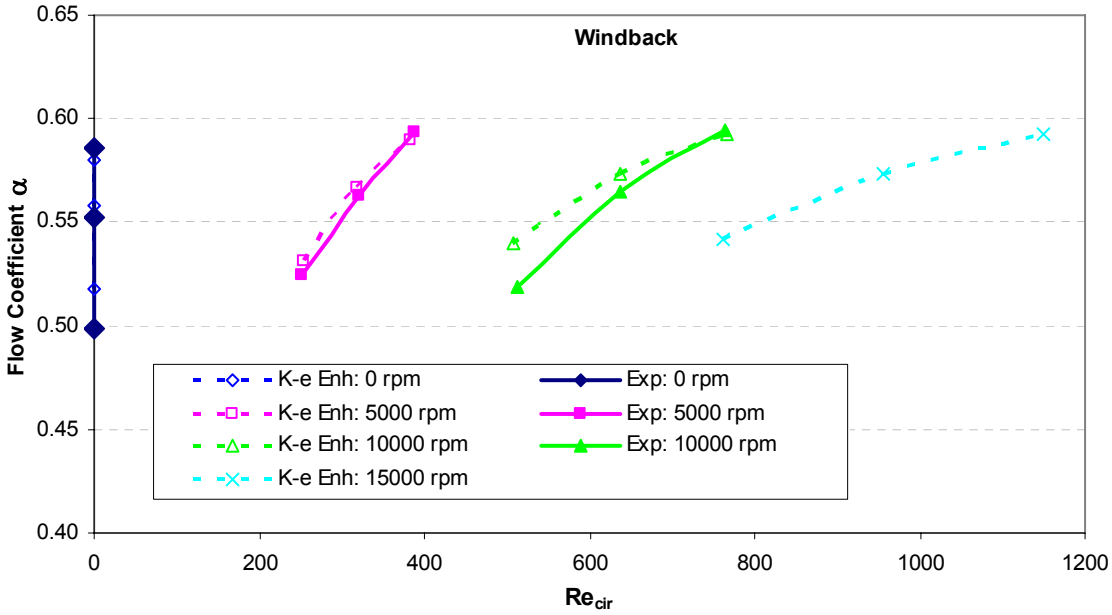

Fig. 34 Windback flow coefficient versus circumferential Reynolds number for different rotor speed.

Figs. 34 and 35 show the flow coefficient versus the circumferential Reynolds number, Re_{cir}, for different rotor speeds and pressure ratios, respectively. Increasing Re_{cir} at constant shaft speeds will increase the flow coefficients due to the increase of the air density as a result of decreasing the pressure ratio across the seal. The effect of shaft speed upon the flow coefficient can be seen clearly in Fig. 35. Increasing Re_{cir} at constant pressure ratios increases the flow coefficient, α. Figs. 36 and 37 show the Taylor number, Ta, which has the same effect upon α as Re_{cir} except that it expands the axis range. Fig. 37 shows that α asymptote's with increasing

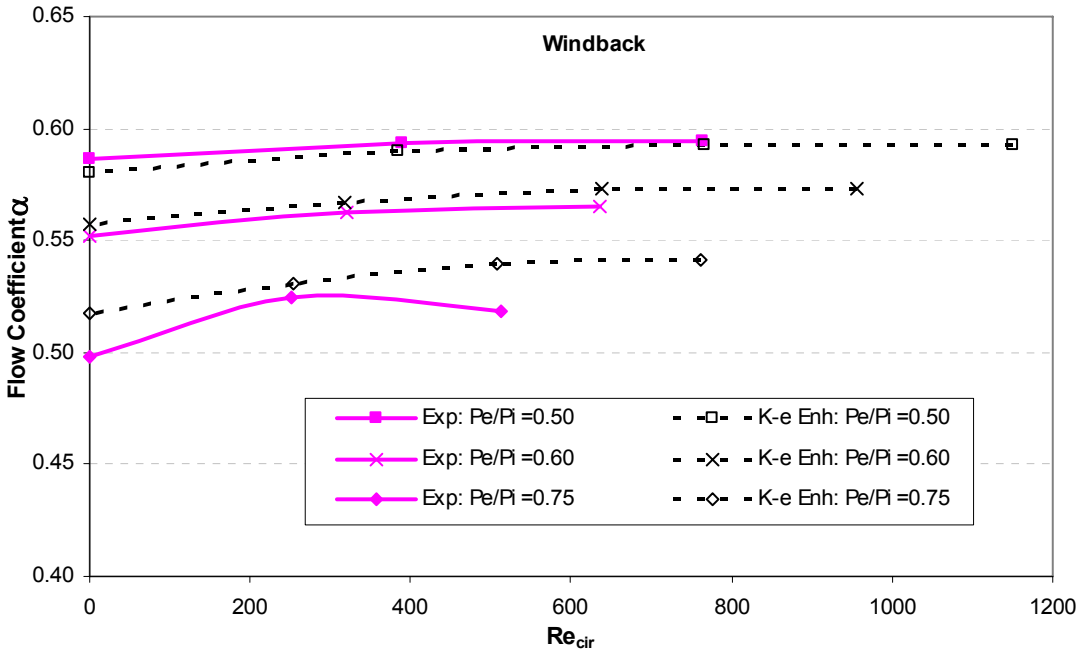

Fig. 35 Windback flow coefficient versus circumferential Reynolds number for different pressure ratios.

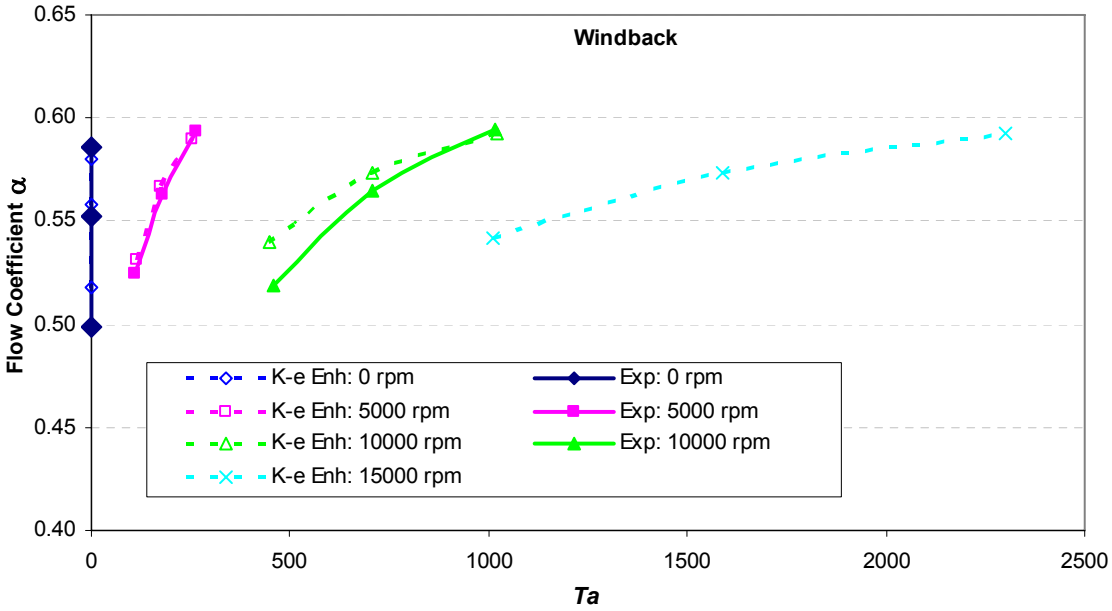

Fig. 36 Windback flow coefficient versus Taylor number for different rotor speeds.

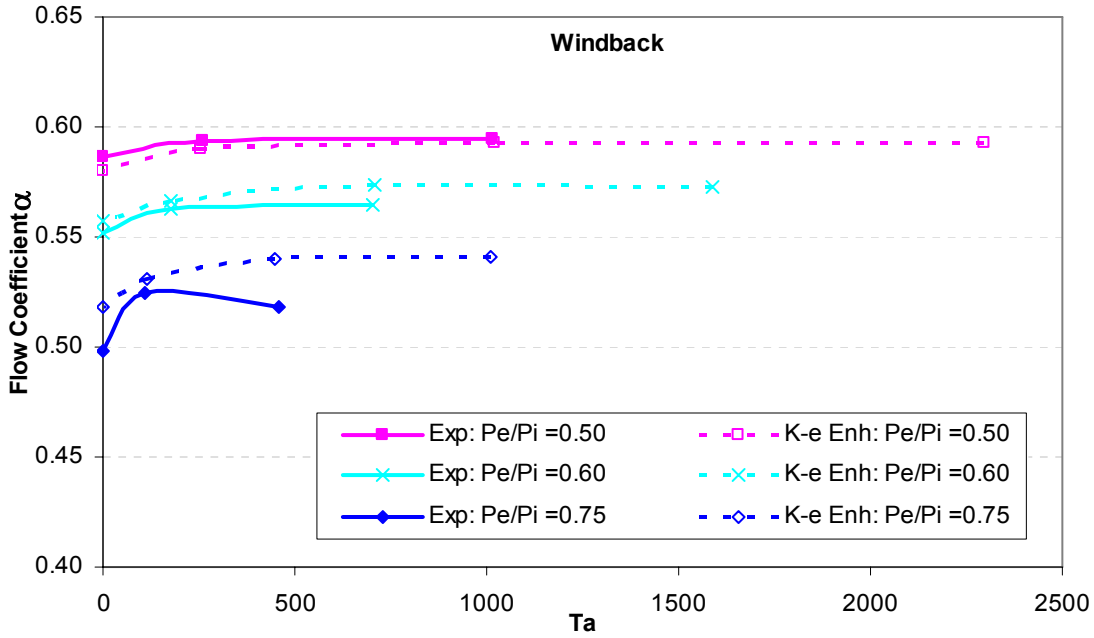

Fig. 37 Windback flow coefficient versus Taylor number for different pressure ratios.

Ta up to a constant value which is a function of pressure ratio. This means that the shaft speed has a maximum limited effect on leakage rate with a maximum increase at the highest pressure ratio.

Static Pressure

The pressure inside the windback seal cavities was measured using seven wall pressure taps located along the length of the seal wall with approximately eight degrees separation in the circumferential direction for the ease of installation. Fig. 38 compares the measured and predicted values for different rotor speeds and up to 15000 rpm. The exit pressure of the seal was atmospheric pressure (0 *kPag*). The flow goes through a sudden contraction from the constant pressure plenum to the inlet of the seal clearance, resulting in a sudden acceleration of the flow accompanied by inlet pressure losses resulting in larger axial pressure gradient just downstream seal entrance. The axial pressure gradient increases in the downstream direction up to exit plane, here the pressure gradient becomes smaller due to a pressure recovery at the exit through flow expansion. The CFD simulation predicts well the inlet pressure losses and exit pressure recovery. On the other hand, the pressure measurements show an increase in the negative slope toward the

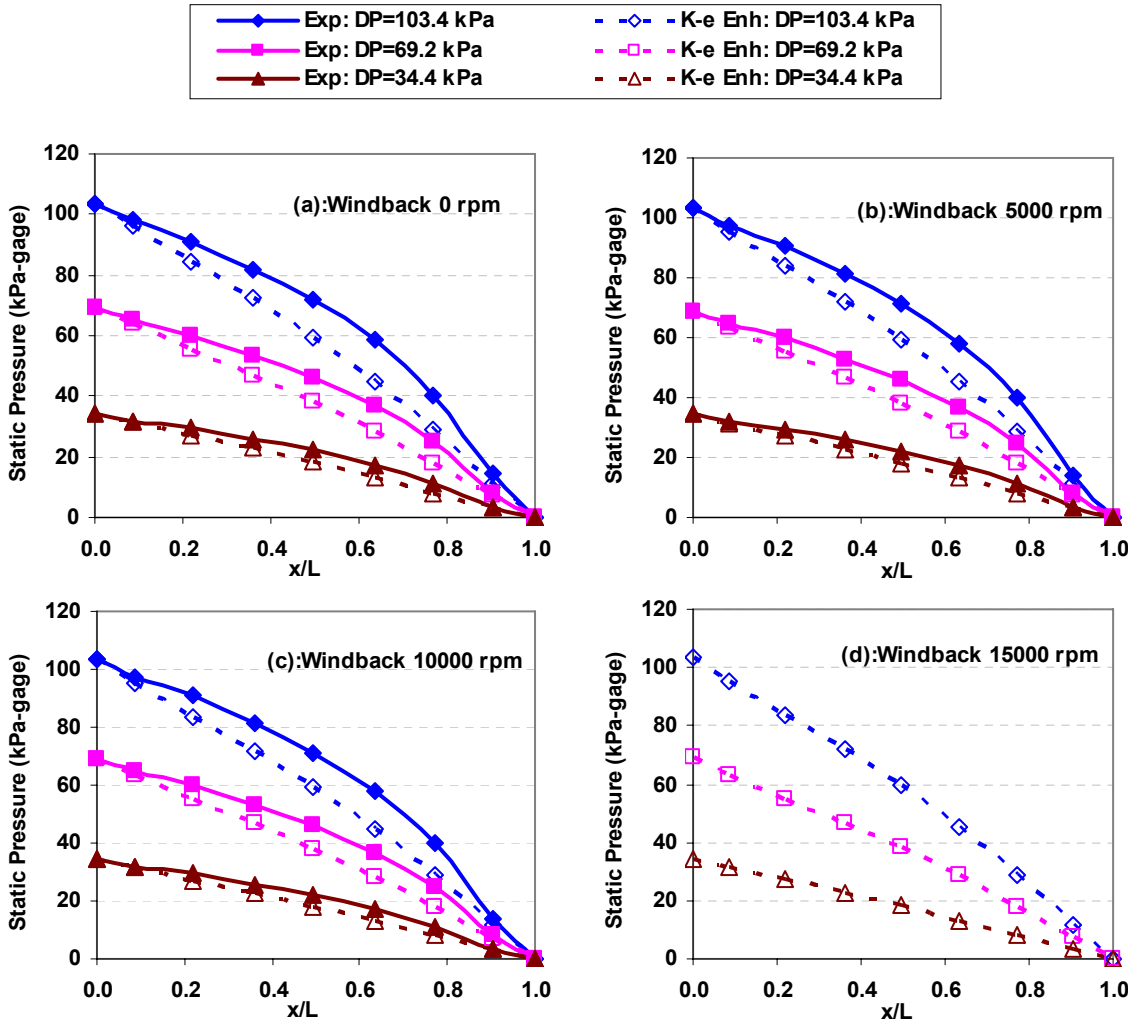

Fig. 38 Windback measured and predicted axial pressure distributions for different shaft speeds.

exit of the seal while the simulation predictions show a nearly uniform pressure drop. The computer simulation solution included the energy equation and the effects of air compressibility with a maximum Mach number of approximately 0.25. Thus, the flow was never choked. The maximum difference between the measured and predicted pressures was about 25% of the local value and less than 10% of the absolute pressure measurement. Fig. 39 shows that both the measurement and predicted pressures inside the seal cavity are independent on the shaft speed for both low and high differential pressures. The pressure measurement shows higher compressibility effects than predictions as indicated by the increased pressure gradient near the seal exit. The CFD simulations under-predict the outlet velocity within the seal cavity, as we will

see later in Fig. 41, and that agrees well with the compressibility effect implied by the pressure measurements.

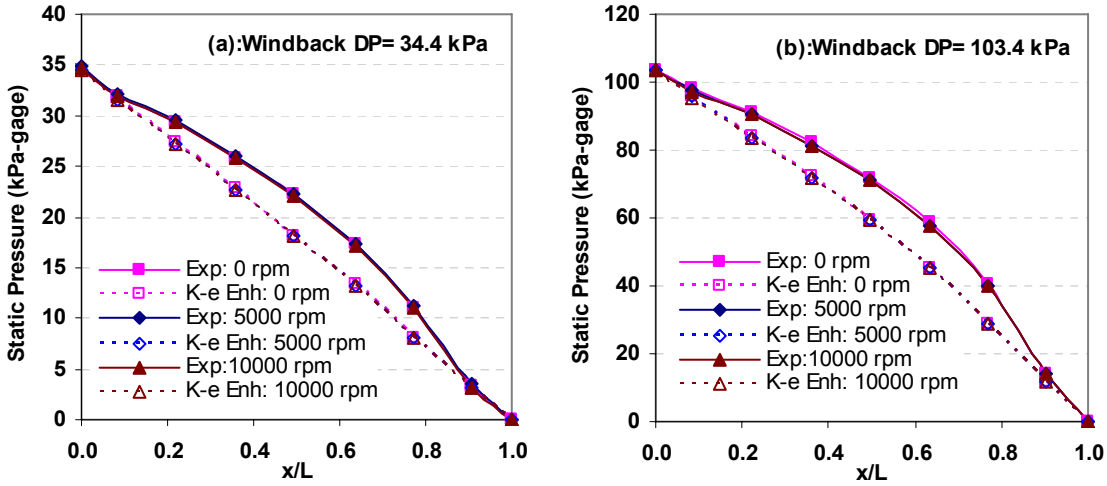

Fig. 39 Windback measured and predicted axial pressure distributions for different rotor speeds at DP=34.4 kPa and DP= 103.4 kPa.

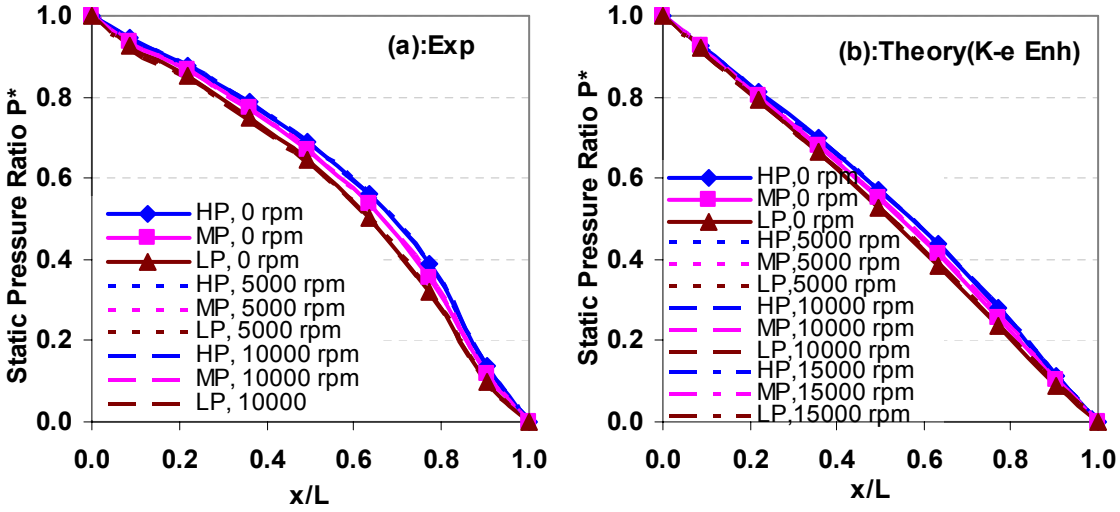

Fig. 40 Windback axial pressure ratio distributions for different rotor speeds and DP; (a) Experimental measurements and (b) Theoretical predictions.

Fig. 40 represents the axial pressure distributions as a pressure ratio $P^* = (P-P_{out})/(P_{in}-P_{out})$. It contains the same data information shown in Figs. 38 and 39, but presented in a different

way. The purpose is to determine if a non-dimensional grouping can be used as a reference for axial pressure distribution for similar windback seals. Both the experimental measurements and the CFD predictions show that the pressure ratios are independent of rotor speed for all *DP*'s. In addition, Fig.40a and b show increasing curvature of the *P** line with increasing *DP* while lowering the inlet head pressure loss and exit pressure recovery. Higher *DP* means higher compressibility effect (higher average air density) which helps explain the highest hump at the highest *DP* compared to the lowest *DP*.

Inlet and Exit Velocities

The inlet (V_2) and exit (V_6) air velocities were measured at the middle of the second and the sixth cavity, respectively, using Pitot probes oriented in the direction of the circumferential flow inside these cavities (see Fig. 11 page 17). The maximum predicted Mach number (nearly 0.25) justified ignoring compressibility effects and using Bernoulli equation Eq.(6) to calculate the experimental velocities.

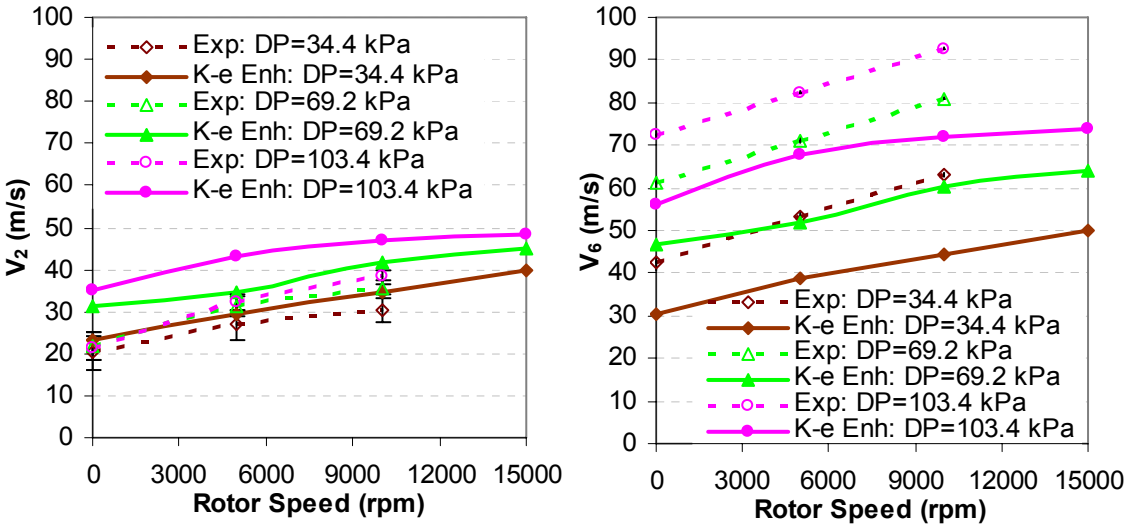

Fig. 41 Windback measured and predicted inlet and exit air velocities versus rotor speed for different DP's.

Figs. 41 and 42 show the measured and predicted inlet and exit air velocities versus rotor speed for different differential pressures. Increasing the shaft speed increases the shear stresses

within the flow field through transferring the effect of shaft rotation to the flow in the seal cavity and clearance through the air viscosity and hence, increasing the drag force. This increases the circumferential air velocity. Both velocities increase with increasing shaft speed and/or differential pressure *DP*. The measurement of the inlet and exit velocities agrees with the static pressure measurement. The predicted uniform pressure drop versus the increasingly negative slope of the measured pressure suggested that the predicted inlet velocity will be higher than the measured, while the measured outlet velocity is higher than predicted. However, due to the pressure drop and decreasing air density, the leakage velocity within the seal groove continually increased towards the exit of the seal. The maximum increase of the measured inlet velocity due to the increase in rotor speed from 0 to 10000 rpm is seen at the highest *DP* and is around 80%, while the increase in the inlet velocity due to the increase in *DP* is around 25% at 10000 rpm. On the other hand, the measured outlet velocity increases linearly with rotor speed with a maximum increase of 48% at the lowest *DP*. Fig. 42 shows that the outlet velocity increases linearly with increasing *DP* with a maximum increase of 71% at 0 rpm. The maximum difference between the measured and predicted velocities was about 45% at the lowest *DP* with no rotation. Both measured and predicted velocities show the same trend and nearly the same percent increase with increasing rotor speed and *DP*.

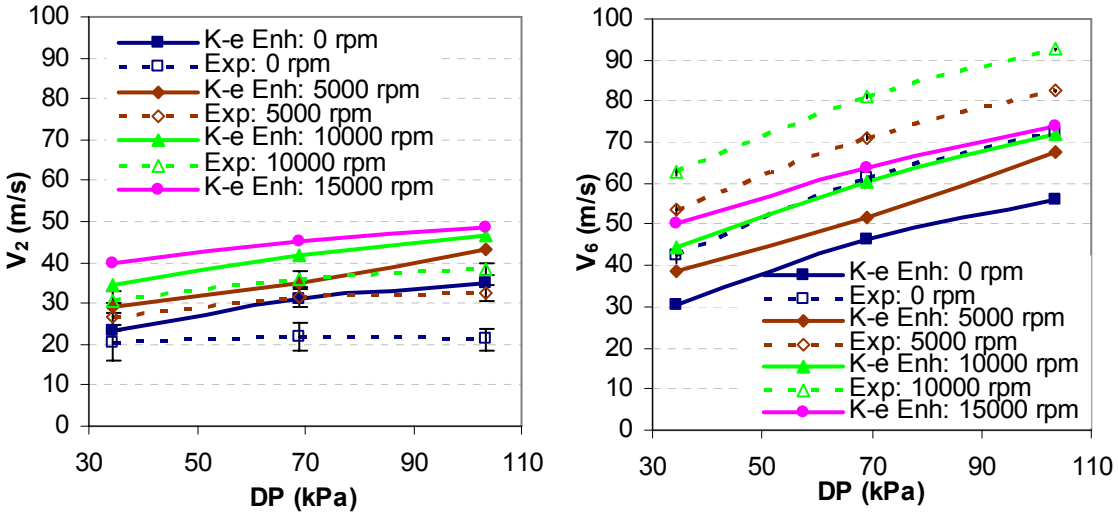

Fig. 42 Windback measured and predicted inlet and exit air velocities versus DP for different rotors.

CFD Flow Field

The CFD simulations provide detailed information about the operation of a windback seal in terms of flow field variables such as pressure and velocities. A three dimensional (3D) figure of these flow field variables will not show the inside flow detail. Besides, the 3D figure will be too complex to read and compare the variables at different conditions. Therefore, four radial sectional views (illustrated in Fig.43) along the seal axis, 90 degrees apart were taken from the windback seal simulation to study the effects of the operational and geometrical parameters on the pressure and velocities flow fields. The 0° and 180° sectional views were taken at y=0 in the x-z plane, and the 90° and 270° sectional views were taken at z=0 in the x-y plane. In addition, the four views were arranged, as if the 3D seal was cut and unfold along the circumferential direction. A zoomed view of the seal clearance is shown at the lower portion of the 270° sectional view. These angle views will be presented on all contours plots. This will provide more insight into the flow detail and help explain the trends observed in the two dimensional Figs. 29 through 37 of the leakage flowrates. All pressure and velocities contours for all operating condition are shown in the appendixes.

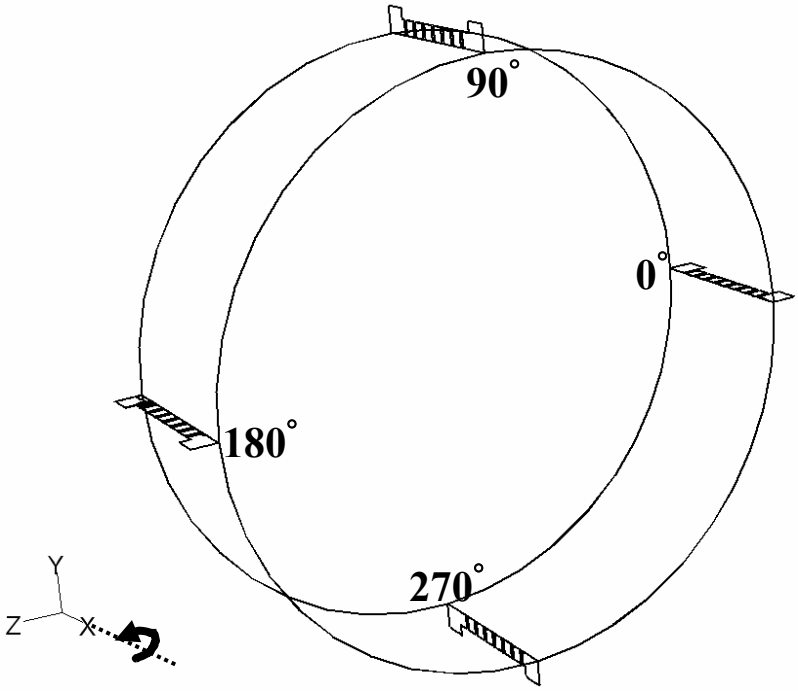

Fig. 43 Location of the four sectional views.

Static Pressure Contours

The static pressure contours are shown in Fig. 44 for a single case at 15000 rpm and *DP* of 103.4 *kPa*. Fig. 44 shows that the static pressure in a windback seal decreases along the axial direction of the seal through the clearance cavity due to frictional losses and to the fact that the flow is expanding under the continuous tooth. In addition, the static pressure drops in a continuous fashion along the cavity length in a windback seal, different from a labyrinth seal, in which the pressure is uniform in the circumferential direction. Furthermore, the enlarged seal clearance pressure contour shows that the pressure is uniform across the clearance and almost independent on the seal radial direction *r*. All other static pressure contours cases have the same trend as observed in Fig. 44.

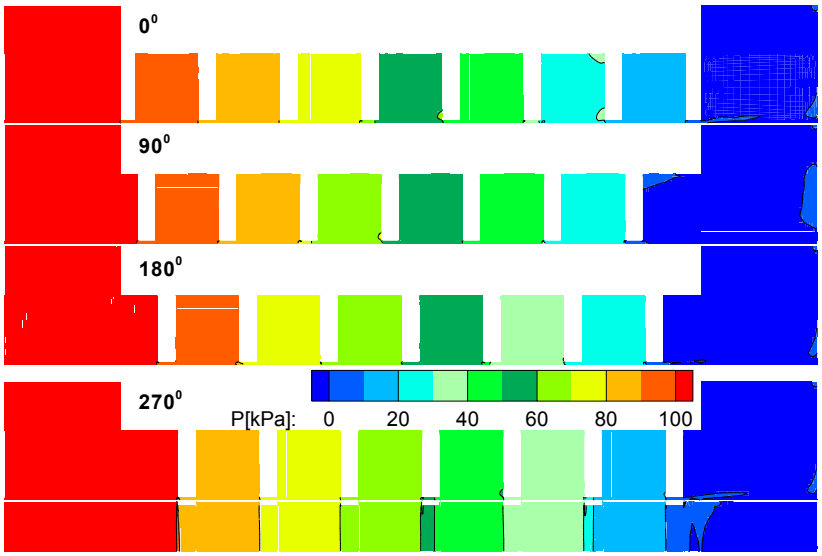

Fig. 44 Predicted pressure contours for single start geometry: Ω=15000 rpm, DP=103.4 kPa, c=0.1 mm, s=3.56 mm, and h=2.94 mm.

Contour plots do not show the small variations in the static pressure along the seal axis due to inlet losses or to flow expanding under the tooth. Therefore, the static pressure is plotted along an axial line passing through the center of the clearance at the 90° seal sectional view. Considering all cases in Fig. 45, the plot starts with a straight line representing the inlet pressure condition, followed by a sudden drop in the pressure, due to the inlet losses. The expansion of the flow under the tooth is seen clearly by the uniform drop of the pressure, resulting in an

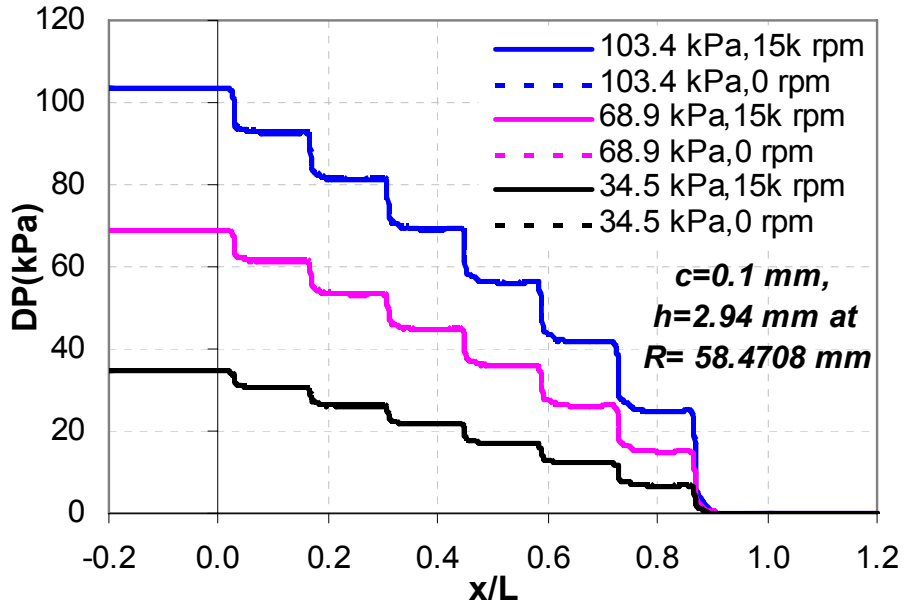

Fig. 45 Predicted axial pressure distribution at the middle of the clearance for different DP's and shaft speeds at 90° seal sectional view.

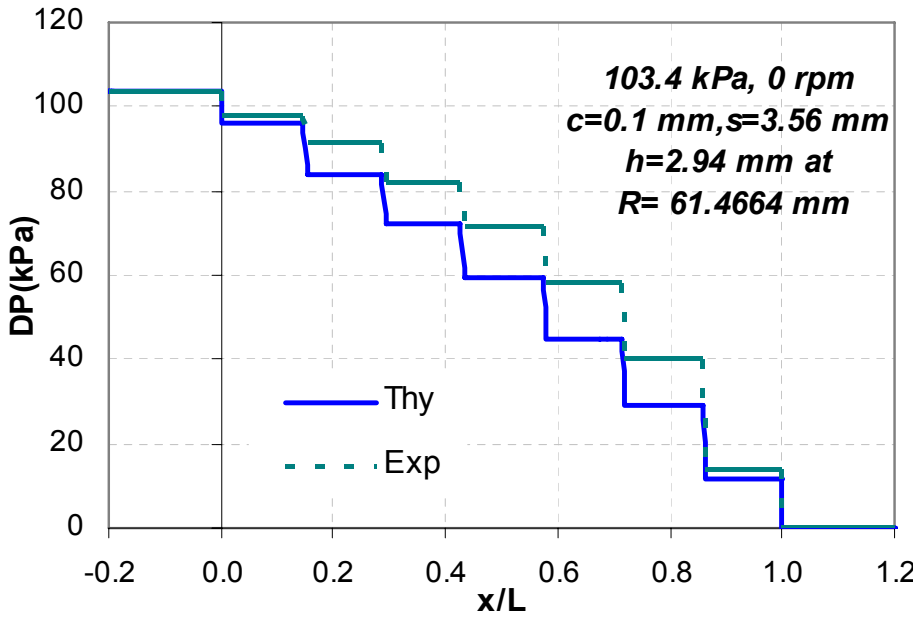

Fig. 46 Experimental measurements versus predictions of expanded axial pressure distribution at 0 rpm, 103.4 kPa.

increase in the flow kinetic energy. At the exit of the first tooth, part of this kinetic energy will be carried over to the next tooth increasing the axial velocity. The other part will recover back to static pressure (Fig. 45 shows that small portion of the kinetic energy will be recovered just downstream the tooth exit, about 250 *Pa*, then the pressure remains constant at the lowest pressure under the tooth for the whole cavity length) and some will be lost as heat. This is almost the same as described by Egli's [11] for labyrinth seals. Fig. 45 also shows that the pressure across the cavity in the axial direction is almost constant. In addition, the inlet losses increase from one stage to the other stage, due to the increase of the kinetic energy. Again, Fig. 45 shows that the rotor speed has negligible effect on the static pressure distribution.

Figs. 38 to 40 reflect the difference between the measured and CFD predicted *DP* across each tooth in the axial direction of the seal. It is evident from Figs. 44 and 45 that the axial pressure is uniform and constant for a single cavity at constant circumferential angle. Therefore the predicted and measured pressures were expanded in the seal cavity in the axial direction, ignoring the tooth thickness and presented in Fig. 46. The experiential pressure measurements axial distribution looks the same as Fig. 45, with a well predicted inlet loss as seen in the first step. The predicted pressure drop in the 2 step is higher than measured, and that agrees with a lower inlet velocity measurement than predicted. On the other hand, the predicted pressure loss in the last step before the exit is lower than measured and that agrees with a higher exit velocity measurement than predicted. The pressure measurements show a higher compressibility effect with higher average density than the CFD simulation predictions, even when including the ideal gas law and solving for the energy, continuity and momentum equations for the CFD.

Velocity Contours

Figs. 47 to 49 show the contour plots for the three velocity components V_x , V_r and V_θ at *DP*=103.4 *kPa* and 15000 rpm. Figs. 47 and 48 show there is a large vortex in the seal cavity. This vortex is a result of the jet action of the flow expanded under the seal tooth. The vortex axis is perpendicular to the flow direction through the cavity. In addition, the flow is accelerating along the cavity axis as a result of pressure drop and shaft speed as seen in Fig. 49. Therefore, the flow in the cavity has a helical shape, circulating and rotating at the same time and can be seen clearly from particle trace path shown in Fig. 50. Fig. 47 shows that the axial velocity within the seal cavity has a small increase with increasing *x*, and that the shape of axial velocity distribution profile does not change with *x*. However, within the seal clearance, V_x increases

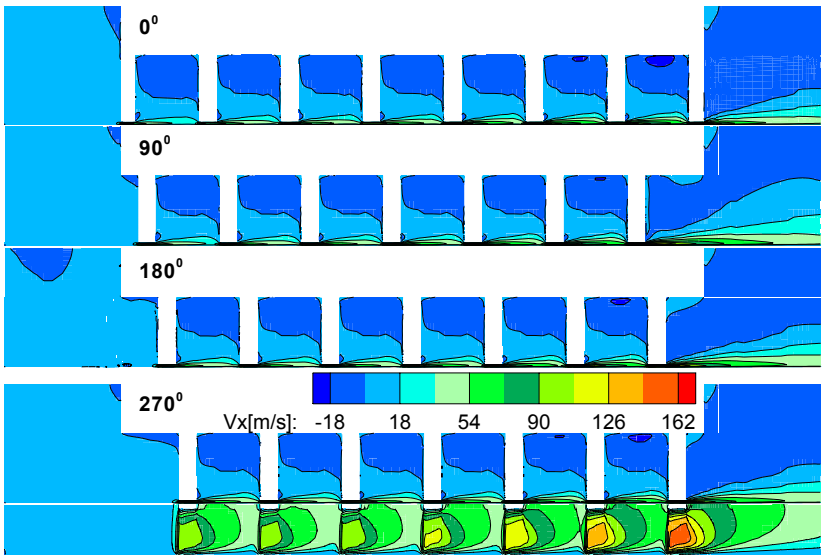

Fig. 47 Axial velocity for single start geometry: Ω=15000 rpm, DP=103.4 kPa, c=0.1 mm, s=3.56 mm, and h=2.94 mm.

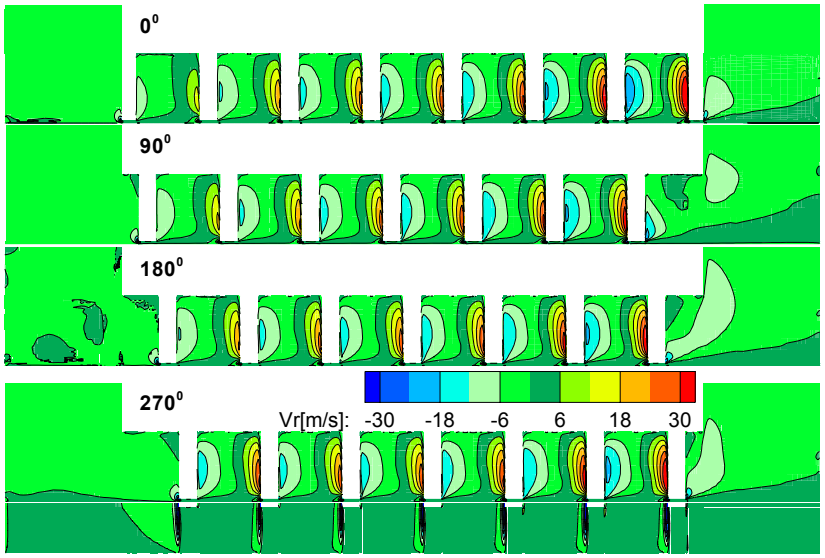

Fig. 48 Radial velocity contours for single start geometry: Ω=15000 rpm, DP=103.4 kPa, c=0.1 mm, s=3.56 mm, and h=2.94 mm.

considerably with increasing x. This results in an increase in the upward or positive radial velocity within the seal cavity. The positive V_r covers a smaller portion of the cross sectional

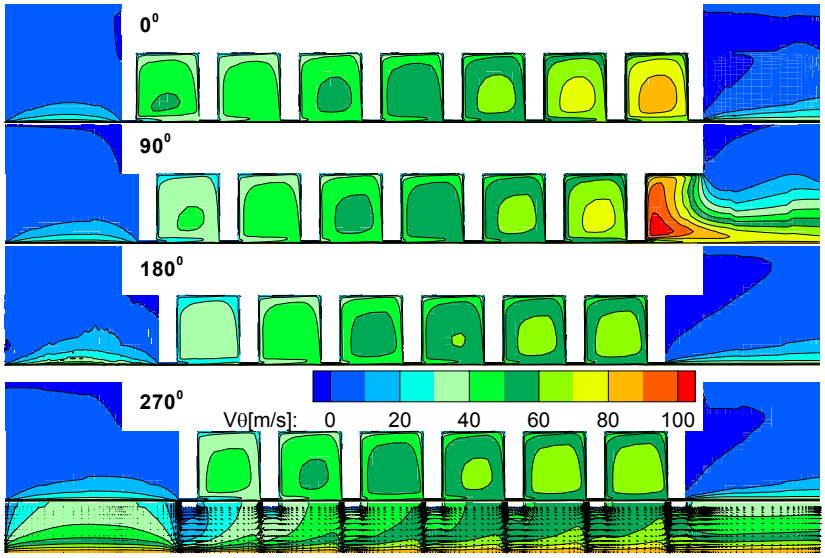

Fig. 49 Circumferential velocity contours for single start geometry: Ω=15000 rpm, DP=103.4 kPa, c=0.1 mm, s=3.56 mm, and h=2.94 mm.

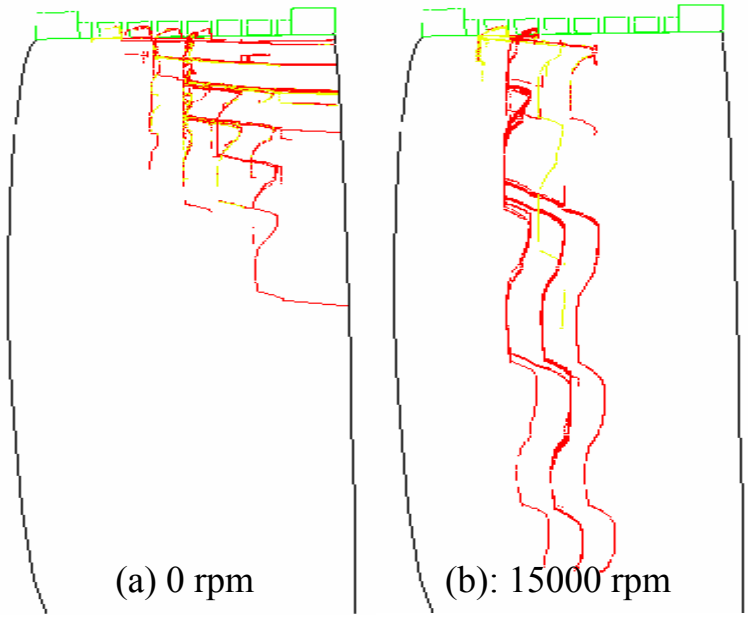

Fig. 50 Particle trace path for a rectangular clearance area *c.s* starting at first tooth for a windback seal with c=0.1 mm, h=2.94 mm, s=3.56 mm, at DP=103.4 kPa and rotor speed of (a) 0 rpm and (b) 15000 rpm.

area of the seal cavity than the negative values. Hence, the downward or negative V_r will be smaller in magnitude than the upward V_r to preserve the continuity of mass as seen in Fig. 48. The vortex strength increases with increasing x along the cavity axis. This enhances the turbulence toward the exit of the seal, making the seal more efficient in preventing contamination.

Fig. 51 shows part of the data shown in Figs. 47 to 49, as a 2D plot for the velocity components along a line passing through the center of the clearance for the 90° sectional plane. High pressure drop across the seal tooth at the inlet of each stage increases the flow velocity components along the seal axis. The ratio between the cavity height and seal clearance *h/c* is 29. Therefore, when the flow goes through a sudden contraction in area (inversely proportional to *h/c*) accompanied by a pressure drop, the axial velocity will also increase rapidly by a factor much less than *h/c* due to air compressibility (density), carry over and Vena Contracta effect as seen in Fig. 51 at the inlet of each stage. Then the axial flow velocity increases as the flow goes under the seal tooth in a uniform linear way, due to pressure losses across the tooth, followed by a drop in the axial velocity due to flow expansion from under the tooth through increasing the flow jet area (see Fig. 47) in the axial direction of that cavity. The sudden contraction in area and *DP* effect at the start of each stage, results also in directing the flow downward at the entrance of each stage, hence, increasing the negative radial velocity. Fig. 51 shows that the large negative spike in radial velocity is followed by a slow upward velocity, due to the constant flow area under the tooth.

The circumferential velocity in the clearance increases along the seal axis, due to the increase in the circumferential velocity inside the seal cavity as a result of pressure drop a long the axis of the cavity (see Fig. 52, V_θ zoomed view). In addition, V_θ increases from one stage to the next stage. However, the rotor speed has a dominant effect on increasing the circumferential velocity in both seal clearance and cavity (see Fig. 53, V_θ). The effect of rotation is reduced farther from the rotor surface. Therefore, V_θ along a line passing through the center of the clearance at 15000 rpm and *DP*=103.4 *kPa* has an approximate average value of 60 *m/s*. V_θ increases slowly along the axial direction in the clearance for stage one (one cavity and one tooth) due to effect of seal walls, where the flow is stationary. Hence, Figs. 49 and 51 show that, under the tooth, V_θ is small and increases slowly in the axial direction to reach a maximum in the cavity vicinity, and then V_θ decreases as the second stage tooth is approached. Fig. 51 shows that the rotor speed has no effect on V_x and V_r and mainly affects V_θ. The increase in both axial

and circumferential velocity along the axial direction is mainly due to compressibility effects (decrease in density in the axial and circumferential directions) and small increase is due to kinetic energy carry over from one stage to the next. This is demonstrated through plotting the mass flowrate flux in both x and θ directions in Fig. 51. These figures show that the increases in V_x and V_θ in the axial direction are primarily due to the density variation. The constant mass flux indicates a constant mass flowrate along the axis of the seal in both the axial and tangential direction.

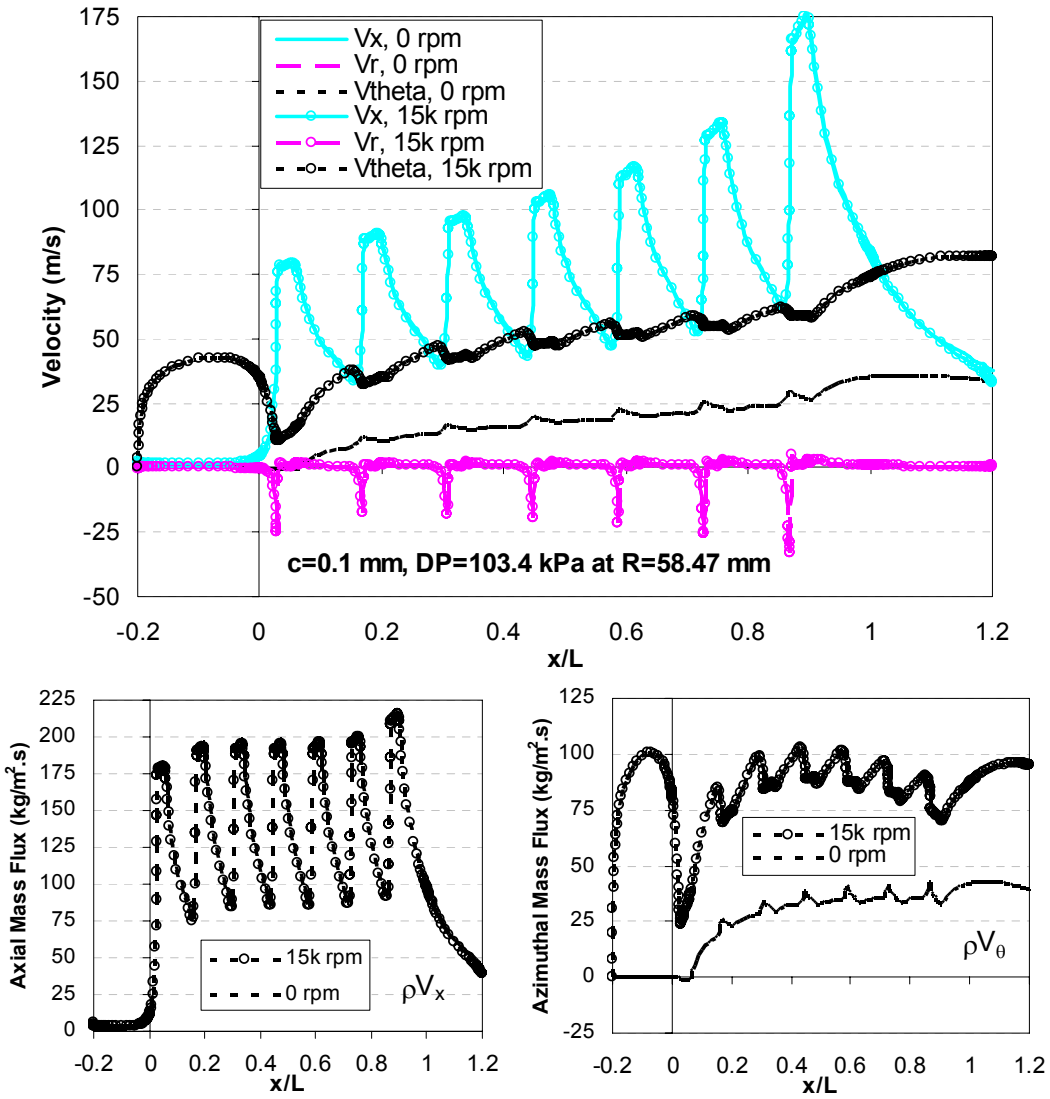

Fig. 51 Axial velocity distribution and mass flux for DP=103.4 kPa at 0 and 15k rpm at the middle of the clearance at 90° seal sectional view.

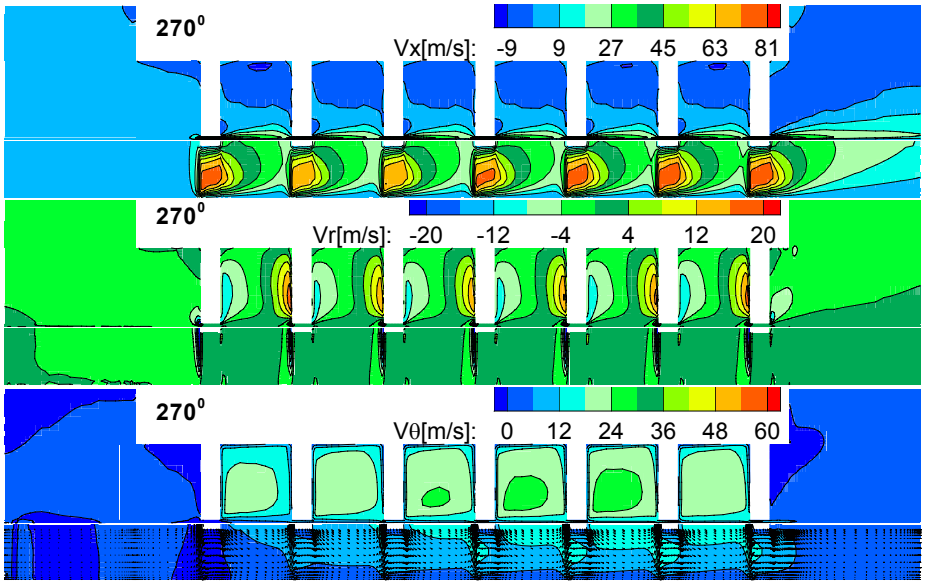

Fig. 52 Velocity contours for single start geometry: Ω= 0 rpm, DP=34.5 kPa, c=0.1 mm, s=3.56 mm, and h=2.94 mm.

Two cases were studied to illustrate the effects of rotor speed on the velocity flow fields. Figs. 52 and 53 show the three velocity component contours using a differential pressure of 34.5 *kPa* for rotor speed of 0 and 15000 rpm, respectively, at a fixed azimuthal angle of 270° . The following observations can be drawn from Figs. 52 and 53:

- With no rotation, the influence of *DP* on the circumferential velocity distribution inside the cavity increases as the flow propagates along the axis of the cavity, with a maximum range of 24-30 *m/s*. Fig. 54a shows that this increase is mainly due to compressibility effects. The mass flux is almost constant in the seal cavities except for the first cavity where the flow is developing and the last cavity where the seal geometry changes. The tooth thickness starts decreasing toward the exit of the seal in the last stage, directing more flow in the axial direction and decreasing the circumferential flux. Increasing the rotor speed from 0 to 15000 rpm increases the maximum circumferential velocity in the seal cavity from 24-30 *m/s* to 42-48 *m/s*. Fig. 54 demonstrates the effect of increasing the rotor speed from 0 to 15000 rpm on the mass flux. Increasing the rotor speed from 0 to 15000 rpm increases the maximum mass flux in the seal cavities from 30-40 to 60-70 $kg/m^2.s$, respectively.

- Circumferential flow in the seal cavities due to *DP* only affects the circumferential flow within the seal clearance up to 75% of clearance height toward the seal exit with V_θ ranges from 6-18 *m/s*.

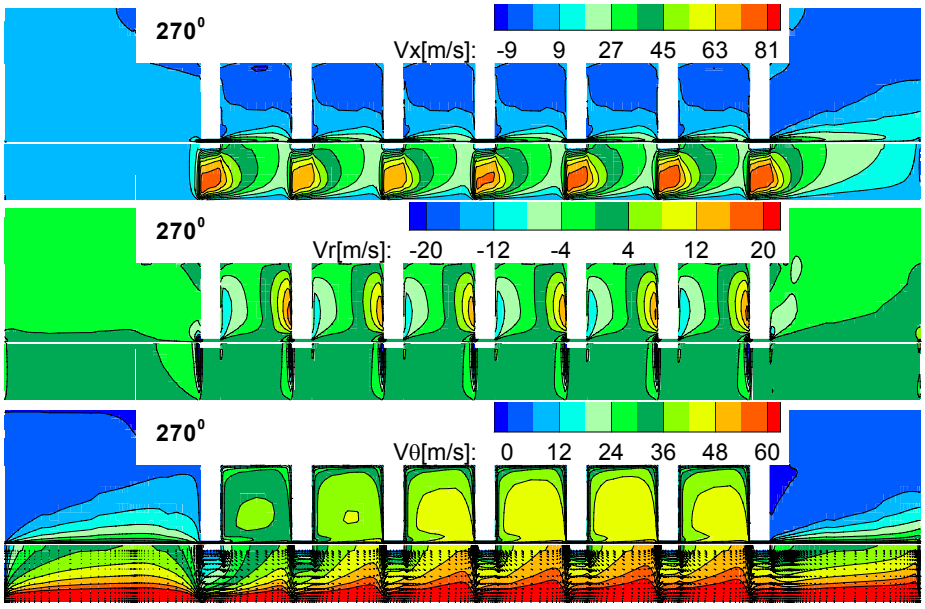

Fig. 53 Velocity contours for single start geometry: Ω=15000 rpm, DP=34.5 kPa, c=0.1 mm, s=3.56 mm, and h=2.94 mm.

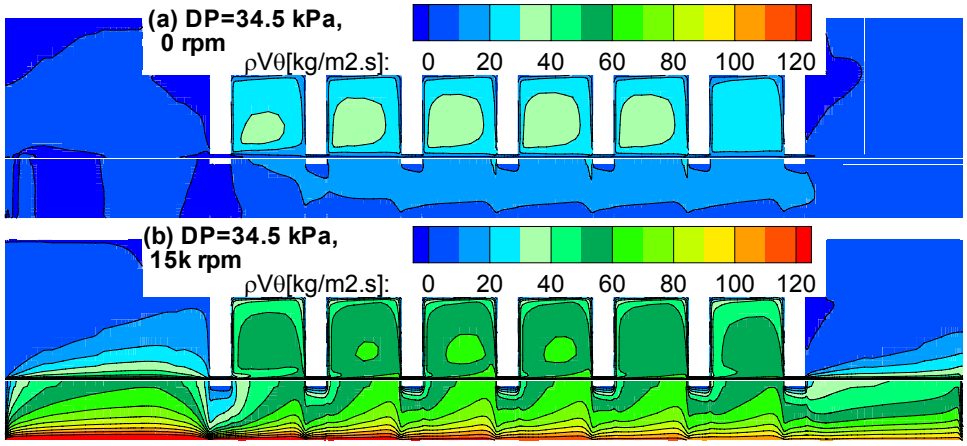

Fig. 54 Mass flowrate flux contours for single start geometry: c=0.1 mm, s=3.56 mm, and h=2.94 mm for DP=34.5 kPa at 0 and 15000 rpm.

- Rotor speed affects mainly the circumferential velocity with a minimal effect on axial and radial velocities. Therefore, the vortex in the cavity does not change and its strength is independent on rotor speed and mainly a function of *DP* and other geometrical parameters which will be explained in a later chapter.
- Rotor speed increases V_θ inside the seal cavity for almost the whole seal length with a range of 30-48 *m/s*.
- Flow helical shape in the cavity due to both *DP* and rotor speed affects the flow through the whole clearance height with V_θ ranges from 30-92 *m/s*.

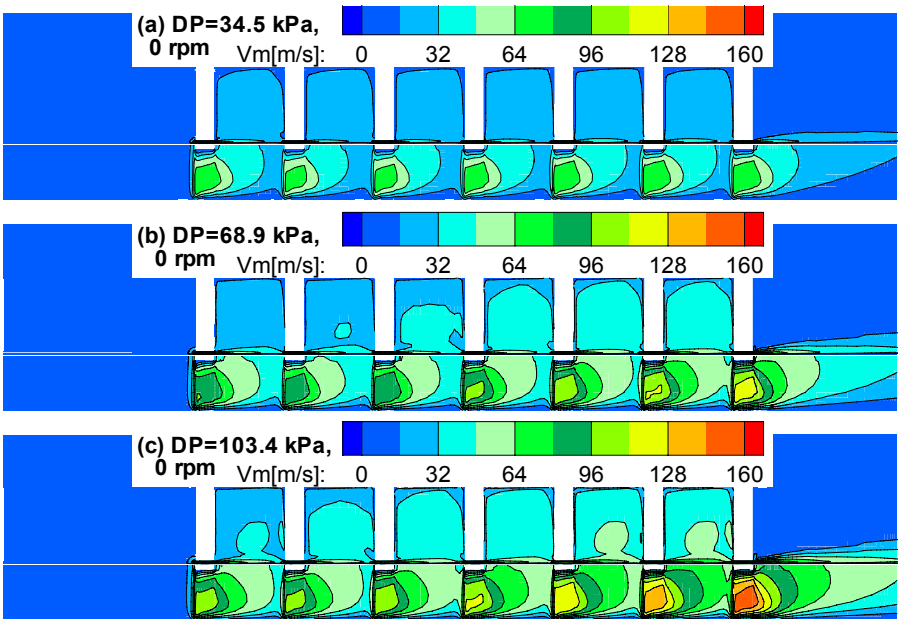

Fig. 55 Velocity magnitude counters at 0 rpm for; (a) DP=34.5 kPa, (b) DP=68.9 kPa and (c) DP=103.4 kPa.

Figs. 55 and 56 show the velocity magnitude contours for three differential pressures each, and for two rotor speeds of 0 and 15000 rpm, respectively. Table 6 summarized Figs. 55 and 56. The maximum influence of changing rotor speed from 0 to 15000 rpm on velocity magnitude in the seal cavity occurs at the lowest *DP* with a 50% increase, compared to a 25% increase at the highest *DP*. However, increasing rotor speed form 0 to 15000 rpm increases the maximum velocity magnitude for both *LP* and *HP* the same span, 16 *m/s*. Therefore, the effects

of rotor speed on increasing the velocity within the seal cavity is constant and adds to the effect of pressure drop. On the other hand, the effect of rotation within the seal clearance changes these percents to 20 and 5 at the lowest and highest *DP*, respectively. Therefore, the highest effect of rotor speed on velocity magnitude is at low *DP*, which explains the highest percent increase of leakage flowrate at low *DP*.

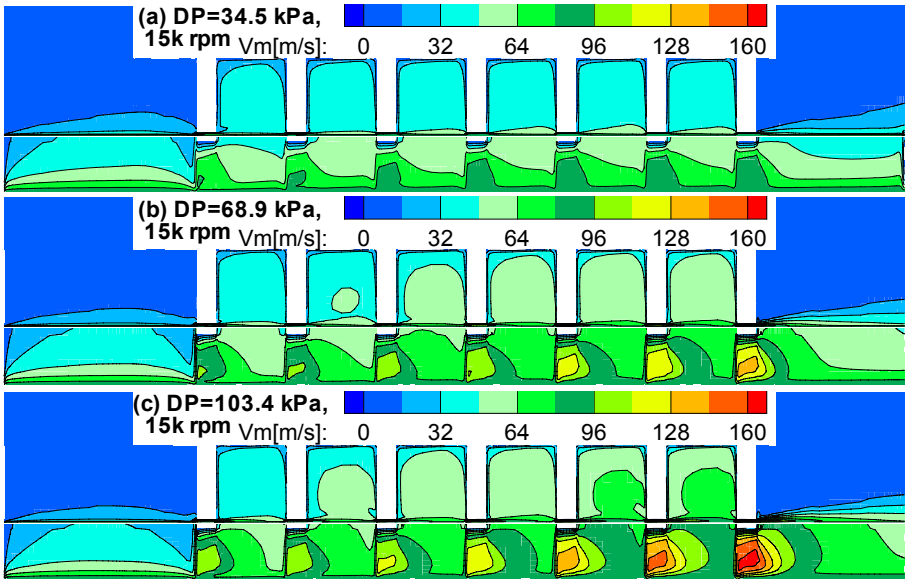

Fig. 56 Velocity magnitude counters at 15000 rpm for; (a) DP=34.5 kPa, (b) DP=68.9 kPa and (c) DP=103.4 kPa.

Table 6 Figs. 55 and 56 summary.

Ω (rpm)	Cavity, V_m (m/s)			Clearance, Max. V_m(m/s)		
	LP	MP	HP	LP	MP	HP
0	16-32	16-48	16-64	64-80	112-128	144-160
15000	32-48	32-64	32-80	80-96	128-144	160-168
Max. % increase 0→15000 rpm	50	33	25	20	12.5	5

Effect of Eccentricity

The effect of eccentricity on leakage flowrates, and pressure and velocity distributions was studied experimentally for a 0.1 mm clearance windback seal. The stator shown in Fig. 6

was moved to eccentric positions in the *y*-direction using the hydraulic shaker system. A positive eccentricity corresponds to pushing the stator against the rotor, making a smaller clearance near the instrumentation. On the other hand, a negative eccentricity corresponds to pulling the stator against the rotor making a larger clearance near the instrumentation as shown in Fig. 18.

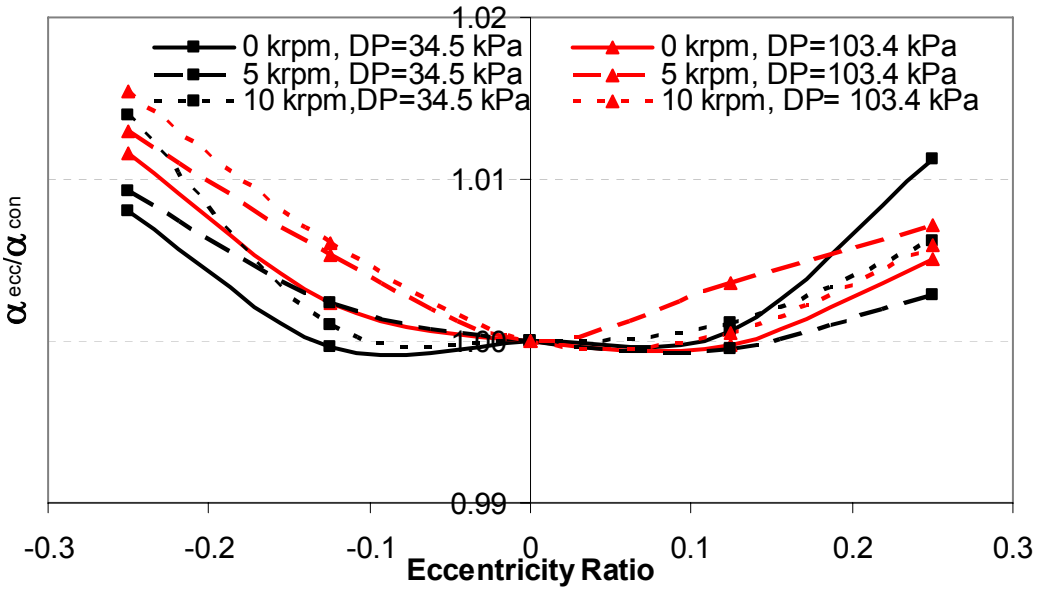

Fig. 57 Flow coefficient ratio versus eccentricity for different shaft speeds and DP's.

The ratio between eccentric and concentric flow coefficients $\alpha_{ecc}/\alpha_{con}$ is shown in Fig. 57 for different shaft speeds and *DP*'s. The experimental data shows that eccentric windback seals leak more than concentric ones, from 0.8 to 1.5% at e=-0.25, and from 0.3 to 1.1% at e=0.25 for all differential pressures and shaft speeds under consideration. Therefore the effect of eccentricity ratio up to 0.25 is small and can be neglected compared to other operational parameters such as rotor speed and *DP*'s.

Figs. 58 and 59 show the axial pressure ratio distribution, P^*, for different *DP*'s and eccentricity ratios at 0 and 10000 rpm, respectively. The data align along three curves in which each curve coincides to one of the three *DP*s (*HP*, *MP*, and *LP*) due to compressibility effects. The pressure measurements were recorded at the top wall of the cavities, which has a depth of 29 times larger than the seal clearance. Therefore, the effect of eccentricity and rotor speed on axial pressure ratio distribution is very small and, as previously explained, the rotor speed affects

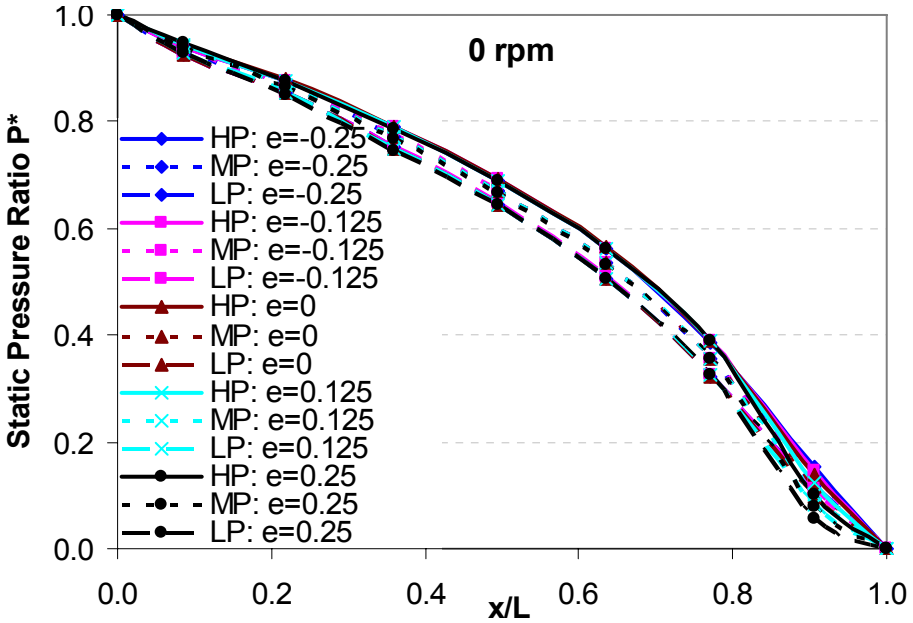

Fig. 58 Axial static pressure ratio distributions for different DP's and eccentricity ratios at 0 rpm.

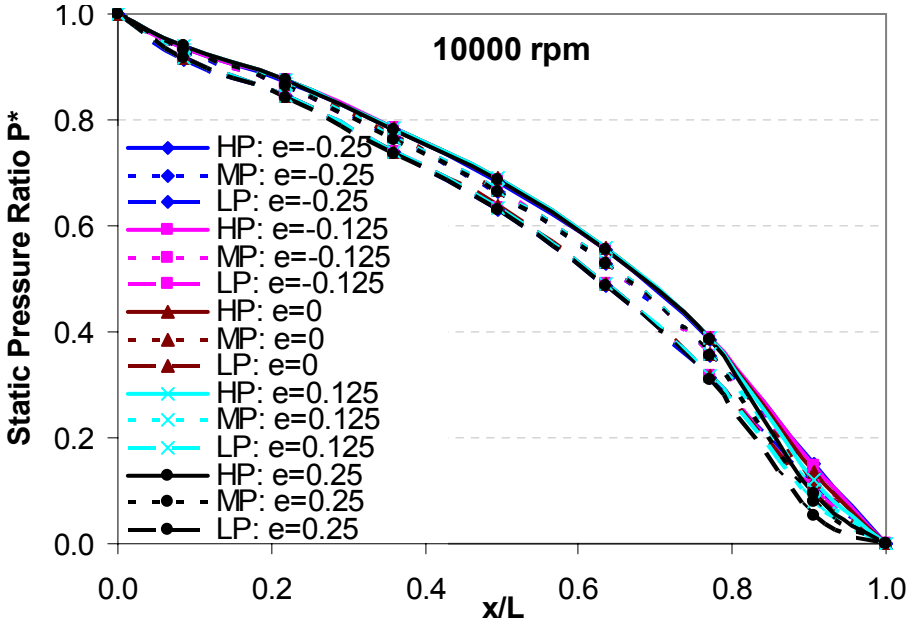

Fig. 59 Axial static pressure ratio distributions for different DP's and eccentricity ratios at 10000 rpm.

mainly the circumferential velocity of air, with a maximum effect near the rotor surface and decreases with increasing the radial distance from the rotor surface because the of the low

viscosity of air. Consequently, the flow kinetic energy in the cavity will not transform back into static pressure to be sensed by the pressure sensor installed perpendicular to the flow direction. Fig. 60 shows the effect of eccentricity on V_2 and V_6 velocities. V_2 increases with increasing positive eccentricity and decreases with increasing negative eccentricities, due to the increase and decrease of leakage flowrate through the cavity, respectively. V_6 has a different trend because of the installation location of the Pitot probe, in which it is not collinear with V_2 velocity Pitot probe but 66^0 apart in the circumferential direction.

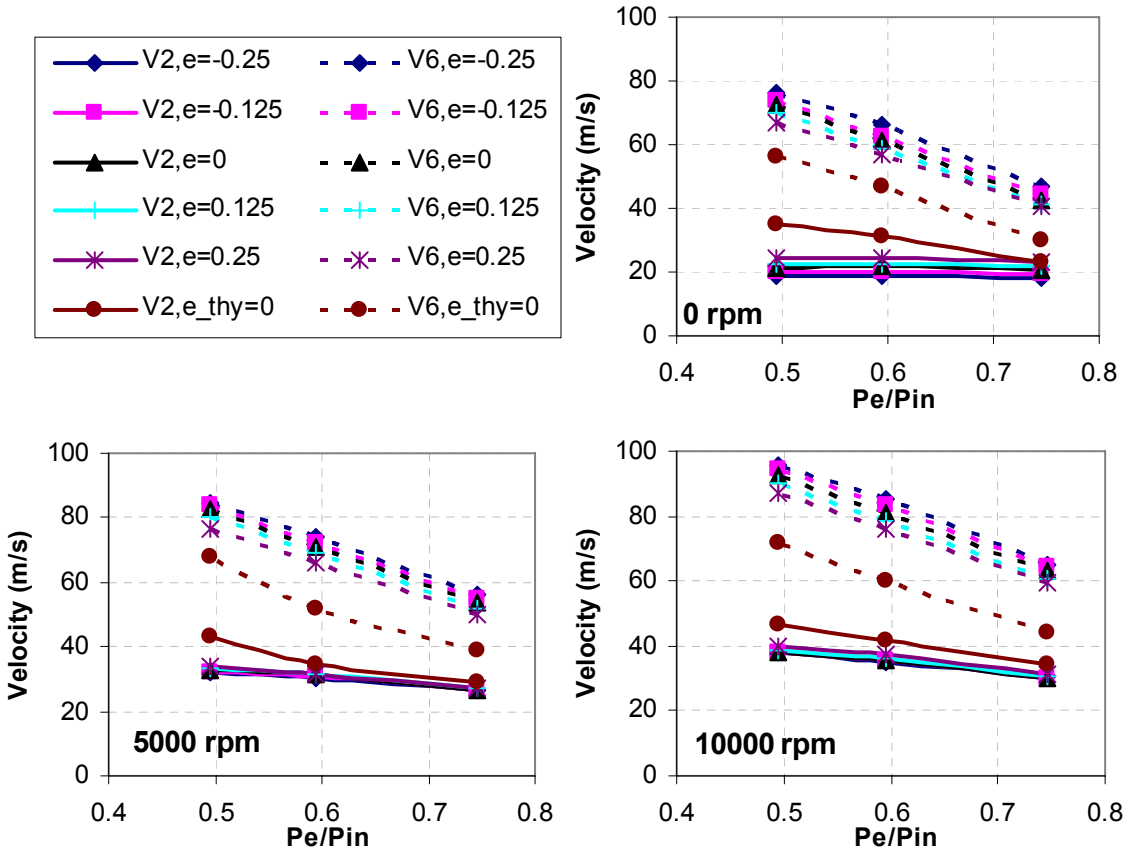

Fig. 60 Inlet and outlet velocities for different DP's, shaft speeds and eccentricity ratios.

Smooth Seal

Turbulent flow numerical simulations indicate that the smooth seal has the lowest leakage rate. This is opposite to a labyrinth seal where the least leakage occurs for a very thin

tooth. Due to this trend, the smooth annular seal was selected for study to verify the predictions. The comparison did not include the inlet and exit velocities because they could not be measured since the Pitot probe head was almost 5 times larger than the smooth seal clearance (0.1 mm). The smooth seal was experimentally tested and numerically simulated. It represents the limiting case for the windback seal in terms of the geometrical parameters shown in Table 7. The experimental results were compared to two theoretical flow models; laminar flow and turbulent flow with enhanced wall treatment. Interestingly, these two flow models represent upper and lower limiting cases of the leakage observed in the smooth seal. Based upon accepted standards, Szeri [28] and Pinkus and Sternlicht [29], this flow condition is classified as neither laminar nor turbulent. This suggests that the flow is transitional. The maximum calculated axial or circumferential Reynolds numbers were less than 1200, and this indicates that the flow is transitional.

Table 7 Windback seal limiting geometrical parameters.

Geometrical parameter	*Limiting case*
Number of Tooth starts	0
Cavity depth *h*	0
Pitch *s*	0
Tooth thickness *t*	25.4 mm

Szeri [28] provides a clear discussion of flow instabilities that usually preceded the flow transition from laminar to turbulent flows. These instabilities occur in two types: one is a centrifugal instability and is represented by Taylor vortices and the second is parallel flow instability which is represented by Reynolds number. The Taylor vortices start to appear at a critical Taylor number of 1707.8 for concentric cylinders with the rotation of the inner cylinder. Using $Ta = \mathrm{Re}_{cir}^2 (2c/D)$, the critical Reynolds number for a 0.1 mm seal clearance and a shaft diameter of 0.1168 mm is 990. Table 8 shows that the circumferential Reynolds numbers calculated from the experiment. Their values range above and below the critical value of 990.

Pinkus and Sternlicht [29] show that for adiabatic flows of a horizontal annulus using air as the working fluid, the flow can be classified as a function of Taylor's and axial Reynolds numbers into four instability regimes; laminar, turbulent , turbulent plus vortices and laminar

plus vortices flows. According to this classification, the flow through the 0.1 mm smooth seal was laminar for the *LP* case, turbulent for the *HP* case and transitional for the *MP* case.

Table 8 Reynolds and Taylor number for the smooth seal.

Ω(rpm)	P_{in}(Pa)	Re_{axial}	Re_{cir}	Re_{max}	Re_{min}	Ta
15070	204136	932	1151	1482	1101	2306
9945	204551	985	764	1247	1058	1015
5020	205292	1030	387	1100	1048	261
0	205448	1037	0	1037	1037	0
15000	171239	676	960	1174	893	1604
9975	169968	684	637	935	787	705
5095	169915	709	325	780	736	184
0	171031	723	0	723	723	0
15050	135904	348	764	839	681	1016
10030	135178	349	509	617	523	451
5050	135825	373	257	453	422	115
0	135974	367	0	367	367	0

Leakage Mass Flowrate

The smooth seal leakage mass flowrate was measured for three different inlet pressures and four rotor speeds including the no rotation condition. The exit pressure was atmospheric. Fig. 61 shows a comparison between the measured and the predicted leakage mass flowrate. The laminar flow model over-predicts the leakage flowrate and agrees more with the experiment at low rotor running speeds with a maximum difference of 2.5%. This difference increases with increasing rotor speeds up to 11% at the highest *DP* and shaft speed. On the other hand, the turbulent flow model under-predicts the leakage flowrate with a maximum difference of 15% at 0 rotor speed. The difference decreases with increasing rotor speeds to a maximum difference of 8% at the highest *DP*. As opposed to the laminar flow model, the turbulent flow model captures the trend of decreasing the leakage mass flowrate with increasing rotor speed. Likewise, the experimental leakage flow rate decreases with increasing rotor speeds. The measurements show a higher dependency on rotor speed than the predictions. In term of percentage, the decrease in experimental leakage flowrate with increasing rotor speed is almost independent on *DP* for this study with a maximum reduction of 10% compared to 3% reduction using the turbulent flow model. Increasing the rotor speed with a 0.1 mm seal clearance will increase the circumferential

velocity component of the flow. Therefore, the velocity magnitude increases as V_θ goes up, which increases the frictional drag losses directing a portion of the axial flow in the circumferential direction, as a result the leakage flowrate decreases with increasing rotor speed. Fig. 62 presents the effect of *DP* on leakage flowrate for different rotor speeds. The measurements and both prediction models agree well at the lowest *DP*, the difference between the prediction flow models starts increasing in almost a linear relationship with increasing *DP*. This is due to the flow being driven mainly by the axial pressure difference. The turbulent and laminar prediction models represent the two extremes of the experimental leakage flowrate. Turbulent and laminar flows represent the lower and upper boundaries, respectively, of the measures leakage mass flowrate as clearly seen in Fig. 62. Since the Darcy's friction factor given in Eq. (23) is higher for turbulent flows than laminar flows, the turbulent flow will have higher resistance, and hence lower leakage flowrate predictions by turbulent models than laminar models.

$$f = 4\rho\pi^2 D^2 c^3 \frac{-\partial P/\partial x}{\dot{m}^2} \tag{23}$$

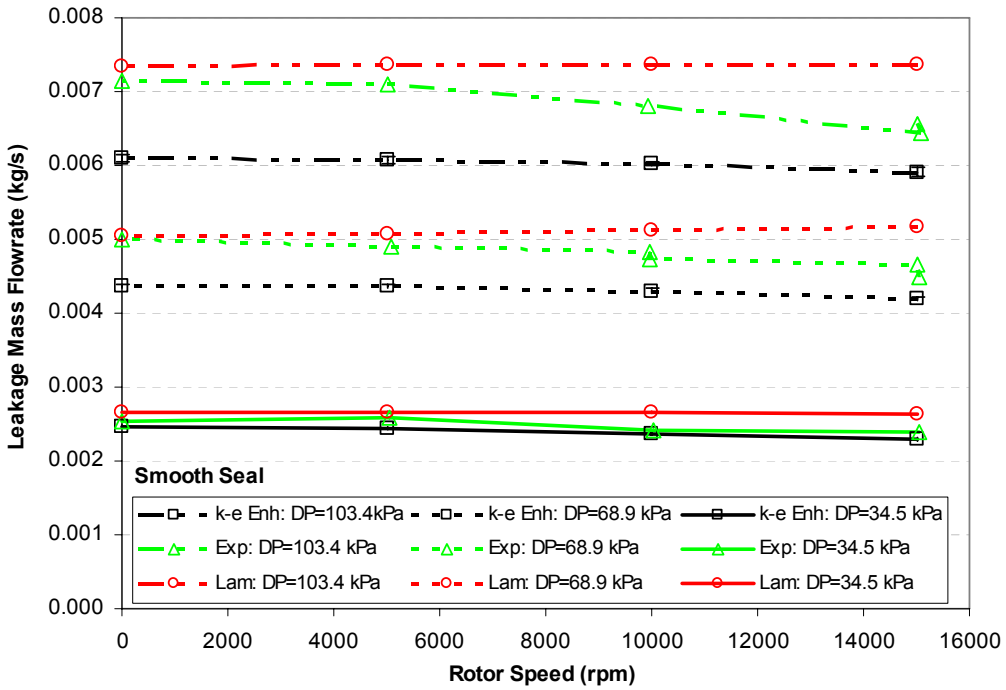

Fig. 61 Smooth seal leakage mass flowrate versus rotor speed for different DP.

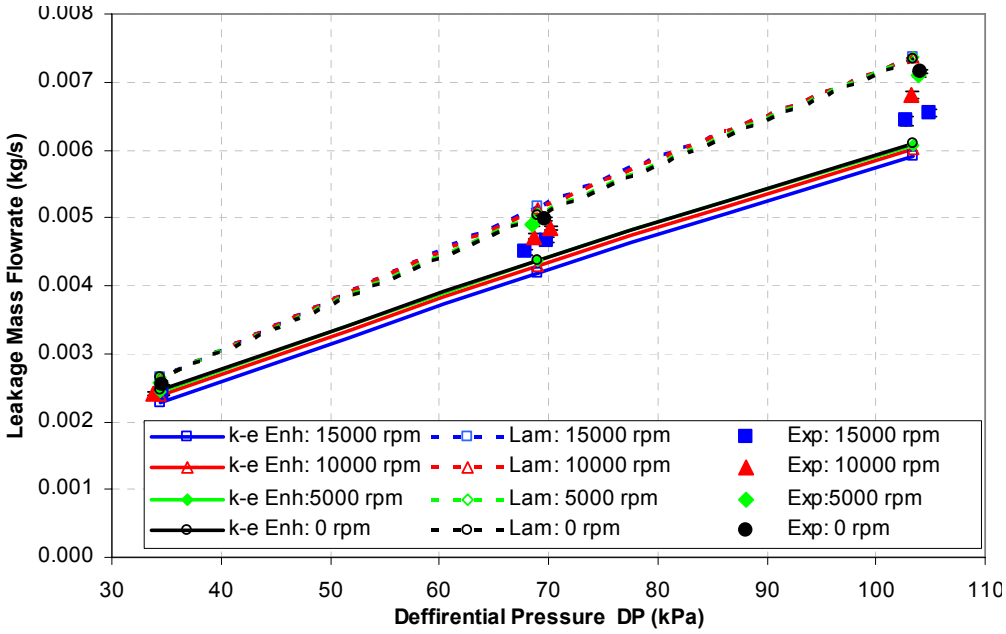

Fig. 62 Smooth seal leakage mass flowrate versus DP for different rotor speeds.

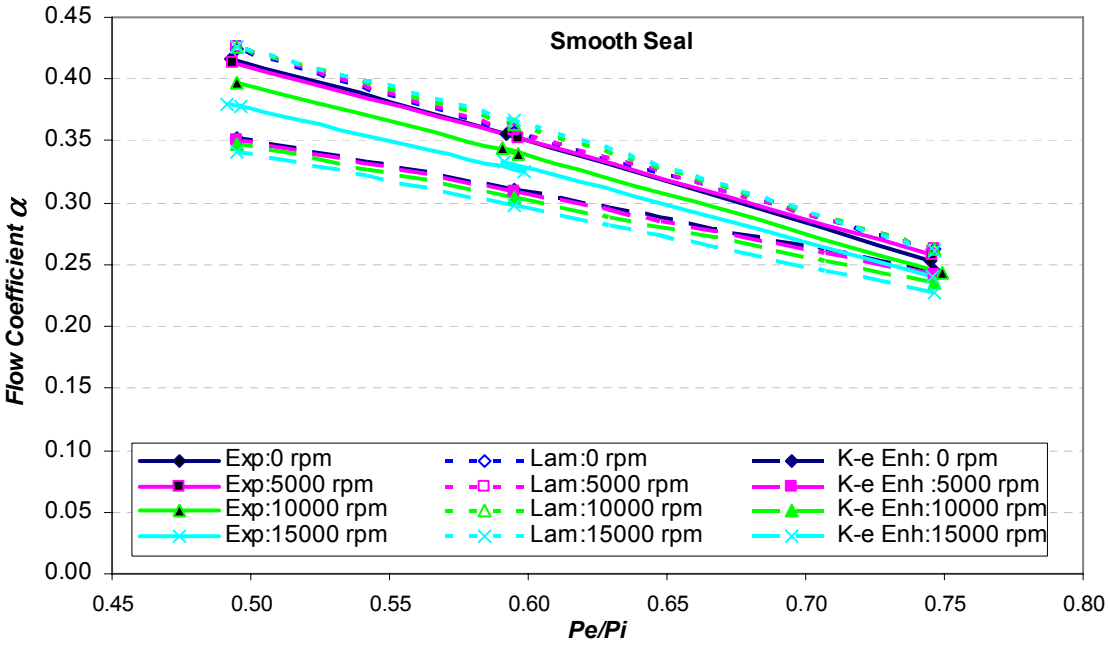

Fig. 63 Smooth seal flow coefficient versus pressure ratio for different rotor speeds.

It is worth pointing out that the turbulent model predicts the leakage flowrate in a windback seal so much better than in a smooth seal having the same operating conditions of *DP* and rotor speed. This is due to the geometry of the windback seal interacting with the flow going under the tooth and the flow going along the seal cavity creating turbulent flow. Whereas, in a smooth seal, the absence of seal cavities with such small seal clearance, the flow remains laminar in nature rather than being forced turbulent by the cavity geometry.

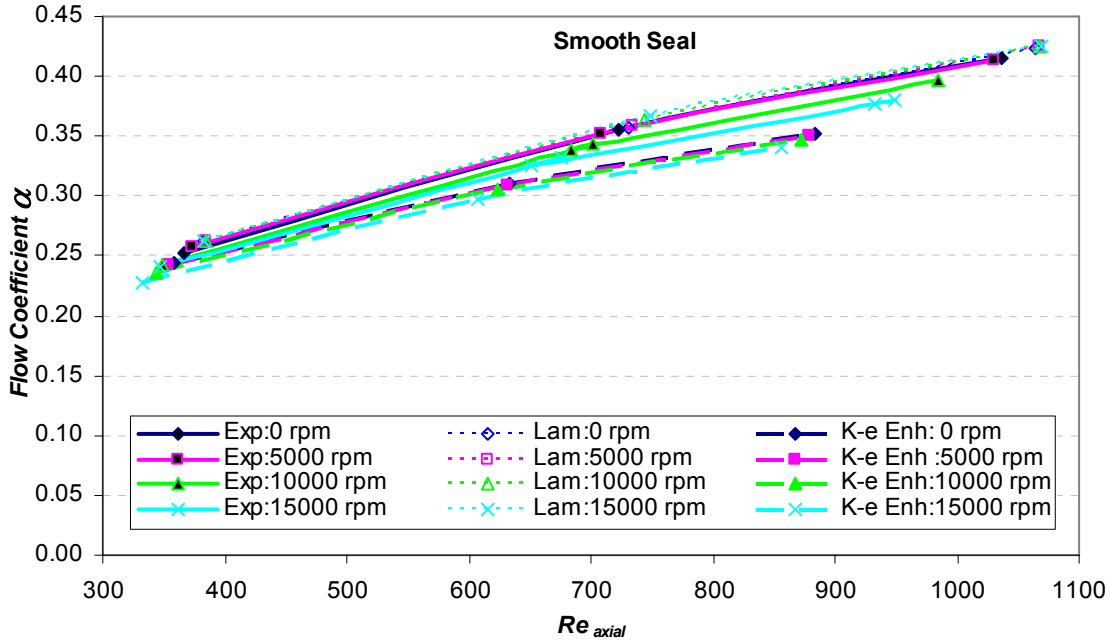

Fig. 64 Smooth seal flow coefficient versus axial Reynolds number for different rotor speeds.

The flow coefficient was calculated in the same way as for the windback seal, except that the carry-over coefficient in Eq. (3) is set to 1. Figs. 63 to 69 represent the same data shown in Figs. 61 and 62 but in a non dimensional form. Fig. 63 shows the flow coefficient versus the pressure ratio. Increasing the pressure ratio reduces the flow coefficient in a linear manner. Both CFD models predict the flow coefficient well, especially at high pressure ratios with a maximum difference of 10% at the lowest pressure ratios. The effect of axial Reynolds number on the flow coefficient is shown in Fig. 64 for different rotor speeds and Fig. 65 for different pressure ratios. Increasing Re_{axial} increases the flow coefficient. On the other hand, increasing the rotor speed

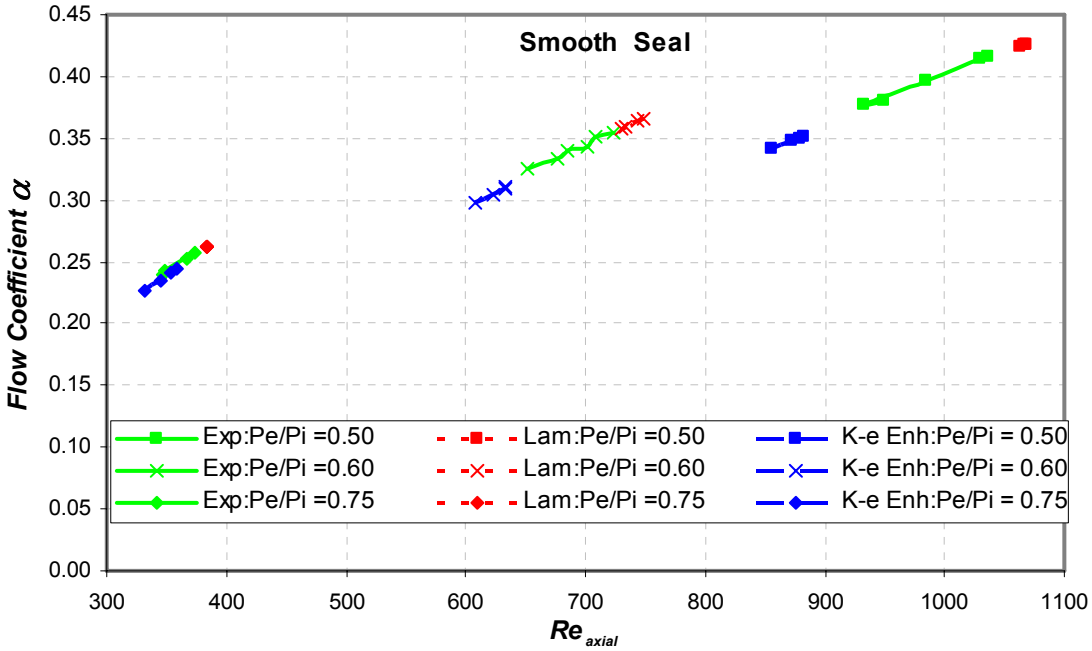

Fig. 65 Smooth seal flow coefficient versus axial Reynolds number for different pressure ratios.

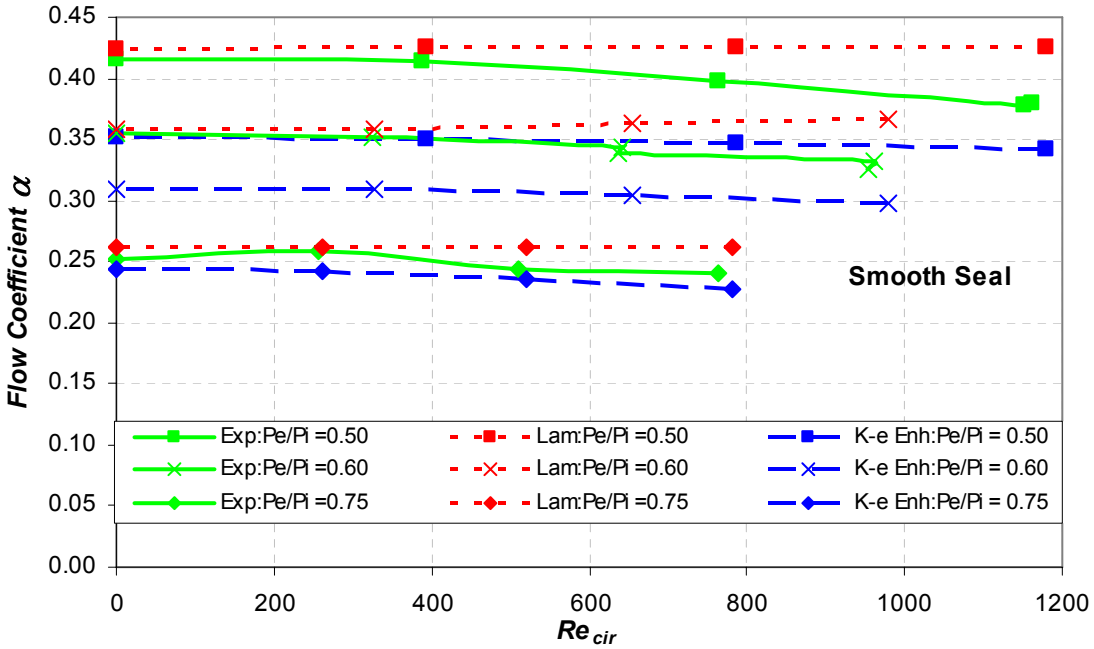

Fig. 66 Smooth seal flow coefficient versus circumferential Reynolds number for different pressure ratios.

will decrease the flow coefficient. Fig. 65 shows that for constant pressure ratio, the experimental and both CFD models flow coefficient follow the same line, which can be characterized by a linear relationship between the flow coefficient and the Re_{axial} with γ=1 in Eq.(22) as,

$$\frac{\alpha}{\mathrm{Re}_{axial}} = \frac{\mu}{c} f(T_i, P_i, P_e) \tag{24}$$

Similar to the windback seal, for constant *DP* the right hand side of Eq. (24) is constant and therefore the theory predictions and experimental results are lined up as seen in Fig. 65.

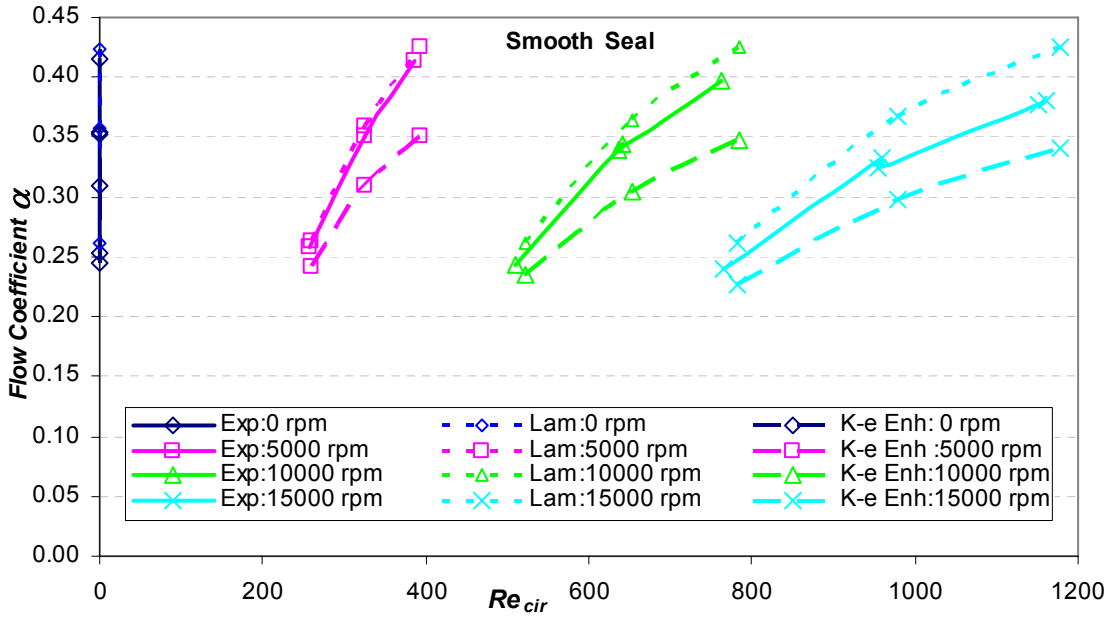

Fig. 67 Smooth seal flow coefficient versus circumferential Reynolds number for different rotor speeds.

Figs. 66 and 67 show the effect of circumferential Reynolds number Re_{cir} on the flow coefficient for different pressure ratios and rotor speeds, respectively. The excellent agreement between the experimental and laminar flow models flow coefficients is seen clearly in Fig. 66 at low rotor speeds. At high rotor speed, both CFD models predict the flow coefficients with the same percent difference from the measurement. Figs. 68 and 69 show the Taylor number effects on the flow coefficient, which have the same effect of Re_{cir} on the flow coefficient.

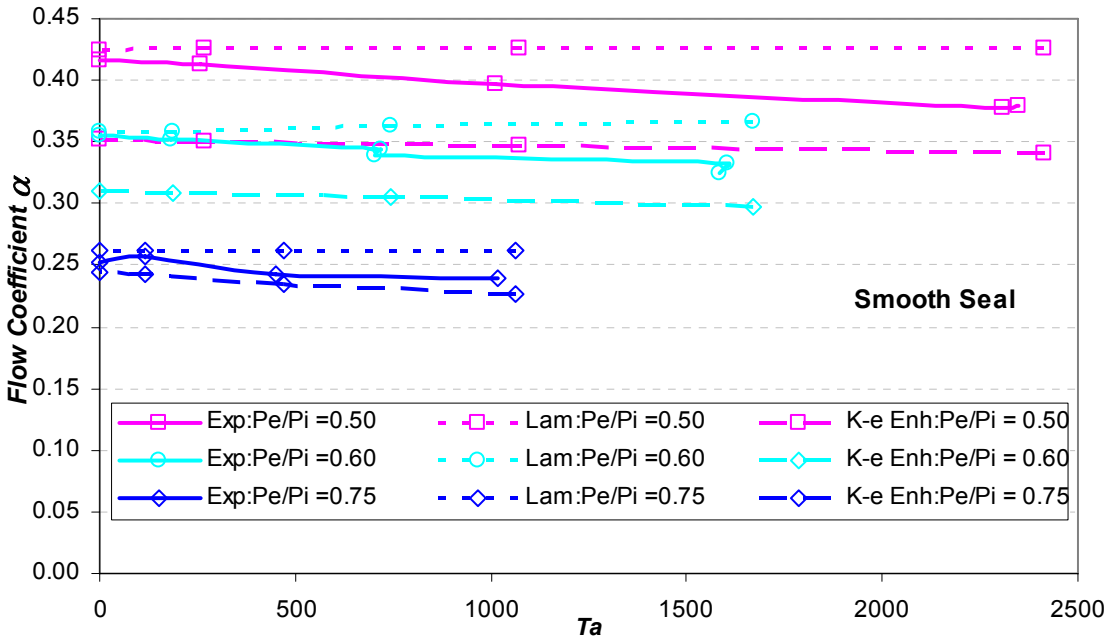

Fig. 68 Smooth seal flow coefficient versus Taylor number for different pressure ratios.

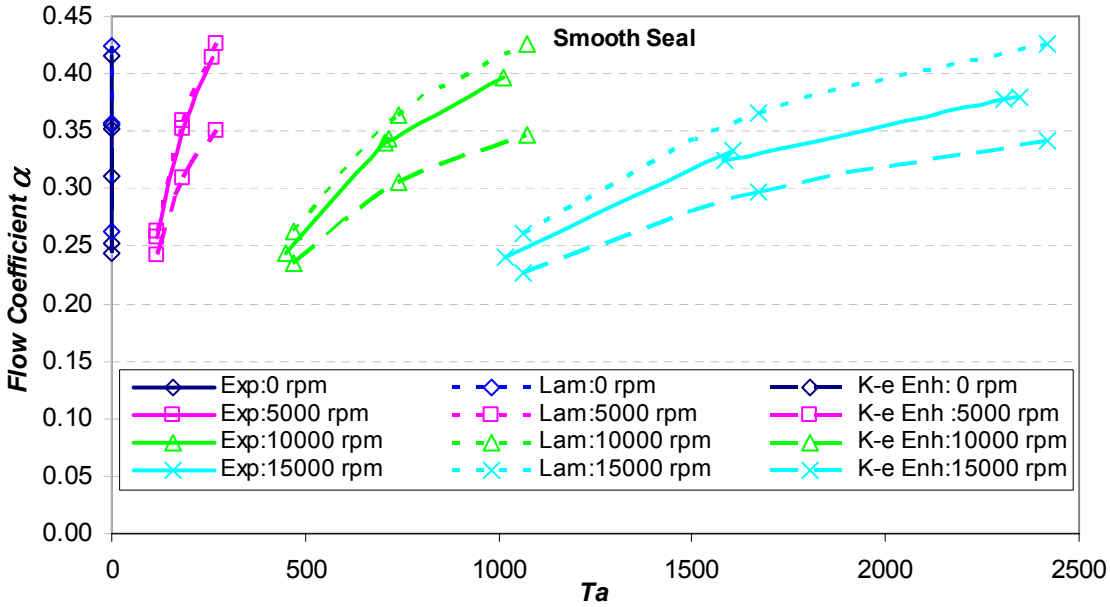

Fig. 69 Smooth seal flow coefficient versus Taylor number for different rotor speeds.

Static Pressure Distribution

The pressures along the smooth seal axial wall were measured using seven wall pressure taps eight degrees apart in the circumferential direction. Fig. 70 compares the measured and predicted values for different rotor speeds up to 15000 rpm. The exit pressure of the seal was atmospheric pressure (0 *kPag*). The pressure measurements and the turbulent flow model predictions compare well at the inlet, indicating that the inlet pressure losses are well predicted

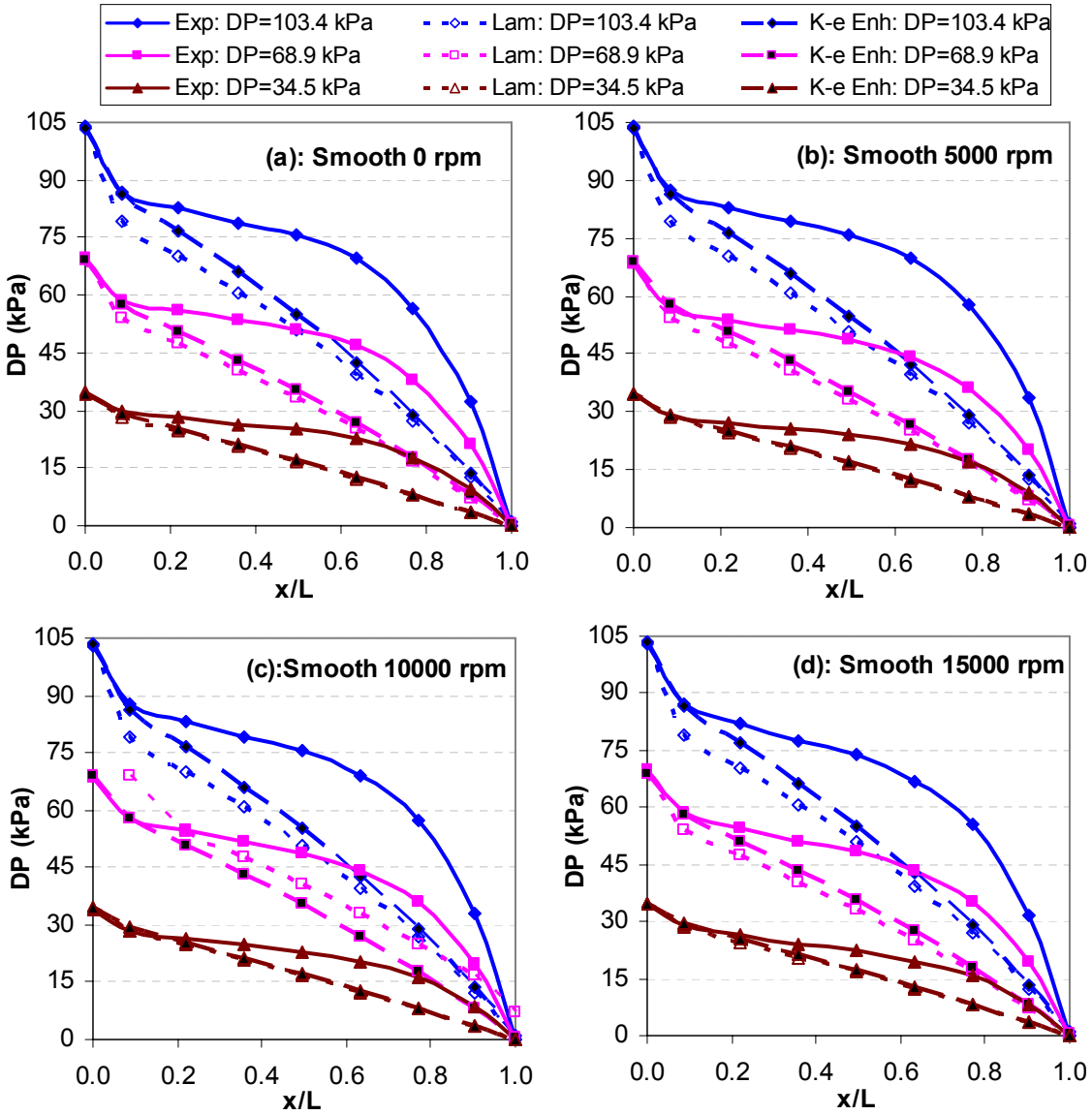

Fig. 70 Smooth seal measured and predicted axial pressure distributions for different shaft speeds.

by the turbulent model. On the other hand, both laminar and turbulent flow models under-predicts the pressure measurements toward the exit of the seal. The pressure measurements show a linear pressure drop up to the middle of the seal length, and then an increase in the negative slope toward the exit of the seal, while both simulation predictions show a nearly uniform pressure drop. The pressure measurement behaves as if the flow becomes compressible near the exit, while the pressure ratio of 0.751 at the exit indicates that the flow is not choked and that the Mach number is 0.65. That agrees with the predictions of the maximum Mach number of 0.51 taking into account the effect of air compressibility and including the energy equation in the CFD simulation solution. The local measurements in some cases were double in value compared to the predictions.

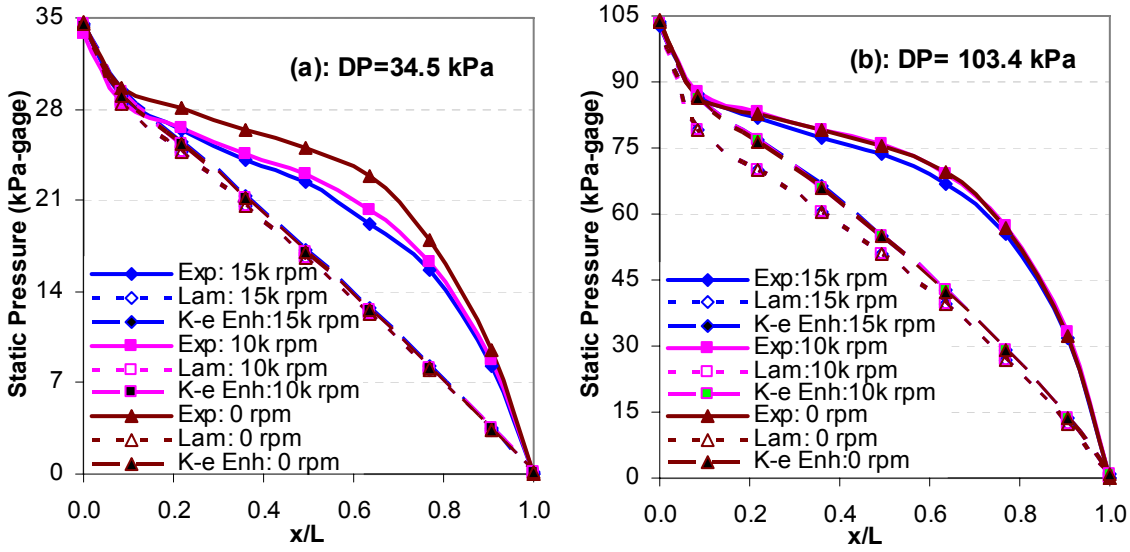

Fig. 71 Smooth seal measured and predicted axial pressure distributions for different rotor speeds at DP=34.5 kPa and DP=103.4 kPa.

Fig. 71 demonstrates that increasing the rotor speed from 0 to 15000 rpm decreases the static pressure measurements, especially at low *DP* by a maximum of 3.7 *kPa*, while both CFD models predicts a small decrease in static pressure, less than 0.5 *kPa*. This explains some of the differences between the measured and predicted values of the static pressure. In addition to the fact that the flow is most likely to be a transitional flow operating in a narrow gap of 0.1 mm (clearance). Fig. 69a shows that at low *DP* both CFD models predict well the pressure at the

inlet. While Fig. 71b shows that at high *DP* the turbulent model performs much better than the laminar model, especially the inlet pressure losses.

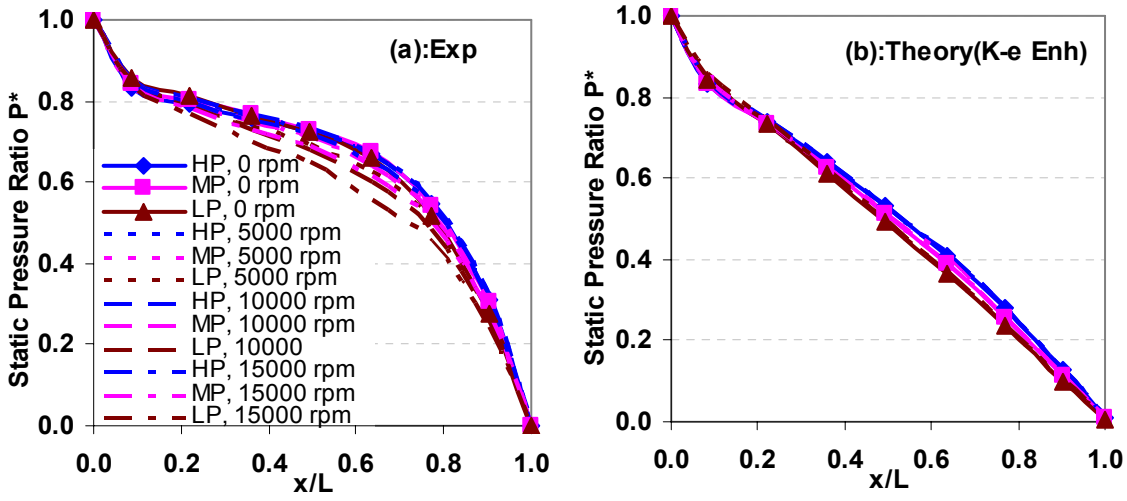

Fig. 72 Smooth seal axial pressure ratio distributions for different rotor speeds and DP; (a) Experimental measurements and (b) Theoretical predictions.

Fig. 72 represents a non dimensional axial pressure distribution. Where, the pressure ratio *P** is plotted against the non dimensional seal length *x/L*. It contains the same data information shown in Figs. 70 and 71. It can be used as a reference for axial pressure distribution for similar smooth seals. The experimental measurements in Fig. 72a show that the pressure ratios dependency on rotor speeds increases with decreasing DP. While the CFD predictions in Fig.72b show no or very small rpm effects for all *DP*s. In addition, Fig. 72a and b show that increasing *DP* increases the axial static pressure ratio distribution. Higher *DP* means higher compressibility effect (higher average air density) and that explains the highest bump at the highest *DP* compared to the lowest *DP*. Darcy's friction factor is defined as $f = -(\partial P/\partial x)D_h/(\frac{1}{2}\rho V_x^2)$, where D_h is the hydraulic diameter and equal to twice the seal radial clearance. A simplified calculation of the average friction factor across the seal using Eq. (23) is shown in Fig. 73. The high friction factor at low *DP* explains the faster drop of the axial pressure at low *DP* in Fig. 72.

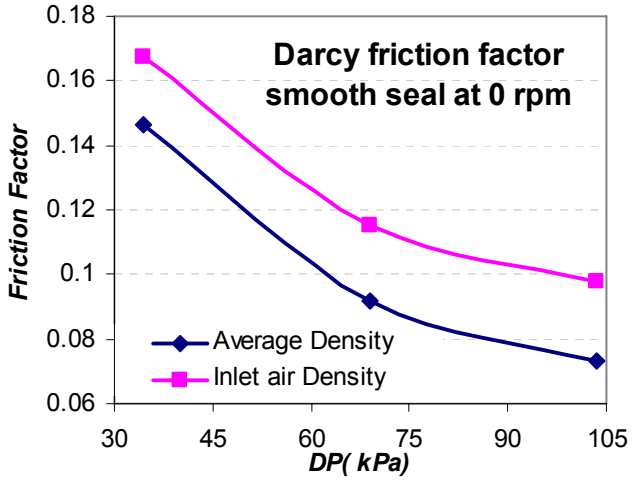

Fig. 73 Average Darcy friction factor at 0 rpm.

Effect of Eccentricity

The effect of eccentricity on leakage flowrates, and pressure distributions was studied experimentally for a 0.1 mm clearance smooth seal. The assembly of the smooth seals stator was similar to the windback stator, with the same shaker system described in Fig. 6. Positive eccentricity refers to reducing the seal clearance near the pressure measurement installation, while negative eccentricity increases the clearance near the pressure instrumentation.

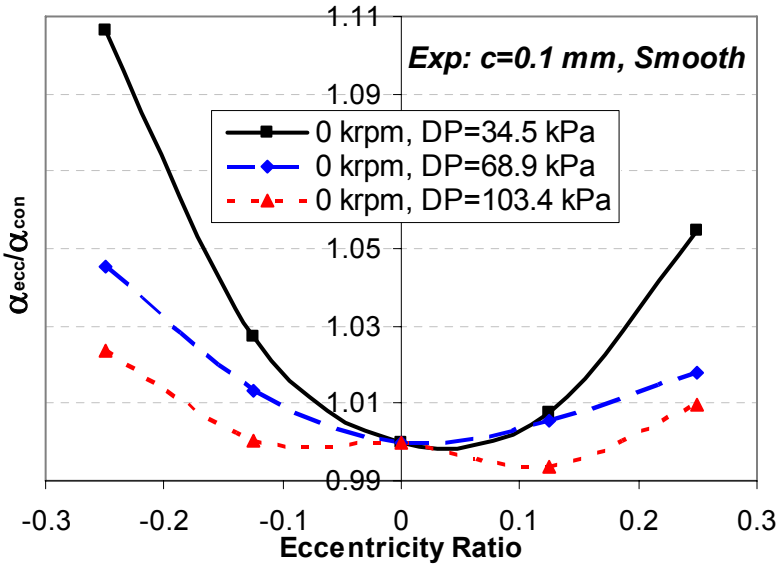

Fig. 74 Flow coefficient ratio versus eccentricity for different shaft speeds and DP's.

The ratio between eccentric and concentric flow coefficients $\alpha_{ecc}/\alpha_{con}$ is shown in Fig. 74 for different *DP*'s at 0 rpm. The experimental data shows that eccentric smooth seals leak more than concentric ones, specifically at low *DP* with a maximum increase of 11% at *e*=-0.25. The minimum increase was about 1% at *e*=0.25 and the highest *DP*. Therefore, the effect of eccentricity has a major influence on leakage flowrates for annular seals, especially at low *DP*.

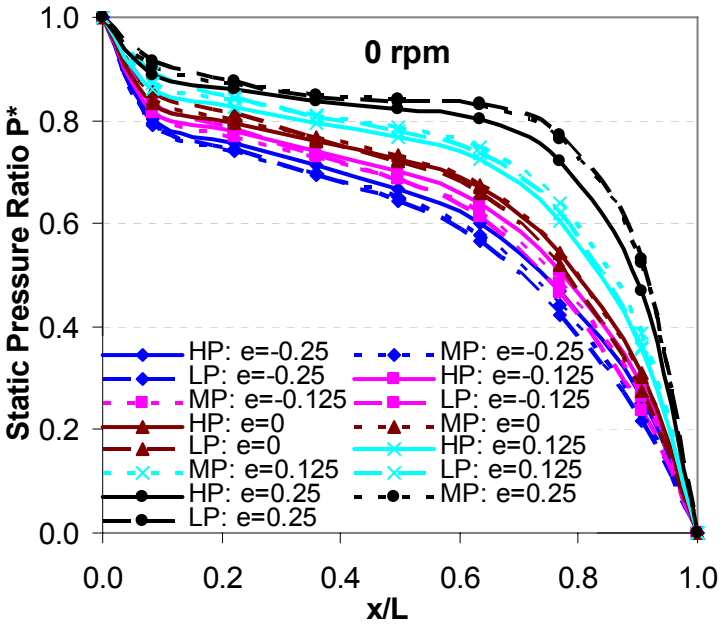

Fig. 75 Smooth seal axial pressure ratio distributions for different seal eccentricity at 0 rpm.

Figs. 75 and 76 show the axial pressure ratio distribution *P** for different *DP*'s and eccentricity ratios at 0 rpm. The effect of eccentricity on axial pressure ratio distribution is very obvious. Such that moving the seal in either direction from the concentric position result in a significant increase or decrease in the pressure ratio. Negative eccentricities will increase the clearance in the side of the pressure instrumentation and result in higher friction factor and hence higher inlet pressure losses. Positive eccentricities have an opposite effect and seen clearly in Figs. 75 and 76. This may explain the differences between the pressure measurement and predictions. Fig. 76 also shows that negative eccentricities reduce the differences between the measurements and predictions, while positive eccentricities make it worse.

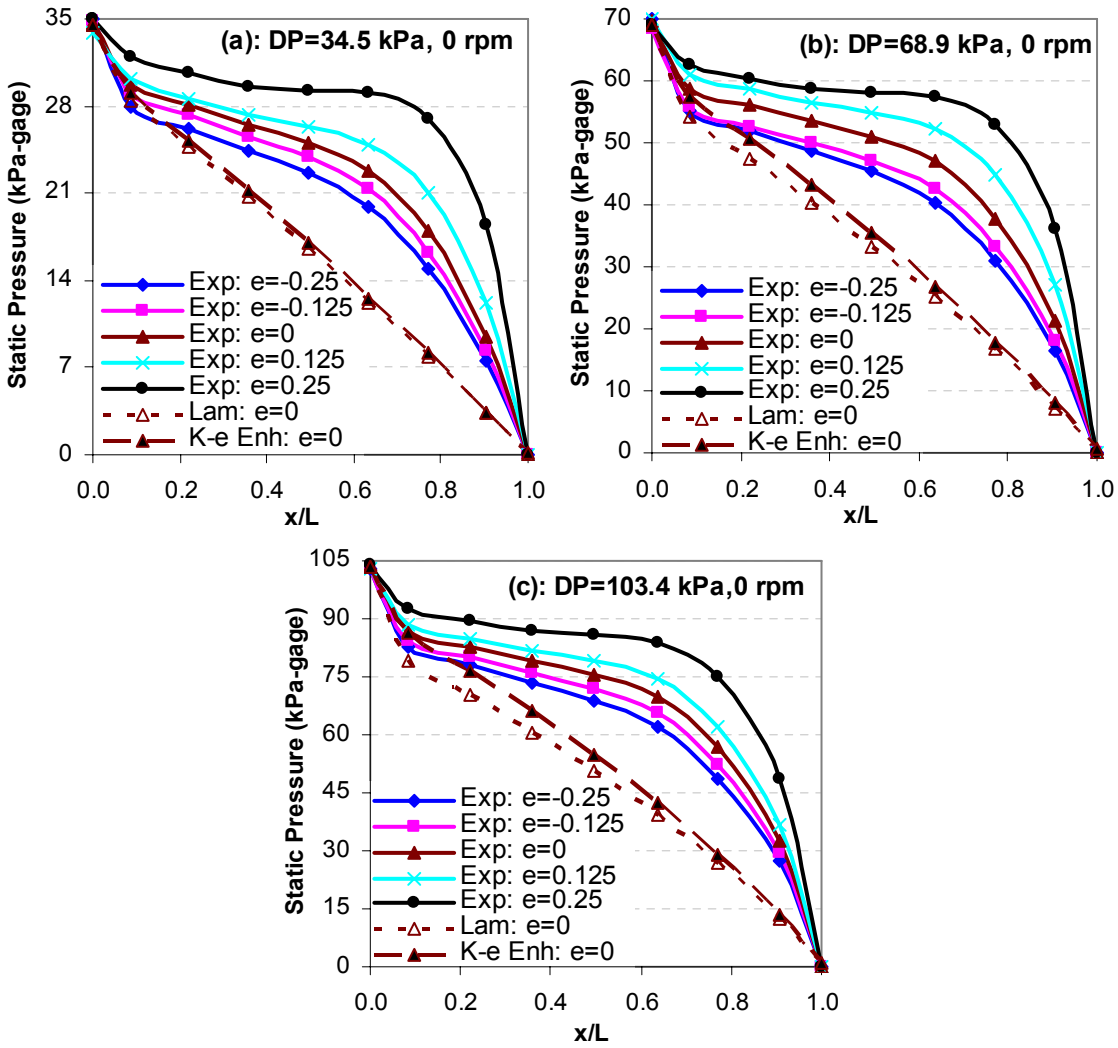

Fig. 76 Smooth seal axial pressure ratio distributions for different seal eccentricity at 0 rpm and different DP; theory versus experiment.

Summary

The windback measurement and prediction comparison shows an excellent agreement. The leakages were predicted within 5%, absolute and local static pressure distribution within 10% and 25%, respectively. The circumferential velocity shows higher maximum difference of about 45%. On the other hand, the smooth seal measurement versus prediction shows that the laminar flow model predicts leakage flowrate to within 2.5% at 0 rpm, while the turbulent flow model predicts the leakage flowrate with a maximum difference of 8% at *HP* and 15000 rpm. This is also considered an excellent agreement between measurement and predictions. However,

the measured and predicted local pressure distributions show a 50% difference. For the smooth seal, the turbulent flow model with enhanced wall treatment capture the decrease in leakage flowrate with increasing the shaft speed and predicts well the leakage flowrate especially at high *DP* and rotor speeds. Hence, the turbulent flow model is recommended for numerical simulations where shaft rotations are present, while the laminar flow model is recommended for numerical simulations involving low shaft speeds.

The effect of eccentricity can explain some of the differences between measurement and prediction. The leakage rate and the pressure distribution for the windback seal show a very small change with eccentricity. As a result, there was excellent agreement with predictions. On the other hand, V_θ changes considerably with eccentricity and since the two seals were assembled together around the shaft using a 0.0762 mm shim, there is a possibility that the stator was eccentric and this explains some of the differences. The same applies for the smooth seal, except that both leakage flowrates and static pressure distributions are sensitive to eccentricities as previously seen.

NUMERICAL SIMULATION

The Fluent CFD numerical simulation program is used to study the effects of varying the design geometry of a windback seal on its performance. The effects of clearance, tooth height, tooth pitch and the number of tooth starts upon the leakage flowrate and the flow field are studied in this chapter. The maximum difference between measurements and predictions occur at low *DP*. In addition, the maximum effect of shaft speed on leakage flowrate occurs also at low *DP*. Therefore, among the three *DP* cases, the *LP* cases were selected in this chapter to demonstrate the effects of pressure and velocities on leakage flowrate. All cases are shown in the Appendices.

CFD Solver

Fluent CFD numerical simulation program version 6.1.22 was used in all simulations. 3-D model solutions were obtained for all cases under study except for the smooth seal where a 2-D model was used. A segregated solver with implicit formulation was used to solve the mass, momentum, energy, and turbulence equations. The standard κ-ε turbulent model with enhanced wall treatment was selected for modeling the flow turbulence.

Clearance Effect

Three windback seals with radial clearances of 0.05, 0.10 and 0.15 mm were compared for different rotor speeds and *DP*'s. Fig. 77 compares the leakage mass flowrates for different rotor speeds at constant *DP*'s. The leakage flowrates increase with increasing rotor speed, with a maximum of 12.4% at the lowest *DP* and radial clearance. Increasing the radial clearance from 0.05 to 0.15 mm will minimize the effect of rotor speed on leakage rates, with a maximum increase of 2.7% at DP=34.5 kPa. Fig. 78 shows that increasing the clearance will increase the leakage flowrate in a linear but not in a proportional way to the increase in the cross sectional area under the teeth, πDc. The clearance increases by 200% while the leakage flowrate increases by a maximum of 300% at the lowest *DP* with no rotation and by a minimum increase of 244% at the highest *DP* and 15000 rpm. Therefore, the rate of increase in leakage flowrate due to the increase in radial clearance decreases with increasing rotor speed and *DP*.

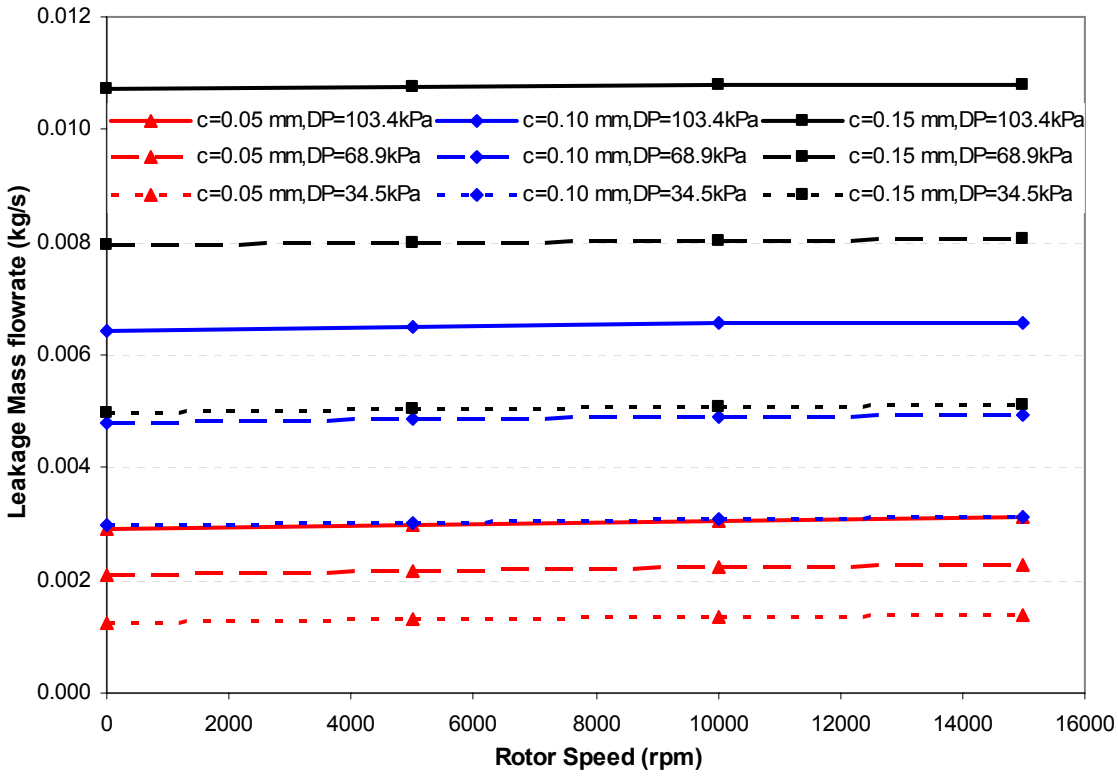

Fig. 77 Leakage mass flowrate versus rotor speed for different Windback seal clearances.

To explain the effects of changing the seal clearance and rotor speed on leakage flowrates, the flow velocity components and pressure field contour plots were plotted at the 270° plane sectional view for different seal clearances, with the same number of color levels and scale. In addition, the whole clearance region was expanded in the radial direction and plotted below the sectional view for the three different windback seal clearances at 0 and 15000 rpm, and 34.5 *kPa*. All other pressure cases are shown in the Appendices. Due to the limited number of contour levels that can be shown in a given contour plot without degrading its quality and clearness, the velocity components and pressure field variables were plotted along two axial lines, one passing through the center of the seal clearance and the other passing through the center of the seal cavity. A cross sectional view of the seal geometry was plotted at the top of Fig. 79 for clarification of the tooth and cavity location with the true axial seal scale.

Figs. 79, 80 and 81 show the axial velocity components contours for the three different seal clearances, the following were observed:

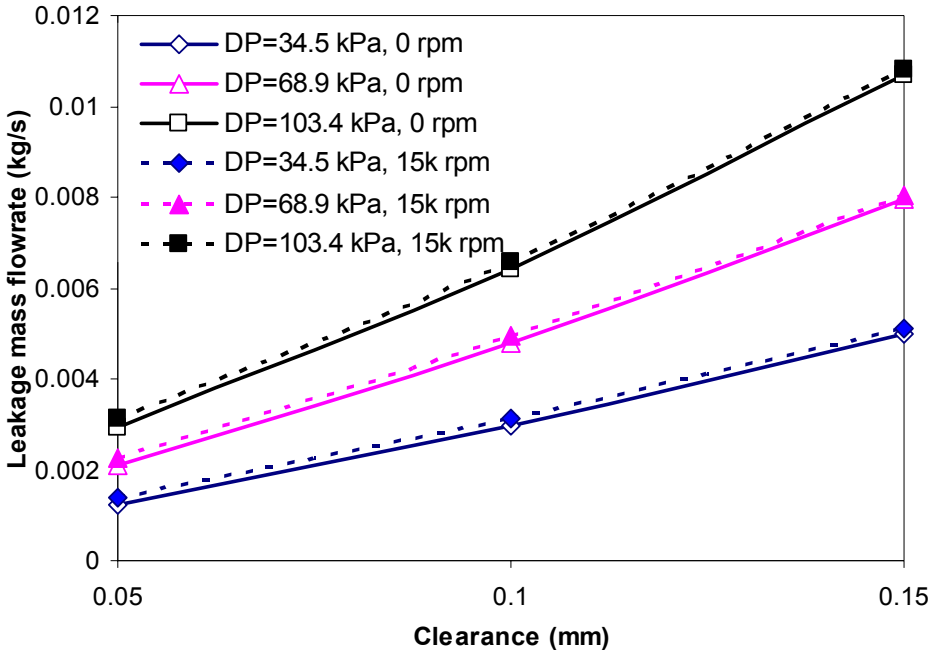

Fig. 78 Leakage mass flowrate versus clearance for different DP's and rotor speeds.

- The rotor speed has a negligible effect on the axial velocity distribution within the contour plots increments for all clearances. Fig. 79 shows that increasing the rotor speed from 0 to 15000 rpm decreases V_x along the seal axis at the middle of the clearance by a maximum of 3% at c=0.05 mm, which decreases to 0.8% at c=0.15 mm, where V_x at 0 rpm was 51.7 *m/s* and 75.1 *m/s* for c=0.05, and 0.15 mm, respectively.
- At the middle of the cavity, the maximum V_x is about -1.5 *m/s* which can be considered small since the main flow is in the circumferential direction. In addition, Figs. 80 and 81 show a negative axial velocity at the upper half of the cavity and a positive axial velocity in the lower half, suggestion that the flow is rotating in the counter clock-wise direction around the cavity center.
- Looking at both radial and axial velocity components at the same time, it is clearly seen that, there is a vortex generated in the seal cavity in the counter clock-wise direction. For a seal clearance of c=0.05 mm, the vortex generated is very small compared to the other two clearances. This can be explained by the wall effect, such that the low flow axial jet going through under the tooth and expanding through the seal cavity in which, the maximum axial velocity that produces these vortices is about 20-30 *m/s* and does not cover the whole cavity

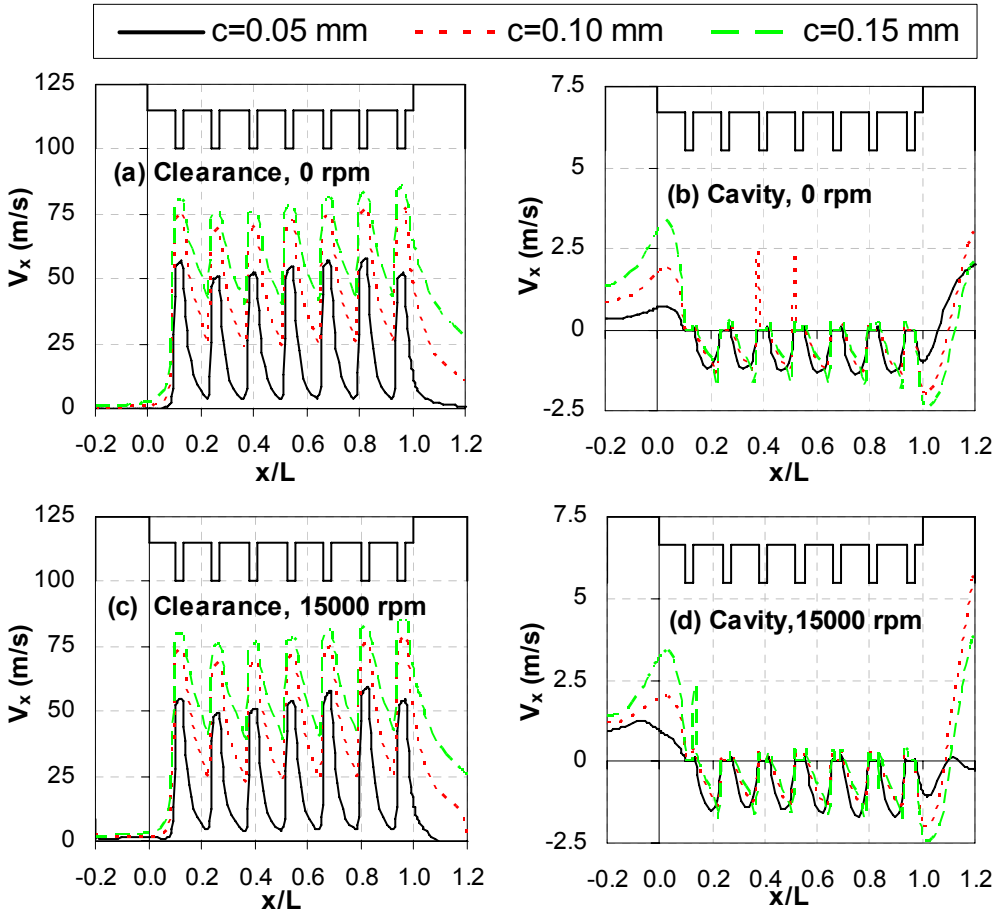

Fig. 79 Axial velocity distribution along a line passing through the middle of the clearance and cavity at DP=34.5 kPa.

length in the axial direction for c=0.05 mm, compared to 30-40 *m/s* and 40-50 *m/s* for c=0.1 mm and c=0.15 mm, respectively, which cover mostly all the cavity length in the x-direction, and can be clearly seen in Fig. 79c.

- The maximum axial velocity under the seal teeth was 50-60 *m/s*, 70-80 *m/s*, and 80-90 *m/s* for seal clearances 0.05 mm, 0.1 mm, and 0.15 mm, respectively. Increasing the seal clearance reduces the effects of seal walls (boundary layer) on the main axial flow stream at the center of the clearance. Increasing the seal clearance from 0.05 to 0.1 mm increases the maximum V_x by 46%, while increasing the seal clearance from 0.1 to 0.15 increases the maximum V_x by 7%. Therefore, a windback seal with a clearance of 0.05 mm will be influenced the most by the boundary layer and hence a reduction in the axial velocity distribution. V_x

increases in the axial direction under the tooth due to kinetic energy carry over, and to the compressibility effect (decrease in air density as a result of pressure drop across the seal tooth).

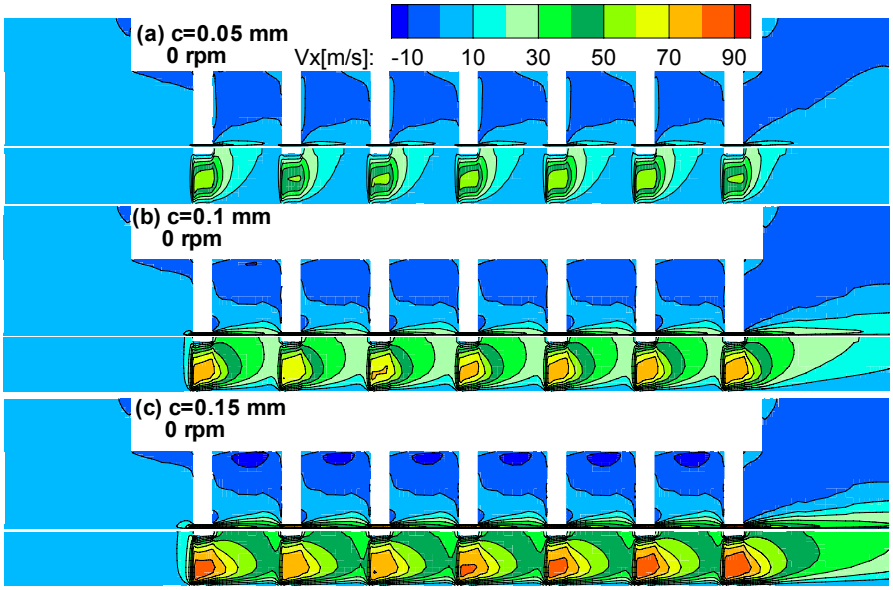

Fig. 80 Axial velocity contours for different seal clearances at Ω= 0 rpm and DP=34.5 kPa.

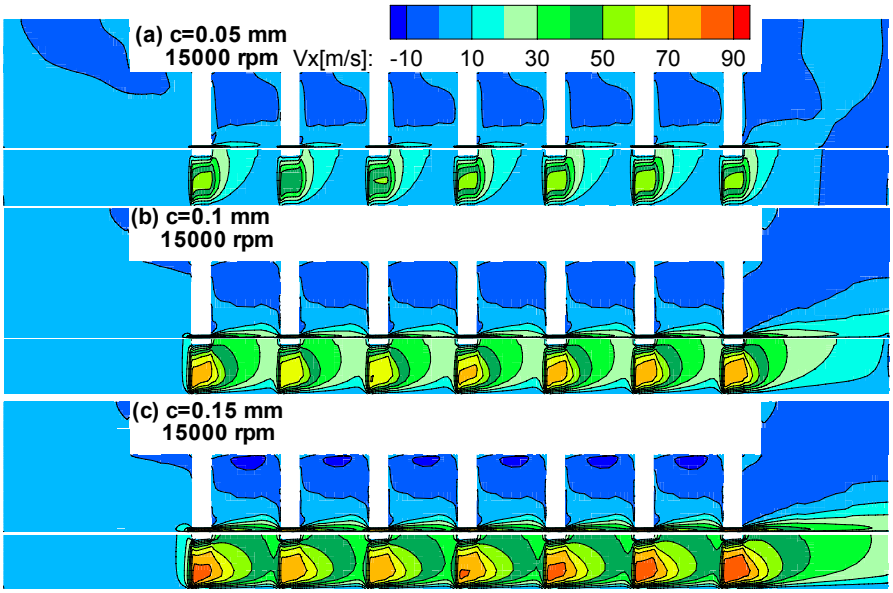

Fig. 81 Axial velocity contours for different seal clearances at Ω=15000 rpm and DP=34.5 kPa.

Table 9 Carry over coefficient for different c, Ω, P.

c (mm)	Ω (rpm)	P	V_{min}^2/V_{max}^2	β	γ	$\gamma_{Hodkinson}$
0.05	0	LP	0.0055	68.57	1.003	1.25
	15000	LP	0.0063	65.95	1.003	1.25
	0	MP	0.0156	41.71	1.008	1.25
	15000	MP	0.0168	39.46	1.009	1.25
	0	HP	0.0204	34.11	1.010	1.25
	15000	HP	0.022	32.20	1.011	1.25
0.10	0	LP	0.12	11.81	1.07	1.42
	15000	LP	0.11	12.81	1.06	1.42
	0	MP	0.17	7.94	1.10	1.42
	15000	MP	0.17	7.85	1.10	1.42
	0	HP	0.20	6.30	1.12	1.42
	15000	HP	0.20	6.46	1.12	1.42
0.15	0	LP	0.29	6.02	1.18	1.55
	15000	LP	0.27	6.41	1.17	1.55
	0	MP	0.34	4.67	1.23	1.55
	15000	MP	0.33	4.85	1.22	1.55
	0	HP	0.40	3.61	1.29	1.55
	15000	HP	0.39	3.71	1.29	1.55

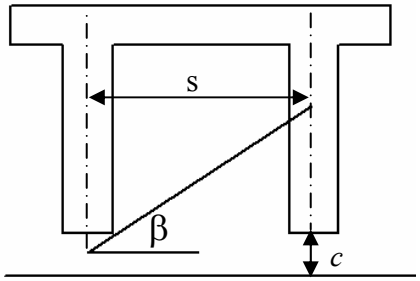

Fig. 82 Stream flow angle.

Hodkinson [12] defines the carry over coefficient, γ, and the stream spread angle, β (see Fig. 82), using the kinetic energy ratio as

$$\gamma^2 = 1/(1-\chi) \tag{25}$$

$$\tan\beta = c\,(1-\chi)/(\chi s) \tag{26}$$

$$\chi = V_{\min}^2 / V_{\max}^2 \tag{27}$$

where, χ is the kinetic energy ratio between the inlet of the second tooth and the exit of the first tooth or the ratio between the minimum and maximum kinetic energy in the seal cavity.

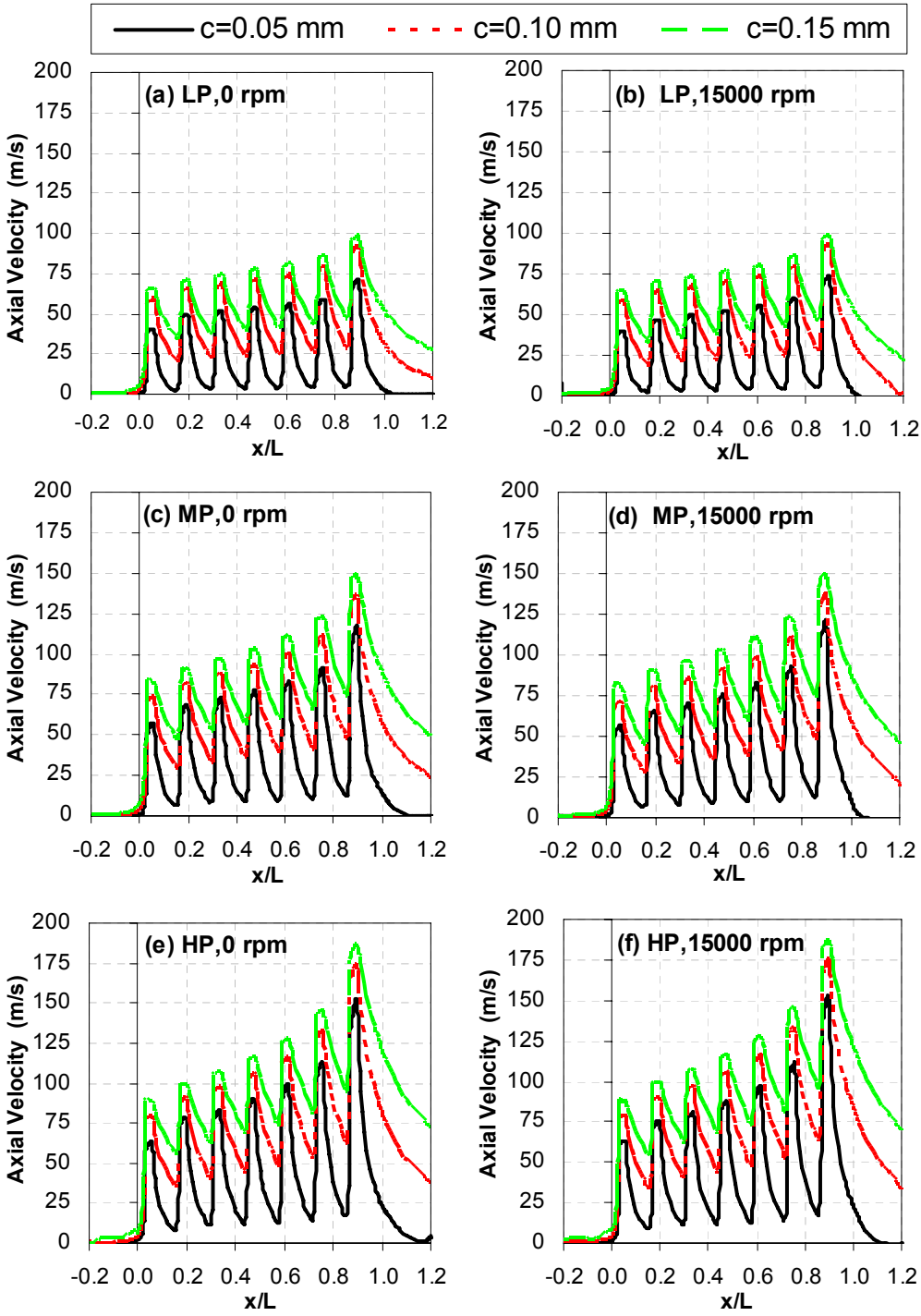

Fig. 83 Axial velocity distribution along a line passing through the middle of the clearance for different DP, rotor speed at 90° sectional view.

Increasing the carry over coefficient increases the leakage flowrates by increasing V_x in the axial direction. Therefore, a comparison between the carry over coefficient calculated using Eq.(3), and the calculated γ from the CFD simulation using Eq.(25) based on the values of V_x in Fig. 83, is shown in Table 9 for different seal clearances, rotor speeds and *DP*'s. γ_{CFD} in Table 9 represents the average value of all γ's calculated using Eq.(25) for all seal cavities between the first and last tooth. Hodkinson [12] assumes a constant stream spread angle β of 1.15° ($\cong$0.02 *rad*) with no dependency on *DP* or rotor speed in deriving γ in Eq.(3), based on his test data for different labyrinth seal clearances of 0.1, 0.23, 0.48 mm and *DP*'s from 2 to 6 *atm*. The *DP* for this study ranges from 0.34 to 1.02 *atm* with a maximum seal clearance of 0.15 mm. β equal to 90° (γ=1) represents an ideal seal with no kinetic energy carry over, and β=0° represents theoretically infinite carry over coefficient, in this case it losses its significance because γ is limited to approximately $\sqrt{n}$ using Eq.(3). Table 9 shows that β decreases with increasing *DP* from 34.5 kPa to 103.4 kPa by almost 50%. Increasing c from 0.05 to 0.1 mm and from 0.1 to 0.15 mm decreases β by 80%, and 50%, respectively. This explains the difference between Hodkinson carry over and the calculated γ based on the CFD simulations for this study. Increasing the rotor speed from 0 to 15000 rpm decreases β by a maximum of 6% for c=0.05 mm, and increases it by a maximum of 6% for *c*=0.1 mm, and 0.15 mm with small *DP* effect. For windback seal with *c*=0.05 mm at low *DP*, and 0 rpm, β has the value of 68.6°.This indicates that most of the kinetic energy is dissipated within the seal cavity and not carried over to the next tooth. On the other hand, for *c*=0.15 mm at low *DP*, and 0 rpm, β has the value of 6°, which shows that about 29% of the kinetic energy is carried over to the next tooth. It is speculated that the significant difference between this study and Hodkinson [12] is the much lower pressure difference, since the values tend to converge for higher *DP*.

Figs. 84, 85, and 86 show the radial velocity component. Increasing the seal clearance from 0.05 to 0.1 mm increases the radial velocity distribution inside the seal cavity significantly, by 260%, from a maximum of 4.9 *m/s* to 16.7 *m/s*, respectively. On the other hand, increasing the clearance from 0.1 mm to 0.15 mm increases V_r by 40% from a maximum of 16.7 *m/s* to 23.5 *m/s*, respectively. Additionally, increasing the clearance increases the leakage flowrate under the tooth; therefore more flow will be directed from the upstream plenum and thus increases the radial velocity upstream of the tooth edge.

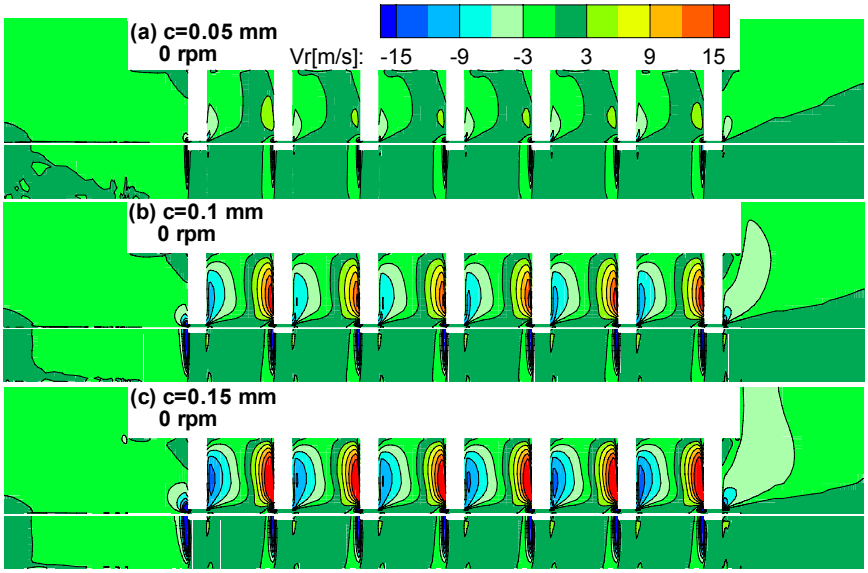

Fig. 84 Radial velocity contours for different seal clearances at Ω=0 rpm and DP=34.5 kPa.

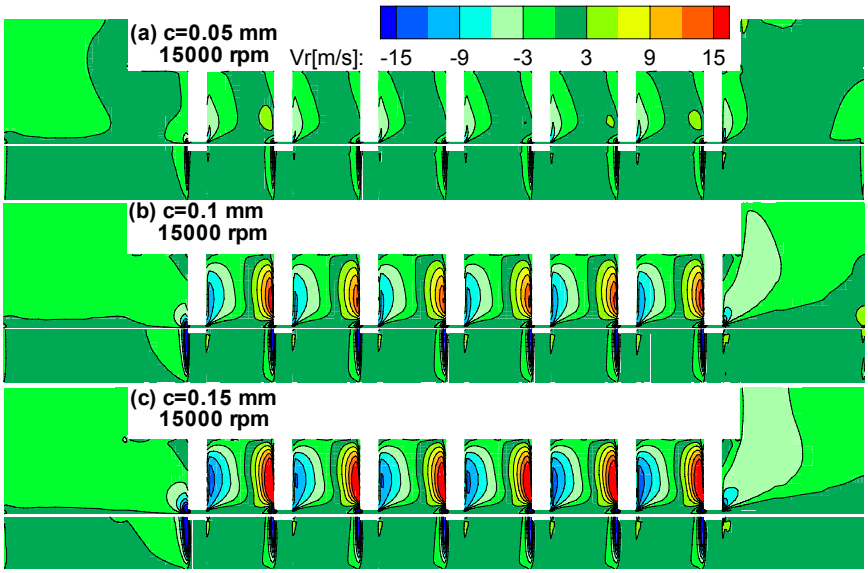

Fig. 85 Radial velocity contours for different seal clearances at Ω=15000 rpm and DP=34.5 kPa.

Figs. 86b and 86d show the effect of the jet flow under the tooth, such that the up-flow radial velocity downstream a line along the middle of the cavity is almost twice as large as down flow radial velocity upstream in the cavity. The non symmetrical nature of V_r distribution within the seal cavity is due to a nearly constant mass flux in the tangential direction of the cavity.

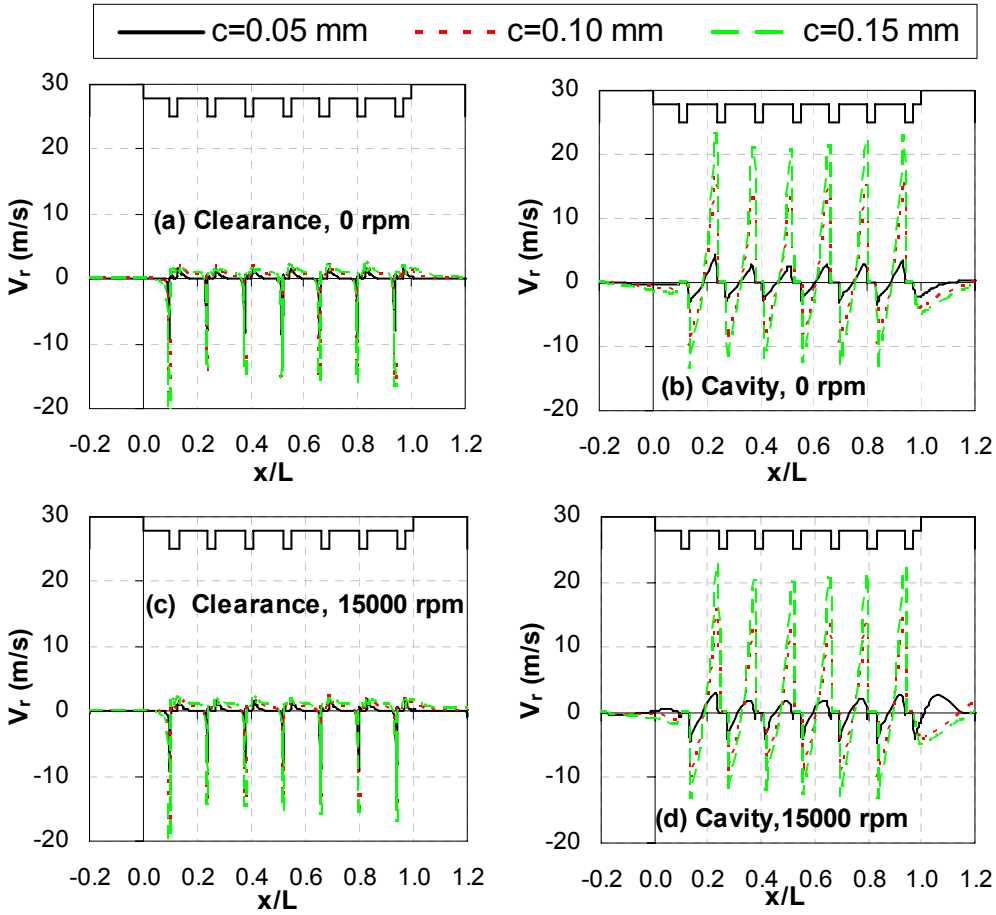

Fig. 86 Radial velocity distribution along a line passing through the middle of the clearance and cavity at DP=34.5 kPa.

Integrating V_r along a line passing through the center of cavity, is equal to zero within 5% of the absolute sum of the positive and negative areas under V_r lines in Figs. 86b and 86d. Therefore, the up-flow radial velocity covers less area of the seal cavity than the down-flow radial velocity.

Figs. 87, 88, and 89 show the circumferential velocity component. Decreasing the seal clearance increases V_θ within the seal cavity and upstream of the tooth along a line passing through the middle of the clearance. The maximum V_θ in the cavity at 0 rpm and for c=0.05, 0.1, and 0.15 mm was 35.1, 25.9, and 21.6 *m/s*, respectively. Increasing the rotor speed to 15000 rpm increases V_θ to 51.2, 46.6, and 43.1 *m/s*, respectively. Smaller clearances result in higher skin friction and more resistance to flow under the seal tooth. Therefore, more flow will be directed

through the seal cavity and higher V_θ results. On the other hand, at 0 rpm the circumferential velocity within the seal clearance and between two consequent teeth is higher for the *c*=0.1, 0.15 mm compared to *c*=0.05 mm, therefore more depth influence within the seal clearance. But the opposite is observed directly at the inlet of each tooth, where the V_θ is higher for smaller clearances. Smaller clearances result in higher V_θ in the seal cavity. Increasing the rotor speed from 0 to 15000 rpm is accompanied by a substantial increase in V_θ. Fig. 88a demonstrates that V_θ inside the cavity increases from a maximum of 27-36 *m/s* to 45-54 *m/s* for *c*=0.05 mm. Increasing rotor speed to 15000 rpm increases V_θ throughout the whole seal clearance height with a minimum V_θ in the range of 45-54 *m/s* except near the tooth wall, where V_θ is nearly zero. Increasing the clearance decreases the effect of rotor speed on the circumferential velocity in the seal radial direction. The viscosity effect and hence the rate of shear stresses have a limited depth influence as seen in both Figs. 88b and 88c. The enlarged clearance view under Figs. 87 and 88 represents the whole seal clearance height. Fig. 89 shows the limited depth influence of the rotor drag through increasing rotor speed on V_θ within the seal clearance and cavity. Increasing the rotor speed from 0 to 15000 rpm for c=0.05, 0.1, and 0.15 mm increases V_θ along the middle of the clearance from a maximum of 16.4, 14.7, and 12.5 to 77.7, 58.2, and 50.2, respectively.

Seal clearance is one of the most important geometrical design parameter in a seal. Not only influencing the leakage flowrate but also the flow patterns within the seal. Flow vortices are a measure of the fluid element rotation, as it moves in the flow field and is defined as the curl of the velocity vector. Flow vortices are generated in the seal cavity as a result of both axial and circumferential velocities due to pressure drop in both axial and circumferential directions. The axial velocity under the tooth and V_θ in the seal cavity affect greatly the generation of such a vortex. Fig. 90 shows the vorticity magnitude versus axial location within the seal cavity. The vorticity magnitude was integrated over the seal cavity area at the 180° seal sectional view. Fig. 90 shows that the vorticity in the seal cavity increases in a linear relationship along the *x*-axis, due to the accompanied increase in both V_x and V_θ along the *x*-direction, except for the first and the last cavities, where the cavities are opened to the inlet and exit plenums, respectively. Increasing seal clearance, *DP*, and rotor speeds increase vorticity magnitude. Fig. 91 shows the percent increase in vorticity with increasing rotor speed and *DP*. Fig. 91a shows that increasing the rotor speed from 0 to 15000 rpm increases the vorticity magnitude by 30-40% and 10-20% for *LP* and *HP*, respectively, with small variation along the *x*-direction. The 0.1 mm seal

clearance has the highest percent increase with increasing the rotor speed at both low and high *DP*. Increasing rotor speed will increase V_θ in the seal cavity greatly specially with decreasing

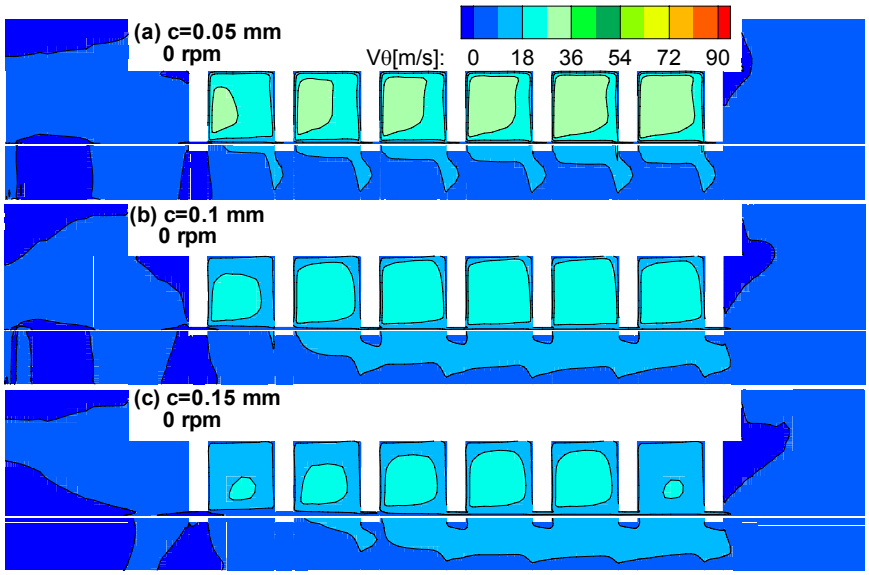

Fig. 87 Circumferential velocity contours for different seal clearances at Ω=0 rpm and DP=34.5 kPa.

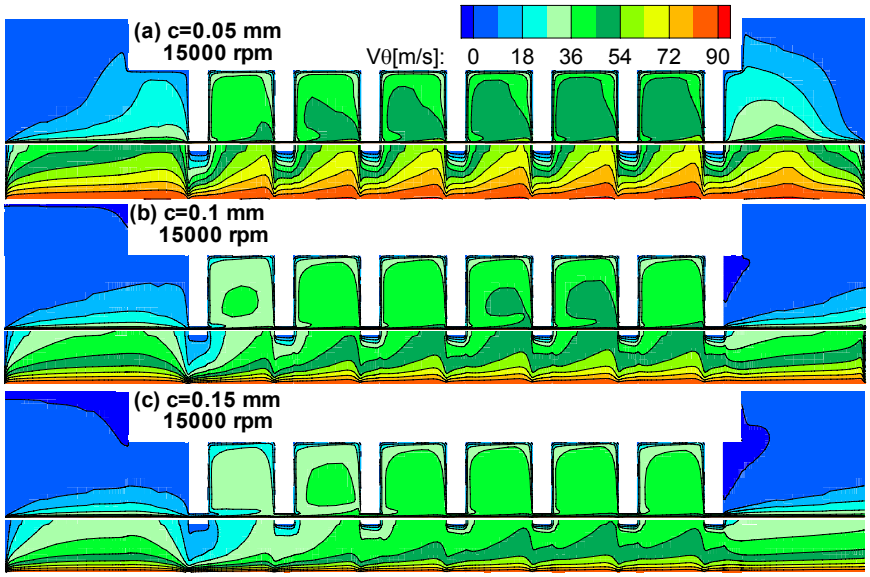

Fig. 88 Circumferential velocity contours for different seal clearances at Ω=15000 rpm and DP=34.5 kPa.

the seal clearance. But the axial jet velocity plays here a major role in increasing V_r. Since V_r is comparable for both 0.1 and 0.15 mm clearances and is much higher than V_r for the 0.05 mm clearance seal, the 0.1 mm clearance seal has the highest percent increase in vorticity with increasing rotor speed. The other seals perform comparably since for c=0.05 mm V_θ is almost twice as for c=0.15 mm, where for c=0.15 mm V_r is about 5 times higher than for c=0.05 mm. Fig. 91b shows the percentage increase in vorticity with increasing *DP* from *LP* to *HP*. Increasing *DP* increases the percentage increase in vorticity along the x-direction in an exponential way, due to the large increase in both V_x and V_θ with *DP* in the x-direction. For c=0.1 mm and 0.15 mm, both seal clearances have a comparable percent increase in vorticity with increasing *DP*, and much higher than the 0.05 mm clearance seal.

The overall velocity comparison for different seal clearances is shown in Fig. 92, where the velocity magnitude is plotted along the seal axial direction for 0 and 15000 rpm at *DP*=34.5 *kPa*.

Table 10 Clearance effect on velocity magnitude.

c (mm)	V_m(m/s)		% incease	V_m(m/s)		% incease
	0 rpm	15000 rpm		0 rpm	15000 rpm	
	Clearance $_{middle}$			Cavity $_{middle}$		
0.05	58.5	79.5	35.9	35.2	51.3	45.7
0.10	78.0	92.3	18.3	26.1	46.8	79.3
0.15	86.4	97.5	12.8	22.1	44.9	103.2

Table 10 summarizes the effect of clearance on velocity magnitude. Increasing clearance from 0.05 to 0.1 mm increases the velocity magnitude along an axial line passing through the middle of the clearance, throughout increasing the axial velocity by 33.3% and 16.1% at 0 and 15000 rpm, respectively. Additional increase in clearance from 0.1 to 0.15 mm results in smaller percent increase in the velocity magnitude, 10.8% and 5.6% at 0 and 15000 rpm, respectively. On the other hand, increasing clearance from 0.05 to 0.1 mm decreases the velocity magnitude along an axial line passing through the middle of the cavity, throughout decreasing the circumferential velocity component, by 25.9% and 8.8% at 0 and 15000 rpm, respectively.

Additional increase in clearance from 0.1 to 0.15 mm results in a smaller percent decrease in the velocity magnitude, 15.3% and 4.1% at 0 and 15000 rpm, respectively. This shows that the rpm effect reduces the difference in velocity magnitude for different windback seal clearances, since all seals have the same cavity depth and as previously seen that the rpm influences mostly the circumferential velocity component in which it has comparable values at the middle of the cavity with comparable V_x. On the other hand, the difference at the middle of the clearance comes mainly from the axial velocity component.

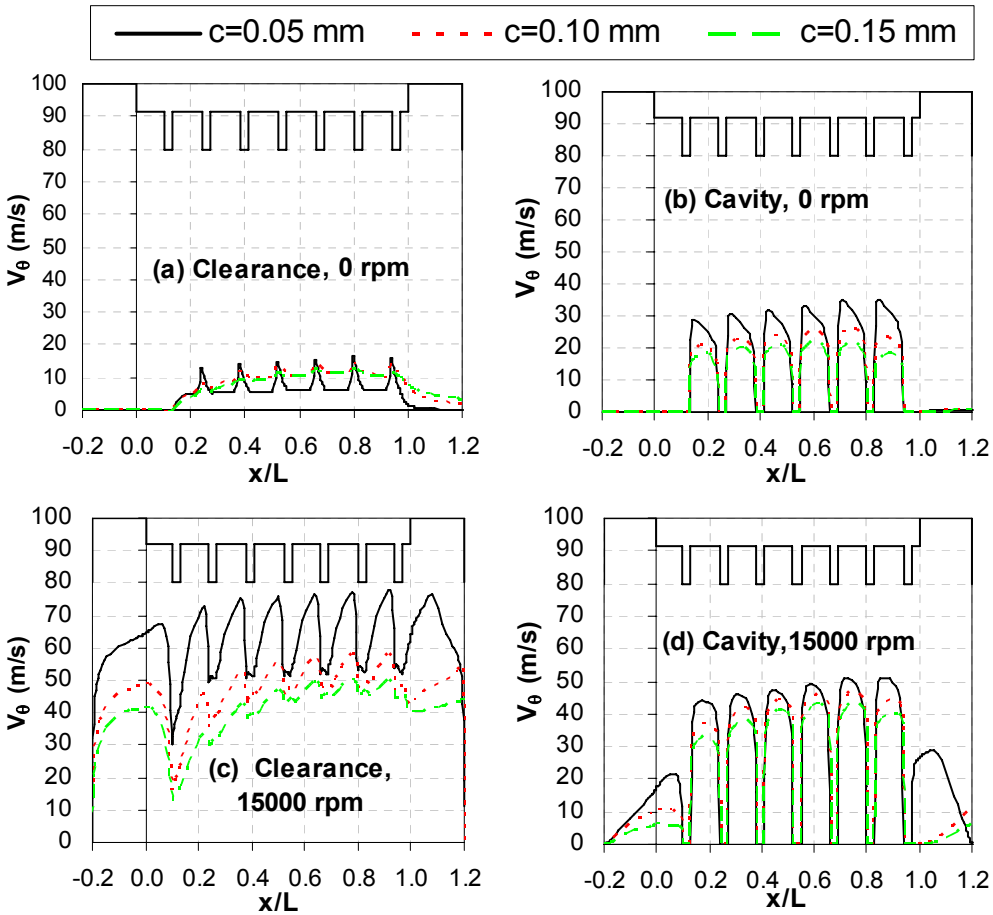

Fig. 89 Circumferential velocity distribution along a line passing through the middle of the clearance and cavity at DP=34.5 kPa.

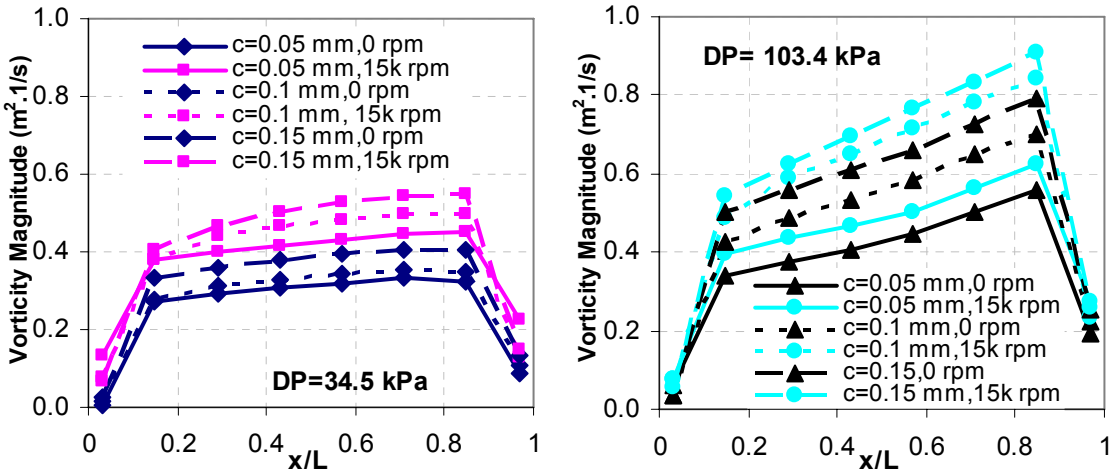

Fig. 90 Vorticity magnitudes in the seal cavities at 180° sectional view for different *c*, *Ω*, and DP's.

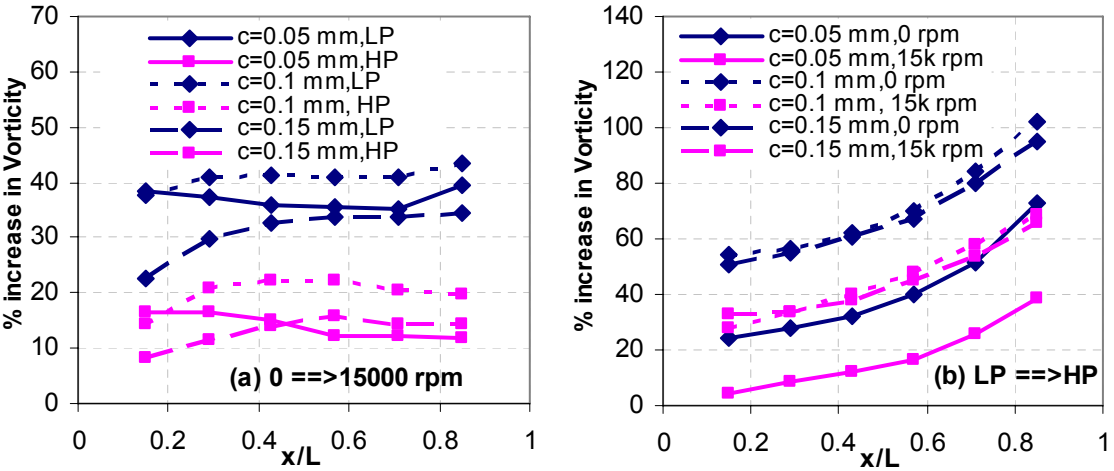

Fig. 91 % increase in vorticity versus x/L for different c, DP, and Ω for: (a) 0➔15000 rpm, (b) LP➔ HP.

The pressure contours are shown in Figs. 93, 94 and 95. The axial pressure distribution has a small difference for different seal clearances. Increasing the seal clearance increases the pressure drop at the inlet of the seal, which agrees with the higher inlet axial velocity distribution in Fig. 81. In the axial direction, the pressure drop across the seal tooth decreases with higher clearances. Toward the end the seal, all seals with different clearances have similar pressure drop. The pressure distribution within the cavity and through out the rotor surface is similar

except near the edges of the tooth which vary by a maximum of 0.25 *kPa*. Increasing the rotor speed from 0 to 15000 rpm decreases the pressure by a maximum of 0.17 *kPa* in both seal clearance and cavity. This value is very small and can be neglected for comparison purposes. Fig. 95 shows that the pressure within the seal cavities is constant. This suggests that the decrease in the axial kinetic energy is dissipated and not recovered back to static pressure. Therefore, all the losses in the kinetic energy within the seal cavities are due to viscous dissipation only.

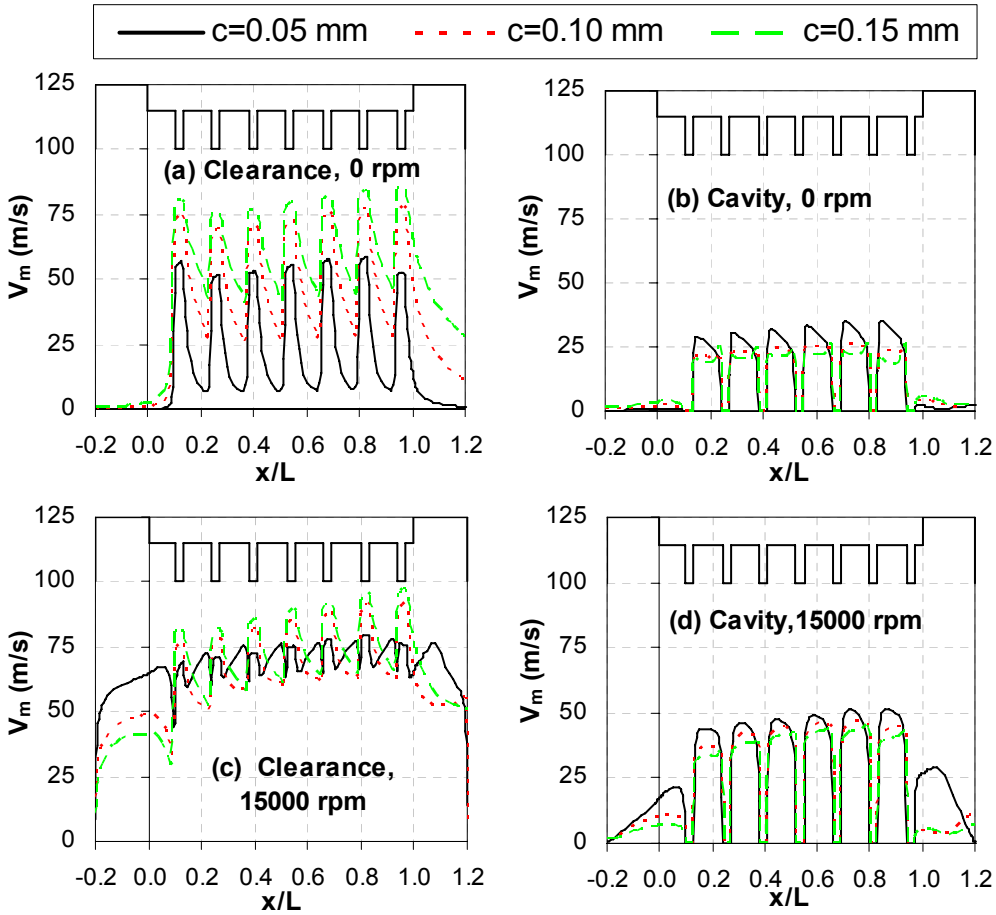

Fig. 92 Velocity magnitude distribution along a line passing through the middle of the clearance and cavity at DP=34.5 kPa.

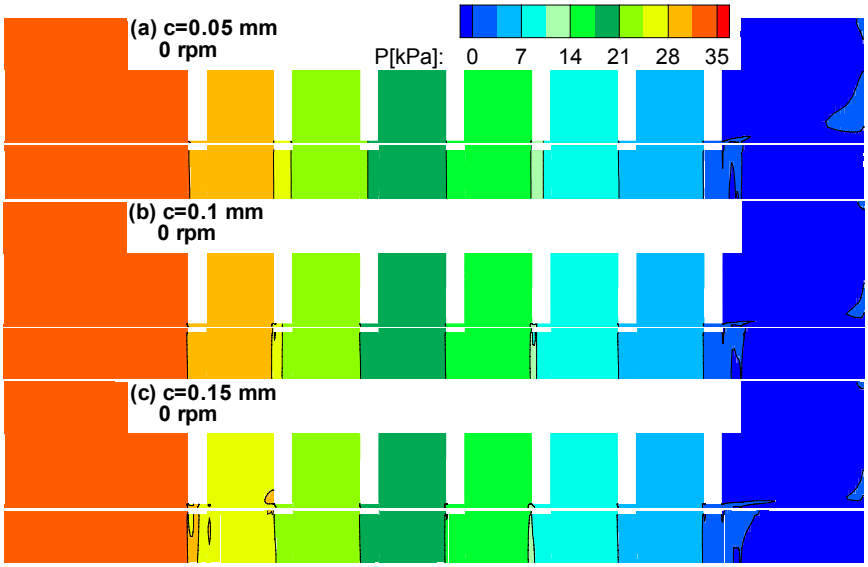

Fig. 93 Pressure contours for different seal clearances at Ω=0 rpm and DP=34.5 kPa.

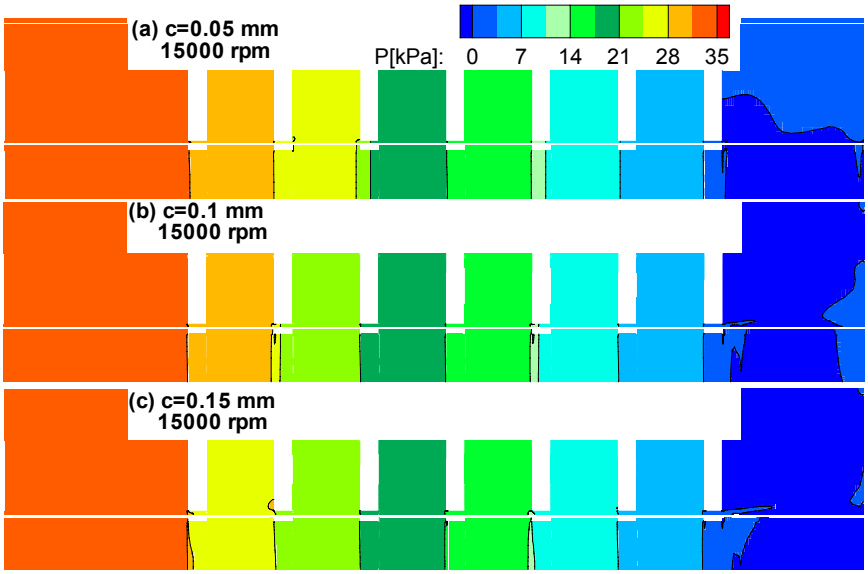

Fig. 94 Pressure contours for different seal clearances at Ω=15000 rpm and DP=34.5 kPa.

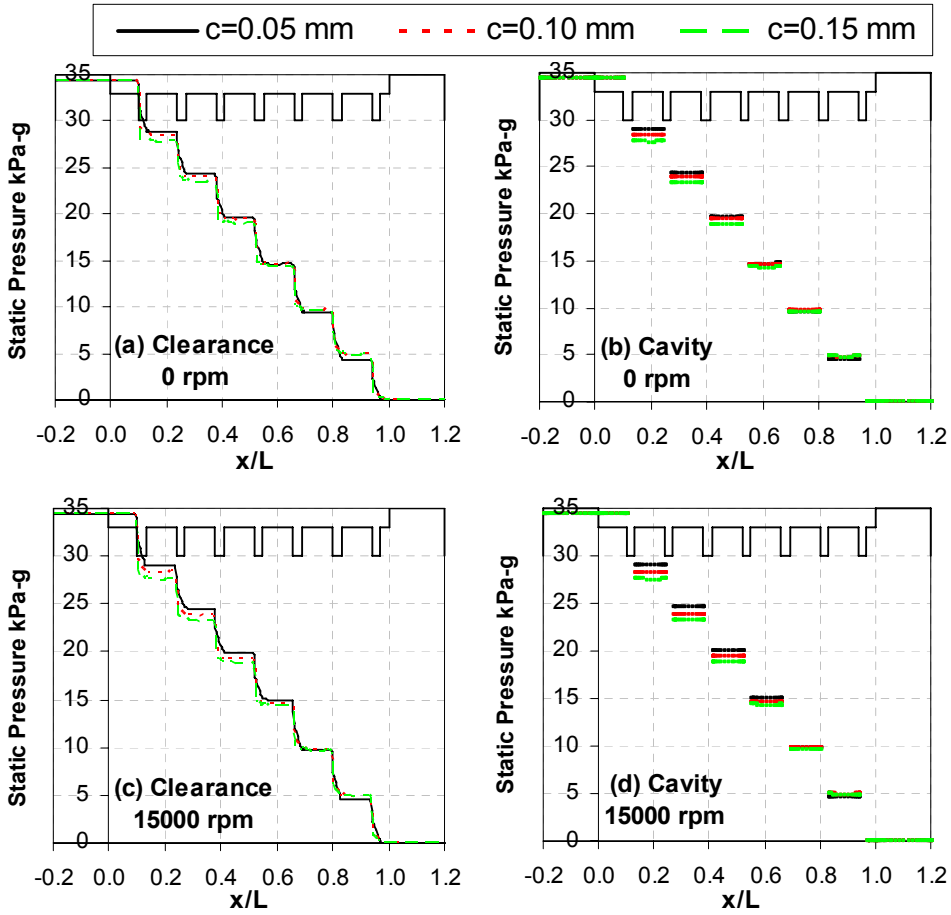

Fig. 95 Pressure along a line passing through the middle of the clearance and cavity.

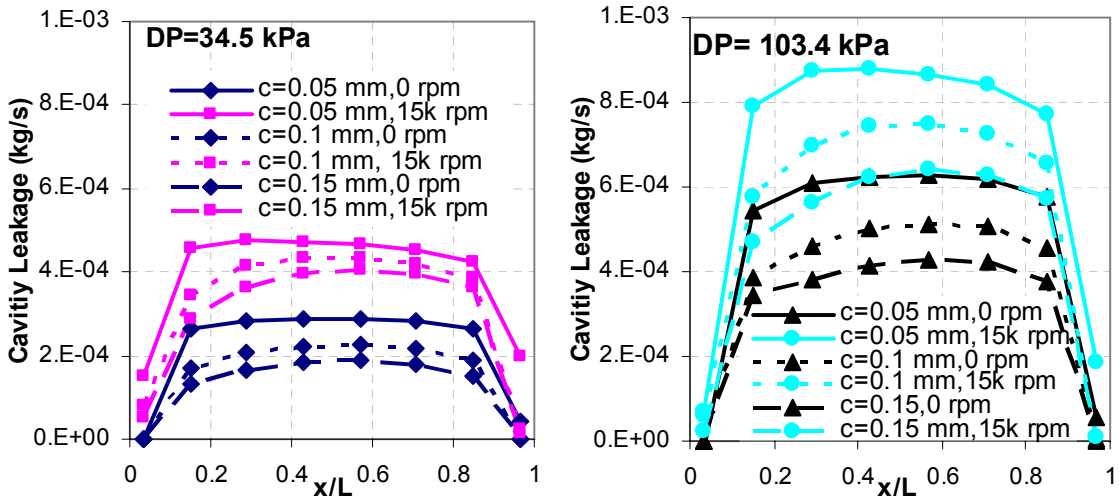

Fig. 96 Variation in cavities leakages along the seal axial direction for different *c* and DP's.

Fig. 96 shows the variation in cavities leakages along the axial direction of the seal for different seal clearances and *DP*'s. The leakage flowrates were evaluated in the seal cavities along the 180° seal sectional view. Fig. 96 shows that the leakages within the seal cavities are nearly constant at low *DP*, except at the first and last cavities. The leakage flowrate within the seal cavities increases with increasing rotor speed and decreases with increasing seal clearance. The same applies at high *DP* with a small increase in cavities leakage flowrates toward the middle cavity. The maximum leakage flowrate within the cavities were used for calculating the leakage flowrate under the seal tooth in the following figures.

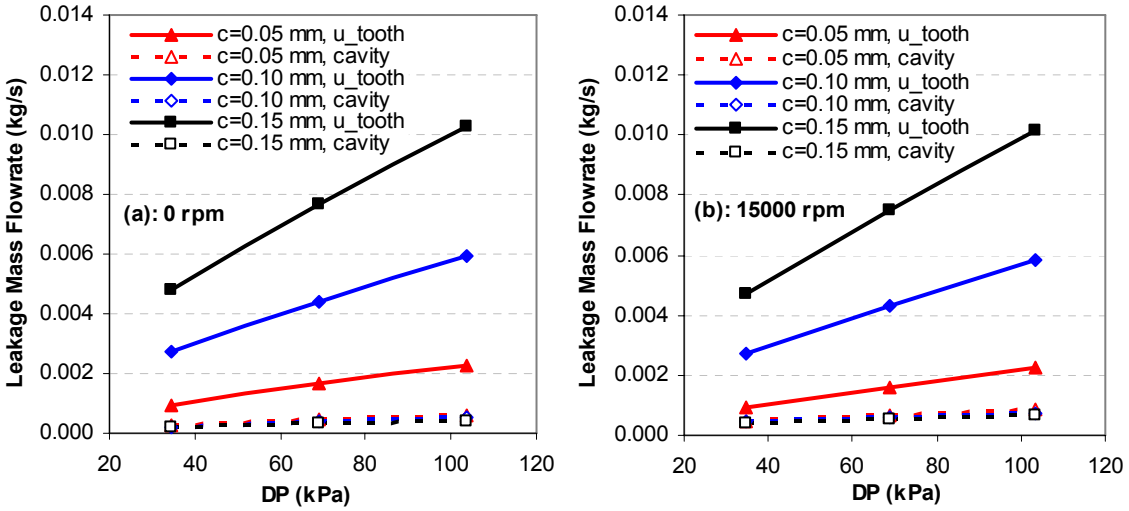

Fig. 97 Cavity and under tooth leakage mass flowrate versus DP for different clearances; (a) 0 rpm and (b) 15000 rpm.

Figs. 97 and 98 show how much the windback seal will leak through the cavity and under the tooth. Fig. 97 shows that, the leakage flowrate through the cavity is almost constant in value for different seal clearances, and increases with increasing *DP* and/or rotor speeds. In term of percentage, Fig. 98 shows that increasing the clearance will reduce the percentage of the flow going through the cavity. Further more, increasing *DP* will increase the percentage of flow under the tooth and reduce it through the cavity. Fig. 99 shows that increasing the rotor speed increases the leakage flowrate through the seal cavity, this is also accompanied with a reduction of leakage flowrate under the seal tooth. This supports the observation discussed previously regarding the

influence of clearance, rotor speed and *DP* on flow velocity components and axial pressure distribution.

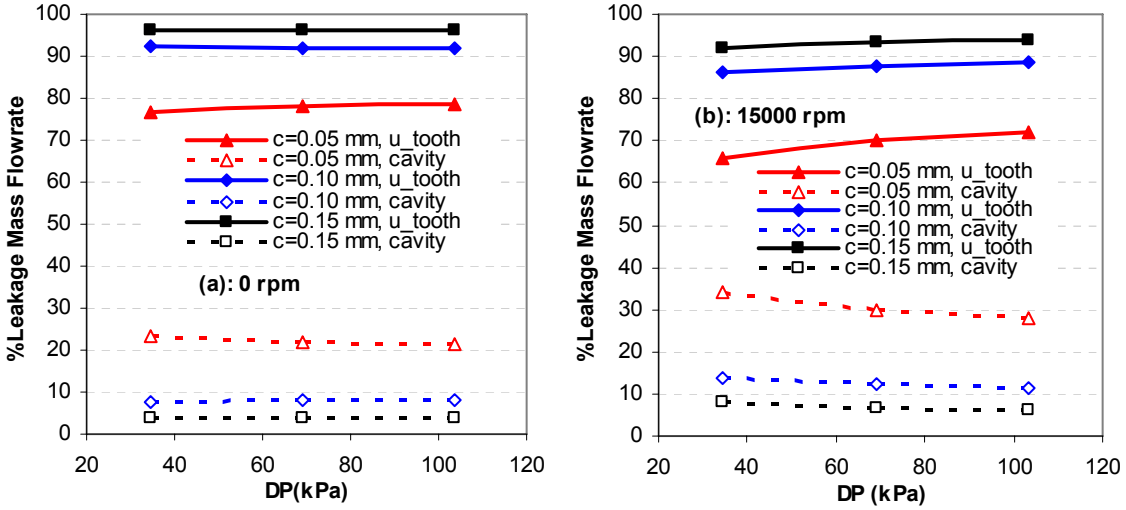

Fig. 98 Percent cavity and under tooth leakage mass flowrate versus DP for different clearances; (a) 0 rpm and (b) 15000 rpm.

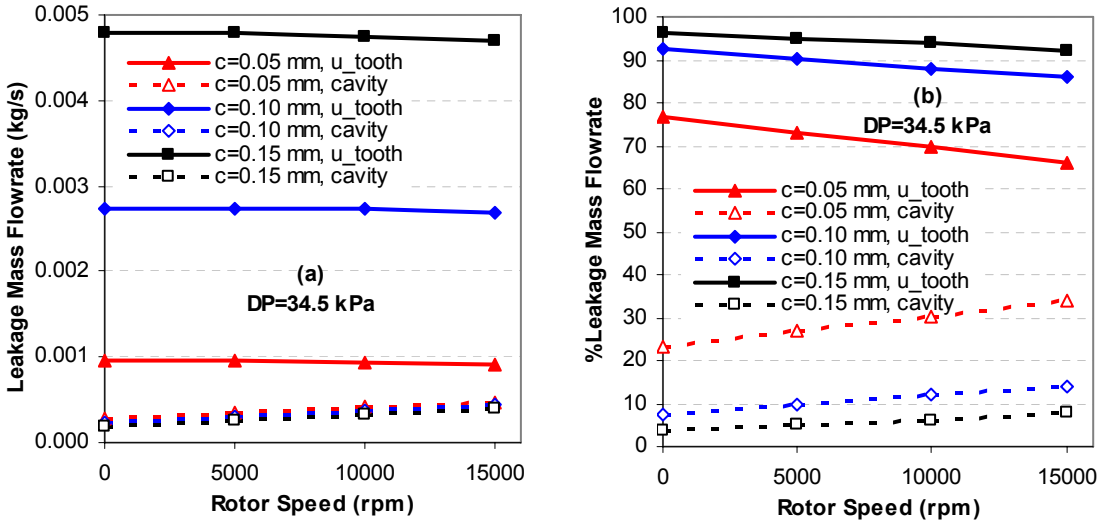

Fig. 99 Cavity and under tooth leakage mass flowrate versus rotor speed for different clearances,. DP=34.5 kPa: (a) leakage in kg/s and (b) percent from total leakage.

Tooth Height Effect

The effect of tooth height or cavity depth on leakage flowrates was studied for three different seals with 0.10 mm clearance. One with zero cavity depth and represents the smooth seal, while the other two were windback seals with cavity depths of 1.47 mm and 2.94 mm. As one may expect, the windback seal will leak more than the smooth seal, since it has a cavity groove in which the air will leak through. This is true but not for all operating conditions. Fig. 100 shows that the smooth seal leaks less than a windback seal for low and medium differential pressures (*DP*), but for high *DP*, the windback seal with groove depth *h*=1.47 mm leaks less than a smooth seal, especially at low rotor speeds where the flow in the smooth seal is laminar as seen in the previous chapter with Re_{axial} around 1000 and therefore leaks more than a windback seal.

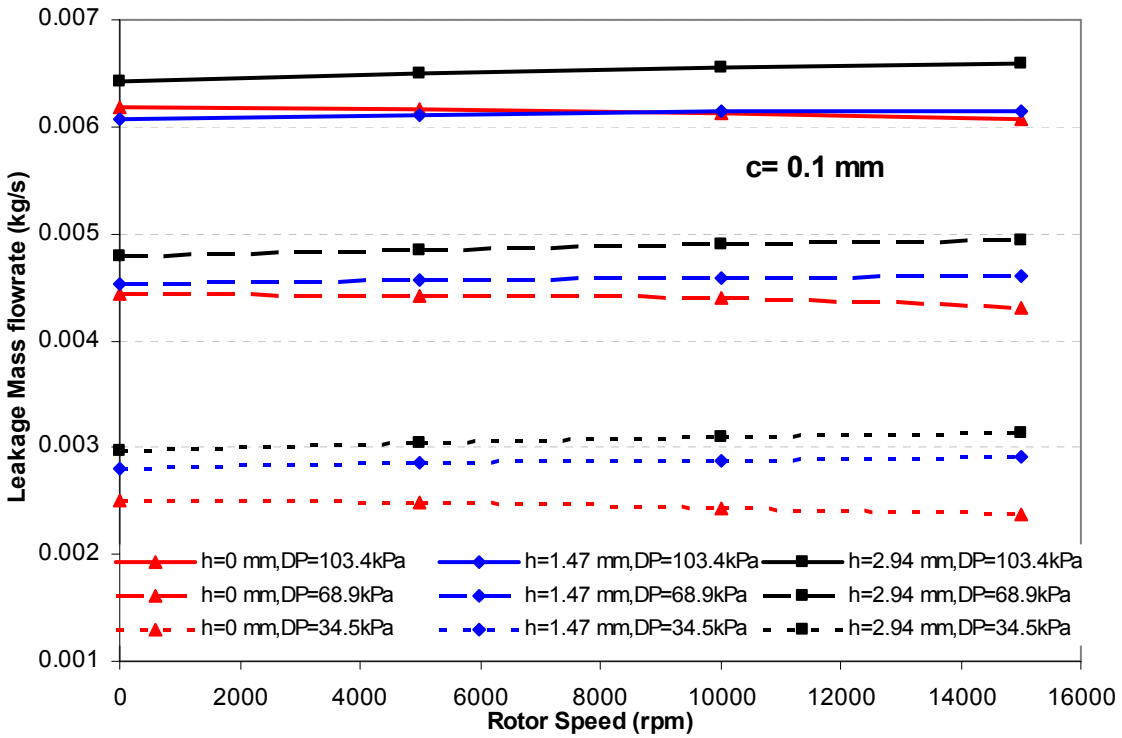

Fig. 100 Leakage mass flowrate versus rotor speed for different cavity depths and DPs, c=0.1 mm.

The turbulent flow in the windback seal plays a major role in increasing the friction factor, and hence reducing the leakage flow, especially at zero running speed. This turbulence is

generated from circulating the air in the cavity of the windback seal and from flow expansion under the tooth forming a jet that creates helical vortices along the windback seal cavity. Another source of turbulence is the rotor speed. Increasing the rotor speed will increase the friction factor and hence reduce the leakage flowrate which can be seen in Fig. 100 for the smooth seal. Similarly, for the windback seal, increasing the rotor speed increases the total flowrate through the seal by increasing the flow circumferential velocity in the cavity and redirecting the flow in the circumferential direction which reduces the flowrate under the tooth, as shown in Fig. 99. Figs. 100 and 101 show that decreasing *h* decreases the leakage flowrates due to the reduction in the cavity cross sectional area. Fig. 101 represents the same data in Fig. 100 but plotted against the differential pressure for two rotor speeds; 0 and 15000 rpm.

To explain the effects of changing the cavity depth and rotor speed on leakage flowrates, Figs. 102 to 114 show the flow velocity components and pressure field contour plots for the 270° plane sectional view, for the three different windback seal cavity depths 0,1.47, and 2.94 mm at 0 and 15000 rpm, and 34.5 *kPa*. The following observation can be drawn:

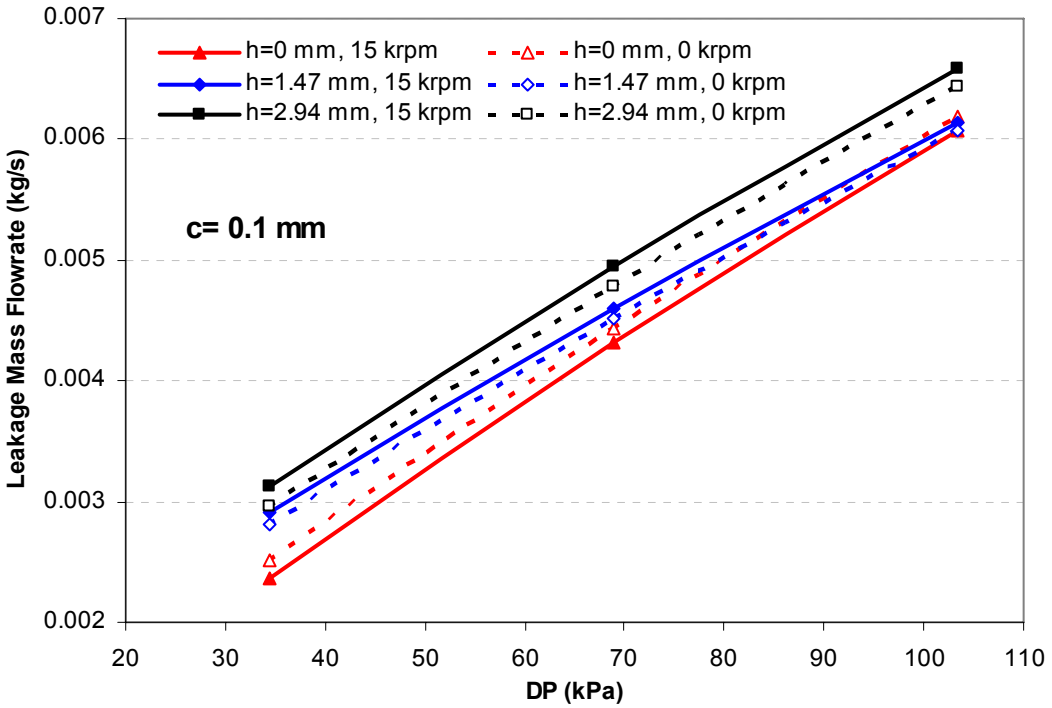

Fig. 101 Leakage mass flowrate versus DP for different cavity depths and rotor speeds, c=0.1 mm.

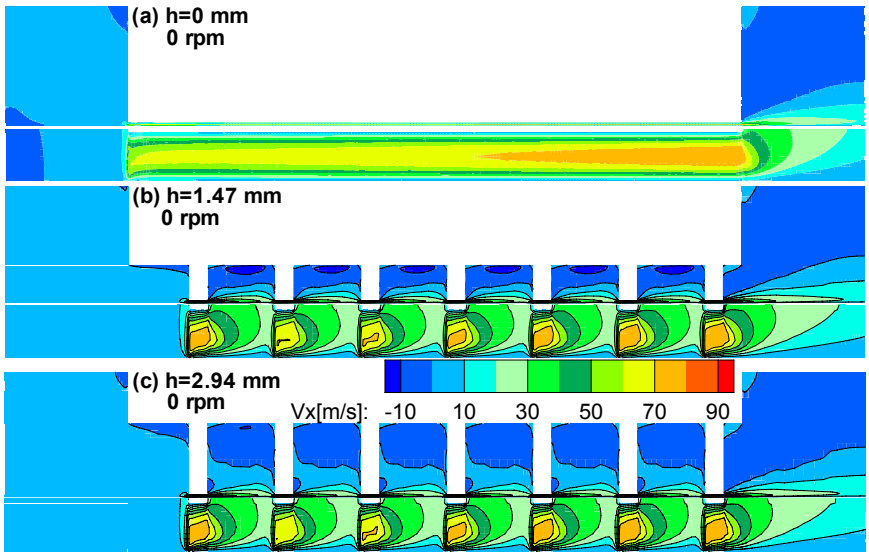

Fig. 102 Axial velocity contours for different h at Ω=0 rpm and DP=34.5 kPa.

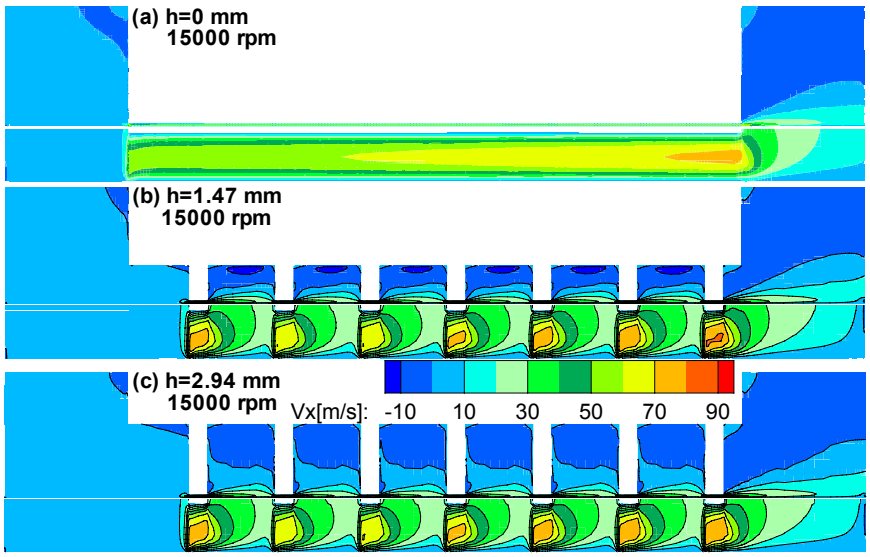

Fig. 103 Axial velocity contours for different h at Ω=15000 rpm and DP=34.5 kPa.

Comparing Figs. 102, 103 and 104, the rotor speed has a negligible effect on the axial velocity for the cases were $h\neq0$ and a considerable effect for h=0. For the former cases, the flow

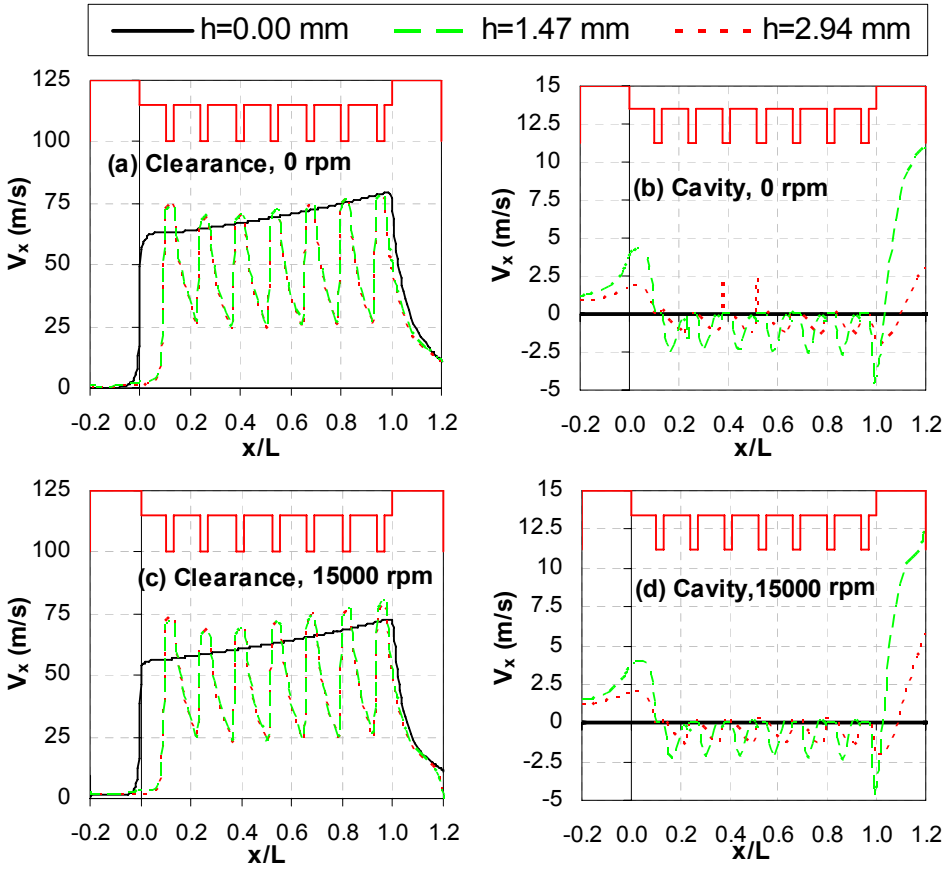

Fig. 104 Axial velocity distribution along a line passing through the middle of the clearance and cavity at DP=34.5 kPa.

is already directed in the circumferential direction throughout the seal cavity and therefore the rotor speed has a negligible effect. On the other hand, for h=0 and with no rotation, the flow is in one direction and probably laminar in the x-direction along the axial pressure drop, where V_r and V_θ are equal to zero. When introducing the rpm effect from the no-rotation status, part of the flow will be directed in the circumferential direction due to the viscosity effect and hence, reducing the axial velocity distribution within the seal clearance. In addition, increasing shear stress on the rotor surface by increasing rotor speed may push the flow into a transitional turbulent regime. This will increase the energy dissipated by friction which deprives V_x from that energy resulting in slower V_x.

Figs. 102 and 104(a, b) show that the maximum axial velocity for the three cavity depths is comparable and falls between 70-80 *m/s* at 0 rpm under the seal tooth. For the cases of h not equal to zero, the axial velocity under the tooth in the first stage is comparable, 70-80 *m/s*, and

higher than the inlet axial velocity, 60-70 *m/s*, for the smooth seal where *h*=0. This can be explained by the higher pressure drop across the tooth of a windback seal compared to the almost uniform pressure drop (decrease in air density) across the smooth seal. For this reason, the axial velocity for the smooth seal is continuously increasing in the downstream direction of the flow.

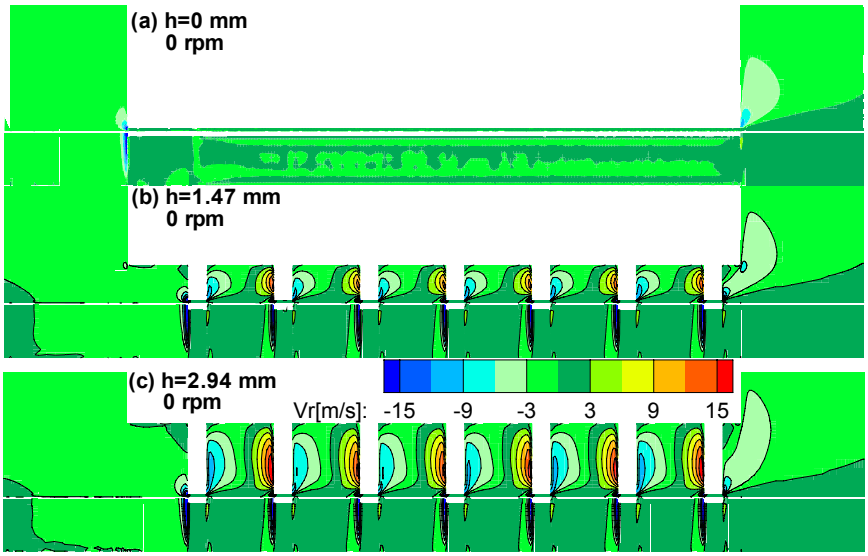

Fig. 105 Radial velocity contours for different *h* at Ω=0 rpm and DP=34.5 kPa.

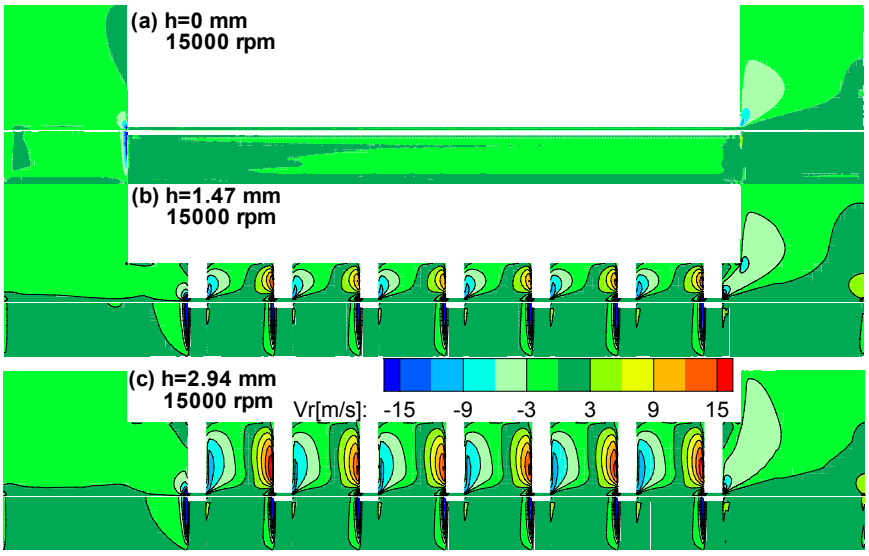

Fig. 106 Radial velocity contours for different *h* at Ω=15000 rpm and DP=34.5 kPa.

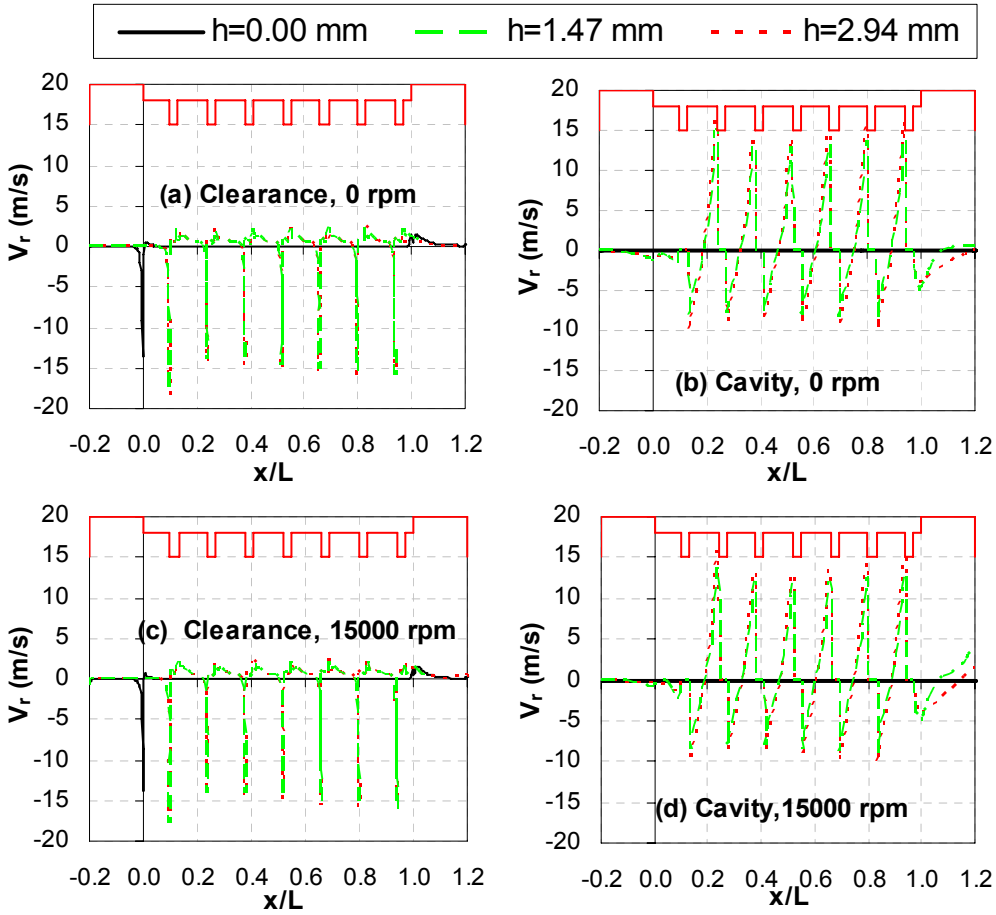

Fig. 107 V_r along a line passing through the middle of the clearance and cavity at DP=34.5 kPa.

Additionally, reducing *h* by 50% has a negligible effect on the axial velocity in the seal clearance, and increases the axial velocity in the seal cavity.

Figs. 105, 106 and 107 show that increasing the cavity depth increases the radial velocity component within the seal cavity. The rpm has a negligible effect on radial velocity component.

Figs. 108, 109 and 110 show the circumferential velocity component V_θ, with no-rotation. Increasing the cavity depth from 0 to 2.94 mm increases V_θ from 0 to 18-27 *m/s*, respectively, in the seal cavity and hence V_θ increases in the seal clearance. Again, increasing rotor speed increases V_θ substantially in both the seal clearance and the cavity. Larger cavity depths results in a greater increase in V_θ than for lower cavity depths, but still comparable within 10%.

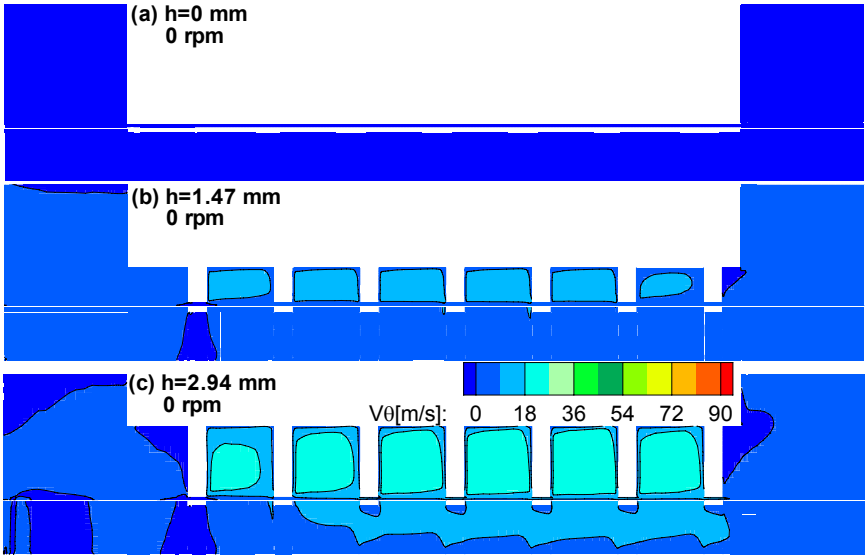

Fig. 108 V_θ contours for different h at Ω=0 rpm and DP=34.5 kPa.

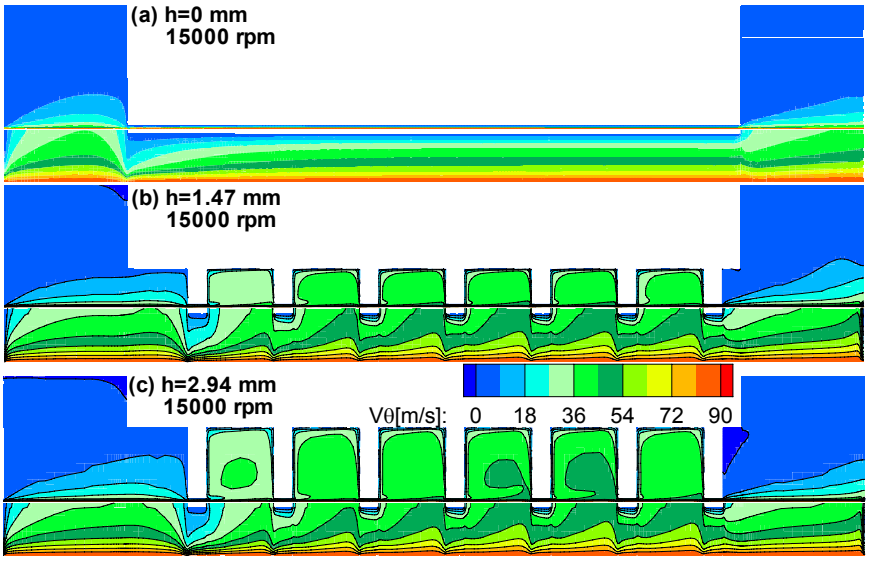

Fig. 109 V_θ contours for different h at Ω=15000 rpm and DP=34.5 kPa.

Windback seals with larger cavity depths have a greater influence on increasing the circumferential velocity component at no running speed. Fig. 110a and b show that increasing h from 1.47 to 2.94 mm increases the maximum V_θ in the seal clearance and cavity from 7 to 14 *m/s* and from 13 to 26 *m/s*, respectively. This can be utilized in cleaning the seal cavities from oil

residual before running the turbomachine, and justify the small increase in leakage flowrate. Figs. 109 and 110(c, d) show that for h=0, V_θ shows the transition from a developing velocity profile downstream the seal entrance to a fully developed V_θ profile for the rest of the seal length, where V_θ reaches a steady value around 45 *m/s*. Fig. 110c shows that, within the seal clearance, V_θ for $h\neq0$ are larger than V_θ for h=0, due to the lack of air drag on the stator wall. The drag due to air in the seal cavity is less than the drag from a smooth stator wall 0.1 mm above the rotor surface. Still they all asymptote to a maximum value about the same way. In addition, for $h\neq0$, each tooth starts a new V_θ development region along the seal axial direction within the seal clearance, while V_θ reaches a fully developed flow profile within the seal cavity reaching nearly a steady state in the last few cavities.

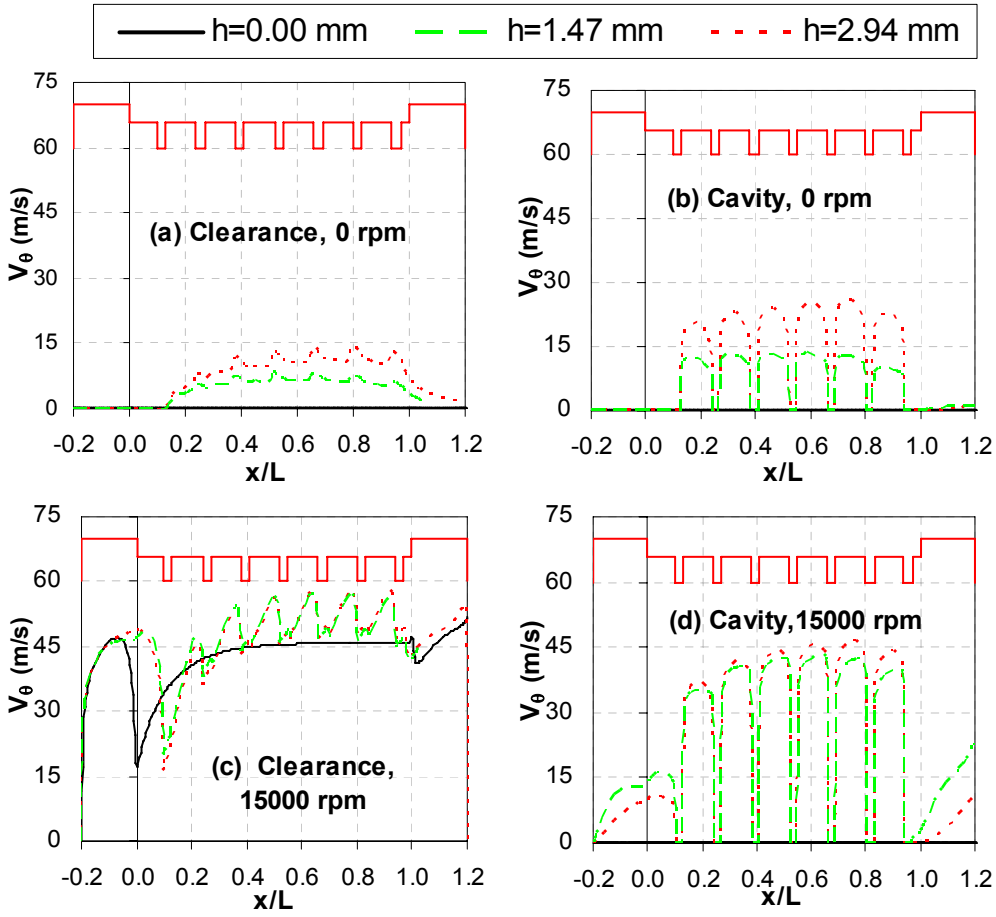

Fig. 110 V_θ along a line passing through the middle of the clearance and cavity at DP=34.5 kPa.

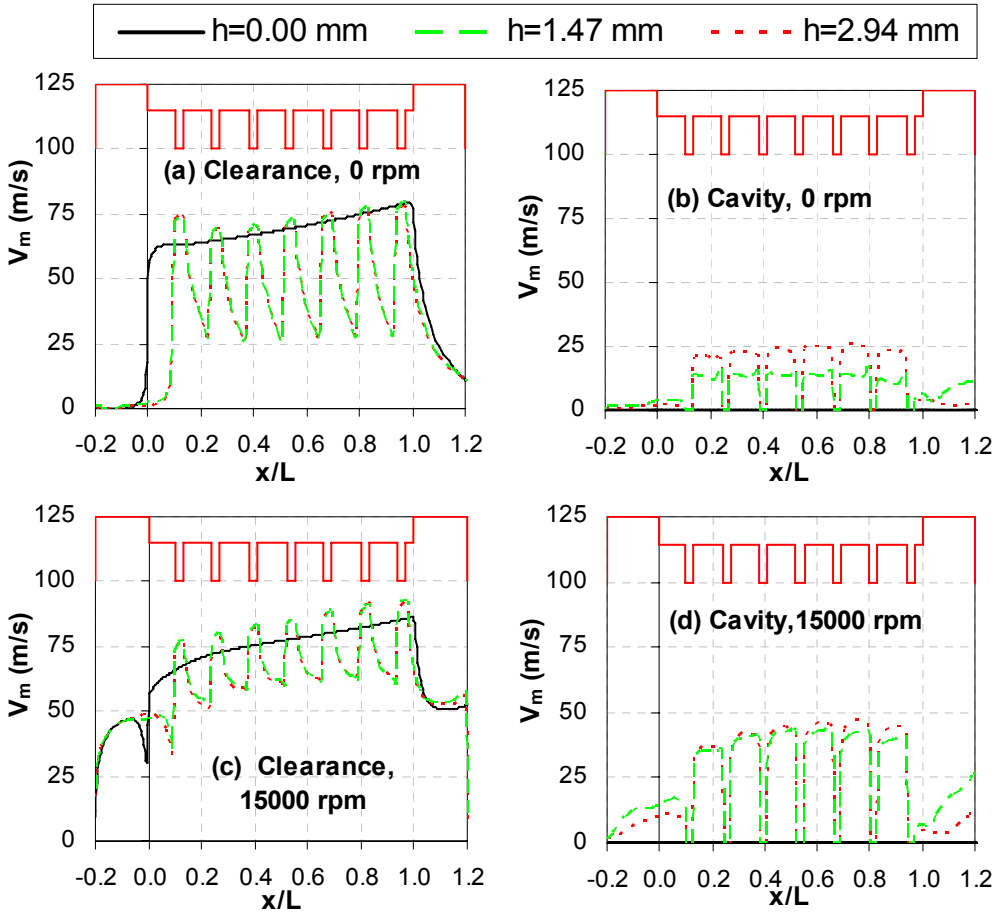

Fig. 111 V_m along a line passing through the middle of the clearance and cavity at DP=34.5 kPa.

Fig. 111 shows the velocity magnitude. It is clear that within the seal clearance, the axial velocity is dominant under the tooth and the circumferential velocity component is dominant between two consecutive teeth. On the other hand, within the seal cavity, V_θ is dominant, and for that reason both V_m and V_θ appears similar.

Figs. 112, 113 and 114 demonstrate the pressure contours for 0 and 15000 rpm cases, respectively. Because of the absence of a cavity for the smooth seal, the pressure drop is almost a linear relationship, while for a windback seal it is a stair step distribution. Different windback cavity depths and rotor speeds have no effect on the axial pressure distribution. There are three conditions that generate a hydrodynamic pressure; rotation, converging surface, and viscous fluid. The low viscosity of air and the absence of seal eccentricity minimize the effect of rotor speed on pressure.

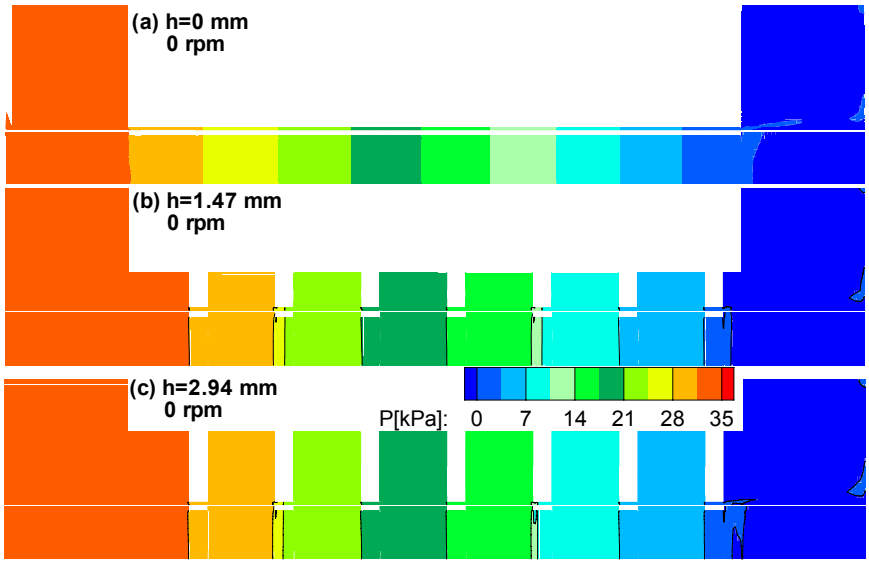

Fig. 112 Pressure contours for different h at Ω=0 rpm.

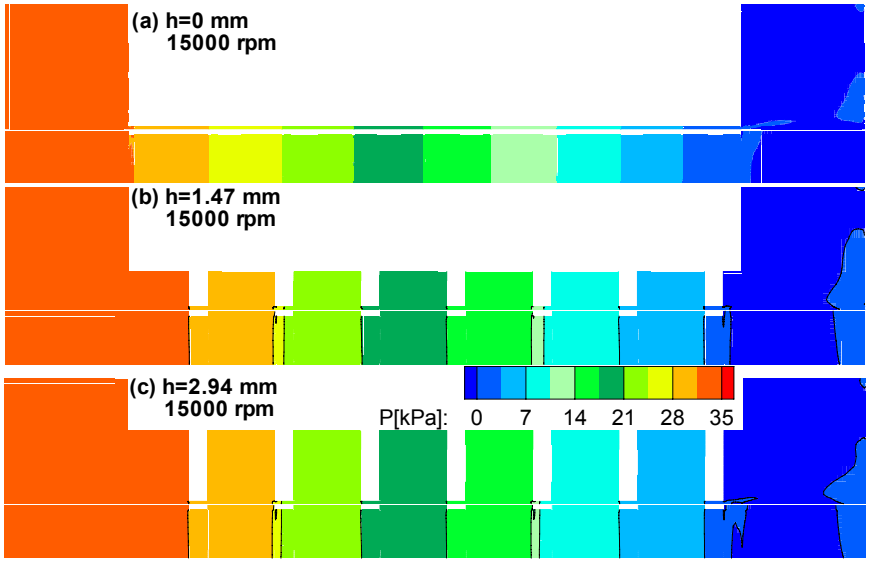

Fig. 113 Pressure contours for different h at Ω=15000 rpm.

Fig. 115 shows the vorticity magnitude for different cavity depths, and is similar to Fig. 90. Increasing the rotor speed and DP increases the vorticity magnitude as previously observed in Fig. 90. For h=0 there was no cavity and therefore the vorticity is equal to zero. Increasing the cavity depth increases the vorticity magnitude within the seal cavities due to the increase in V_θ.

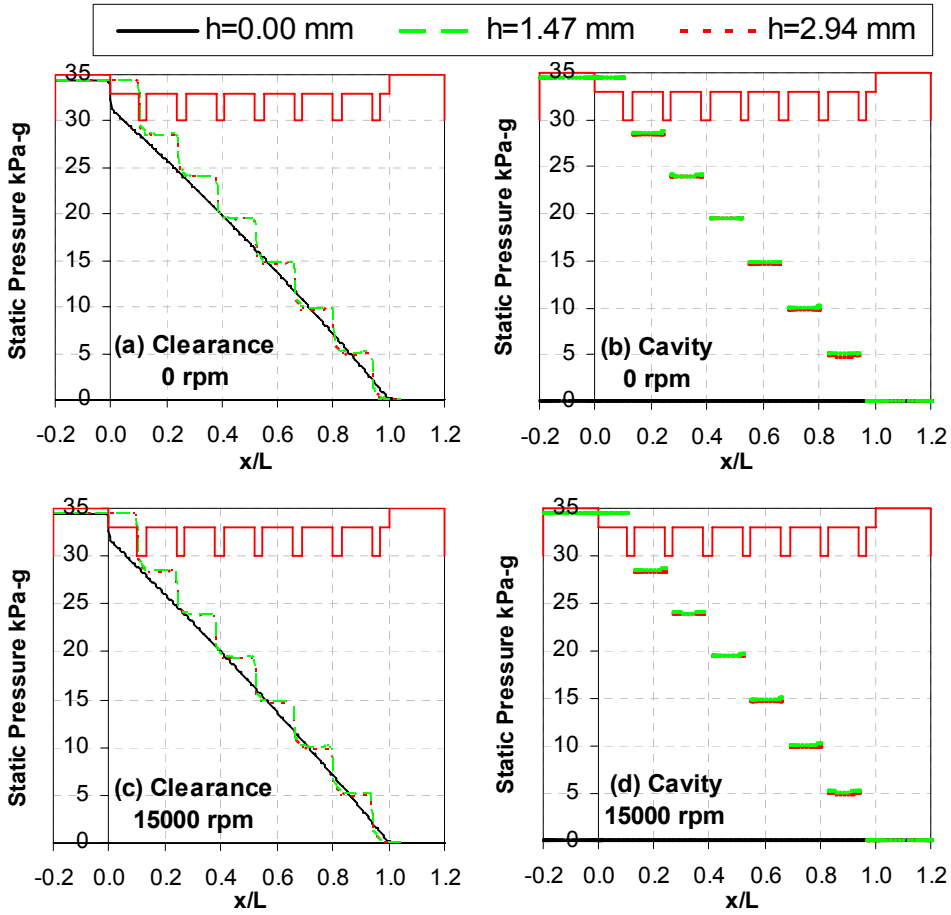

Fig. 114 P along a line passing through the middle of the clearance and cavity for different *h*.

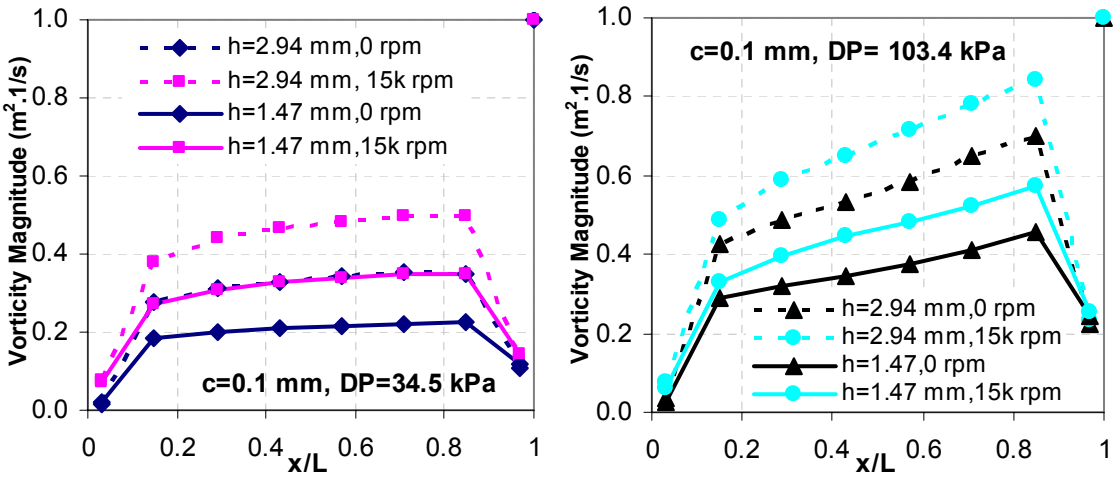

Fig. 115 Vorticity magnitudes in the seal cavities at 180° sectional view for different *h*, Ω and DP's.

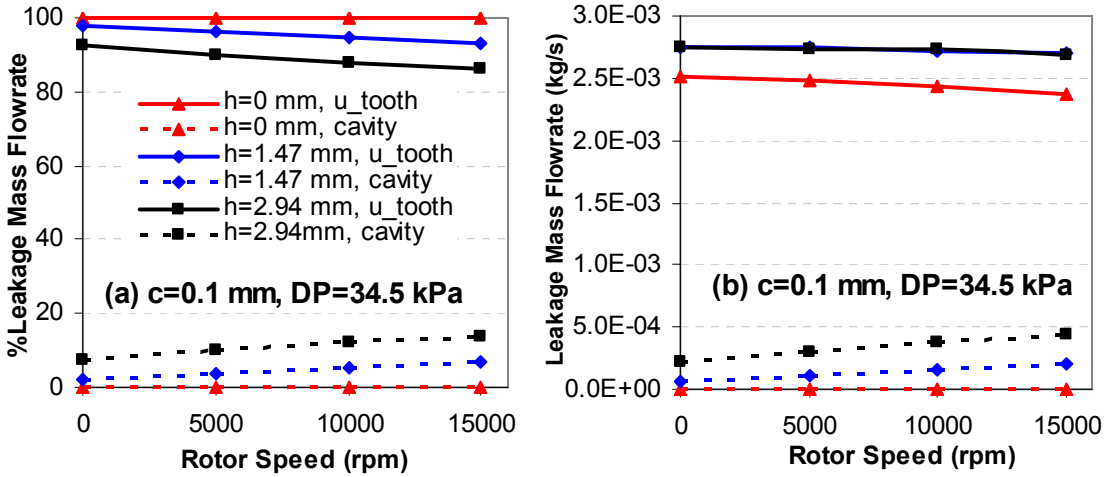

Fig. 116 Cavity and under tooth leakage mass flowrate versus Ω for different cavity depths, c=0.1 mm and DP=34.5 kPa; (a) Percentage, (b) *kg/s*.

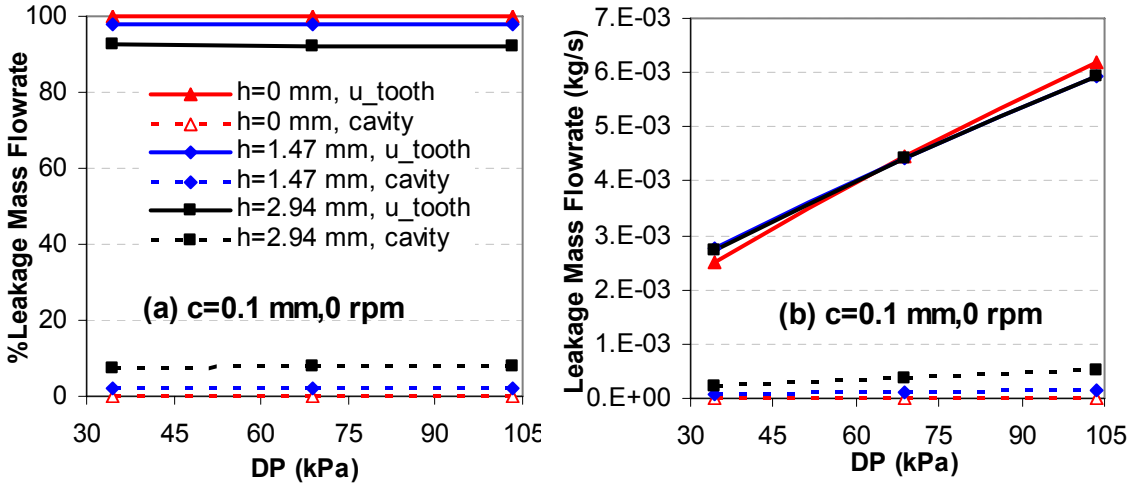

Fig. 117 Cavity and under tooth leakage mass flowrate DP for different cavity depths at 0 rpm and c=0.1 mm; (a) Percentage, (b) *kg/s*.

Figs. 116 and 117 present the effect of rotor speeds and the differential pressure on the leakage flowrate under the tooth and through the cavity. Figs. 116a and 117a show that increasing *DP* has no effect on the percent leakage flowrate at 0 rpm. On the other hand, increasing the rotor speed will increase the flow percent in the cavity and reduce it under the

tooth. Furthermore, Fig. 116b shows that $\dot{m}_{under\ tooth}$ decreases with increasing rotor speed due to the increase in friction with rpm, while $\dot{m}_{cavity}$ increases with increasing rotor speed due to the increase in V_θ as a result of increasing rotor drag. Fig. 117b shows that both $\dot{m}_{under\ tooth}$ and $\dot{m}_{cavity}$ increases with increasing *DP* due to the increase in both V_x and V_θ with increasing *DP*. $\dot{m}_{under\ tooth}$ for h=0 is the lowest compared to the cases where $h \neq 0$ at low *DP*, and almost equal at *MP*, and higher at *HP*. Fig. 118 shows the cavity depth effect on total leakage flowrate. In general, increasing h increases the leakage flowrate. However, increasing rpm for h=0 has an opposite trend in reducing the leakage flowrate compared to $h \neq 0$. Since h=0 represent the smooth seal, and increasing rotor speed reduces the leakage flowrate throughout decreasing the axial velocity, due to the increase in the frictional losses. As a result, part of the flow will be directed in the circumferential direction as previously observed.

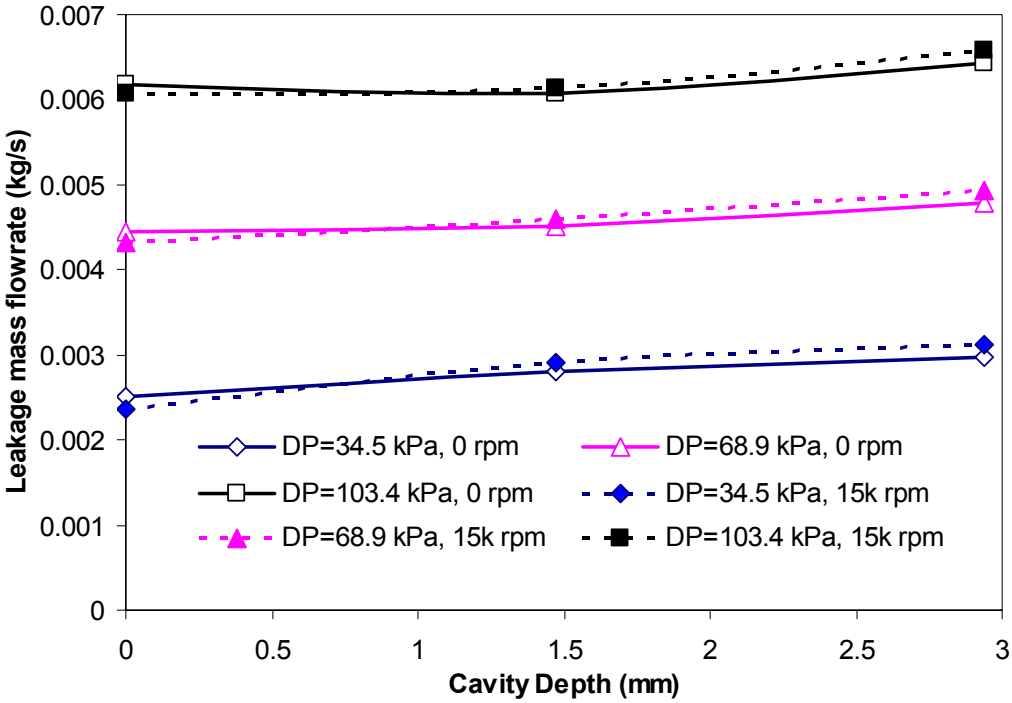

Fig. 118 Leakage mass flowrate versus cavity depth for different DP's and rotor speeds.

Tooth Pitch Effect

The effects of changing the tooth pitch (helix angle) for windback seals were studied numerically for three different tooth pitches, s = 3.12 mm, 3.56 mm and 4.14 mm, which corresponds to the following helix angles 0.49°, 0.56°, 065°, respectively. In addition, the three different tooth pitches, s = 3.12 mm, 3.56 mm and 4.14 mm, also correspond to $n \cong 6, 7, 8$, respectively. The three seals have the same length (L= 25.4 mm), clearance (c=0.1 mm), tooth height (h=2.94 mm) and tooth thickness (t =0.7874 mm). The seals have been numerically simulated for three differential pressures of 34.5, 68.9, and 103.4 *kPa*. Furthermore, for each *DP*, the effect of rotor speed on leakage flowrates was studied for 0, 5000, 10000, and 15000 rpm.

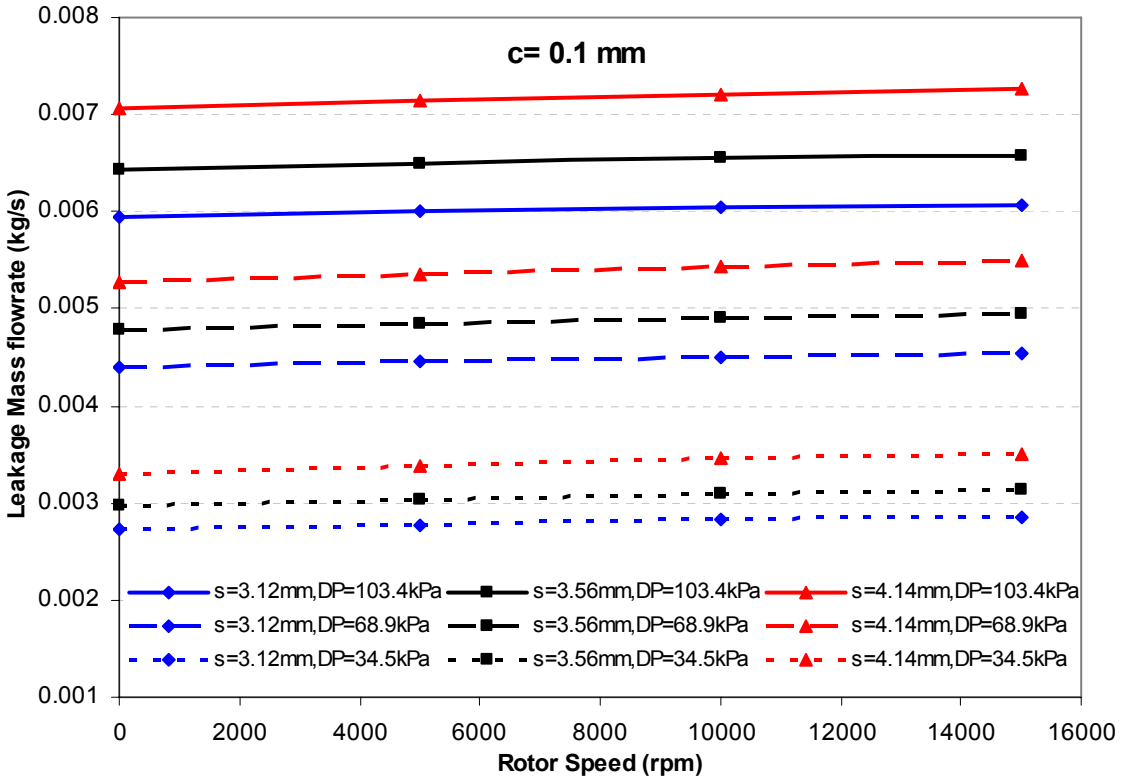

Fig. 119 Leakage mass flowrate versus rotor speed for different tooth pitches and DPs at c=0.1 mm.

Fig. 119 shows the effects of different tooth pitches, *DP*, and rotor speeds on leakage flowrates. It is clear that changing the tooth pitch does not change the trends observed in

previous sections relating the changes of leakages flowrates with changing *DP* and rotor speed. Increasing rotor speed and/or *DP* increases the leakage flowrate. Increasing the tooth pitch, while maintaining a constant seal length will result in a decrease in the effective number of teeth, *n*, compared to the number of restrictions in a labyrinth seal. Table 11 shows that increasing tooth pitch from *s*=3.12 mm (*n*≅8) to *s*=4.14 mm (*n*≅6) increases the leakage flowrates by 21% and 19% at *LP* and *HP*, respectively, at 0 rpm. Also, the percent increase in the leakage flowrates at 15000 rpm was 23% and 20% at *LP* and *HP*, respectively. This suggests that the percent increase in leakage flowrate due to increasing *s* is nearly constant with an average of 20.75%, and is independent of rotor speed and *DP*. Table 12 illustrates the increase in leakage flowrate due to the increase in rotor speed from 0 to 15000 rpm for different *DP*'s. The rotor speed effect is almost constant, for constant tooth pitch and for all different *DP*, despite the fact that in terms of percentages, the maximum increase in leakage flowrate is at low *DP*. Given that, the seal leaks substantially less at low *DP* compared to high *DP*. In addition, increasing the tooth pitch from 3.12 mm to 4.14 mm increases the effect of rotor speed on leakage flowrates with a maximum increase at low *DP*. Again Figs. 120 and 121 show the same data presented in Fig. 119, plotted against tooth pitch and *DP*, respectively, for 0 and 15000 rpm. It is clear from these figures that the leakage flowrate varies in almost a linear relationship with rotor speeds, *DP*, and tooth pitch. Therefore, this linear relationship can be utilized with other geometrical seal effects in designing a similar windback seal. Fig. 122 shows that when plotting the flow coefficient versus Re_{axial} for the three different seal pitches for constant *DP*, they lay on the same line due to the compensation of the equivalent number of teeth in calculating the flow coefficient. This linear relationship was described previously in Eq. (23).

The flow velocity components and the static pressure comparison for different tooth pitches are shown as contour plots in Fig. 123 through Fig. 135, at the 270° plane sectional view for *DP*=34.5 *kPa* at 0 and 15000 rpm. The complete contour plots for different *DP*'s, and rotor speeds showing the four sectional views for windback seals are shown in the appendixes (A to H). The following observations can be drawn from Figs. 123 to 135.

Figs. 123 to 128 show that the axial velocity under the tooth increases with increasing tooth pitch. As a result of decreasing the effective number of teeth, higher axial pressure drop across each tooth is expected. In addition, increasing *s* strengthens the vortices generated inside the seal cavity, as shown by the increasing axial and radial velocity components inside the seal

cavity. A longer cavity results in less wall effect on the main flow inside the cavity. Again, the rotor speed has a negligible effect on the axial and radial velocity distributions.

Table 11 Effect of tooth pitch on % change in leakage flowrate.

$\Delta\dot{m}/\dot{m}_{s=3.12}\times 100\%$ from s=3.12 to 4.14 *mm*			
rpm	LP	MP	HP
0	21.2	20.0	18.7
15000	22.9	21.0	19.6

Table 12 Effect of rotor speed for different tooth pitch on leakage flowrate.

$\Delta\dot{m}(kg/s)$ from 0 to 15000 rpm			
s(*mm*)	LP	MP	HP
3.12	0.000130	0.000138	0.000124
3.56	0.000160	0.000152	0.000152
4.14	0.000205	0.000212	0.000202
$\Delta\dot{m}/\dot{m}_{0,rpm}\times 100\%$			
3.12	4.8	3.1	2.1
3.56	5.4	3.2	2.4
4.14	6.2	4.0	2.9

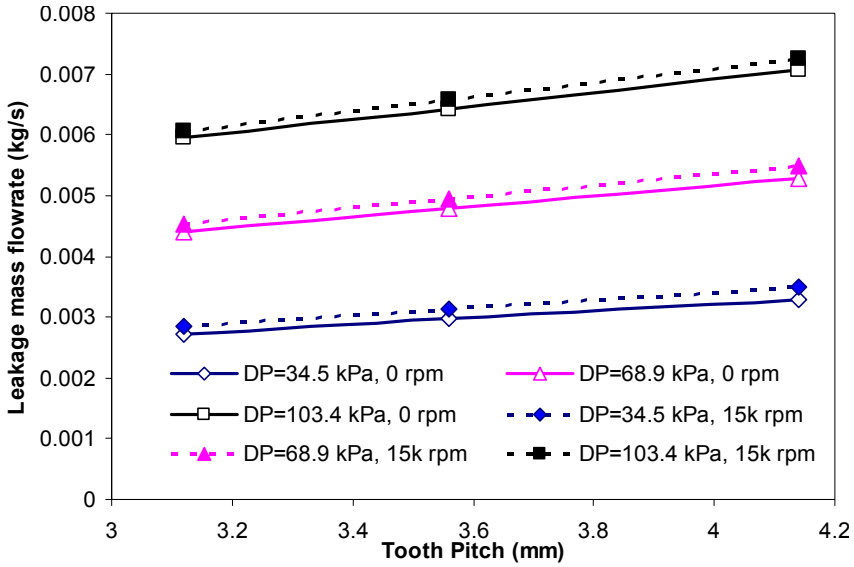

Fig. 120 Leakage mass flowrate versus tooth pitch for different DPs and rotor speeds at *c*=0.1 mm.

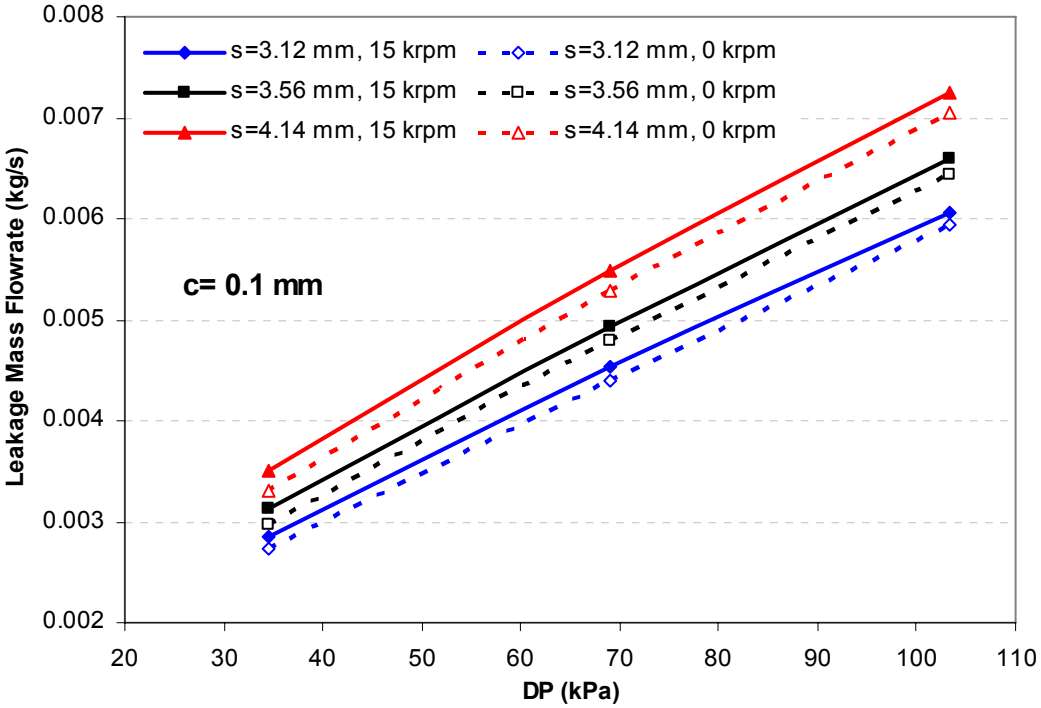

Fig. 121 Leakage mass flowrate versus DP for different tooth pitches and rotor speeds at c=0.1 mm.

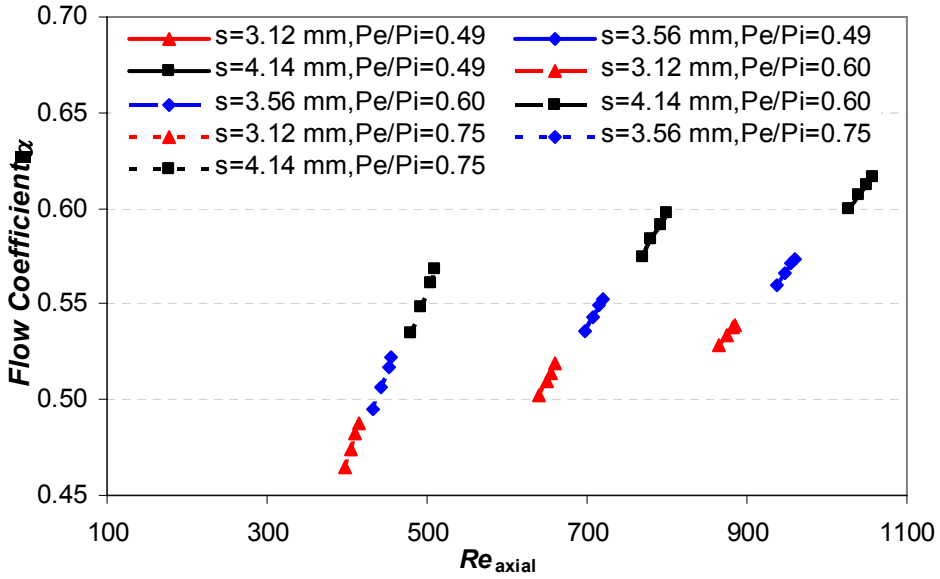

Fig. 122 Flow coefficient versus Axial Reynolds number for different s, pressure ratios.

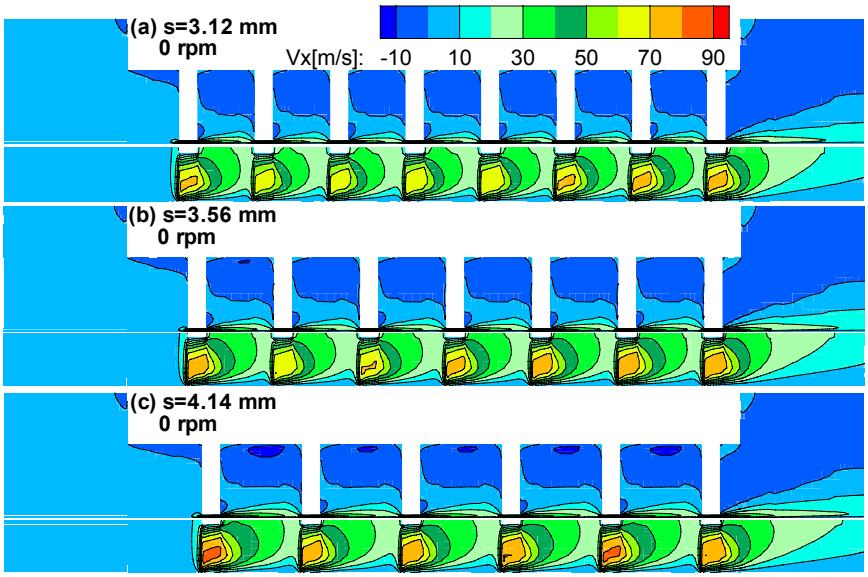

Fig. 123 V_x contours for different *s* at Ω=0 rpm and DP=34.5 kPa.

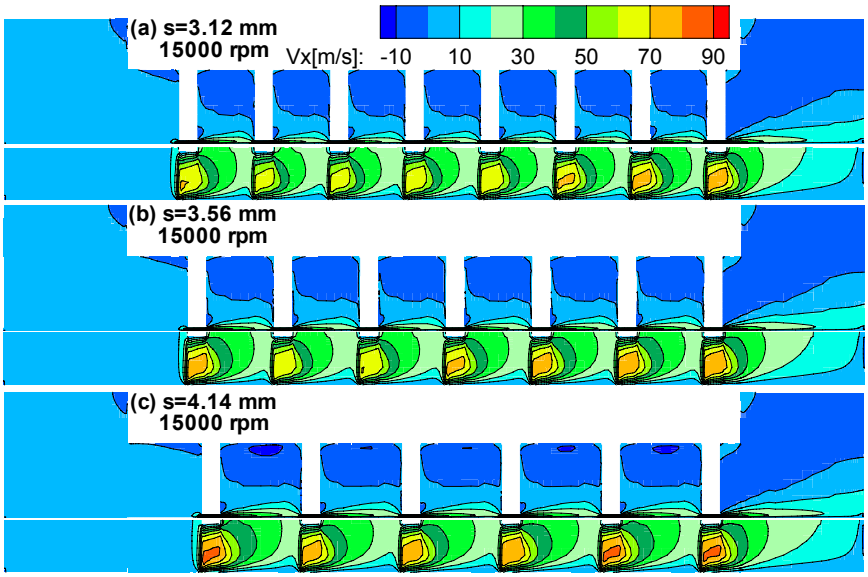

Fig. 124 V_x contours for different *s* at Ω=15000 rpm and DP=34.5 kPa.

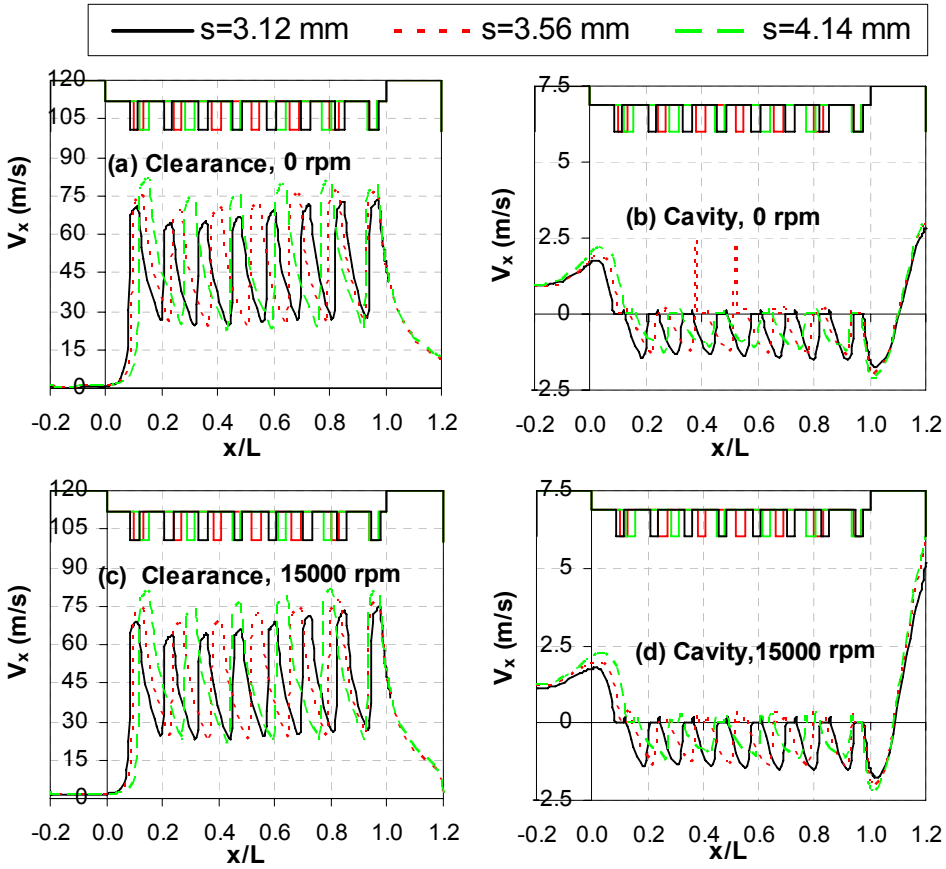

Fig. 125 V_x along a line passing through the middle of the clearance and cavity for different *s*, DP=34.5 kPa.

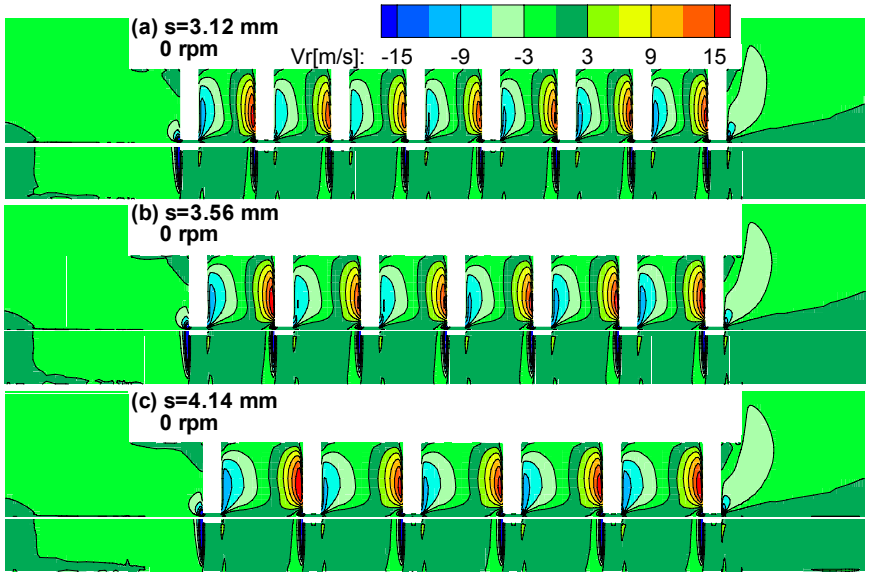

Fig. 126 V_r contours for different *s* at Ω=0 rpm and DP=34.5 kPa.

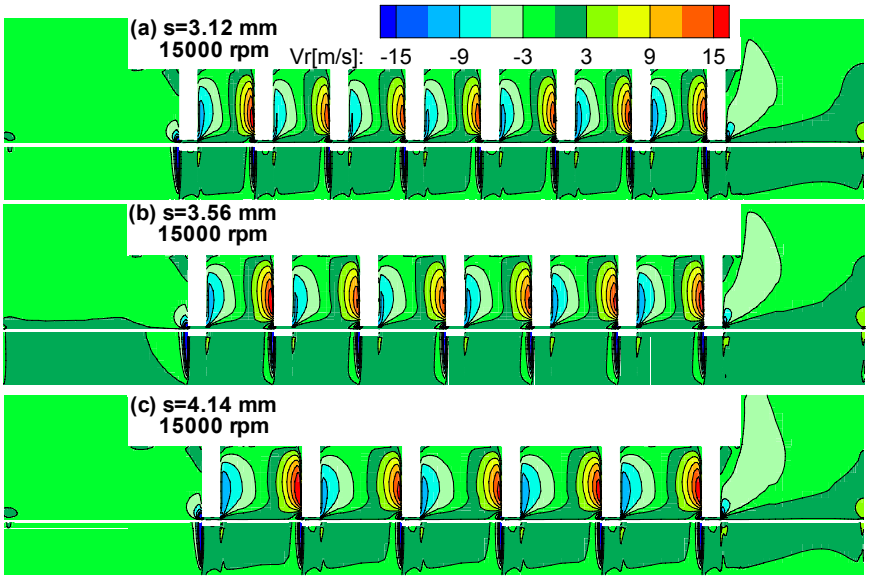

Fig. 127 V_r contours for different *s* at Ω=15000 rpm and DP=34.5 kPa.

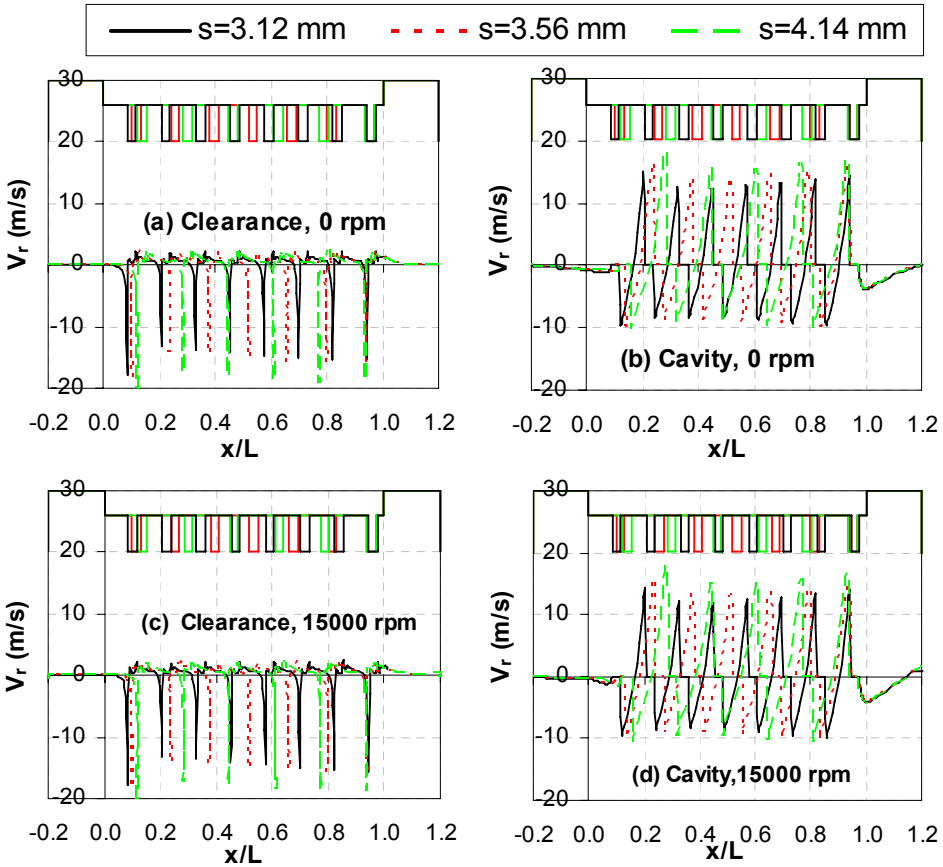

Fig. 128 V_r along a line passing through the middle of the clearance and cavity for different *s*, DP=34.5 kPa.

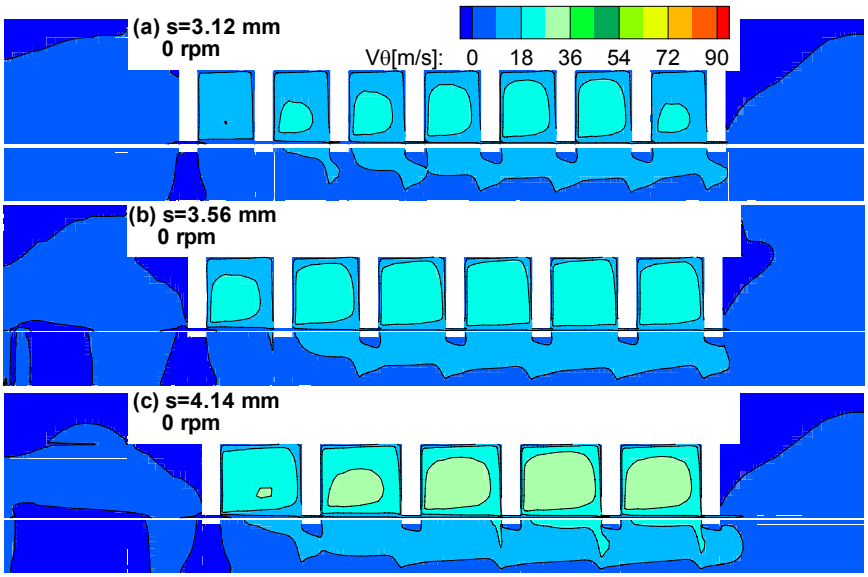

Fig. 129 V_θ contours for different *s* at Ω=0 rpm and DP=34.5 kPa.

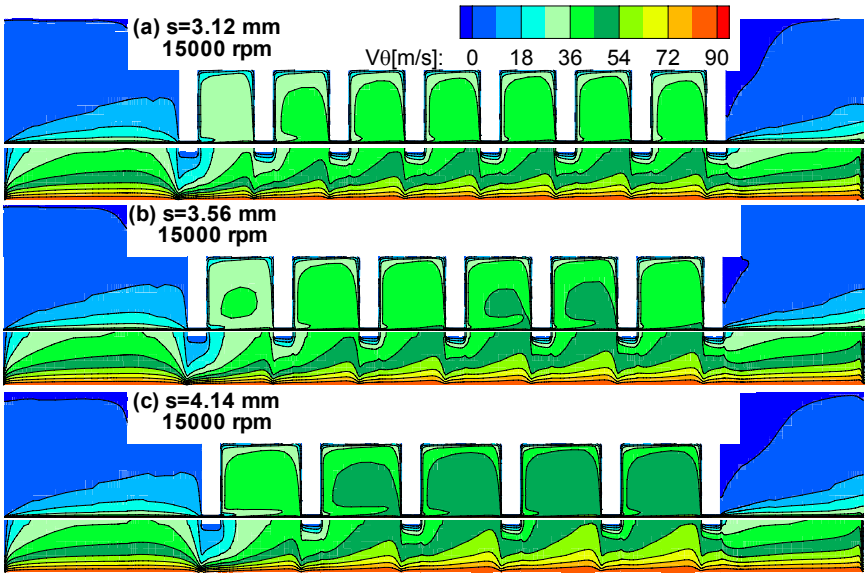

Fig. 130 V_θ contours for different *s* at Ω=15000 rpm and DP=34.5 kPa.

Figs. 129, 130 and 131 show that increasing *s* from 3.12 mm to 4.14 mm increases the circumferential velocity at 0 rpm from a maximum of 21.4 *m/s* to 33.1 *m/s*, and from 12.5 *m/s* to 19.3 *m/s*, inside the seal cavity and clearance, respectively. Due to the increase of V_θ in the seal

cavity, V_θ also increased in the seal clearance as a result of increasing s. Increasing the rotor speed from 0 to 15000 rpm produces a large increase in the circumferential velocity within the seal clearance and cavities. The maximum percent increase in the seal cavity was 60% and 98% for s=4.14, 3.12 mm, respectively. The maximum percent increase in the seal clearance was 224% and 343% for s=4.14, 3.12 mm, respectively.

Fig. 132 summarizes the net effect of changing the tooth pitch in a windback seal on the flow velocity within the seal cavity and clearance in terms of the velocity magnitude, V_m. Increasing the tooth pitch from 3.12 mm to 4.14 mm increases the velocity magnitude at 0 rpm in the seal cavity and clearance by 50% and 12%, respectively. By increasing the rotor speed to 15000 rpm, the percents increase in the seal cavity and clearance 23% and 15%, respectively.

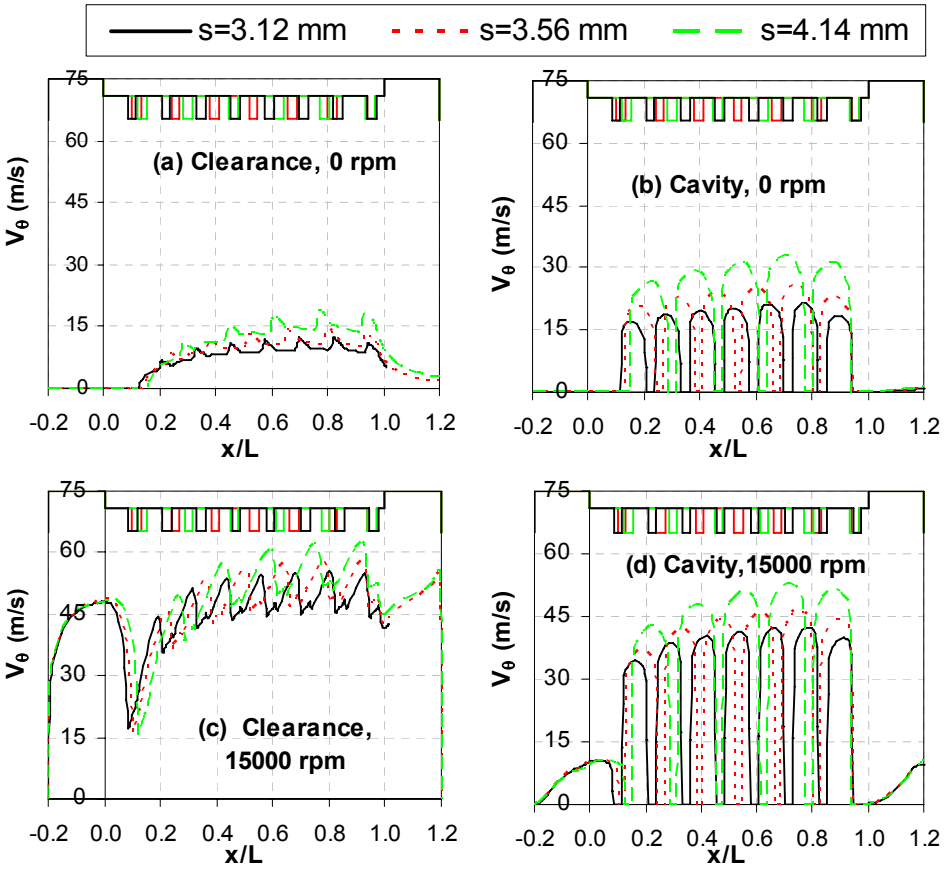

Fig. 131 V_θ along a line passing through the middle of the clearance and cavity for different s, DP=34.5 kPa.

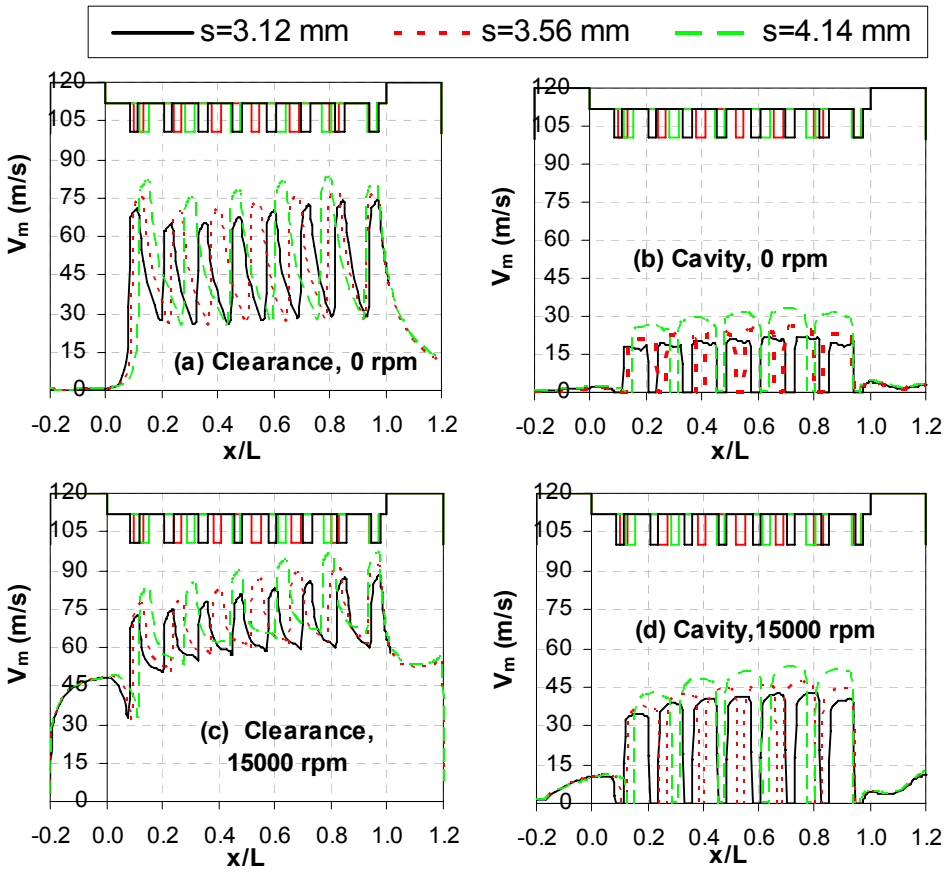

Fig. 132 V_m along a line passing through the middle of the clearance and cavity for different *s*, DP=34.5 kPa.

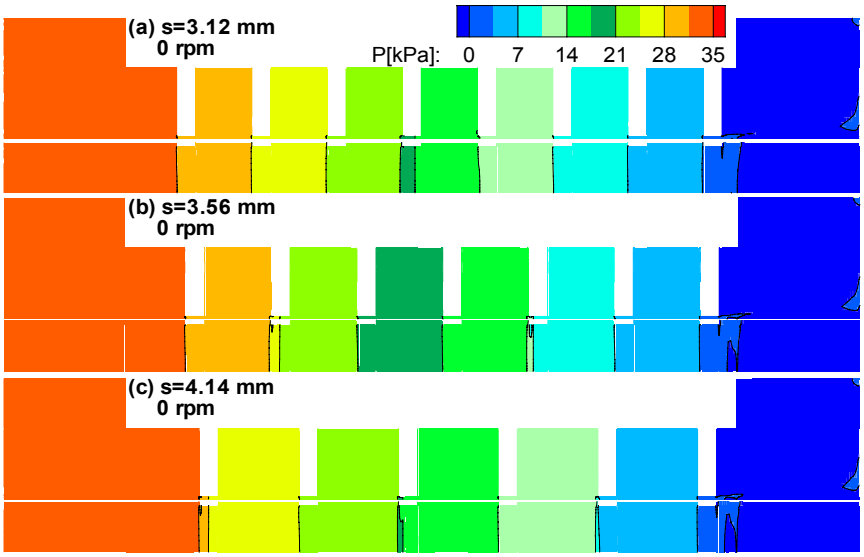

Fig. 133 P contours for different *s* at Ω=0 rpm and DP=34.5 kPa.

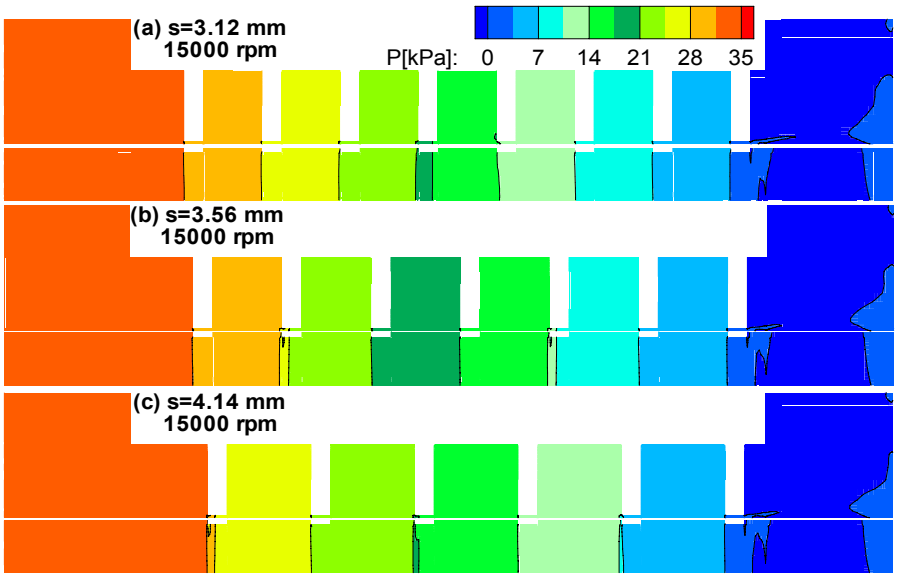

Fig. 134 P contours for different *s* at Ω=15000 rpm and DP=34.5 kPa.

The pressure contour plots in Figs. 133, 134 and 135 show larger pressure drops across each seal tooth with higher tooth pitches, due to the reduction of the effective number of teeth. The axial pressure distribution with higher pressure drops for high tooth pitches agrees with the axial velocity distribution in Figs. 123 to 125. Fig. 135 illustrates that even though the equivalent number of teeth vary, the axial pressure distribution within the seal clearance and cavities follows the same trend with the step pressure changes all following limiting maximum and minimum values. Negligible rpm effects on the axial static pressure distributions were observed for different tooth pitches.

Figs. 136 and 137 present the effect of differential pressure and rotor speeds on the percentile of leakage flowrate which goes under the tooth and through the cavity. The maximum leakage flowrate within the seal cavities at the 180° seal sectional view was considered when calculating the under tooth leakage. Fig. 136 shows that increasing *DP* with no rotation has a very small effect on the leakage flowrate percentile under the tooth and through the cavity which remains constant within 0.4%. The flowrate percentile through the seal cavity is 10.4%, 7.6% and 5.9% for tooth pitches of *s*=4.14, 3.56 and 3.12 mm, respectively at 0 rpm. Increasing the tooth pitch increases the leakage rate through the seal cavity and decreases the leakage flowrate under the seal tooth. This is a result of reducing the cavity channel length while increasing the tooth pitch which results in a decrease of the friction losses in the cavity channel, similar to flow

in pipes. Fig. 137 demonstrates the effect of rotor speed on the flowrate; increasing rotor speed will increase the flow percentile in the cavity and reduces it under the seal tooth. Increasing rotor speed from 0 to 15000 rpm changes the percent leakage in the seal cavity from 10.4% to 16.9% at *LP* and for *s*=4.14 mm. The other tooth pitch cases show the same percent increase in cavity flowrate with increasing rotor speed from 0 to15000 rpm and is about 6%. As seen previously, increasing the rotor speed increases the circumferential air velocity in the seal cavity resulting in a linear increase in the leakage flowrate.

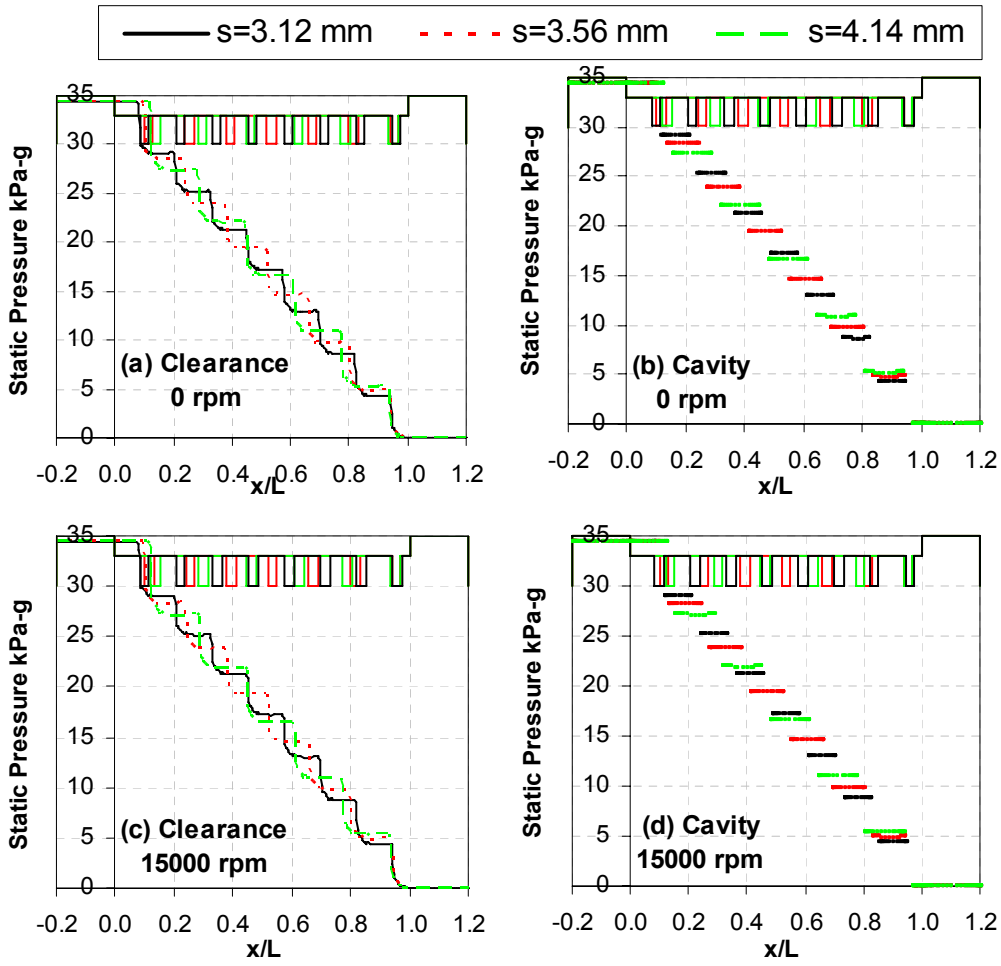

Fig. 135 P along a line passing through the middle of the clearance and cavity for different *s*.

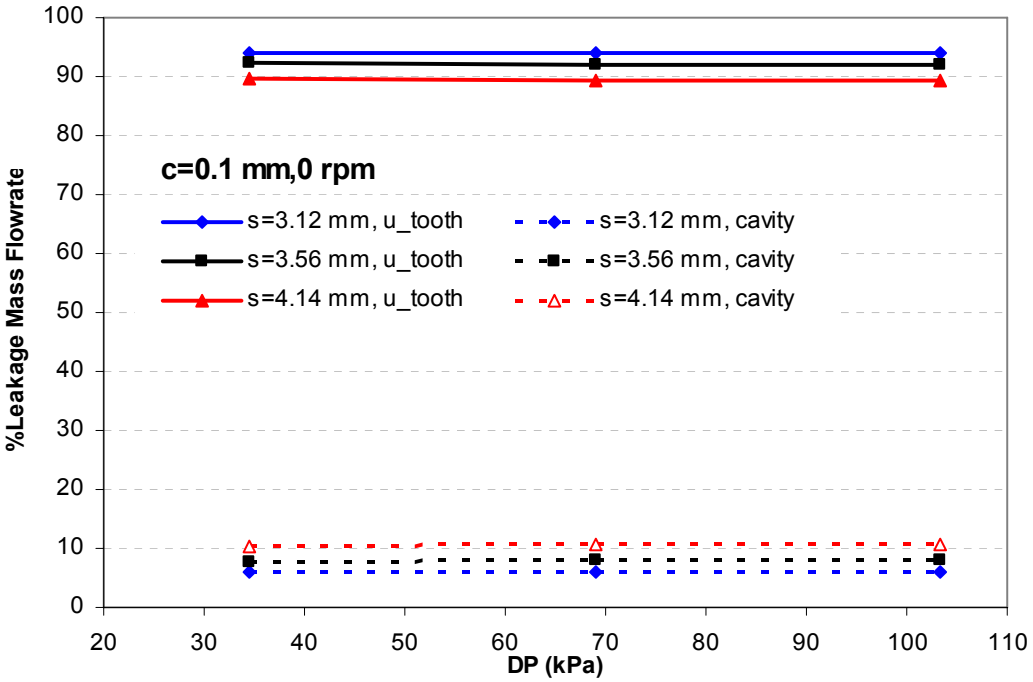

Fig. 136 Percent cavity and under tooth leakage mass flowrate versus DP for different tooth pitches at 0 rpm and c=0.1 mm.

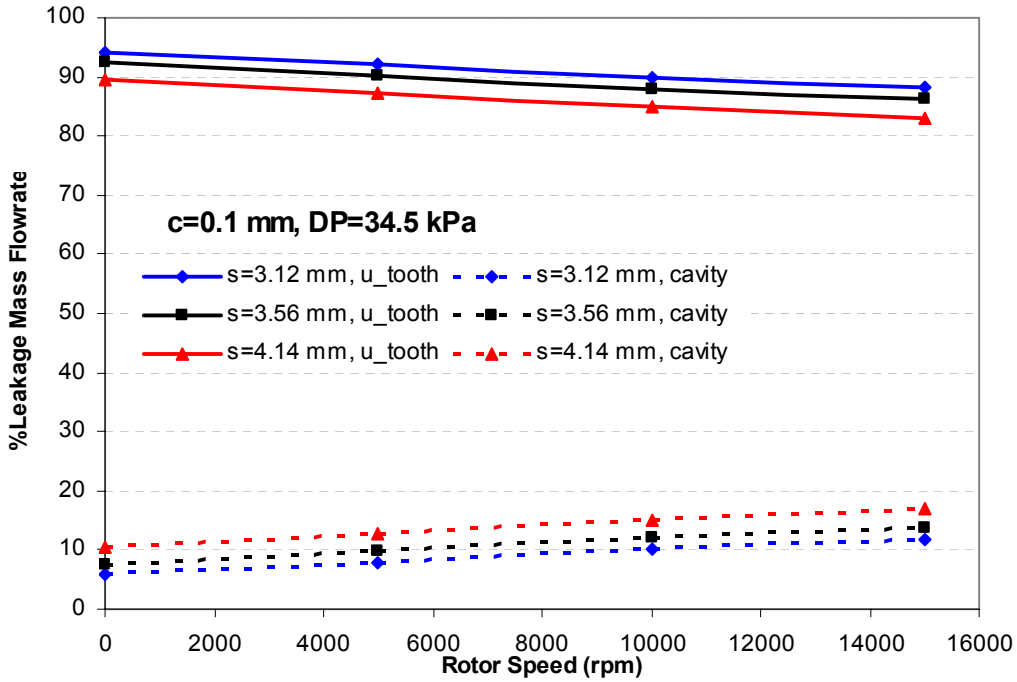

Fig. 137 Percent cavity and under tooth leakage mass flowrate versus rotor speed for different tooth pitches, c=0.1 mm and DP=34.5 kPa.

Tooth Number of Starts

The effects of changing the number of tooth starts for windback seals were studied numerically for three different tooth start configurations; zero-start (represented by the smooth seal geometry), one-start with tooth pitch s=3.56 mm and two-start with a tooth pitch s=7.12 mm. For the two-start case, the tooth starts were separated by 180°. The three seals have the same length (L= 25.4 mm), clearance (c=0.1 mm), tooth height (h=2.94 mm) and tooth thickness (t =0.7874 mm). The seals were numerically simulated for three differential pressures of 34.5, 68.9, and 103.4 *kPa*. Furthermore, for each *DP* the effect of rotor speed on leakage flowrates was studied for 0, 5000, 10000, and 15000 rpm. Both one-start and two-start seals were simulated using the κ-ε turbulent flow model with enhanced wall treatment. Therefore, for comparison purposes, the data representing the zero-start (smooth seal) were extracted from the turbulent flow model.

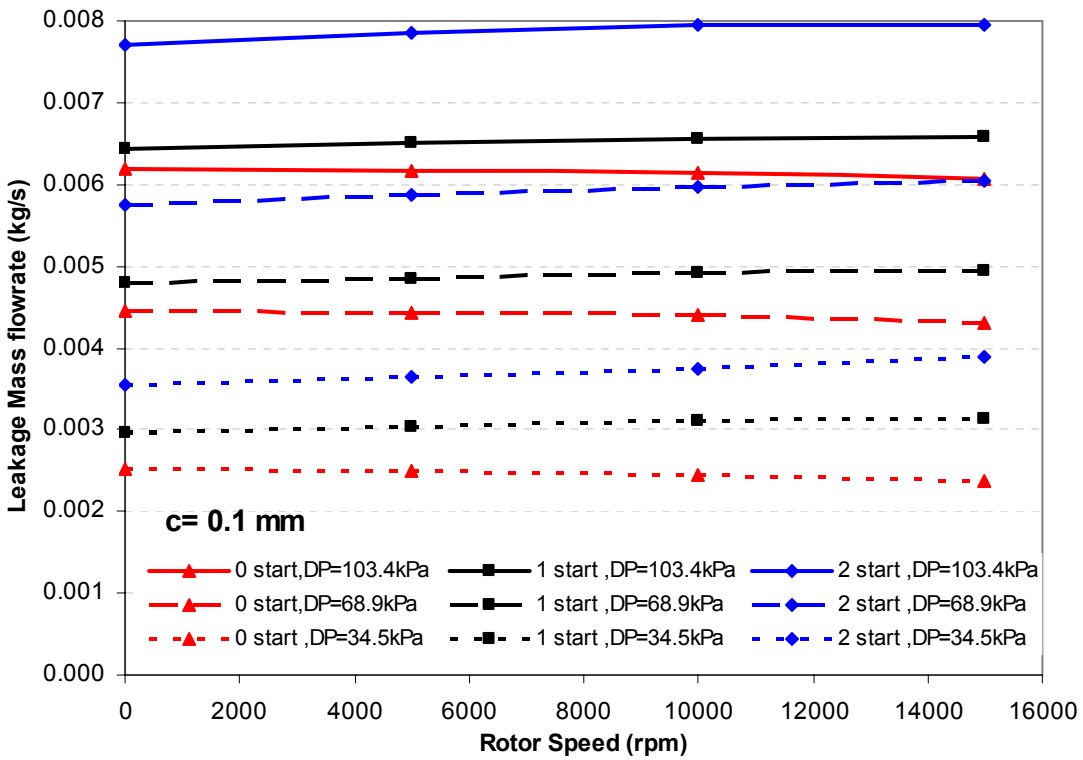

Fig. 138 Leakage mass flowrate versus rotor speed for different number of tooth starts and DPs.

Fig. 138 shows the effects of different tooth starts, *DP* and rotor speeds on leakage flowrates. The zero-start represents the smooth seal, the effects of increasing *DP* and rotor speeds have been previously discussed such that the leakage flowrate increases with increasing *DP* and decreases with increasing rotor speeds. In addition, the one-start seal is the regular windback seal discussed in previous sections. The three seal configurations, zero, one and two starts were plotted together to see if there is a relationship of the leakage flowrate to various geometrical parameters. It is clear that the two-start seal follows the general trends of the one-start, regarding how the leakage flowrates are influenced by changing *DP* and rotor speed. Increasing the rotor speed and/or *DP* increases the leakage flowrate. Increasing the rotor speed decreases the leakage flowrate for the zero start seal. Fig. 139 shows that for the zero-start seal, the solid line representing the rpm affect is below the dashed line (no-rotation). This is opposite to the trends seen for the one and two start seals. However, the leakage flowrate increase is almost twice as large for the two-start seal compared to the one-start seal with increasing the shaft speed from 0 to 15000 rpm. Since, the two-start seal has two cavity channels, each with a length equal to half the cavity length in the one-start seal, given that the rotor speed affects mainly the circumferential flow velocity inside the seal cavity, it follows that the shaft speed affects the two-start seal more. Fig. 140 shows this clearly, through the percent of leakage flowrate in the cavity and under the tooth. For the two-start seal, both cavity leakages were added together in order to compare with the one-start seal. Additionally, the two-start case can be compared to the high tooth pitch case in which the leakage through the seal cavity was higher than the lower tooth pitch seal cases. Fig. 140a shows that at no-rotation the percentile leakage flowrate in the seal cavity and under the tooth is almost constant and varies less than 1% for different *DP*. Fig. 140b shows that the leakage flowrate percentiles in the cavity and under tooth increases and decreases in a linear relationship, respectively, with increasing rotor speeds.

The contour plots showing the three velocity components and static pressure distributions for the three different number of tooth starts are presented in Figs. 141 to 154. Since the zero and one start seals geometry have been previously discussed, we will summarize the effects of the two-start seal geometry on the velocity and pressure axial distributions considering Figs. 141 to 154.

Figs. 141, 142 and 143 show that the two-start seal has similar axial velocity distribution compared to the one-start seal, except near the inlet and exit of seal, where there is a slight difference in the axial velocity distribution, due to the angle separating the two-start seal

resulting in a small geometrical variation from the one-start seal. There is no rpm effect on the axial velocity.

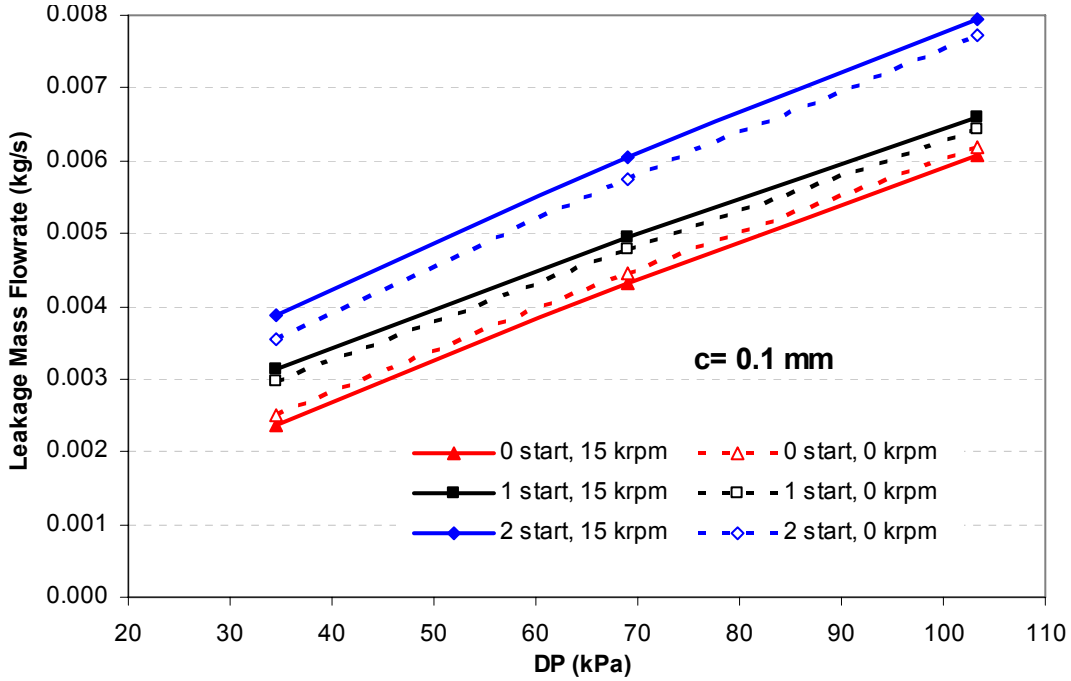

Fig. 139 Leakage mass flowrate versus DP for different number of tooth starts and rotor speeds.

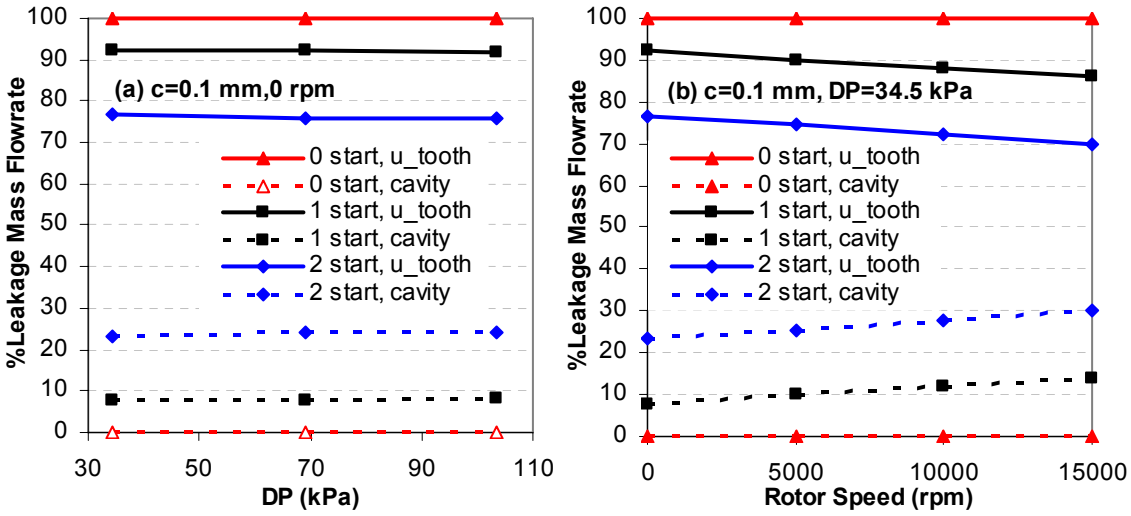

Fig. 140 Percent cavity and under tooth leakage mass flowrate for different number of tooth starts versus (a) DP at 0 rpm and (b) rotor speed at DP=34.5 kPa.

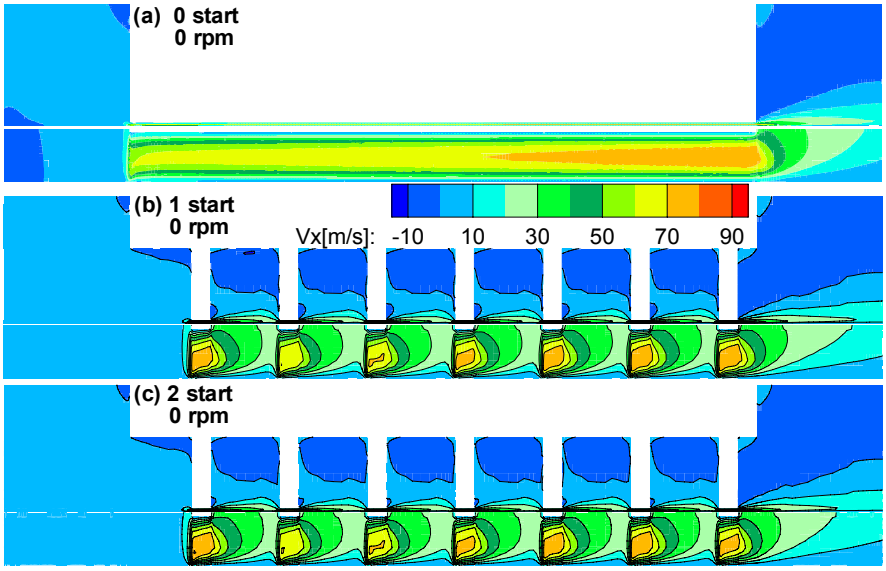

Fig. 141 V_x contours for different number of starts at Ω=0 rpm and DP=34.5 kPa.

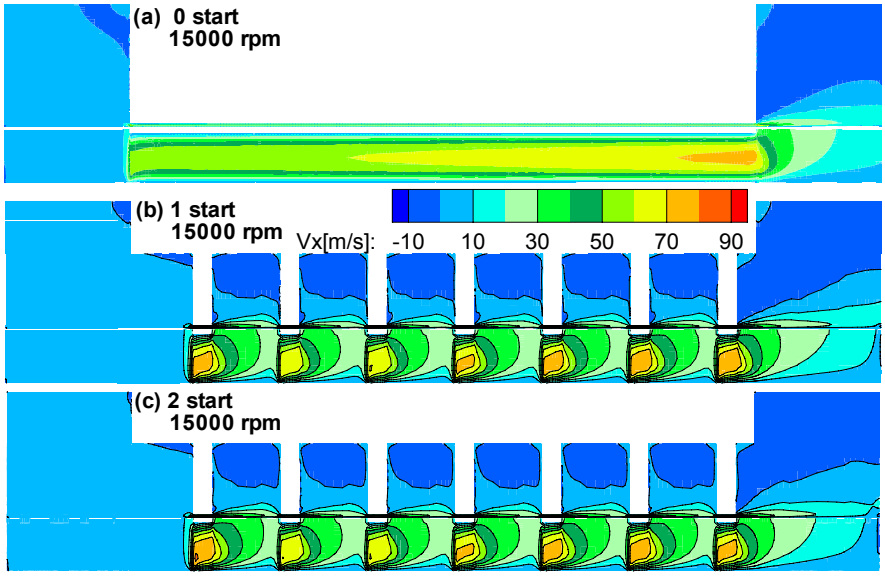

Fig. 142 V_x contours for different number of starts at Ω=15000 rpm and DP=34.5 kPa.

Figs. 144 to 147 show that the radial velocity distributions for the one and two starts are almost identical with no rpm effect.

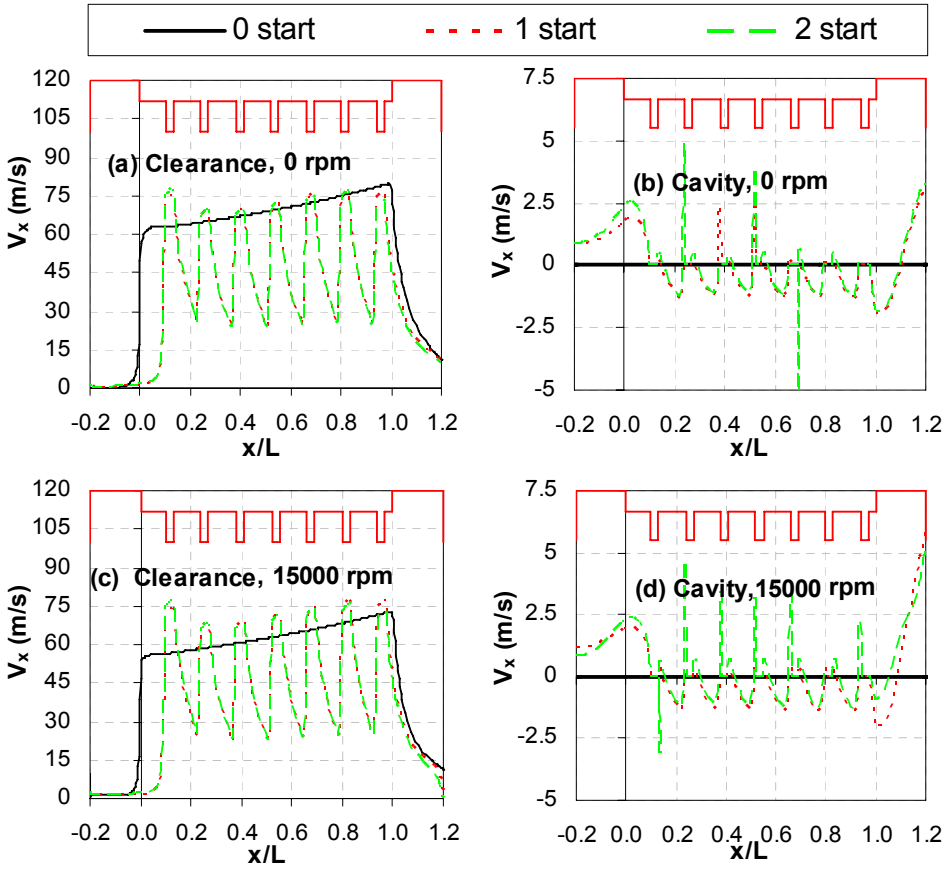

Fig. 143 V_x along a line passing through the middle of the clearance and cavity for different number of starts, DP=34.5 kPa.

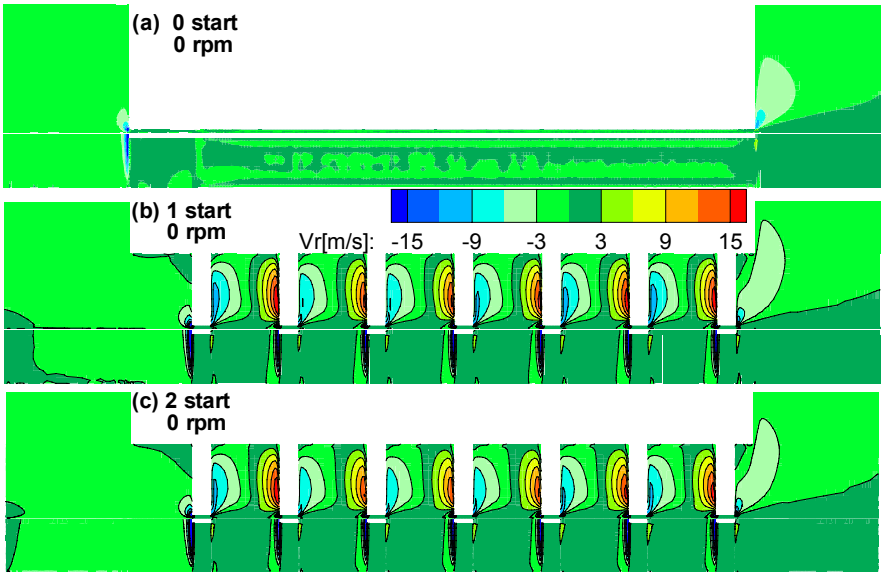

Fig. 144 V_r contours for different number of starts at Ω=0 rpm and DP=34.5 kPa.

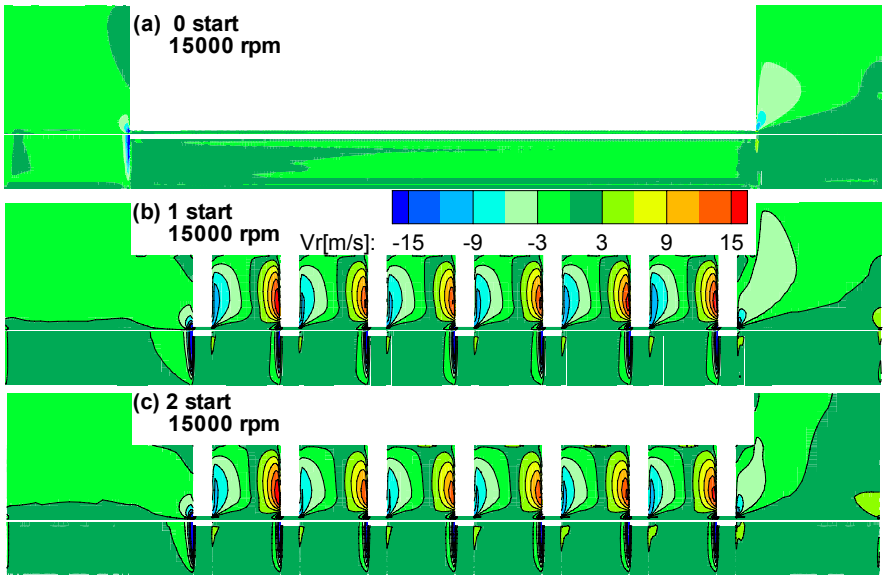

Fig. 145 V_r contours for different number of starts at Ω=15000 rpm and DP=34.5 kPa.

The major effect of the two-start geometry seal is shown in Figs. 147 to 149, by the increase in the circumferential velocity component, even at the no rotation condition. Since both one and two start seals have similar geometrical parameters except the channel length, where for each tooth start in the two-start seal the cavity length is cut in half compared with the one-start seal. Higher pressure gradient along these shorter channels is expected resulting in much higher circumferential velocity inside the seal cavity. As a result of this, the circumferential velocity within the seal clearance is also higher than the one-start seal. Figs. 147 to 149 show that at 0 rpm and *DP* of 34.5 *kPa*, V_θ in the cavity for the one and two starts seals reach a maximum of 27-36 *m/s* and 45-54 *m/s*, respectively. Likewise, the maximum range of V_θ in the seal clearance for the one and the two starts seal is 9-18 *m/s* and 27-36 *m/s*, respectively. Increasing the rotor speed from 0 to 15000 rpm increases the maximum circumferential velocity in the seal cavities ranges from 26 to 47 *m/s* and from 47 to 63 *m/s* for the one and two starts seals, respectively, indicating that the shaft speed has more influence on flows with no or small circumferential velocity. Increasing the rotor speed from 0 to 15000 rpm increases V_θ in the seal cavity by 81% and 34% for one and two start seals, respectively. The low viscosity of air and hence low shear rate and air drag, results in a limited maximum influence of rotor speed throughout the cavity depth. The same applies within the seal clearance where increasing the rotor speed from 0 to

15000 rpm increases V_θ from 15 to 57.7 *m/s* and from 27.4 to 66 *m/s* for the one and two starts, respectively. In term of percentages, V_θ increases by a maximum of 285% for the one-start seal compared to 141% for the two-start seal when increasing rotor speed from 0 to 15000 rpm within the seal clearance. Hence, rotor speed increases V_θ in the one-start seal by almost twice the percent increase in the two-start seal. Fig. 150 shows that the velocity magnitude for the two-start seal is higher than that of the one-start seal. This is mainly due to the increase in the circumferential velocity component.

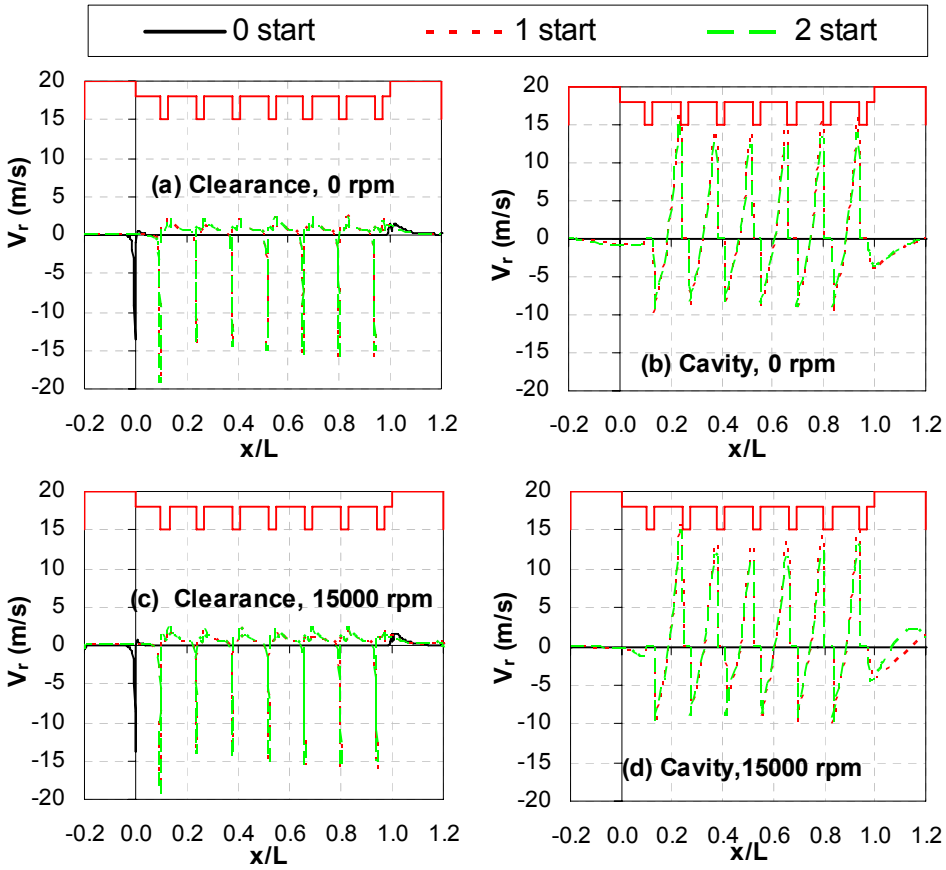

Fig. 146 V_r along a line passing through the middle of the clearance and cavity for different number of starts, DP=34.5 kPa.

Figs 151 to 153 show the axial static pressure distribution for different seal start geometries. The two-start seal has a higher pressure gradient in the cavity channel if each

channel is considered separately compared to the one start seal. But when considering the whole seal length, both the one and two-start seals geometry have the same axial static pressure distribution following the same trend with the step pressure changes both following the same envelope with a limiting maximum and minimum values. There is no rpm effect, and only a slight difference due to geometry at the seal inlet and exit, due to 180° angle separating the tooth start in the two-start seal.

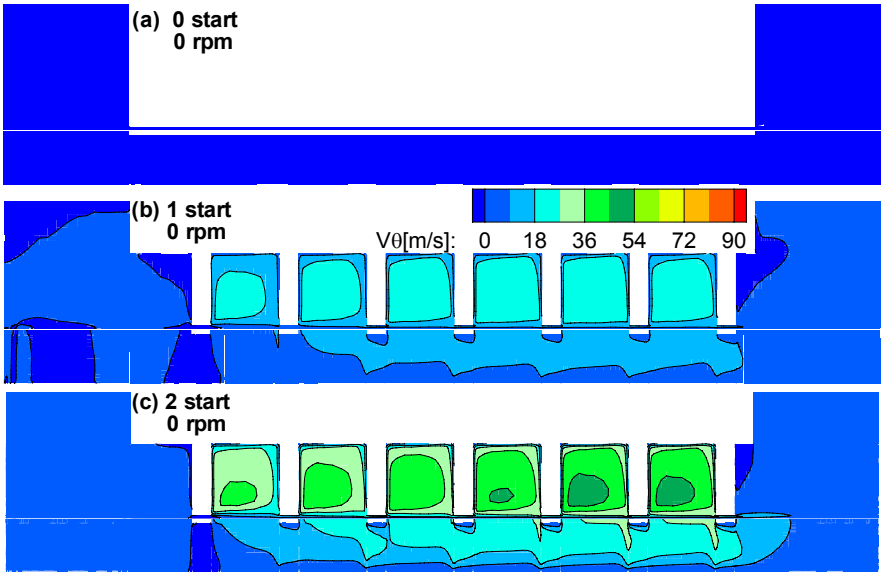

Fig. 147 V_θ contours for different number of starts at Ω=0 rpm and DP=34.5 kPa.

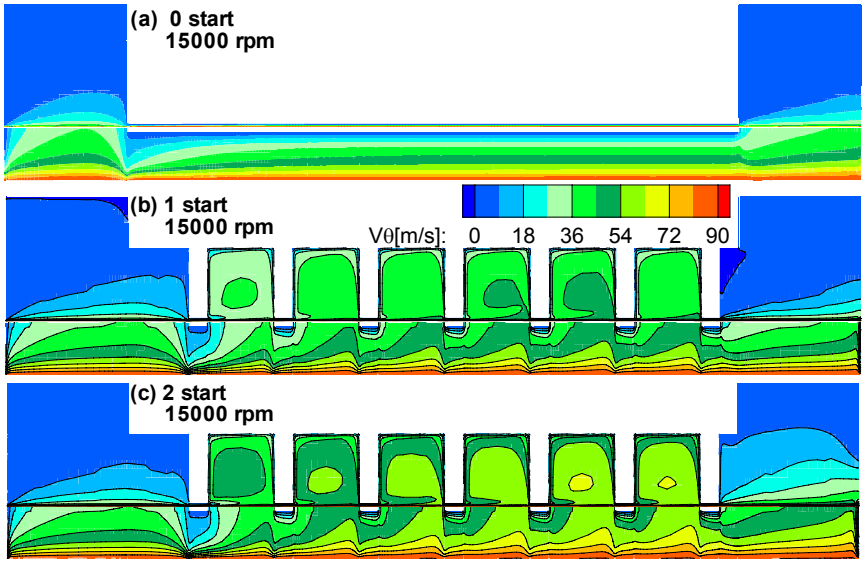

Fig. 148 V_θ contours for different number of starts at Ω=15000 rpm and DP=34.5 kPa.

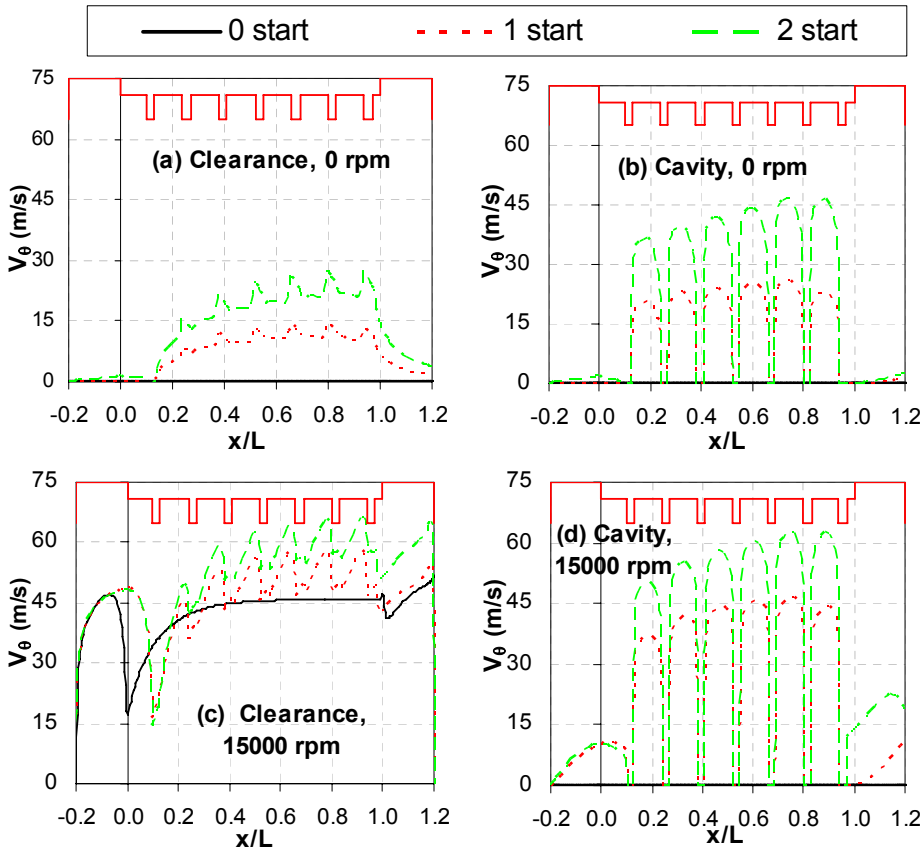

Fig. 149 V_θ along a line passing through the middle of the clearance and cavity for different number of starts, DP=34.5 kPa.

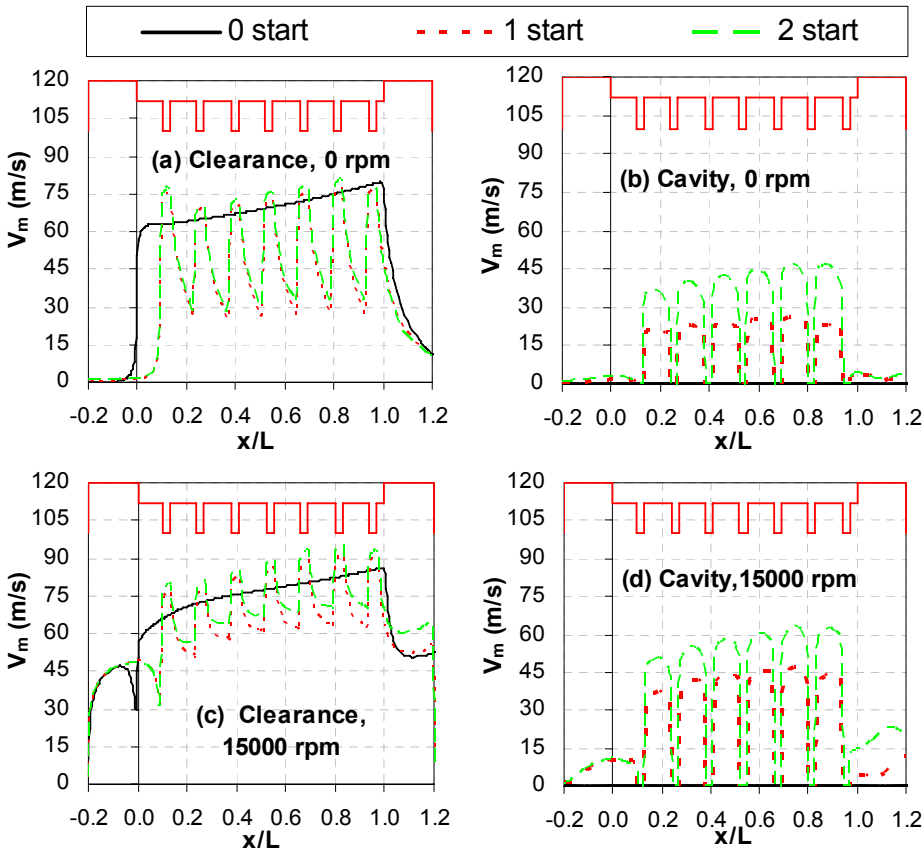

Fig. 150 V_m along a line passing through the middle of the clearance and cavity for different number of starts, DP=34.5 kPa.

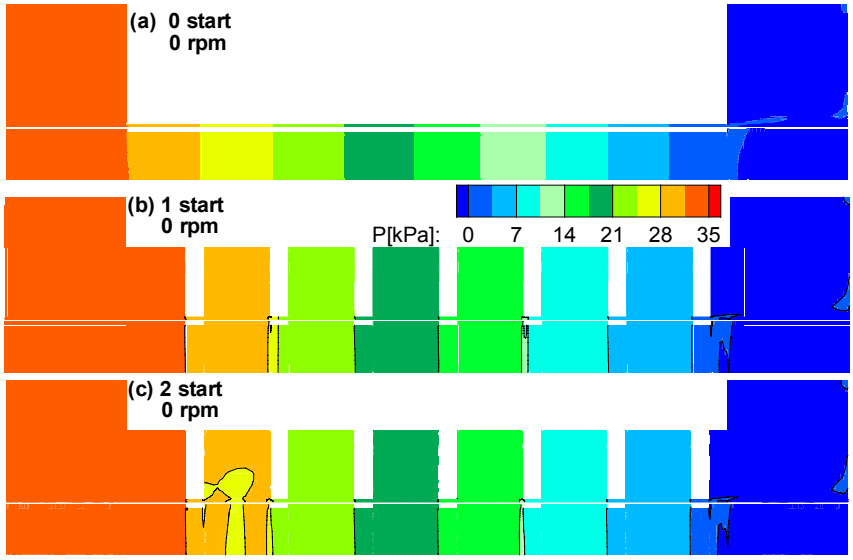

Fig. 151 P contours for different number of starts at Ω=0 rpm and DP=34.5 kPa.

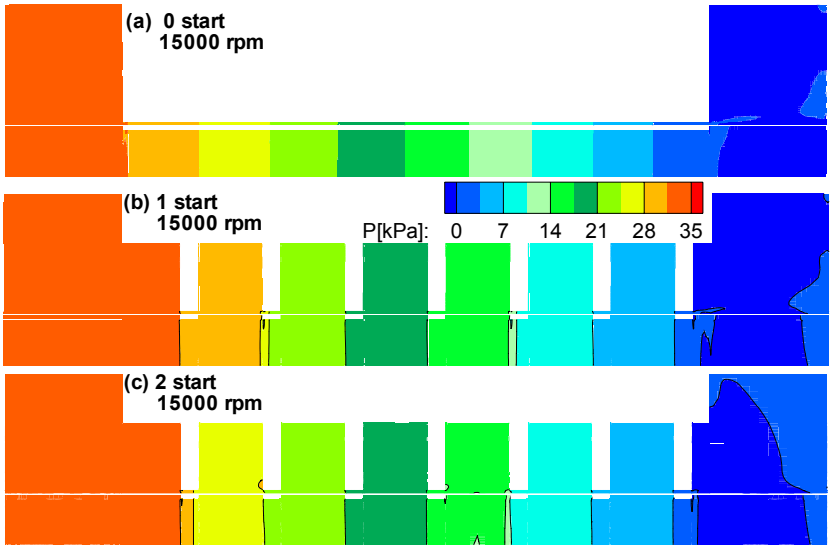

Fig. 152 P contours for different number of starts at Ω=15000 rpm and DP=34.5 kPa.

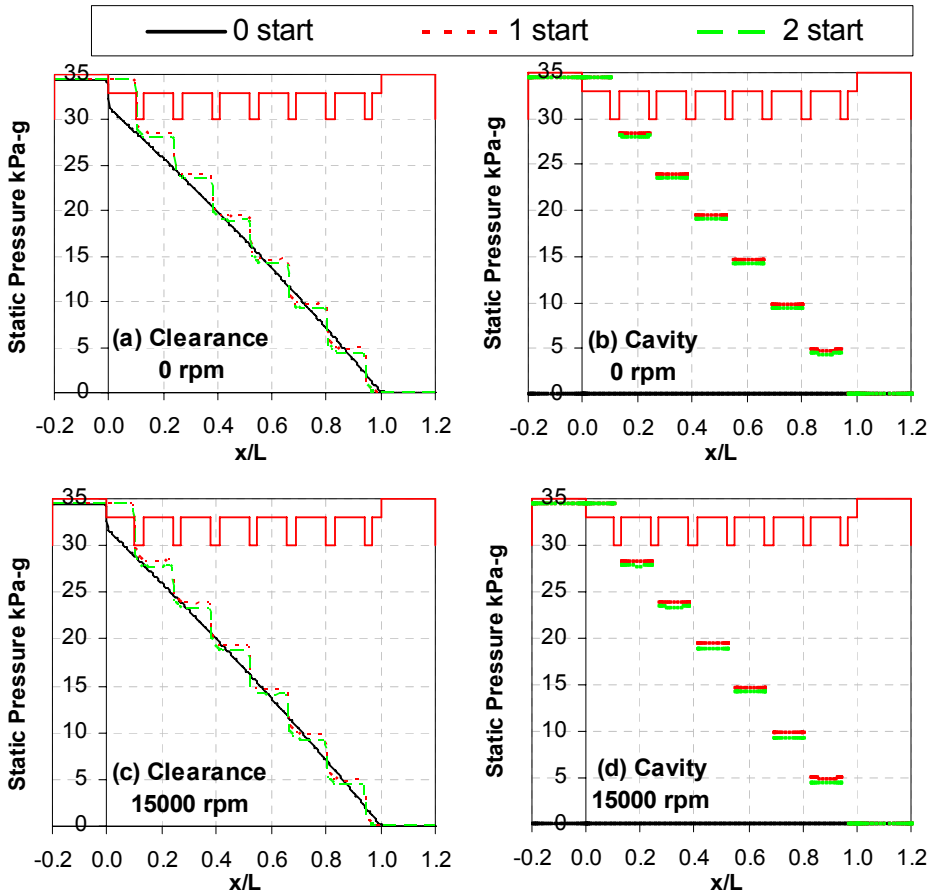

Fig. 153 P along a line passing through the middle of the clearance and cavity for different number of starts.

Wall Shear Stresses

In previous sections we studied the effects of variable geometrical parameters (clearance, tooth pitch, and cavity depth) on leakage flowrates and how that changes the distribution of flow velocity components (V_r, V_x, V_θ). Changing the geometrical parameter of a windback seal will not only change the velocity distribution, but also the shear stresses near the seal walls. The geometric seal parameters and operating conditions (*DP*, rotor speed) affect both the velocity and the shear stresses in the same way.

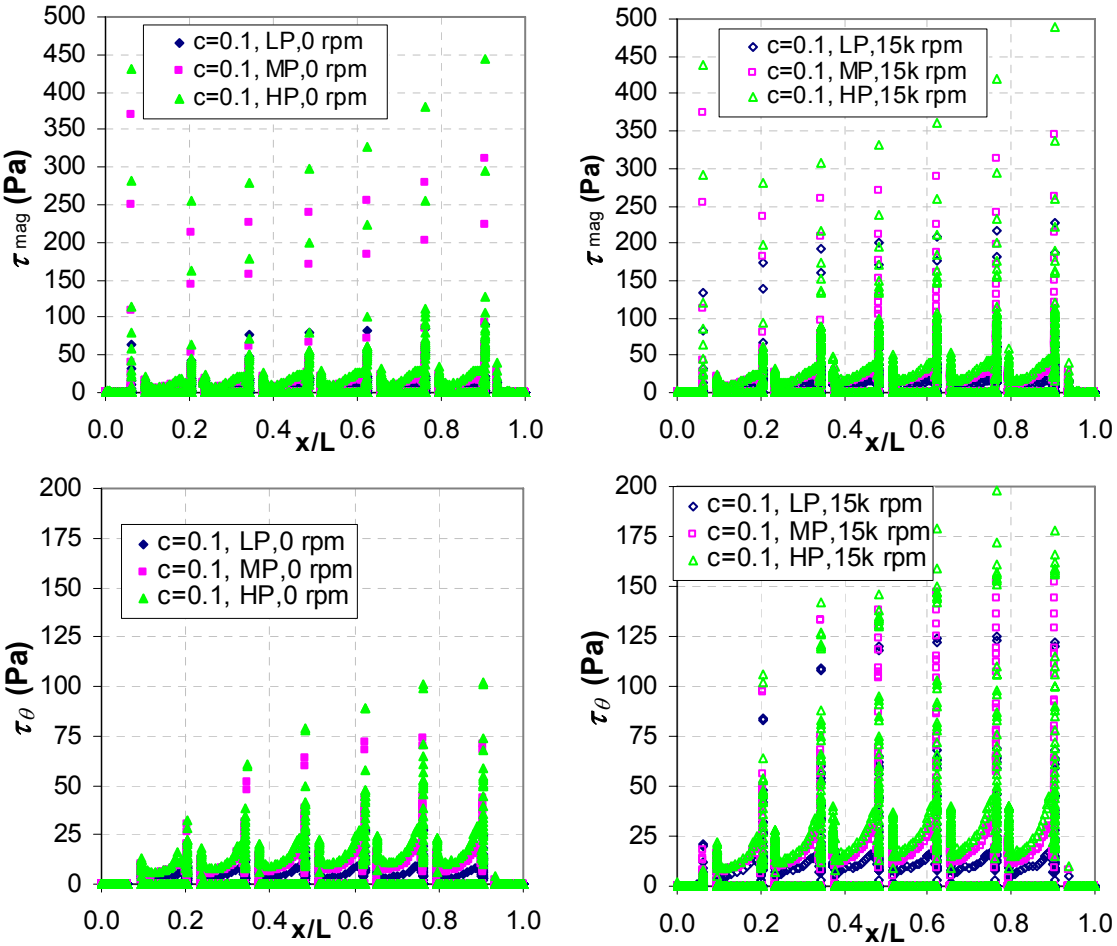

Fig. 154 Wall shear stress magnitude and τ_θ for different DP and rotor speeds in the seal cavities at c=0.1 mm, 180° seal sectional view.

The wall shear stresses were calculated for the seal cavities at the 180° seal sectional view. Fig. 154 shows the shear stresses magnitude, τ_{mag}, and the wall shear stress in the circumferential direction, τ_θ, for different *DP*'s and rotor speeds. As expected, increasing the differential pressure across the seal and /or rotor speed increases both τ_{mag} and τ_θ. Since, increasing *DP* and/or the shaft speed increases the circumferential velocity in the seal cavities. Fig. 155 shows the effect of changing the seal clearance on the wall shear stresses in the circumferential direction for all seal cavities at 15000 rpm and for different *DP*'s. Increasing the seal clearance reduces τ_θ on the seal cavity walls in region I (see Fig. 156) for all *DP*'s, due to the decrease in V_θ with increasing *c*. On the other hand, increasing the seal clearance increases the radial velocity distribution in region II (see Fig. 156) due to the high axial jet flow. Therefore, τ_θ increases with increasing *c* in region II.

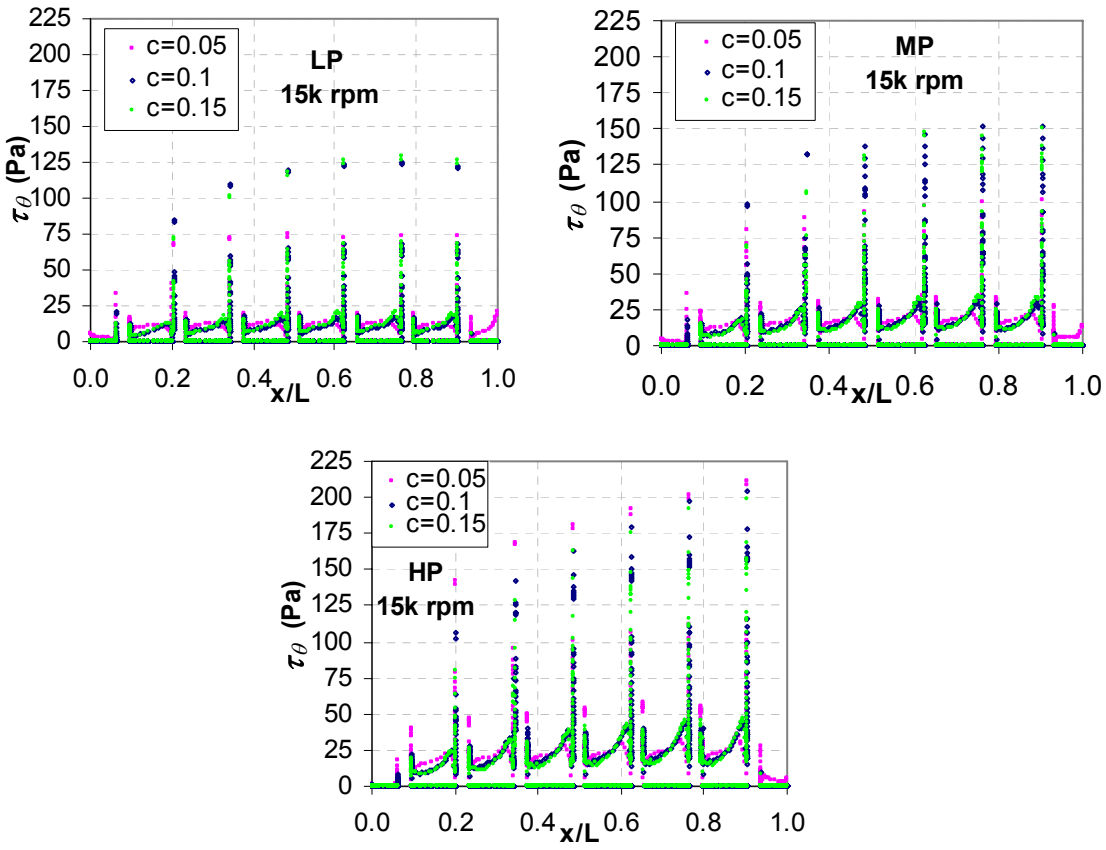

Fig. 155 τ_θ for different DP and rotor speeds in the seal cavities, at c=0.1 mm, 180° seal sectional view.

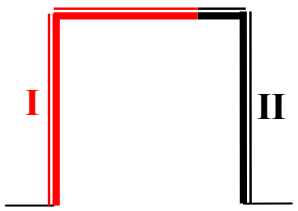

Fig. 156 Cavity wall regions.

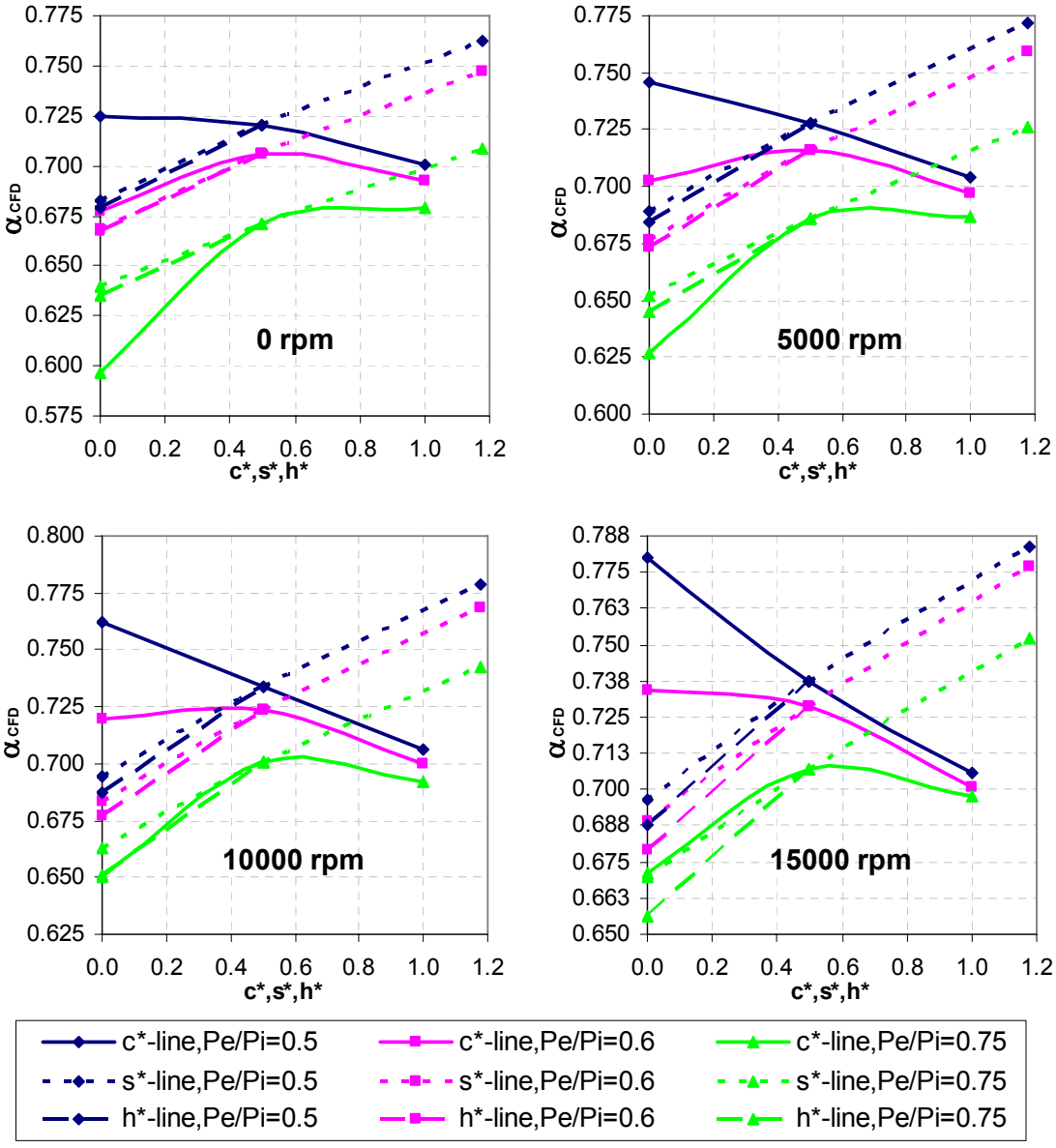

Fig. 157 CFD flow coefficient design graph for windback seals.

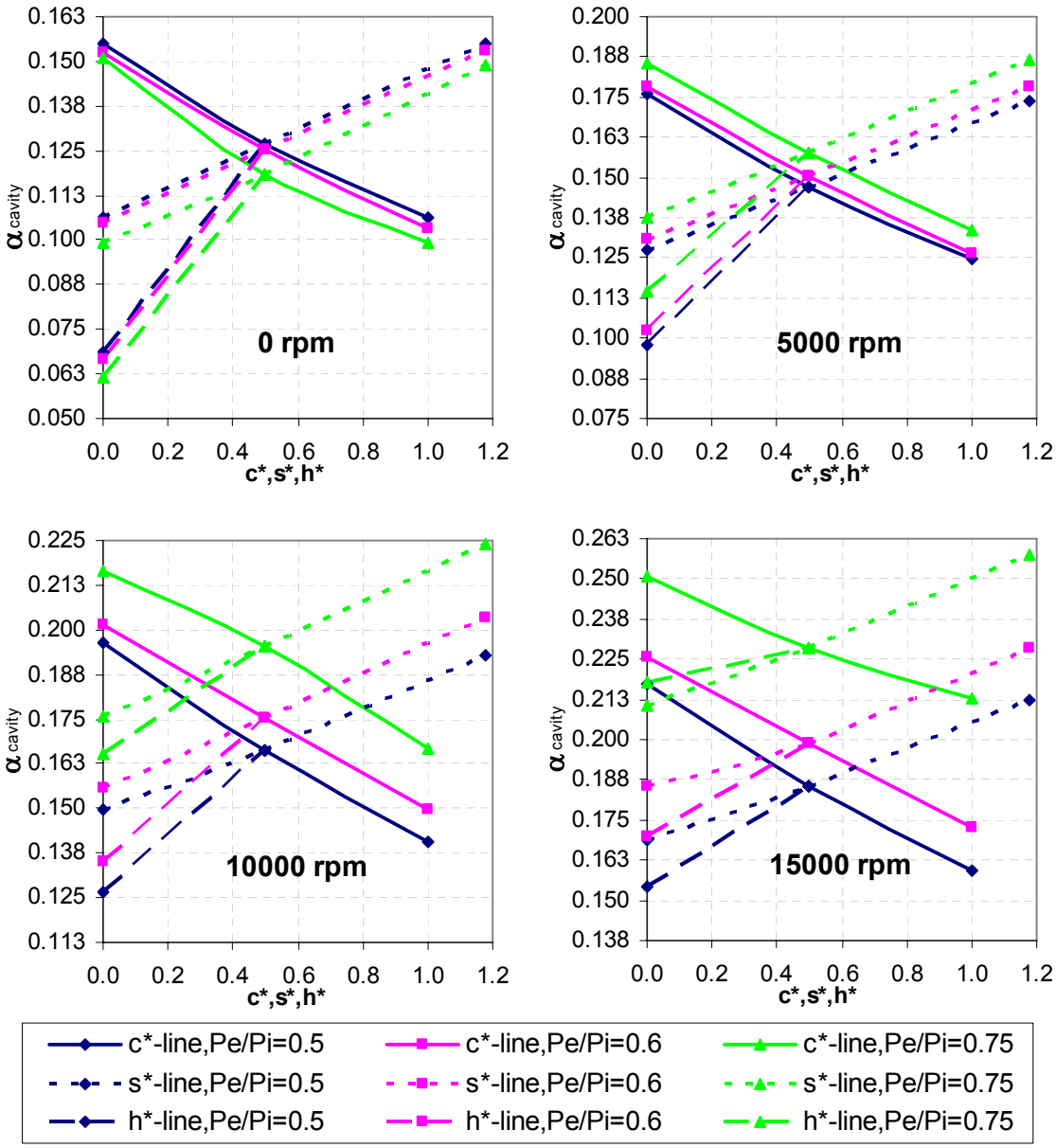

Fig. 158 CFD flow coefficient design graph for windback seals cavity.

Windback Seal Design

The effectiveness of a windback seal in preventing a contamination depends on the flow velocity distribution. Boyman et al. [23] show that increasing the buffering fluid axial velocity for a straight through labyrinth seal reduces the transport of oil-vapour by diffusion. In addition, they found that the back flow of oil droplets in the opposite direction of the buffering fluid

results from the axial velocity fluctuation under the seal teeth, due to the complex flow in the seal cavities. Labyrinth seal operation principle is to change the available static pressure head into kinetic energy across a constriction. The flow kinetic energy in the next cavity in a real seal will be (1) dissipated by turbulence viscosity interaction into heat (2) recovered as a static pressure (3) carried over to the next cavity. The recovery of the static pressure in labyrinth seal cavities can be one source of the axial velocity fluctuation under the seal teeth. For windback seals, the CFD simulations show no static pressure recovery, due to the existence of the helical cavity. Therefore, the windback seal, unlike the labyrinth seal, will have less back flow problem (oil contamination). This can be achieved by proper selection of the seal geometrical parameters, which will result in the required maximum axial velocity under the tooth and the maximum circumferential velocity in the seal cavity to reduce back flow.

The numerical analysis for the windback seal presented in the previous sections for different geometrical parameters was used to develop 2D design curves for windback seals. The effects of windback seal clearance, tooth pitch, and cavity depth on the total and cavity flow coefficients are shown in Figs.157 and 158 for different rotor speeds and pressure ratios.

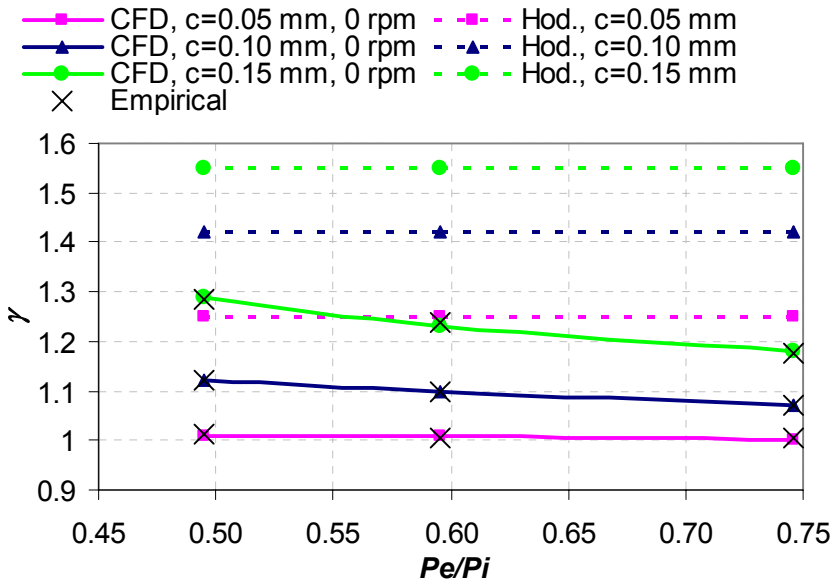

Fig. 159 Carry over coefficient comparison.

To study the effects of different seal geometrical parameters on the seal total and cavity flow coefficients and hence V_x and V_θ, the seal clearance, tooth pitch, and cavity depth were normalized and plotted on the same axis in Figs. 157 and 158 according to the following equations,

$$c^* = (c - 0.05)/(0.15 - 0.05) \tag{28}$$

$$s^* = (s - 3.124)/(2(3.56 - 3.124)) \tag{29}$$

$$h^* = (h - 1.473)/(2(2.946 - 1.473)) \tag{30}$$

where, c, s, h are in mm.

The carry-over coefficient was calculated using CFD analysis based on the values presented in Table 9 page 75. A generalized carry-over coefficient for windback seals for different *c/s* and P_e/P_i ratios was established by curve fitting an empirical formula through the data, the result is:

$$\begin{aligned}\gamma_{CFD} = {} & 1.101 - 0.651(P_e/P_i) + 6.277(c/s) + 108.651(c/s)^2 + 0.678(P_e/P_i)^2 - \ldots \\ & 12.766(c/s)(P_e/P_i)^2 + 27.099(c/s)^2(P_e/P_i)^2\end{aligned} \tag{31}$$

Fig. 159 compares the carry-over coefficients calculated directly from the CFD results and Eqs. 3 and 31. The difference between the carry-over coefficient calculated using the CFD and the empirical formula is less than 1%. Increasing the clearance to pitch ratio and decreasing the pressure ratio result in the empirical carry over coefficient converging to the value of Hodkinson carry-over coefficient. For example both $\gamma_{empirical}$ and $\gamma_{Hodkinson}$ are equal to 1.55 at *c/s*=0.0422, and P_e/P_i = 0.015. Therefore, the windback seal total flow coefficient, α_{CFD}, is calculated using Egli's Eq. (1) using the carry-over coefficient γ_{CFD} in Eq. (31),

$$\alpha_{CFD} = \dot{m}_{total}/(A\psi\gamma_{CFD}\sqrt{\rho_i P_i}) \tag{32}$$

where, $\psi = \sqrt{\dfrac{1-(P_e/P_i)^2}{n - \ln(P_e/P_i)}}$,and $A = \pi Dc$

The air flow in the windback seal cavity is similar in nature to the air flow in ducts or pipes. Therefore, the flow coefficient α_{cavity} was defined in a similar way to the flow coefficient in pipes according to,

$$\alpha_{cavity} = \dot{m}_{cavity}/(A_{cavity}\sqrt{\rho_i DP}) \tag{33}$$

where, $A_{cavity} = h(s - t)$

The effects of windback seal tooth pitch and cavity depth was studied numerically for a radial clearance of 0.1 mm. For the same pressure ratios (P_e/P_i) and rotor speeds, the three lines (clearance line, pitch line and cavity depth line) shown in Figs. 157 and 158 share the same normalized point, $c^*=h^*=s^*=0.5$. This point represents a reference windback seal, where changing the geometrical parameters under study result in changing the total and cavity flow coefficients starting from that point. The tooth thickness was constant and equal to 0.787 mm, for all numerical simulations.

The flow coefficient of a windback seal can be determined from Figs. 157 and 158 for different pressure ratios and rotor speeds, for any geometrical parameters which are within the range of seal clearance, tooth pitch, and cavity depth studied. The procedure of determining the total and cavity leakage flowrates of a windback seal is described through solving the following example.

Example:

Air enters a windback seal at 202.65 *kPa* (*DP* ≅ 15 *psi*) and 300° *K* and exits to atmospheric conditions. The windback seal is installed on a shaft with a diameter of 116.8 mm operating at 15000 rpm, the seal has the following geometrical parameters: *L*=25.4 mm, *c*=0.08 mm, *s*=3.39 mm, *t* = 0.787 mm, and *h*=2.06 mm.

(a) Find the leakage flowrate?

(b) How much leaks through the seal cavity and under the tooth?

(c) What is the maximum average circumferential velocity in the seal cavity?

(d) What is the maximum average axial velocity under the tooth?

Solution steps:

The solution steps for finding α_{CFD} and α_{cavity} are graphical and are illustrated in Figs. 160 and 161, respectively.

I- Calculate the normalized clearance, pitch and cavity depth and pressure ratio.

Using Eqs.(28-30)

$c^*=0.30$

$s^*=0.30$

$h^*=0.2$

$P_e/P_i = 0.5$

II- For calculating the total leakage flow coefficient α_{CFD}, choose the corresponding part in Fig. 157 representing the desired shaft speed, 15000 rpm in this case, and identify the lines (clearance, pitch, and cavity depth) corresponding to the calculated pressure ratio, for this example P_e/P_i =0.5 lines are selected, then mark on the clearance, pitch, and cavity depth lines the corresponding points from step one (see Fig. 160 step II). If different rpm and/or pressure ratio lines are needed, an interpolation between the corresponding values on Fig. 157 can be used.

III- On the clearance line, starting with the marked point draw a line or a curve parallel to the pitch line in the direction of the point marked on the pitch line (see Fig. 160 step III). Similarly, draw a line or a curve parallel to the clearance line starting from the marked point on

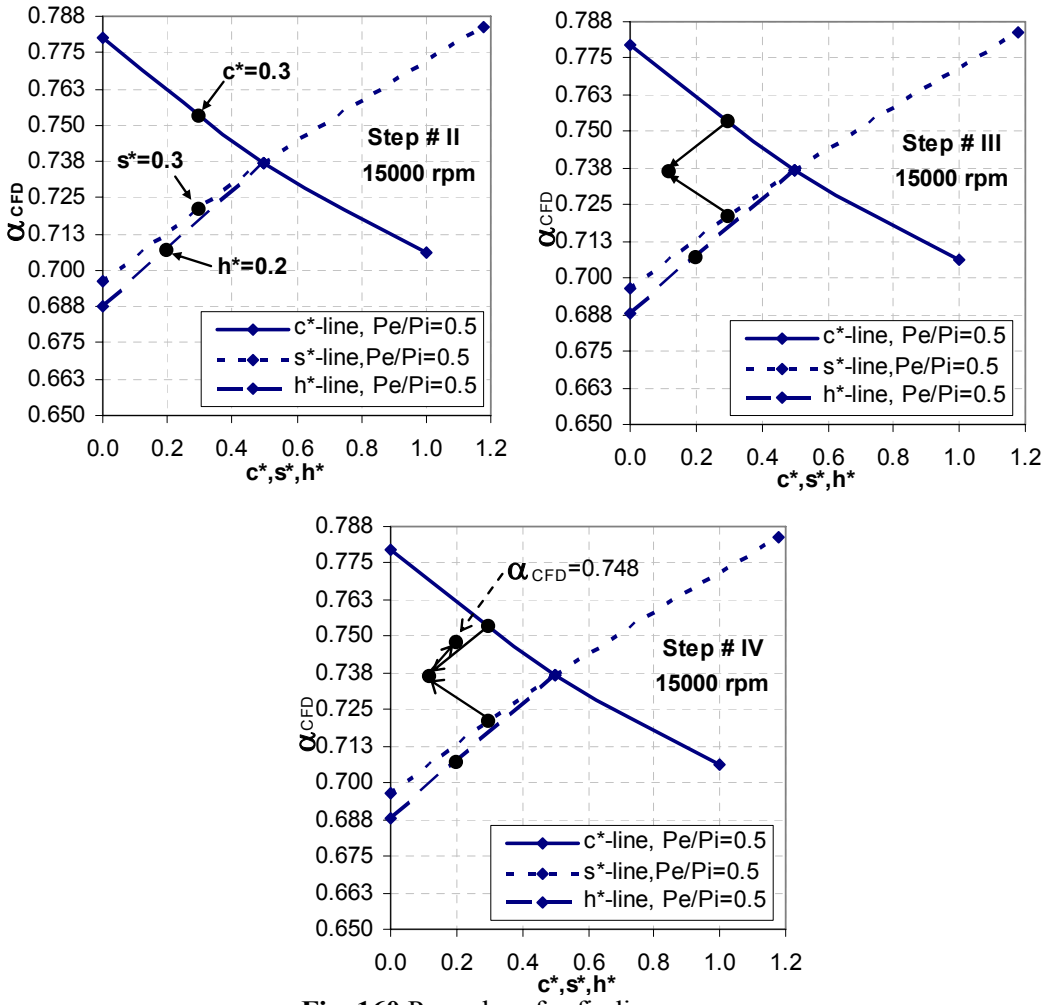

Fig. 160 Procedure for finding α_{CFD}.

the pitch line in the direction of the marked point on the clearance line. Then, mark the intersection of the new two lines, the point formed from this intersection corresponds to the total flow coefficient.

IV- The last step is to include the effect of cavity depth. From the intersection point in step three, draw a line parallel to the cavity line in the direction of the point marked on the cavity depth line (for this case h^*=0.2) until they interest (see Fig. 160 step IV). Then the total flow coefficient can be determined by projecting the last point into the y-axis to read (α_{CFD} = 0.748).

For calculating the flow coefficient inside the seal cavity repeat steps II-IV using the 15000 rpm part in Fig. 158. Fig. 161 demonstrates the procedure of calculating cavity flow coefficient α_{cavity}, and results in α_{cavity} = 0.197. Once we have the flow coefficients, the leakage flowrates can be calculated using Eqs. (31-33) and the ideal gas law equation.

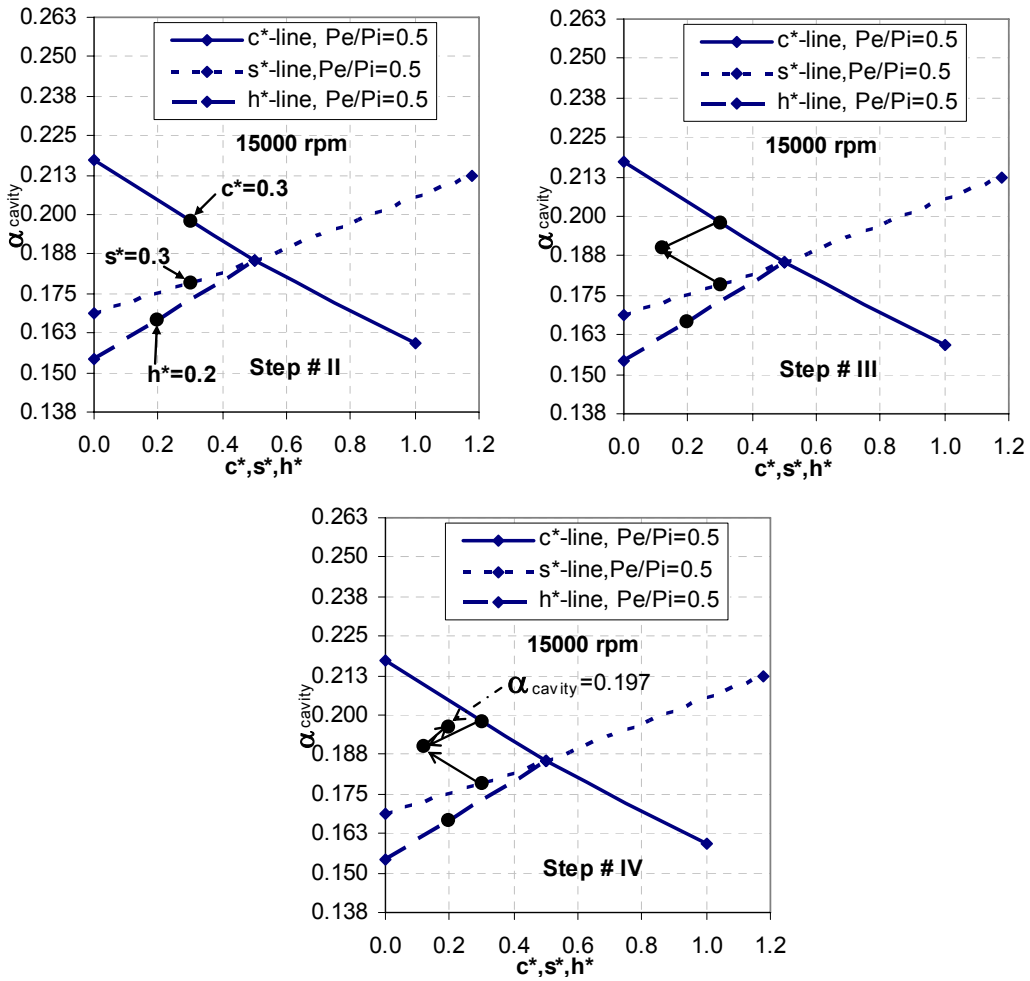

Fig. 161 Procedure for finding α_{cavity}.

(a) Calculation of the seal total leakage flowrate

$\gamma_{CFD} = 1.082$

$\alpha_{CFD} = 0.748$

$n = L/s \cong 7.49$

$\psi = 0.3027$

$A = \pi Dc$

$= 2.9355 \times 10^{-5}\ m^2$

$\rho_i = 202650/(300*287.04)$

$= 2.353\ kg/m^3$

$$\dot{m}_{total} = \alpha_{CFD} A \psi \gamma_{CFD} \sqrt{\rho_i P_i}$$
$$= 0.00497\ kg/s$$

(b) Calculation of the leakage flowrate in the seal cavity

$\alpha_{cavity} = 0.197$

$A_{cavity} = h(s-t)$

$= 0.00206(0.00339-0.000787)$

$= 5.36218 \times 10^{-6}\ m^2$

$DP = P_e - P_i = 101.325\ kPa$

$$\dot{m}_{cavity} = \alpha_{cavity} A_{cavity} \sqrt{\rho_i DP}$$
$$= 0.197(5.36218x10^{-6})\sqrt{2.353(101325)}$$
$$= 0.00052\ kg/s$$

(c) Maximum average circumferential velocity in the seal cavity

$\rho_{atm} = 101325/(300*287.04)$

$= 1.177\ kg/m^3$

$$V_{\theta,average} = \dot{m}_{cavity} / (\rho_{atm} A_{cavity})$$
$$= 82.4 \quad m/s$$

(d) Maximum average axial velocity within seal clearance.

$$V_{x,average} = (\dot{m}_{total} - \dot{m}_{cavity}) / (\rho_{atm} A)$$
$$= 128.8\ m/s$$

The calculation of the axial and circumferential velocity gives an idea about the performance of the windback seal in preventing oil contamination (oil-mist or oil droplets). Higher axial velocities will prevent oil droplet from transport to the neighboring cavity in the

upstream direction of the flow, while higher circumferential velocity in the seal cavities cleans out the oil-mist or oil droplets in the downstream direction of the flow. This agrees with Boyman and Suter [23] visualization test for labyrinth seals. On the other hand, when an oil droplet or oil-mist enters the cavity of a labyrinth seal through back flow or during machine start up or shut down, the 360° labyrinth seal cavities will increase the probability of oil droplets transport in the opposite direction of the axial flow (back-flow). While for the windback seals under study, the existence of the helical cavity will greatly reduce the oil back flow.

SUMMARY AND CONCLUSIONS

The primary objective of this study is to compare the CFD simulations to measurements to evaluate a prediction tool and then performing simulations to: (i) develop a better understanding of the flow physics of the windback seal, and (ii) develop a design methodology for the windback seal. Two seals with geometrical parameters given in Table 5 were experimentally tested and numerically simulated. The κ-ε turbulent flow model with enhanced wall treatment was used in these simulations.

CFD Code Validation

Windback Seal

The following results were observed when comparing the measurements and predictions:

- Measured leakage flowrates were predicted within 5%.
- Leakage flowrate increases slightly with increasing rotor speed from 0 to 15000 rpm within 2% and 4.5% at high and low pressures, respectively.
- Predictions show almost a uniform pressure gradient across the seal, while measurements show an increasing negative axial pressure gradient except at the seal inlet and exit.
- CFD simulations predict well the inlet head losses and exit pressure recovery.
- CFD simulation under-predicts the static pressure by a maximum of 10% of the absolute pressure values. The pressure measurements show compressibility effects, even though the flow was never choked with maximum Mach number of 0.25 and 0.52 in the seal cavities and clearance, respectively.
- CFD simulations under-predict V_θ in the second cavity and over predicts it in the sixth cavity, the maximum difference between measured and CFD predictions of V_θ are around 45% at low pressure. V_θ increases with increasing the rotor speed from 0 to 15000 rpm by 80% at high pressure. This result is consistent with the difference in measured and predicted axial pressure distributions.
- Pressure and velocity measurements and predictions were consistent, over-predicting pressure drops, over-predicting velocity.

- Increasing eccentricity ratio up to 0.25 for a 0.1 mm clearance windback seal increases the flow coefficient by a maximum 1.5%. Eccentricity has no effect on static pressure distribution.

Smooth Seal

The following were observed when comparing the measurements and predictions:

- Depending on *DP* and rotor speed, the flow within the smooth seal was classified as a laminar, turbulent, or transitional flow. Two CFD simulation models were used to predict the leakage flowrates. The turbulent flow model does a better job at high rotor speeds, while the laminar flow model performs much better at 0 rpm. The laminar flow model over-predicts leakage flowrate at 0 rpm and for all *DP*'s by a maximum of 2.5% and by 11% at high pressure and 15000 rpm. The turbulent flow model under predicts leakage flowrate by 15% at low pressure and 0 rpm and by 8% at high pressure and 15000 rpm.
- The measured leakage flowrate decreases with increasing rotor speed by 10% compared to 3% predicted by simulations, and is independent of *DP*.
- Both CFD models under-predict pressure local measurement by a maximum of 50%. Measurements show larger compressibility effects than CFD simulations.
- The leakage mass flowarte and pressure distributions show high sensitivity to eccentricity. Increasing eccentricity ratio up to 0.25 for a 0.1 mm clearance smooth seal increases the flow coefficient by a maximum of 11%. Positive eccentricities of the seal show higher pressure gradient than for the concentric position, while negative eccentricities show lower pressure gradient.

Numerical Simulation Results

The common characteristics, which all windback seals share, can be summarized in the following:

- Static pressure contours show that the pressure decreases in both axial direction and along the cavity axis. The pressure across each cavity in the axial direction is constant. This indicates that there is no pressure recovery within the seal cavity, and all losses in kinetic energy are dissipated through viscous dissipation, unlike labyrinth seals. However, the pressure difference across the seal is much smaller for the windback which may explain the difference.

- CFD simulations show there is a helical vortex within the seal cavity. Its strength increases with increasing rotor speed, *DP*, cavity depth, tooth pitch, number of tooth starts, and clearance.
- Axial velocity increases in the axial direction within the seal clearance, mainly due to the decrease in density and a small percent increase, due to the kinetic energy carry over from previous stages.
- Mass flowrate in the tangential direction is almost constant, within 5%. Up-flow radial velocity in the downstream portion of the cavity is higher than the down flow radial velocity in the upstream portion of the cavity, due to the axial jet flow under the tooth. This results in the vortex axis being located downstream of the cavity center.
- Vortex strength increases in the axial direction, as a result of pressure drop across the seal. It increases with *DP*, rotor speed and clearance.
- Mass flux in the seal cavities is nearly constant in the axial direction except for the first and last cavities.
- Shaft speed has no effect on static pressure, due to the low viscosity of air.
- Leakage flowrate increases linearly with increasing *DP*.
- Increasing rotor speed increases leakage flowrate within the seal cavity due to the increase in V_θ as a result of rotor drag.
- Increasing rotor speed decreases leakage flowrate under the tooth due to the increase in the frictional losses in the tooth/rotor clearance.
- Rotor speed has more effect on increasing V_θ, specifically when V_x is less than V_θ, at low pressure, due to the higher shear stresses in circumferential direction.
- Shaft speed has a limited maximum effect on increasing leakage flowrate and α with a maximum increase at the highest pressure ratios (low *DP*).
- The CFD accurately predicts leakage flowrate, and rpm effects are well represented, so only a 0 rpm measurement is needed to verify the CFD simulations.

The effects of variable geometrical parameters of a windback seal such as clearance, tooth height, tooth pitch and the number of tooth starts on the leakage flowrate were studied and summarized as follows.

Effect of Clearance

- Increasing the seal clearance increases the leakage flowrate in almost a linear relationship, with a percent higher than the increase in cross sectional area. Rotor speed affects most the lowest clearance seal with a 12.4% maximum increase in leakage flowrate at low *DP*.
- Increasing clearance increases the strength of the vortex in the cavity, although there is an optimum radial clearance where the percent increase in vorticity, due to increase in the rotor speed and *DP*, is maximum, which is the 0.1 mm seal clearance for this study.
- Increasing the seal clearance increases the carry over coefficient and decrease the flow spread angle β. β increases with decreasing clearance and with lowering *DP*. The rotor speed has a small effect on β. β approaches a constant value with increasing *DP* and clearance. The carry over coefficient for windback seals in this study is smaller than γ proposed by Hodkinson [12] for labyrinth seals and is sensitive to *DP*'s below 2 *atm* for c=0.15. Decreasing clearance to 0.05 mm requires *DP* to be more than 1 *atm* to see the effect of carry over.
- Increasing the seal clearance increases V_x within the seal clearance, and increases and decreases V_r and V_θ, respectively, within the seal cavities. Lower seal clearances increase the percent leakage within the seal cavities. Increasing rotor speed and decreasing *DP*, increases the percent leakage mass flowrate in the seal cavities and lowers it under the tooth.
- Static pressures have similar distributions for different seal clearances with no rpm effect.

Effect of Cavity Depth

- Decreasing the cavity depth decreases the leakage flowrate. Cavity depth of 1.47 mm leaks less than a smooth seal at high pressure and up to 10000 rpm. Increasing the cavity depth increases V_θ and V_r and hence, increases the vortex strength within the seal cavity. For $h \neq 0$, static pressure and the axial velocity distributions are similar within the seal clearance.

Effect of Tooth Pitch

- Increasing the tooth pitch increases leakage flowrate in a linear relationship. Decreasing the effective number of tooth from $n \cong 8$ to 6 increases the flowrate by 21% with small rpm effect. Higher seal pitches result in a smaller percent leakage rate under tooth and higher percentage through the seal cavity for all differential pressures and rotor speeds.

- Increasing the tooth pitch increases all velocity components, and strengthens the vortices within the seal cavity.
- All axial pressure distributions follow the same trend with step pressure changes, all following maximum and minimum limits.
- At 0 rpm, increasing *DP* does not change the percent of leakage flowrate within the seal cavity and under the seal tooth.

Effect of Number of Tooth Starts

- Increasing the number of tooth starts increases V_θ.
- V_x, V_r and P are similar for both one and two starts seal.
- Higher number of starts results in stronger vorticies in the cavities.
- Increasing the number of starts increases the total leakage flowrate.
- Two-starts seal results in a smaller percent leakage rate under the tooth and higher percentage through the seal cavities for all differential pressures and rotor speeds.

Based on this work, an optimum windback seal design can be described. If the main objective of the seal is just to minimize the leakage flowrate, labyrinth seals will do the job, using the smallest operational seal clearance available. However, the main objective of a windback seal is to keep contamination out and at the same time minimizing the leakage flowrate. One should ask the question, what geometrical parameters affect these two objectives? In this work, we studied the effect of seal clearance, tooth pitch, cavity height and tooth number of start on leakage flowrate and flow field variables to answer this question. Considering the same DP and rotor speed for all comparisons, smaller clearance seal results in smaller leakage rate with low axial velocity under the tooth and high circumferential velocity in the seal cavity, compared to larger clearance seal. In addition, vortex strength increases with increasing clearance, so there is an optimum value for the seal clearance and in this study it was the 0.1 mm clearance seal, where it leaks less than the 0.15 mm seal with almost the same flow characteristics in terms of velocities. While the 0.05 mm seal leaks the least, the weak vortices in the seal cavity do not qualify it for keeping the oil contamination out. Decreasing the cavity height from h=2.94 mm to 1.47 mm decreases the leakage flowrate by a small mount, by reducing the cavity area to half, while in the same time reducing the circumferential velocity almost to half at 0 rpm. At high shaft speed, both cavity depths perform similar in terms of velocity distributions. Higher cavity depth also results in stronger vortices, hence h=2.94 mm

will be the optimum value in this case. Increasing the tooth pitch (reducing the effective number of teeth or increasing the helix angle) and fixing all other seal geometry parameters, will increase the leakage flowrate and at the same time increase the velocity and hence the vorticity, compared to lower tooth pitches. Therefore, the leakage rate needed to keep contamination out determines what tooth pitch to choose. However, if we are dealing with a predetermined seal length, and higher vortices strength is required, increasing the tooth pitch will be one solution, the other solution is to double the number of tooth starts. The later will increase the circumferential velocity in the seal cavity greatly, especially at no rotation condition, with similar axial and radial velocity distributions. The leakage of the one and two tooth start seals is the same from under the tooth, while in the cavity the leakage rates for the one-start is much lower than the two-start seal.

The Fluent CFD numerical simulation program can accurately predict the leakage flowrate of windback seals within 5%. In addition, the CFD simulations provide detailed information of all flow field variables of interest such as velocity and pressure distributions. Hence, the CFD presents an effective tool for studying the performance of windback seals, and ultimately minimizing the seal leakage flowrate without degrading its performance. A 2D graphical based design tool for windback seals was introduced to determine the total and cavity leakage flowrates and hence the maximum axial and circumferential velocities for different seal geometrical parameters. Wall shear stress magnitude and the shear stress in the circumferential direction were calculated in the seal cavities to give an idea if they are large enough to displace oil residue from the seal cavities and present a starting point for future work.

REFERENCES

[1] Dresser-Rand, 2006, "Windback Seals," Houston, TX, http://www.dresser-rand.com/, Web Site accessed January 2006.

[2] John Crane USA, 2006, "High Pressure, Gas Lubricated, Non-Contacting Gas Seal for Turbo Compressors Type 28EXP," Houston, TX, http://www.johncrane.com/amer/english/product/28exp.html/, Web Site accessed October 2006.

[3] Gansle, A., and Childs, D., 1996, "Experimental Leakage and Rotordynamic Results for Helically Grooved Annular Gas Seals," ASME Trans., J. of Engineering for Gas Turbines and Power, **118**, pp. 389-393.

[4] Bootsma, J., 1975, "Liquid – Lubricated Spiral – Groove Bearings," Ph.D. thesis. Technology University Delft, Delft, Netherlands.

[5] Sneck, H. J., 1974, "Labyrinth Seal Literature Survey," Journal of Lubrication Technology, **96**, pp.579-582.

[6] Parsons, C. A., 1938, "The Labyrinth Packing," The Engineer, **165**, No.4280, January 21, pp.83-84.

[7] Cogan, K. C., 1982, "Leakage Prediction of Incompressible Fluids in Labyrinth Seals," M.S. thesis. Texas A&M University, College Station, Texas.

[8] Martin, H. M., 1908, " Labyrinth Packings," Engineer, **85**, Jan. 10, 1908, pp.35-38.

[9] Stodola, A., *Steam and Gas Turbines*, 6th edition, McGraw-Hill, NewYork 1, 1927.

[10] Dollin, F., and Brown, W. S., "Flow of Fluids through Openings in Series," Engineer, **164**, No. 4259, Aug. 27, 1937, pp.223-224.

[11] Egli, A., 1935, "The Leakage of Steam through Labyrinth Seals," Trans. ASME, **57**, pp. 115-122.

[12] Hodkinson, B., 1939, "Estimation of the Leakage through a Labyrinth Gland," Proceedings of the Institute of Mechanical Engineers, **141**, pp. 283-288.

[13] Zabriskie, W., and Sternlicht, B., "Labyrinth Seal Leakage Analysis," Journal of Basic Engineering, Trans. ASME, Series D, **81**, No.3, Sept. 1959, pp.332-340.

[14] Heffner, F. E., "A General Method for Correlating labyrinth Seal Leak-Rate Data," Journal of Basic Engineering, Trans. ASME, Series D, **82**, No.2, June 1960, pp.265-275.

[15] Prasad, B. V. S. S. S., Sethu Manavalan, D. L., Nanjunda Rao, N. V., 1997, "Computational and Experimental Investigations of Straight-Through Labyrinth Seals," ASME Paper 97-GT-326, International Gas Turbine and Aeroengine Congress and Exhibition, Orlando, Florida, June 2-June 5.

[16] Rhode, D. L., and Hibbs, R. I., 1986, "A comparative Investigation of Corresponding Annular and Labyrinth Seal Flow fields," ASME Paper No. 89-GT-195, International Gas Turbine and Aeroengine Congress and Exhibition, Toronto, Ontario, Canada, June 4-June 8.

[17] Yucel, T., and Kazakia, J. Y., 2001, "Analytical Predictions Techniques for Axisymmetric Flow in Gas Labyrinth Seals," ASME Journal of Engineering for Gas Turbines and Power, **123**, pp. 255-257.

[18] Willenborg, K., Kim, S., and Wittig, S., 2001, "Effects or Reynolds Number and Pressure Ratio on Leakage Loss and Heat Transfer in a Stepped Labyrinth Seal," ASME Journal of Turbomachinery, **123**, pp. 815-822.

[19] Komotori, K., and Miyake, K., 1977, "Leakage Characteristics of Labyrinth Seals with High Rotating Speed," 1977 Tokyo Joint Gas Turbine Congress, pp. 371-380.

[20] Stocker, H. L., 1975, "Advanced Labyrinth Seal Design Performance for High Pressure Ratio Gas Turbines," ASME Paper 75-WA/GT-22, Winter Annual Meeting, Houston, Texas, November 30-December 4.

[21] Waschka, W., Wittig, S., and Kim, S., 1992, "Influence of High Rotational Speeds on the Heat Transfer and Discharge Coefficients in Labyrinth Seals," ASME Journal of Turbomachinery, **114**, pp. 462-468.

[22] Zimmermann, H., and Wolff, K. H., 1998, "Air System Correlations, Part 1: Labyrinth Seals," ASME Paper 98-GT-206, International Gas Turbine and Aeroengine Congress and Exhibition, Stockholm, Sweden, June 2-June 5..

[23] Boyman, T., and Suter, P., 1978," Transport Phenomena in Labyrinth-Seals of Turbomachines," AGARD **CP-237**, pp. 8-1-8-10.

[24] Park, S.-Y., and Rhode, D. L., 2003, "Predicted Effects of Bearing Sump and Injection Pressure on Oil Labyrinth Leakage," ASME J. Eng. Gas Turbines Power, **125**, pp. 316-325.

[25] Park, S.-Y., and Rhode, D. L., 2003, "Predicted Geometry Effects on Oil Vapor Flow Through Buffer Gas Labyrinth Seals," ASME J. Eng. Gas Turbines Power, **125**, pp. 193-200.

[26] Kaul, A., 1999, "Design and Development of a Test Setup for the Experimental Determination of the Rotordynamic and Leakage Characteristics of Annular Bushing Oil Seals," M.S. thesis. Texas A&M University, College Station, Texas.

[27] Kline, S. J., McClintock, F. A., 1953, "Describing Uncertainties in Single-Sample Experiments," Mechanical Engineering, **75**, pp. 3-8.

[28] Szeri, A., *Tribology: Friction, Lubrication, and Wear*, McGraw-Hill, NewYork, 1980.

[29] Pinkus, O., Sternlicht, B., *Theory of Hydrodynamic Lubrication*, McGraw Hill Book, NewYork, 1961.

APPENDIX A

This Appendix contains high resolution contour plots of the velocity components and the pressure distribution field for a windback seal with the following geometrical parameters:

Seal type	Windback single start
Clearance, c(mm)	0.1
Pitch, s(mm)	3.56
Cavity depth, h(mm)	2.94
Tooth thickness, t(mm)	0.79
Length, L(mm)	25.4
Shaft diameter, D(mm)	116.81

The contour plots were shown for four axial sectional views, 90° apart in the circumferential direction of the seal. Under the 270° sectional view, the clearance area was enlarged for the whole seal length and clearance. A 2D vector plot of the axial and radial velocities in the enlarged clearance area is shown on top of the contour plot of the circumferential velocity component. The seal was numerically simulated for three differential pressures: 103.4 *kPa*, 68.9 *kPa*, and 34.5 *kPa* (15 *psi*, 10 *psi*, and 5 *psi*), and four rotor speeds: 0 rpm, 5000 rpm, 10000 rpm, and 15000 rpm.

Appendix A can be found in a separate attached file in *pdf* format, under the name *Appendix A.pdf*.

APPENDIX B

This Appendix contains high resolution contour plots of the velocity components and the pressure distribution field for a smooth seal with the following geometrical parameters:

Seal type	Smooth
Clearance, c(mm)	0.1
Pitch, s(mm)	0
Cavity depth, h(mm)	0
Tooth thickness, t(mm)	25.4
Length, L(mm)	25.4
Shaft diameter, D(mm)	116.81

The smooth seal was numerically simulated using a 2D model. The contour plots of the velocity components and pressure field are presented. The clearance area was enlarged for the whole seal length and clearance. A 2D vector plot of the axial and radial velocities in the enlarged clearance area is shown on top of the contour plot of the circumferential velocity component. The seal was numerically simulated for three differential pressures: 103.4 *kPa*, 68.9 *kPa*, and 34.5 *kPa* (15 *psi*, 10 *psi*, and 5 *psi*), and four rotor speeds: 0 rpm, 5000 rpm, 10000 rpm, and 15000 rpm.

Appendix B can be found in a separate attached file in *pdf* format, under the name *Appendix B.pdf*.

APPENDIX C

This Appendix contains high resolution contour plots of the velocity components and the pressure distribution field for a windback seal with the following geometrical parameters:

Seal type	Windback single start
Clearance, c(mm)	0.05
Pitch, s(mm)	3.56
Cavity depth, h(mm)	2.94
Tooth thickness, t(mm)	0.79
Length, L(mm)	25.4
Shaft diameter, D(mm)	116.81

The contour plots were shown for four axial sectional views, 90° apart in the circumferential direction of the seal. Under the 270° sectional view, the clearance area was enlarged for the whole seal length and clearance. A 2D vector plot of the axial and radial velocities in the enlarged clearance area is shown on top of the contour plot of the circumferential velocity component. The seal was numerically simulated for three differential pressures: 103.4 *kPa*, 68.9 *kPa*, and 34.5 *kPa* (15 *psi*, 10 *psi*, and 5 *psi*), and four rotor speeds: 0 rpm, 5000 rpm, 10000 rpm, and 15000 rpm.

Appendix C can be found in a separate attached file in *pdf* format, under the name *Appendix C.pdf*.

APPENDIX D

This Appendix contains high resolution contour plots of the velocity components and the pressure distribution field for a windback seal with the following geometrical parameters:

Seal type	Windback single start
Clearance, c(mm)	0.15
Pitch, s(mm)	3.56
Cavity depth, h(mm)	2.94
Tooth thickness, t(mm)	0.79
Length, L(mm)	25.4
Shaft diameter, D(mm)	116.81

The contour plots were shown for four axial sectional views, 90° apart in the circumferential direction of the seal. Under the 270° sectional view, the clearance area was enlarged for the whole seal length and clearance. A 2D vector plot of the axial and radial velocities in the enlarged clearance area is shown on top of the contour plot of the circumferential velocity component. The seal was numerically simulated for three differential pressures: 103.4 *kPa*, 68.9 *kPa*, and 34.5 *kPa* (15 *psi*, 10 *psi*, and 5 *psi*), and four rotor speeds: 0 rpm, 5000 rpm, 10000 rpm, and 15000 rpm.

Appendix D can be found in a separate attached file in *pdf* format, under the name *Appendix D.pdf*.

APPENDIX E

This Appendix contains high resolution contour plots of the velocity components and the pressure distribution field for a windback seal with the following geometrical parameters:

Seal type	Windback single start
Clearance, c(mm)	0.1
Pitch, s(mm)	3.56
Cavity depth, h(mm)	1.47
Tooth thickness, t(mm)	0.79
Length, L(mm)	25.4
Shaft diameter, D(mm)	116.81

The contour plots were shown for four axial sectional views, 90° apart in the circumferential direction of the seal. Under the 270° sectional view, the clearance area was enlarged for the whole seal length and clearance. A 2D vector plot of the axial and radial velocities in the enlarged clearance area is shown on top of the contour plot of the circumferential velocity component. The seal was numerically simulated for three differential pressures: 103.4 *kPa*, 68.9 *kPa*, and 34.5 *kPa* (15 *psi*, 10 *psi*, and 5 *psi*), and four rotor speeds: 0 rpm, 5000 rpm, 10000 rpm, and 15000 rpm.

Appendix E can be found in a separate attached file in *pdf* format, under the name *Appendix E.pdf*.

APPENDIX F

This Appendix contains high resolution contour plots of the velocity components and the pressure distribution field for a windback seal with the following geometrical parameters:

Seal type	Windback single start
Clearance, c(mm)	0.1
Pitch, s(mm)	4.14
Cavity depth, h(mm)	2.94
Tooth thickness, t(mm)	0.79
Length, L(mm)	25.4
Shaft diameter, D(mm)	116.81

The contour plots were shown for four axial sectional views, 90° apart in the circumferential direction of the seal. Under the 270° sectional view, the clearance area was enlarged for the whole seal length and clearance. A 2D vector plot of the axial and radial velocities in the enlarged clearance area is shown on top of the contour plot of the circumferential velocity component. The seal was numerically simulated for three differential pressures: 103.4 *kPa*, 68.9 *kPa*, and 34.5 *kPa* (15 *psi*, 10 *psi*, and 5 *psi*), and four rotor speeds: 0 rpm, 5000 rpm, 10000 rpm, and 15000 rpm.

Appendix F can be found in a separate attached file in *pdf* format, under the name *Appendix F.pdf*.

APPENDIX G

This Appendix contains high resolution contour plots of the velocity components and the pressure distribution field for a windback seal with the following geometrical parameters:

Seal type	Windback single start
Clearance, c(mm)	0.1
Pitch, s(mm)	3.12
Cavity depth, h(mm)	2.94
Tooth thickness, t(mm)	0.79
Length, L(mm)	25.4
Shaft diameter, D(mm)	116.81

The contour plots were shown for four axial sectional views, 90° apart in the circumferential direction of the seal. Under the 270° sectional view, the clearance area was enlarged for the whole seal length and clearance. A 2D vector plot of the axial and radial velocities in the enlarged clearance area is shown on top of the contour plot of the circumferential velocity component. The seal was numerically simulated for three differential pressures: 103.4 *kPa*, 68.9 *kPa*, and 34.5 *kPa* (15 *psi*, 10 *psi*, and 5 *psi*), and four rotor speeds: 0 rpm, 5000 rpm, 10000 rpm, and 15000 rpm.

Appendix G can be found in a separate attached file in *pdf* format, under the name *Appendix G.pdf*.

APPENDIX H

This Appendix contains high resolution contour plots of the velocity components and the pressure distribution field for a windback seal with the following geometrical parameters:

Seal type	Windback double start
Clearance, c(mm)	0.1
Pitch, s(mm)	7.12
Cavity depth, h(mm)	2.94
Tooth thickness, t(mm)	0.79
Length, L(mm)	25.4
Shaft diameter, D(mm)	116.81

The contour plots were shown for four axial sectional views, 90° apart in the circumferential direction of the seal. Under the 270° sectional view, the clearance area was enlarged for the whole seal length and clearance. A 2D vector plot of the axial and radial velocities in the enlarged clearance area is shown on top of the contour plot of the circumferential velocity component. The seal was numerically simulated for three differential pressures: 103.4 *kPa*, 68.9 *kPa*, and 34.5 *kPa* (15 *psi*, 10 *psi*, and 5 *psi*), and four rotor speeds: 0 rpm, 5000 rpm, 10000 rpm, and 15000 rpm.

Appendix H can be found in a separate attached file in *pdf* format, under the name *Appendix H.pdf*.

VITA

Adnan Mahmoud Al-Ghasem was born in October 1973. In September 1991 after finishing high school, he was admitted to Jordan University of Science and Technology (JUST). He graduated with a B.Sc. degree in mechanical engineering in June 1996. He continued his education and graduated in February 1999 with a M.Sc. degree in mechanical engineering. Adnan was distinguished through his undergraduate and graduate studies, graduating from both with the first rank. He worked as a full time lecturer in the Department of Mechanical Engineering at JUST from February 1999 to August 2001.

In September 2001, Adnan was admitted to Texas A&M University in the Department of Mechanical Engineering. He graduated with a M.S. degree in May 2004. He received his Ph.D. degree in Mechanical Engineering from Texas A&M University in May 2007.

Adnan married in December 2000, and is blessed with three wonderful children: Mahmoud, born in May 2002, Salma, born in August 2003 and Mohammad born in April 2006.

Dr. Adnan Mahmoud Al-Ghasem
Mechanical Engineering Department
Jordan University of Science and Technology
Irbid 22110 - Jordan
Email address: adnan_jaradat@hotmail.com